Curvature in carbon π-conjugated systems: a theoretical and computational study

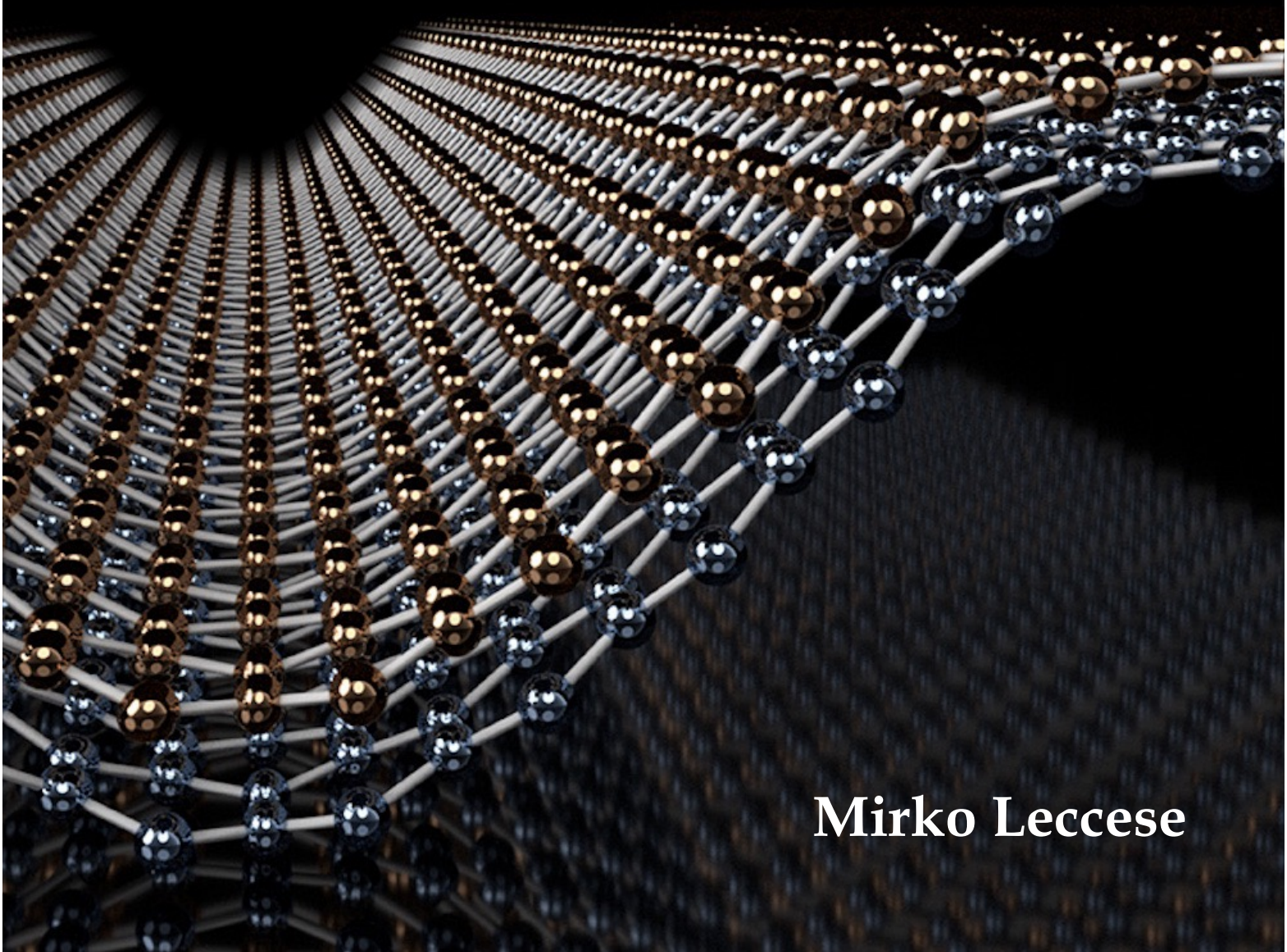

Mirko Leccese

Curvature in carbon π-conjugated systems: a theoretical and computational study

by
Mirko Leccese

Professor Rocco Martinazzo

A thesis submitted in fulfillment
of the requirements for the
Doctor of Philosophy in Chemistry

University of Milan
Milan, Italy
March 6, 2022

Preface

My Ph.D. course has been focused on the theoretical study of curved π-conjugated carbon nanostructures, with the purpose of providing a mathematically rigorous description of curvature and its effect on the chemical and physical properties. For a long time, π-conjugation and aromaticity were considered a unique feature of planar carbon structures. During the last decades, however, the progress of synthesis and material characterization has provided us with a large number of curved π-conjugated structures (annulenes, circulenes, coroannulenes, fullerenes, rippled graphene, etc), thus proving that π-conjugation - and its effect on chemical and physical properties - can exist also in a curved environment. This work was suggested by my supervisor Prof. R. Martinazzo, who recognized during my graduate work my great interest in Mathematics and invited me to join him in the discovery of the *curved world*. The topic was thus approached from two points of view: we selected some curved π-systems - that are interesting from both a fundamental and technological perspective - and we investigated their structures and reactivity through computational methods; meanwhile, we got our hands on maths, and in particular on a field called *differential geometry*, to track down those tools that allow to rigorously describe the curvature of carbon structures - something that, to the best of our knowledge, had not yet done in the literature.

This work is organized into three Parts. Part I and Part II contain the results of our computational investigation. The main attention was given to the study of the H adsorption energetics, a simple reaction that is however relevant in disparate fields, from astrochemistry to hydrogen storage and graphene technology. In Part I, this reaction is considered in a "flat context", which allows us to introduce basic concepts - related to π-conjugation - that are important also for the understanding of the curved world. This Part is a natural development of my graduate Thesis work - which was focused on planar graphene - and is a report of my first year of Ph.D. activity.

In particular, Chapter 1 and 2 are two introductory chapters that present *known* results on flat graphene and polycyclic aromatic hydrocarbons (PAHs) and the H sticking, together with their relevant applications. Chapter 4 contains the results of our Density Functional Theory (DFT) investigation of the stepwise H addition to the *coronene* molecule, a small flat PAH. The choice of the exchange-correlation (XC) functional represented an important part of the work on coronene and is thus extensively discussed in Chapter 3. Chapter 5 is dedicated instead to large PAH clusters.

Part II is entirely devoted to curved systems. Chapter 6 sets the beginning of our *journey* through the curved world and is dedicated to the description of the main curved carbon nanostructure. Emphasis is given here to introduce the systems we investigated: curved PAH such as *coroannulene*, and the *C/Si interface*. Thus, Chapter 7 presents the study of the stepwise H addition to coroannulene. This Chapter is closely related to Chapter 4 since coroannulene can be considered as the curved analog of coronene. Chapter 8 describes the H sticking on a periodic system, namely graphene epitaxially grown on SiC, a.k.a. the C/Si interface. Here, the curvature is due to the interaction of graphene with the substrate. The subsequent Chapter describes a quantum dynamical investigation of the *Eley-Rideal reaction* - leading to the formation of molecular hydrogen - on the C/Si

interface. This work was done during my stay in Toulouse, as a visiting student in the group of Prof. D. Lemoine.

In Part III, the problem of curvature is approached from a conceptual perspective. In particular, Chapter 11 introduces a new model we set up to describe the local curvature at carbon atoms and its relationship with the hybridization - a first step in the development of a new theoretical framework for curved π-systems. The mathematics needed to understand our model is presented in Chapter 10. The latter grew larger than expected but the author used the time of writing as the right moment to re-organized what he learned with enthusiasm during the years of his Ph.D. (in this regard, a good thing (the only one!) of the lockdown during the first COVID-19 outbreak was to give me a lot of time to spend on differential geometry). Finally, in Chapter 12, we draw our conclusions on the work.

List of Abbreviations

STM Scanning Tunnelling Microscopy x
PAH Polycyclic Aromatic Hydrocarbon i
POAV π-Orbital Vector Analysis 66
PDR PhotoDissociation Region 33
PBE Perdew-Burke-Ernzerhof vii
PW Plane Wave vi
QFMLG Quasi-Freestanding Monolayer Graphene 80
UHV Ultra High Vacuum 87
UIE Unidentified Infrared Emission 35
UV UltraViolet 27
vdW van der Walls 118
VV Vydrov and Van Voorhis 44
ZLG Zero Layer Graphene 82
ZPE Zero Point Energy viii
XC Exchange-Correlation i
WIM Warm Ionized Medium 31

List of Tables

List of Figures

Contents

Part I

Carbons in a *flat* world

Chapter 1

Graphene and the H sticking

"*Table, table on the wall, who is the fairest of them all?*". This question, which may sound familiar but odd to a child, has an obvious answer for a chemist: carbon (C). Thanks to its unique properties, carbon is able to form any sort of structure, from simple to complex molecules such as proteins, from 0D to 3D materials. Not by chance, *nature* has thus chosen carbon as the building block of Life. Among the *huge* family of carbon nanostructures, *graphene* is undoubtedly the one that has most attracted the interest of the scientific community in recent years. Graphene is the fewest layer limit of graphite, *i.e.* a two-dimensional sheet of sp^2-hybridized carbon atoms with an extended honeycomb lattice. Its history began in the long 1947 when Wallace[1] wrote a pioneering paper about the electronic structure of a (still theorized) single-layer graphene. For a long time, graphene remained however just a dream of material scientists, and any hope for its experimental observation was lost by strong theoretical arguments (the Mermin's theorem[2], see Box 1.1 on pag. 4) suggesting the inexistence of strictly 2D material - due to intrinsic thermodynamical instability. Surprisingly, in 2004 Novoselov and Geim[3] reported for the first time the development of a simple method to produce and observe few-layer graphene crystals on silicon wafers, thus ushering in the *graphene era*. The enthusiasm of this finding led to the winning of the Nobel Prize in Physics in 2010 for *"groundbreaking experiments regarding the two-dimensional material graphene"*.

Over the last seventeen years, the extraordinary electrical, thermal, and mechanical properties of graphene have generated huge interest for the large variety of possible applications, *e.g.* future generation of high-speed devices[4], thermally and electrically conductive reinforced composites[5], transparent electrodes for display[6], etc. From the chemical point of view, the functionalization of graphene through reactions with species such as H, F, or OH have been widely investigated as a mean to tune its electronic and magnetic properties[7, 8, 9, 10]. In particular, the reactivity of graphene towards H, one of the simplest reactions we can imagine, is of great interest because of its relevance in disparate fields such as astrophysics[11, 12], hydrogen storage[13], nuclear fusion[14], or, not least, graphene technology itself. Despite the numerous amount of both experimental and theoretical works, there are yet some issues in this field that require further investigation. In light of its importance, the sticking of an atomic H to carbon nanostructures was a major focus of this work and guided our understanding of the differences between flat and curved π-sistems, as stated in the Preface. In this Chapter, we review some of the key aspects of such reaction that are well understood, to establish the theoretical background for the comprehension of the next Chapters.

This Chapter is organized as follows: in Section 1, we describe the structure and main physical properties of graphene; in Section 2, we discuss its electronic structure; in Section 3 we extensively discuss the H sticking.

Box 1.1: The *Mermin's theorem* and the existence of graphene

In a paper of 1968 entitled "*Crystalline Order in Two dimensions*"[2], Mermin was able to prove a general result of statistical thermodynamics which excludes the existence of two-dimensional crystals. The theorem establishes that, if N particles interacting through a pair potential $\Phi(\boldsymbol{r})$, are in equilibrium in a parallelogram box, then every $\boldsymbol{k} \neq 0$ Fourier component of the one-particle density $\rho(\boldsymbol{r})$ must vanish in the thermodynamic limit. With this result, Mermin gave firmer ground to what was earlier theorized by Peierls[15] (1934), who gave both qualitative and quantitative arguments about the absence of long-range crystalline order in one-dimension based on the harmonic approximation. Similar conclusions were also reached by Landau[16] (1937), using his general theory of second-order phase transitions.
Apparently, the Mermin's theorem forbids the existence of graphene, which can be characterized experimentally by non-zero Fourier components of the density (*e.g.* with a STM experiment). However, even before the discovering of graphene, the relevance of the asymptotic behavior of the Fourier components of ρ was questioned by both computations and experiments (*e.g.* the Wigner crystallization of electrons on the surface of liquid He[17]). In case of graphene, there two more points to consider that accounts for its stability: (i) graphene is actually "extracted" from stable 3D phase, *i.e. graphite*; (ii) as we shall see in Part II, graphene is actually *not* flat, but it displays corrugations in most of the experimental setups.

1.1 Structure and properties

1.1.1 The honeycomb lattice

Graphene consists of a network of sp^2 carbon atoms forming a honeycomb structure. Strictly speaking, the latter is not a *Bravais lattice*, which requires by definition that, for any choice of direction, the lattice has to appear the same from each of the discrete lattice points when looking in that chosen direction. On graphene, we can instead identify two sets of non-equivalent sites (a.k.a. sublattices). Naming A and B such sites, we note from Figure 1.1 (b) that each A has nns in the north-east, north-west, and sud directions, while B has nns in the north, sud-east, and sud-west directions. Nevertheless, both A and B sublattices are hexagonal (otherwise known as *triangular*) Bravais lattice, and therefore the crystal structure of graphene can be regarded as a hexagonal Bravais lattice with *two-atom basis*.

The three vectors ($\boldsymbol{\delta}_i$) connecting an A site with its nns on the opposite sublattice can be written in terms of a local orthogonal basis ($\boldsymbol{e}_x, \boldsymbol{e}_y$) as

$$\boldsymbol{\delta}_1 = \frac{a}{2}(\boldsymbol{e}_x + \sqrt{3}\boldsymbol{e}_y) \qquad \boldsymbol{\delta}_2 = \frac{a}{2}(\boldsymbol{e}_x - \sqrt{3}\boldsymbol{e}_y) \qquad \boldsymbol{\delta}_3 = -a\boldsymbol{e}_x$$

The basis vectors spanning the bipartite hexagonal lattice (*i.e.* those defining the unit cell) ($\boldsymbol{a}_i$) are

$$\boldsymbol{a}_1 = \frac{a}{2}(3\boldsymbol{e}_x + \sqrt{3}\boldsymbol{e}_y) \qquad \boldsymbol{a}_2 = \frac{a}{2}(3\boldsymbol{e}_x - \sqrt{3}\boldsymbol{e}_y)$$

where a is the C-C bond lenght, which is 1.42 Å in graphene, that is in between a single (≈ 1.54 Å) and double covalent bond (≈ 1.31 Å), due to the extendend π-conjugation.

The reciprocal lattice, shown in Figure 1.1 (a), is spanned by the following dual basis

$$\boldsymbol{a}_1^\star = \frac{2\pi}{3a}(\boldsymbol{e}_x + \boldsymbol{e}_y) \qquad \boldsymbol{a}_2^\star = \frac{2\pi}{3a}(\boldsymbol{e}_x - \sqrt{3}\boldsymbol{e}_y)$$

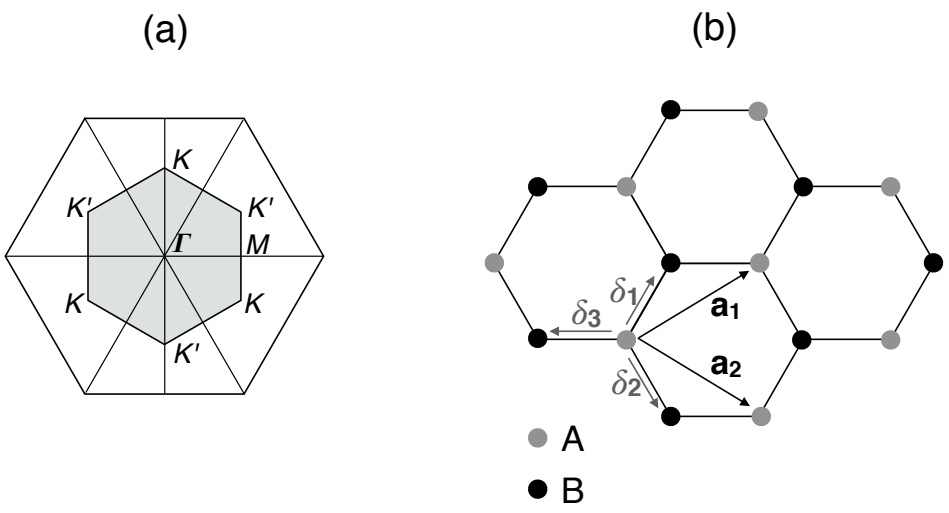

Figure 1.1. (a) Reciprocal lattice and irreducible Brillouin zone (grey) of graphene, with high-symmetry points; (b) Honeycomb lattice: $\boldsymbol{\delta}_i$ are vectors connecting each site with its nns on the opposite sublattice, $\boldsymbol{a}_i$ are basis vectors of the hexagonal lattice.

On the *irreducible Brillouin zone*, also depicted in Figure 1.1 (a), we can identify the high-symmetry points $\boldsymbol{K}$, $\boldsymbol{K'}$ and $\boldsymbol{M}$, which, in terms of $(\boldsymbol{e}_x, \boldsymbol{e}_y)$ are given by

$$\boldsymbol{K} = \frac{2\pi}{3a}\left(\boldsymbol{e}_x + \frac{1}{\sqrt{3}}\boldsymbol{e}_y\right) \qquad \boldsymbol{K'} = \frac{2\pi}{3a}\left(\boldsymbol{e}_x - \frac{1}{\sqrt{3}}\boldsymbol{e}_y\right) \qquad \boldsymbol{M} = \frac{2\pi}{3a}\boldsymbol{e}_x$$

In the following, we will show that the peculiar band structure of graphene around such high-symmetry points determines many of the unique properties of this material.

1.1.2 Physical and chemical properties

Here, we briefly summarize the main physical and chemical properties of graphene. For a more comprehensive discussion, the reader is referred to the excellent reviews by Neto et. al. (2009)[18] and Allen et. al. (2009)[19].
Many of the extraordinary properties of graphene arise from the combination of its dimensionality and its peculiar electronic band structure (that is discussed in detail in the next Section). The band structure, shown in Figure 1.4, around the $\boldsymbol{K}$ symmetry point is indeed responsible for a very curious behavior of the electrons, namely that they mimic *relativistic particles*, moving like they have lost their rest mass. Due to such a unique feature, graphene has first become a *physics toy* to study the relativistic effects in condensed matter.

The valence and conduction bands touch each other at the $\boldsymbol{K}$ point, making graphene a so-called *gapless semiconductor*. A single-point contact in the band structure determines a high sensitivity of graphene towards external perturbations, such as electric fields, mechanical deformations, or dopants. In addition, this confers an *ambipolar* character to graphene, that is charge carriers can be either holes or electrons. Interestingly, the charge carrier sign can be changed by simply acting with local electric fields. These particular electrical properties combined allow the realization of *p-n juctions* with high mobilities[18].

As for the optical properties, the absence of a bandgap makes graphene able to absorb light in a very large range of the electromagnetic spectrum, from infrared ($\lambda \approx 780\,\text{nm} - 1\,\text{mm}$) to the ultraviolet ($\lambda \approx 10\,\text{nm} - 400\,\text{nm}$). Furthermore, its 2.3% absorbance in the white light spectrum, combined with good conductivity, makes graphene an ideal candidate as a transparent electrode in solar cells or liquid crystal devices[20].

The outstanding mechanical properties of graphene are instead determined by the strength of the covalent C-C bonds combined with the 2D structure. Graphene is one of the strongest materials known, with a breaking strength 200 times higher than steel, while retaining at the same time great flexibility and a high Young's modulus[21].

From the chemical point of view, the reactivity of graphene is closely related to that of graphite. However, due to its dimensionality and the absence of bulk, the chemical functionalization of graphene can yield remarkable variations in the physical properties, contrary to graphite. For instance, it has been shown that hydrogen or oxygen adsorbates can induce metal-insulator transition in graphene[22]. Moreover, the possibility of chemical species to approach the graphene from both sides of its surface allows some chemical bond that would be unstable in graphite.

1.1.3 Fabrication techniques

The prerequisite for any widespread application of graphene is the possibility of large-scale production of high-quality samples in a controlled manner. While many fabricating techniques have been designed so far, the mass production of graphene is still a current issue in material chemistry. Here, we briefly describe the most common preparative methods, focusing on their pros and cons.
The most popular method for single or few-layers graphene production is the *mechanical exfoliation*, a.k.a. "scotch tape method"[3]. The procedure consists of the cleaving of a graphite sample, usually *highly-oriented pyrolitic graphite (HOPG)*, with a cellophane-based adhesive tape. Before transferring the flakes to appropriate supports, the peeling can be repeated several times to progressively reduce the number of layers. The main advantage of this method is its simplicity and low cost, but the poor reproducibility and the low-yield compromise the application at large scales.

Another common fabrication method involves the use of graphitic oxide-based solutions[1]. The method, designed by Ruoff and coworkers (2006)[23] relies on the fact that stirring or sonication of graphitic oxide allows the separations of the single layers. Indeed, the oxygen-containing functionalities make the layers hydrophilic, determining the dispersion in water solutions. In the end, the resulting *graphene oxide* can be thermally, chemically, or electrochemically reduced to graphene. This procedure is industrially scalable, low cost, and rapid. On the other hand, the reduction of graphene is often only partial and impurities and defects can strongly affect the quality of the final sample.

Concerning substrate-based methods, the two most common techniques are the *Chemical Vapor Deposition (CVD)* and the *epitaxial growth*. In a CVD, a transition metal surface is exposed to a carbon source, such as hydrocarbons, at high temperatures (T). The underlying principle is that hydrocarbons decompose at high T providing a source of carbon atoms that can rearrange over a catalytic surface to form the honeycomb lattice. The most successful catalysts employed so far are nickel (Ni) and copper (Cu), because of their low affinity towards C. The main advantage of the CVD technique is the possibility, in theory, to produce a single sheet of graphene over the entire wafer, thus representing the simplest way to integrate graphene into semiconductor devices[24]. In practice, however, CVD does not allow fine control over the film thickness and the prevention of secondary crystal formation is difficult.

With the epitaxial method, graphene results instead from the graphitization of SiC substrate at high temperatures. This technique allows the production of high-quality samples with precise control of the number of layers grown. The main disadvantage is that the epitaxial growth graphene remains strongly bound to the substrate, thus losing most of its unique properties, and therefore, it needs to be decoupled in some way from

[1]These are produced through the Hummer's method, that consists in soaking graphite in a solution of sulphuric acid (H_2SO_4) and potassium permanganate (K_2MnO_4).

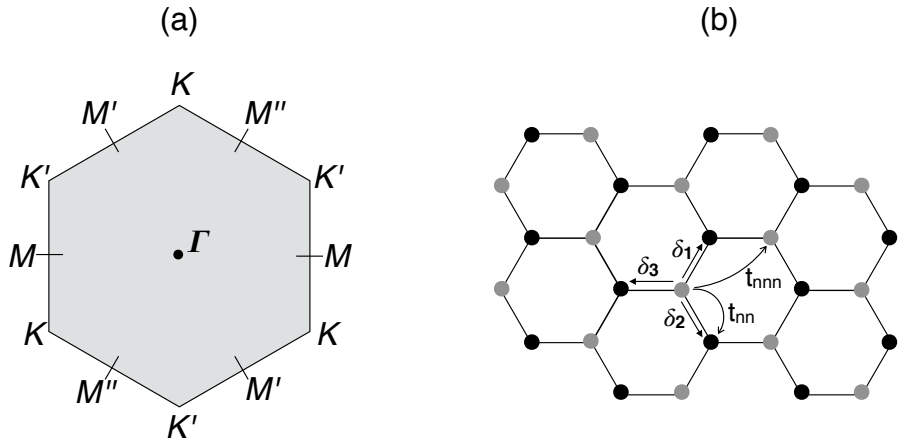

Figure 1.2. (a) Irreducible Brillouin Zone (BZ) of graphene: $\boldsymbol{\Gamma}$ is the center, while $\boldsymbol{K}$ and $\boldsymbol{K'}$ are the two non-equivalent crystallographic points at the corner of BZ; $\boldsymbol{M}, \boldsymbol{M'}, \boldsymbol{M''}$ constitute three pairs of distinct crystallographic points which lie at the middle point of the BZ's boundary; (b) Direct honeycomb lattice: $\boldsymbol{\delta}_i$ are vectors connecting a site A (grey dot) with its three nns B (black dots). t_{nn} (t_{nnn}) is the nn (nnn) hopping term.

the substrate[25]. Among the fabrication techniques, the graphitization of SiC is anyway one of the most appealing and it has attracted the interest of both the experimental and theoretical graphene community in recent years. A more detailed discussion of such a procedure is given in Section 6.4.

In closing this Section, we also mention the so-called *total organic synthesis* approach, where graphene is obtained as the synthesis of large *PAHs*. PAHs are very attractive because they can be functionalized with a wide range of aliphatic chains to modify their solubility, which is one of the key parameters to control in solution-based methods. However, a notable drawback is the limited size range of the samples produced[2]

1.2 Electronic band structure

In this Section, we describe the band structure of graphene in the *tight-binding* (TB) framework[3]. The atomic basis we are interested in is the one constituted by the single-occupied p_z orbitals centered on the carbon atoms. We show that, by solving the Schrödinger's equation with the TB Hamiltonian, two bands, namely the π and the $\pi^\star$ bands, linearly crossing at the Fermi level, naturally emerge.

In Section 1.1, we outlined the structure of the reciprocal lattice and of the irreducible Brillouin zone (BZ), which is replicated in Figure 1.2 (a).

The center of the BZ is the so-called $\boldsymbol{\Gamma}$ point, while the six corners consist in the inequivalent high-symmetry points

$$\boldsymbol{K} = \frac{2\pi}{3a}\left(\boldsymbol{e}_x - \frac{1}{\sqrt{3}}\boldsymbol{e}_y\right) \qquad \boldsymbol{K'} = \frac{2\pi}{3a}\left(\boldsymbol{e}_x + \frac{1}{\sqrt{3}}\boldsymbol{e}_y\right)$$

We show in the following that these two crystallographic points play a crucial role in defining the electronic properties of graphene since the low-energy excitations are centered around those points. Furthermore, we prove that by expanding the Hamiltonian around $\boldsymbol{K}$ or $\boldsymbol{K'}$ and solving the relative eigenvalue-eigenvectors problem, we get solutions describing

[2] One of the most successful results in this field was reached by Müllen et. al. (2008)[26], who reported the synthesis of a nanoribbon-like PAH of 12 nm in length.

[3] The reader who is interested into a more complete and rigorous treatment of the physics of graphene is referred to the excellent book by Katsnelson (2012)[27].

electrons propagating at quasi-relativistic velocities, the so-called *massless Dirac fermions*.

In order to avoid confusion, it is important to stress at the outset that the non-equivalence of the $\boldsymbol{K}$ and $\boldsymbol{K'}$ points has nothing to do with the presence of two sublattices in graphene. On the contrary, the existence of these two high-symmetry crystallographic points together with the presence of two sublattices involves the introduction of two distinct additional degrees of freedom to indexing the electrons, the so-called *isospin* and *pseudospin*.

Let us consider the graphene structure displayed in Figure 1.2 (b). We call $t_{nn} < 0$, the nn hopping, that is the probability amplitude of an electron to hop from a carbon atom of sublattice A to a nn of sublattice B, and *viceversa*. We call $t_{nnn}(< 0)$ the nnn hopping, that is the probability amplitude of an electron to hop from a carbon atom on sublattice A to the nnn on the same sublattice. Let $\boldsymbol{\delta}_i$, with $i = 1, 2, 3$ denote vectors connecting a C atom with its three nn, and $\boldsymbol{\delta}'_i$ with $i = 1, \ldots, 6$ those vectors connecting a C atom with its six nnn. In the tight-binding approximation with both nns and nnns hopping terms, the Hamiltonian matrix of graphene reads as

$$\mathbf{H}(\boldsymbol{k}) = \begin{pmatrix} t_{nnn}\sum_{i=1}^{6} e^{i\boldsymbol{k}\boldsymbol{\delta}'_i} & t_{nn}\sum_{i=1}^{3} e^{i\boldsymbol{k}\boldsymbol{\delta}_i} \\ t_{nn}\sum_{i=1}^{3} e^{-i\boldsymbol{k}\boldsymbol{\delta}_i} & t_{nnn}\sum_{i=1}^{6} e^{i\boldsymbol{k}\boldsymbol{\delta}'_i} \end{pmatrix}$$

For the sake of notation, we define the following functions

$$f(\boldsymbol{k}) = \sum_{i=1}^{6} e^{i\boldsymbol{k}\boldsymbol{\delta}'_i} \tag{1.1}$$

$$g(\boldsymbol{k}) = \sum_{i=1}^{3} e^{i\boldsymbol{k}\boldsymbol{\delta}_i} \tag{1.2}$$

so that, the Hamiltonian matrix[4] can be compactly written as

$$\mathbf{H}(\boldsymbol{k}) = \begin{pmatrix} t_{nnn}f(\boldsymbol{k}) & t_{nn}g(\boldsymbol{k}) \\ t_{nn}g^{\star}(\boldsymbol{k}) & t_{nnn}f(\boldsymbol{k}) \end{pmatrix} \tag{1.3}$$

Note that $\boldsymbol{\delta}_i + (-\boldsymbol{\delta}_j) = \boldsymbol{\delta}'_i$ (see Figure 1.3), hence

$$|g(\boldsymbol{k})|^2 = 3 + \sum_{i \neq j} e^{i\boldsymbol{k}(\boldsymbol{\delta}_i - \boldsymbol{\delta}_j)} = 3 + f(\boldsymbol{k}) \tag{1.4}$$

[4]One can equivalently work in the *second-quantization formalism* and write down a TB Hamiltonian operator as

$$\mathrm{H} = t\sum_{\langle i,j\rangle} a_i^{\dagger}b_j + t\sum_{\langle i,j\rangle} b_j^{\dagger}a_i + t'\sum_{\langle\langle i,j\rangle\rangle} a_i^{\dagger}a_j + t\sum_{\langle\langle i,j\rangle\rangle} b_i^{\dagger}b_j$$

where $a_i^{\dagger}$ ($b_j^{\dagger}$) creates an electron respectively at site i (j) on sublattice A (B), while a_i (b_j) annihilates an electron at site i (j) on sublattice A (B) ($\langle i,j\rangle$ indicates a sum over the nearest-neighbors sites, while $\langle\langle i,j\rangle\rangle$ over the next nearest-neighbors). One can always diagonalize the Hamiltonian by means of a unitary transformation. In the case of a TB Hamiltonian with no particles interaction, the basis which realizes the diagonalization is the $|\boldsymbol{k}\rangle$ basis of wave vectors. Thus, introducing the Fourier-transformed $a_{\boldsymbol{k}}^{\dagger}, b_{\boldsymbol{k}}^{\dagger}$ ($a_{\boldsymbol{k}}, b_{\boldsymbol{k}}$) creation (annihilation) operators collected in the two-components (spinor) representation

$$c_{\boldsymbol{k}}^{\dagger} = \begin{pmatrix} a_{\boldsymbol{k}}^{\dagger} \\ b_{\boldsymbol{k}}^{\dagger} \end{pmatrix}$$

one gets

$$\mathrm{H} = \sum_{\boldsymbol{k}} c_{\boldsymbol{k}}^{\dagger}\mathbf{H}(\boldsymbol{k})c_{\boldsymbol{k}}$$

where the matrix $\mathbf{H}(\boldsymbol{k})$ in the case of graphene is exactly the Hamiltonian matrix given in Equation (1.3). The approach of second quantization is particularly useful when dealing with point defects, such as adsorbates or impurities, in both graphene and graphene-like nanostructures.

The overlap matrix, $\boldsymbol{S}(\boldsymbol{k})$, in the approximation of vanishing overlap between the nnn, reads as

$$\mathbf{S}(\boldsymbol{k}) = \begin{pmatrix} 0 & sg(\boldsymbol{k}) \\ sg^{\star}(\boldsymbol{k}) & 0 \end{pmatrix}$$

where

$$s = \int d^2\boldsymbol{r}\phi_A^{\star}(\boldsymbol{r})\phi_B(\boldsymbol{r}+\boldsymbol{\delta}_i)$$

The corresponding eigenvalue-eigenvector problem to solve is

$$\mathbf{H}(\boldsymbol{k})\Psi = \varepsilon(\boldsymbol{k})\mathbf{S}(\boldsymbol{k})\Psi$$

with the matrices defined above. The eigenvalues are easily obtained by diagonalizing the corresponding $(\mathbf{H} - \varepsilon\mathbf{S}(\boldsymbol{k}))$ matrix, that is by solving the following secular equation

$$\det \begin{pmatrix} t_{nnn}f(\boldsymbol{k}) - \varepsilon(\boldsymbol{k}) & (t_{nn} - s\varepsilon(\boldsymbol{k}))g(\boldsymbol{k}) \\ (t_{nn} - s\varepsilon(\boldsymbol{k}))g^{\star}(\boldsymbol{k}) & t_{nnn}f(\boldsymbol{k}) - \varepsilon(\boldsymbol{k}) \end{pmatrix} = 0$$

After some boring but straightforward algebra, one arrives at the following two solutions

$$\boxed{\varepsilon_{\pm}(\boldsymbol{k}) = \frac{t_{nnn}f(\boldsymbol{k}) \pm t_{nn}|g(\boldsymbol{k})|}{1 \pm s|g(\boldsymbol{k})|}} \tag{1.5}$$

Equation (1.5) represents the analytical form of π $(-)$ and $\pi^{\star}$ $(+)$ bands of graphene, in the full tight-binding approximation. Such expression can be further simplified under some reasonable assumptions. Setting $\eta = \pm$, let first re-write Equation (1.5) as follows

$$\varepsilon_{\eta}(\boldsymbol{k}) = \frac{t_{nnn}f(\boldsymbol{k})}{1 + \eta s|g\boldsymbol{k})|} + \frac{\eta t_{nn}|g(\boldsymbol{k})|}{1 + \eta s|g\boldsymbol{k})|}$$

If $t_{nnn} \ll t_{nn}$ and $s \ll 1$, the first term can be approximated to $t_{nnn}f(\boldsymbol{k})$, while the second term can expanded in power serie, giving at the first order

$$\varepsilon_{\eta}(\boldsymbol{k}) = t_{nnn}f(\boldsymbol{k}) + \eta t_{nn}|g(\boldsymbol{k})| - st_{nn}|g(\boldsymbol{k})|^2$$

Since $f(\boldsymbol{k}) = -3 + |g(\boldsymbol{k})|^2$ (Equation (1.4)), we get

$$\varepsilon_{\eta}(\boldsymbol{k}) = -3t_{nnn} + (t_{nnn} - st_{nn})|g(\boldsymbol{k})|^2 + \eta t_{nn}|g(\boldsymbol{k})| \tag{1.6}$$

therefore the effect of the overlap corrections is a renormalization of the nnn hopping parameter. Equation (1.6) suggests the introduction of an *effective* nnn hopping amplitude defined as

$$t' := t_{nnn} - st_{nn}$$

The expansion of Equation (1.5) is justified if one considers that a fitting of the energy dispersion of Equation (1.6) with more sophisticated bands-structure calculations (*e.g.* DFT), gives $t_{nn} = -2.97\,\text{eV}$ and $t_{nnn} = -0.073\,\text{eV}$, that is $t_{nnn}/t_{nn} \ll 1$. Note that the fitting procedure does not allow to distinguish between the "true" nns hopping amplitude and the contribution arising from the overlap corrections. Hereafter, we use the effective parameter t' to refer to the nnn hopping, omitting any distinction with t_{nnn}. In addition, we set $t_{nn} = t$.

Let now consider the $f(\boldsymbol{k})$ function in Equation (1.1). From Figure 1.3, one can easily

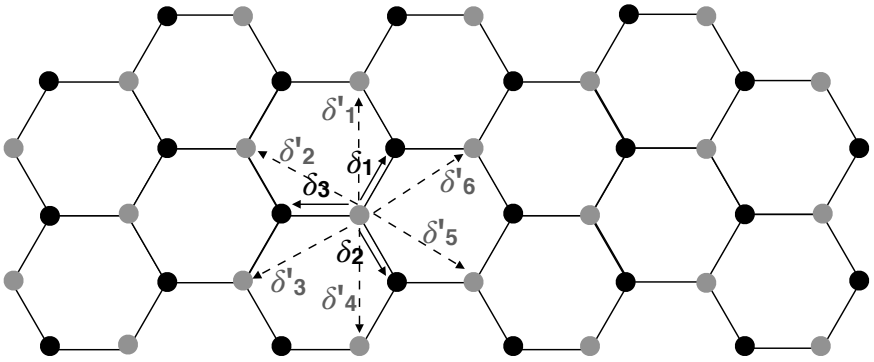

Figure 1.3. An extended representation of the direct honeycomb lattice of graphene: $\boldsymbol{\delta}_i$ are vectors connecting a site A (grey dot) with its three nn B (black dots); $\boldsymbol{\delta}'_i$ are vectors connecting a site A with its six nnn A.

check that each $\boldsymbol{\delta}'_i$ is coupled to an opposite vector $\boldsymbol{\delta}'_k = -\boldsymbol{\delta}'_i$. Then, we can write

$$f(\boldsymbol{k}) = 2\sum_{i=1}^{3}\cos(\boldsymbol{k}\cdot\boldsymbol{\delta}'_i)$$

With this identification, the energy dispersion of Equation (1.6) becomes

$$\begin{aligned}\varepsilon_{\pm}(\boldsymbol{k}) &= -3t' + t'\left(3 + 2\sum_{i=1}^{3}\cos(\boldsymbol{k}\cdot\boldsymbol{\delta}'_i)\right) \pm t\sqrt{3 + 2\sum_{i=1}^{3}\cos(\boldsymbol{k}\cdot\boldsymbol{\delta}'_i)} \\ &= 2t'\sum_{i=1}^{3}\cos(\boldsymbol{k}\cdot\boldsymbol{\delta}'_i) \pm t\sqrt{3 + 2\sum_{i=1}^{3}\cos(\boldsymbol{k}\cdot\boldsymbol{\delta}'_i)}\end{aligned}$$

This energy dispersion is plotted in Figure 1.4. The lower band is the negative solution and it represents the *bonding* π band, while the upper band is the positive solution, representing the *antibonding* $\pi^\star$ band. Since each C contributes with one π electron and each k-point can host at most two electrons with opposite spins, according to the well-known Pauli exclusion principle, it follows that the lower π band is filled, while the upper $\pi^\star$ is empty. Consequently, the Fermi level is situated at the k points where the π and $\pi^\star$ bands touch each other. We prove now, by a direct calculation, that these points are exactly the six corners of the irreducible Brillouin zone, namely the $\boldsymbol{K}$ and $\boldsymbol{K'}$ crystallographic points. Let consider

$$g(\boldsymbol{K}) = e^{i\boldsymbol{K}\boldsymbol{\delta}_1} + e^{i\boldsymbol{K}\boldsymbol{\delta}_2} + e^{i\boldsymbol{K}\boldsymbol{\delta}_3} \tag{1.7}$$

where

$$\boldsymbol{K} = \left(\frac{2\pi}{3a}, -\frac{2\pi}{3\sqrt{3}}\right)$$

$$\boldsymbol{\delta}_1 = \left(\frac{a}{2}, \frac{a}{2\sqrt{3}}\right) \qquad \boldsymbol{\delta}_2 = \left(\frac{a}{2}, -\frac{a}{2\sqrt{3}}\right) \qquad \boldsymbol{\delta}_3 = (-a, 0)$$

A straightforward calculation of the dot products in Equation (1.7) gives

$$g(\boldsymbol{K}) = 1 + e^{i2\pi/3} + e^{-i2\pi/3} = 1 + 2\cos\left(\frac{2\pi}{3}\right) = 0$$

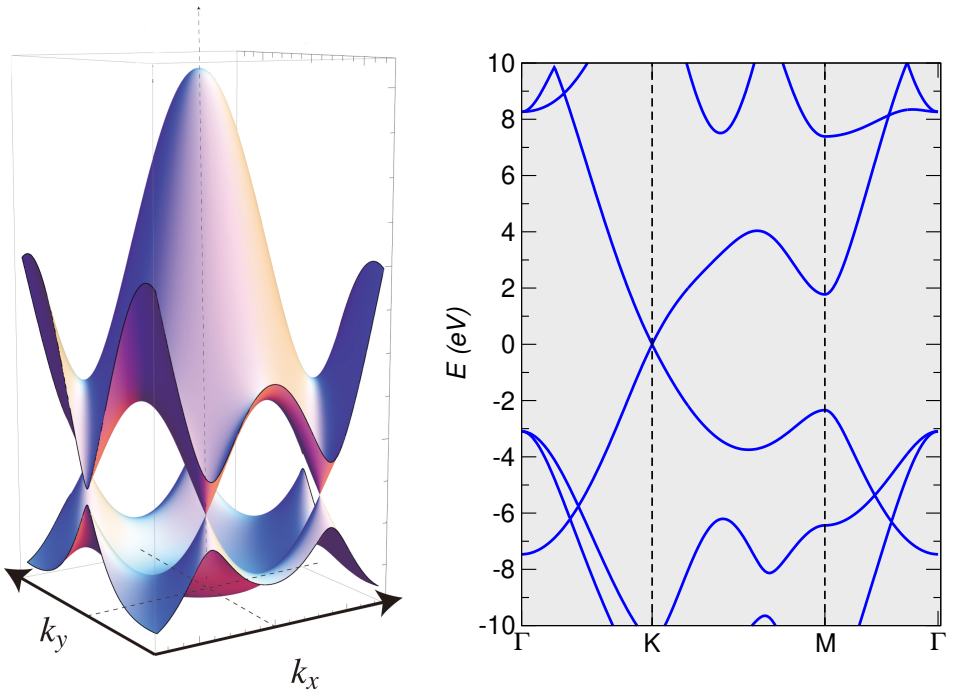

Figure 1.4. Energy dispersion (3D on the left and 2D on the right) of pristine graphene. We can distinguish from: (i) a lower band, which at half-filling condition, is completely filled and described the π system; (ii) an upper band (empty) which is the relative antibonding $\pi^\star$ band. The conical intersections (Dirac points) occur at the points where the π and $\pi^\star$ bands touch each other. For pristine graphene, they occur at the crystallographic points $\boldsymbol{K}$ and $\boldsymbol{K}'$.

Since $|g(\boldsymbol{k})|^2 = 3 + f(\boldsymbol{k})$, then $f(\boldsymbol{K}) = -3$. Therefore, the Hamiltonian matrix at $\boldsymbol{K}$ reads as

$$\mathbf{H}(\boldsymbol{K}) = \begin{pmatrix} -3t' & 0 \\ 0 & -3t' \end{pmatrix}$$

The diagonalization is trivial and gives

$$\boxed{\varepsilon_\pm(\boldsymbol{K}) = 3t'}$$

i.e. the two solutions are degenerate at $\boldsymbol{K}$ and the π band touches the $\pi^\star$ band. The same can be verified also for the $\boldsymbol{K}'$ points. The points in graphene where bands touch each other are known as *Dirac points*. Therefore, in pristine graphene, Dirac points occur exactly at the positions of the $\boldsymbol{K}$ and $\boldsymbol{K}'$ points. Since there are situations in which Dirac points no longer occur at these locations, one has to explicitly distinguish them from $\boldsymbol{K}$ and $\boldsymbol{K}'$, which have to be regarded as just two non-equivalent crystallographic points of the irreducible Brillouin zone. Note that, in case of only nn interactions, namely $t' = 0$, Dirac points are located exactly where the energy dispersion is zero, $\varepsilon_\pm(\boldsymbol{K}) = 0$.

When $t' = 0$, the energy dispersion reduces to

$$\boxed{\varepsilon_\pm(\boldsymbol{k}) = \pm t\sqrt{3 + f(\boldsymbol{k})}}$$

therefore, we have that $\varepsilon_+(\boldsymbol{k}) = -\varepsilon_-(\boldsymbol{k})$, which is known as the *electron-hole symmetry* (*e-h*). In this respect, it is worth anticipating some notions that we will further develop later in this Chapter. The electron-hole symmetry is a feature of the so-called *bipartite lattices*. A bipartite lattice is a system made of two sublattices which form two *disjoint sets* of sites, A and B. In the nn approxiamtion, graphene consistutes exactly a bipartite

lattice. The *e-h* symmetry[5], which characterizes the Hamiltonian of any bipartite system, establishes that for any non-vanishing energy level $\varepsilon(\boldsymbol{k})$ with associated eigenstate

$$|\Psi_{\boldsymbol{k}}\rangle = c_A|A\rangle + c_B|B\rangle$$

$|A\rangle, |B\rangle \neq 0$ respectively on sites A and B, it exists a conjugate energy level $-\varepsilon(\boldsymbol{k})$ with eigenstate[6]

$$|\Psi_{\boldsymbol{k}'}\rangle = c_A|A\rangle - c_B|B\rangle$$

From our previous discussion, we see that the nnn hopping and the overlap corrections break the electron-hole symmetry and shift the Dirac points from $\varepsilon = 0$ to $\varepsilon = 3t'$.

The *e-h* symmetry is just one of the symmetry properties of graphene. Indeed, since $f(\boldsymbol{k}) = f(-\boldsymbol{k})$, we immediately see that $\varepsilon(\boldsymbol{k}) = \varepsilon(-\boldsymbol{k})$. In nn approximation, this means that if $\tilde{\boldsymbol{k}}$ is a solution of $\varepsilon_{\boldsymbol{k}} = 0$, so it is $-\tilde{\boldsymbol{k}}$. A direct consequence of this additional symmetry is that Dirac points always occur in pairs. Here, $\tilde{\boldsymbol{k}} = \boldsymbol{K}$ and $-\tilde{\boldsymbol{k}}$ is $\boldsymbol{K'}$, as mentioned above. Therefore, the zero-energy states of graphene in *nn*s approximation are doubly degenerate. In the field of semiconductors, such a doubly degeneracy is referred to as twofold *valley degeneracy*: $\boldsymbol{K}$ and $\boldsymbol{K'}$ such that $\boldsymbol{K} = -\boldsymbol{K'}$ are said to constitute two different *valleys*. Accordingly, the six corners of the BZ of graphene can be regarded as three pairs of $\boldsymbol{K}$ and $\boldsymbol{K'}$ points.

As shown in Figure 1.4, at the $\boldsymbol{\Gamma}$ point,π and $\pi^\star$ bands are separated by a $\Delta\varepsilon \gg 0$. To determine this energy separation, let consider again the energy dispersion in the nnn approximation

$$\varepsilon_\pm(\boldsymbol{k}) = t' f(\boldsymbol{k}) \pm t\sqrt{3 + f(\boldsymbol{k})}$$

At $\boldsymbol{\Gamma}$, $\boldsymbol{k} = 0$, $f(\boldsymbol{k}) = 2\sum_1^3 \cos(0) = 6$, then

$$\varepsilon_\pm(\boldsymbol{\Gamma}) = 6t' \pm 3t \Longrightarrow \Delta\varepsilon(\boldsymbol{\Gamma}) = 6t$$

i.e., the bandgap at $\boldsymbol{\Gamma}$ is $\approx 16\,\text{eV}$ in both the nn and nnn approximations.

So far, we focused on the energy spectrum obtained through the direct diagonalization of the graphene Hamiltonian matrix. However, by means of the energy eigenvalue representation , we can write down the analytical expression for the corresponding eigenstates. In this respect, let re-write the tight-binding Hamiltonian as follows

$$\mathbf{H}(\boldsymbol{k}) = \begin{pmatrix} t'|g(\boldsymbol{k})|^2 & tg(\boldsymbol{k}) \\ tg^\star(\boldsymbol{k}) & t'|g(\boldsymbol{k})|^2 \end{pmatrix} = t'|g(\boldsymbol{k})|^2\mathbf{1} + t\begin{pmatrix} 0 & g(\boldsymbol{k}) \\ g^\star(\boldsymbol{k}) & 0 \end{pmatrix}$$

where $\mathbf{1}$ is the one-matrix

$$\mathbf{1} = \begin{pmatrix} 1 & 0 \\ 0 & 1 \end{pmatrix}$$

(note that we have omitted the unimportant factor $-3t'$). In the nn approximation the eigenvalues read as $\varepsilon_\eta(\boldsymbol{k}) = \eta t g(\boldsymbol{k})$ (where $\eta = \pm$), then the eigenstates are found by

[5]The term "electron-hole" is here justified considering that, in the case of graphene, due to the half-filling condition and with the Fermi level located at the zero-energy, this symmetry regards exactly the electrons and the holes.

[6]The proof is straightforward: let P being the eigenprojector onto the sublattice A and Q the eigenprojector onto the sublattice B. The operator $\mathrm{C} = \mathrm{P} - \mathrm{Q}$ is adjoint and nihilpotent, hence it satisfy $\mathrm{CHC} = -\mathrm{H}$. Therefore,

$$\mathrm{CHC}|\Psi_{\boldsymbol{k}}\rangle = -\mathrm{H}|\Psi_{\boldsymbol{k}}\rangle = \varepsilon(\boldsymbol{k})C|\Psi_{\boldsymbol{k}}\rangle C$$

multiplying both sides by C on the right

$$\mathrm{HC}|\Psi_{\boldsymbol{k}}\rangle = -\varepsilon(\boldsymbol{k})\mathrm{C}|\Psi_{\boldsymbol{k}}\rangle$$

then $|\Psi_{\boldsymbol{k}'}\rangle = \mathrm{C}|\Psi_{\boldsymbol{k}}\rangle$ is the eigenstate associated to the $-\varepsilon(\boldsymbol{k})$ eigenvalue.

solving the following eigeinvalue equation

$$\mathbf{H}(\boldsymbol{k})(t'=0)|\Psi^{\eta}_{\boldsymbol{k}}\rangle = \eta t g(\boldsymbol{k})|\Psi^{\eta}_{\boldsymbol{k}}\rangle \tag{1.8}$$

Since the Hamiltonian is a 2×2 matrix, the eigenstates are *spinors* in the form

$$|\Psi^{\eta}_{\boldsymbol{k}}\rangle = \begin{pmatrix} a^{\eta}_{\boldsymbol{k}} \\ b^{\eta}_{\boldsymbol{k}} \end{pmatrix}$$

From Equation (1.8) and using the exponential form of complex numbers, we get

$$b^{\eta}_{\boldsymbol{k}} = \eta \frac{t|g(\boldsymbol{k})|}{tg(\boldsymbol{k})} a^{\eta}_{\boldsymbol{k}} = \eta e^{-i\phi_{\boldsymbol{k}}} a^{\eta}_{\boldsymbol{k}}$$

where

$$\phi_{\boldsymbol{k}} = \arctan\left(\frac{\operatorname{Im} g(\boldsymbol{k})}{\operatorname{Re} g(\boldsymbol{k})}\right)$$

From the normalization condition, one can easily check that $a = 1/\sqrt{2}$. Therefore, the normalized eigenstates are

$$|\Psi^{\eta}_{\boldsymbol{k}}\rangle = \frac{1}{\sqrt{2}} \begin{pmatrix} 1 \\ \eta e^{-i\phi_{\boldsymbol{k}}} \end{pmatrix}$$

These eigenstates are also those for the full Hamiltonian in the nnn approximation since the term accounting for the latter is proportional to the one-matrix, $\mathbf{1}$. The two components of the spinors can be interpreted as probability amplitudes of Bloch states on the two different sublattices A and B. As expected, they represent equal probability to find an electron on sublattice A or B, since the latter define C atoms with the same on-site energy.

1.2.1 Massless Dirac fermions

In pristine graphene, we have seen that Dirac points occur exactly at the corners of the irreducible Brillouin zone, namely the $\boldsymbol{K}$ and $\boldsymbol{K'}$ crystallographic points. When the electron excitations are of concern, one generally looks at first at the *low-energy excitations* near the Fermi level, that is the ones characterized by energy much smaller than the bandwidth (here $\approx |t|$). For graphene, this translates to restricting the attention to those states around the Dirac points. In doing so, we need to expand the Hamiltonian around $\boldsymbol{K}$ and $\boldsymbol{K'}$. Let then consider the wave vector $\boldsymbol{k} = \boldsymbol{K} + \boldsymbol{q}$ (the same applies to $\boldsymbol{K'} = -\boldsymbol{K}$), where $|\boldsymbol{q}| \ll |\boldsymbol{K}|$, or equivalently $|q|^{-1} \gg a$, where a is the C-C bond length. The $g(\boldsymbol{k})$ function in $\boldsymbol{K} + \boldsymbol{q}$ is

$$g(\boldsymbol{K}+\boldsymbol{q}) = e^{i(\boldsymbol{K}+\boldsymbol{q})\boldsymbol{\delta}_1} + e^{i(\boldsymbol{K}+\boldsymbol{q})\boldsymbol{\delta}_2} + e^{i(\boldsymbol{K}+\boldsymbol{q})\boldsymbol{\delta}_3}$$

Since $\boldsymbol{q} \simeq 0$, we can Taylor-expand the exponentials $e^{i\boldsymbol{q}\boldsymbol{\delta}_i}$. At the first order, we get

$$e^{i\boldsymbol{q}\boldsymbol{\delta}_i} \simeq 1 + i(\boldsymbol{q}\cdot\boldsymbol{\delta}_i)$$

Then

$$\begin{aligned} g(\boldsymbol{K}+\boldsymbol{q}) &= i\left(\boldsymbol{\delta}_1 + e^{i2\pi/3}\boldsymbol{\delta}_2 + e^{-2\pi/3}\boldsymbol{\delta}_3\right)\boldsymbol{q} \\ &= i\left[\boldsymbol{\delta}_1 + \cos\left(\frac{2\pi}{3}\right)(\boldsymbol{\delta}_2+\boldsymbol{\delta}_3) + i\sin\left(\frac{2\pi}{3}\right)(\boldsymbol{\delta}_2-\boldsymbol{\delta}_3)\right]\boldsymbol{q} \end{aligned}$$

A direct calculation gives

$$g(\boldsymbol{K}+\boldsymbol{q}) = \frac{3a}{2} t\gamma(q_x - iq_y)$$

where q_x, q_y are the components of $\boldsymbol{q}$ and γ is a phase factor

$$\gamma = -\frac{\sqrt{3}}{2} + i\frac{1}{2} = e^{i5\pi/6}$$

which appears due to our specific choice of the unit cell, but that can be neglected by carrying out a unitary transformation on the basis functions. Since $|g(\boldsymbol{K}+\boldsymbol{q})|^2 \simeq 0$, $f(\boldsymbol{K}+\boldsymbol{q}) \simeq -3$ and then the Hamiltonian matrix around $\boldsymbol{K}$ reads as

$$\mathbf{H}(\boldsymbol{K}+\boldsymbol{q}) \simeq -3t'\mathbf{1} + \frac{3}{2}at\begin{pmatrix} 0 & q_x - iq_y \\ q_x + iq_y & 0 \end{pmatrix}$$

For $\boldsymbol{K}' = -\boldsymbol{K}$, the calculation is the same and it involves only a change of sign. We arrive then at the following expression for the nn approximated ($t' = 0$) Hamiltonian around $\pm\boldsymbol{K}+\boldsymbol{q}$

$$\mathbf{H}(\pm\boldsymbol{K}+\boldsymbol{q}) \simeq \frac{3}{2}at\begin{pmatrix} 0 & q_x \mp iq_y \\ q_x \pm iq_y & 0 \end{pmatrix} \tag{1.9}$$

The diagonalization of this matrix gives

$$\frac{3}{2}at\det\begin{pmatrix} -\varepsilon & q_x \mp iq_y \\ q_x \pm iq_y & -\varepsilon \end{pmatrix} = 0 \Longrightarrow \varepsilon_\pm(\boldsymbol{q}) = \pm\frac{3}{2}at|\boldsymbol{q}| \tag{1.10}$$

where the $\pm$ sign at the subscript of the energy dispersion here stands for the two different solutions of the secular equation and not for the valley degeneracy. The relation on the right-hand side of Equation (1.10) represents the energy dispersion of the electrons around the Dirac points. From

$$\frac{1}{\hbar}\frac{\partial\varepsilon_-(\boldsymbol{q})}{\partial\boldsymbol{q}} = v$$

we get the velocity v of the electrons at these points. Reminding that $t < 0$, we have

$$\boxed{v_F = \frac{3}{2\hbar}a|t|}$$

v_F is the so-called *Fermi velocity*: since $t \approx 2.97\,\text{eV}$ and $a \approx 1.42\,\text{Å}$, we get $v_F \approx 0.96 \cdot 10^6$ m/s, that is $v_F \approx 10^{-2}c$ where c is the speed of light. In other words, electrons in the vicinity of the Dirac points behave as *massless*[7] particles, propagating with quasi-relativistic velocities, also known as *massless Dirac fermions*. Figure 1.5 shows the variation of the hopping term t and the Fermi velocity v_F at different uniform strain $\delta = (a - a_0)/a_0$ applied to a graphene sheet, as obtained by DFT-PBE periodic calculations with Atomic Orbitals (AO) basis set.

In terms of v_F, the Hamiltonian given in Equation (1.9) is compactly re-written as

$$\boxed{\mathbf{H}^\kappa_{\boldsymbol{q}} = \kappa\hbar v_F(q_x\boldsymbol{\sigma}^x + \kappa q_y\boldsymbol{\sigma}^y)}$$

where κ is referred to as the *valley isospin*, that is $\kappa = \pm$, with $+$ for the $\boldsymbol{K}$ valley and $-$ for the $\boldsymbol{K}'$ valley, and $(\boldsymbol{\sigma}^x, \boldsymbol{\sigma}^y)$ are the *Pauli matrices*

$$\boldsymbol{\sigma}^x = \begin{pmatrix} 0 & 1 \\ 1 & 0 \end{pmatrix} \qquad \boldsymbol{\sigma}^y = \begin{pmatrix} 0 & -i \\ i & 0 \end{pmatrix}$$

[7] We clearly refer to the rest mass. The intrinsic mass of electrons cannot be "lost" since electrons are elementary particles.

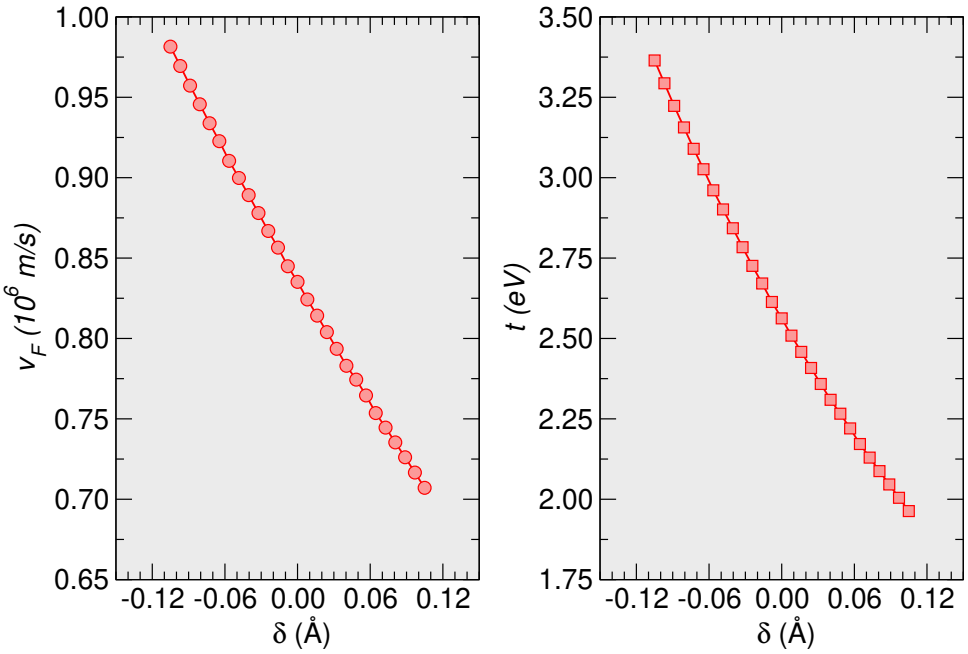

Figure 1.5. Variation of the Fermi velocity (v_F, 10^6 m/s) (left) and of the hopping parameter (t, eV), induced by a uniform strain (δ, Å). DFT calculations are performed with PBE functional as implemented in the SIESTA code[28], with a fine k-mesh to properly describe the reciprocal space and tight-convergence criteria on the optimization.

By the same token, the energy dispersion becomes

$$\boxed{\varepsilon_{\boldsymbol{q}}^{\eta,\kappa} = \eta\hbar v_F|\boldsymbol{q}|} \tag{1.11}$$

Equation (1.11) allows making three important observations:

(i) The energy dispersion in the vicinity of the Dirac points is independent of the valley isospin, that is the twofold degeneracy we mentioned above survives the first-order expansion;

(ii) The energy dispersion is *isotropic* since it depends only on the modulus of $\boldsymbol{q}$ and not on its direction;

(iii) In the nn approximation, the energy dispersion preserves the e-h symmetry.

To conclude the present discussion, we mention that the Hamiltonian matrix can be re-written in a still more compact form. In particular, by introducing the following four-spinor representation for the eigenstates

$$|\Psi_{\boldsymbol{k}}\rangle = \begin{pmatrix} \psi^A_{\boldsymbol{k},+} \\ \psi^B_{\boldsymbol{k},+} \\ \psi^B_{\boldsymbol{k},-} \\ \psi^A_{\boldsymbol{k},-} \end{pmatrix}$$

the Hamiltonian can be expressed in the following form

$$\boxed{\mathbf{H}^{\kappa}_{\boldsymbol{q}} = \hbar v_F \boldsymbol{\tau}_0 \otimes \boldsymbol{\sigma} \cdot \boldsymbol{q}} \tag{1.12}$$

Here, τ_0 denotes the z-component of the Pauli matrices, *i.e.*

$$\boldsymbol{\tau}_0 = \begin{pmatrix} 1 & 0 \\ 0 & -1 \end{pmatrix}$$

and $\boldsymbol{\tau}_0 \otimes \boldsymbol{\sigma}$ stands for the 4×4 matrices

$$\boldsymbol{\tau}_0 \otimes \boldsymbol{\sigma} = \begin{pmatrix} \boldsymbol{\sigma} & 0 \\ 0 & -\boldsymbol{\sigma} \end{pmatrix}$$

In this four-spinor representation, the first and the last two components of the eigenstates represent respectively the lattice components relative to the valleys $\boldsymbol{K}$ and $\boldsymbol{K'}$. Such degree of freedom is the beforementioned valley isospin, and it appears in the Hamiltonian through the Pauli matrix $\boldsymbol{\tau}_0$. In addition, one further distinguishes between the two sublattices, that behave as an additional degree of freedom known as *pseudospin*. The latter is represented in the Hamiltonian by the Pauli matrices $(\boldsymbol{\sigma}^i)$[8]. Equation (1.12), apart from the valley isospin index, is formally analog to a 2D Dirac equation describing relativistic particles, where the pseudospin plays the same role of the traditional spin for *true* Dirac fermions. Therefore, by analogy, one speaks of pseudospin "up" or pseudospin "down", to indicate respectively the sublattice A and B. Finally, the reader can check that the eigenstates of the Hamiltonian (1.12) are

$$|\Psi_{\boldsymbol{k}}^{\eta,+}\rangle = \frac{1}{\sqrt{2}} \begin{pmatrix} 1 \\ \eta e^{-i\phi_{\boldsymbol{q}}} \\ 0 \\ 0 \end{pmatrix} \qquad |\Psi_{\boldsymbol{k}}^{\eta,-}\rangle = \frac{1}{\sqrt{2}} \begin{pmatrix} 0 \\ 0 \\ 1 \\ -\eta e^{-i\phi_{\boldsymbol{q}}} \end{pmatrix}$$

where $\phi_{\boldsymbol{q}} = \arctan(q_y/q_x)$.

1.2.2 Density of states

In closing this section, we briefly comment on the *density of states* (DOS) of graphene, still within the TB approach and the nn approximation. We remind that the density of states is given by

$$\rho(\varepsilon) = 2 \sum_n \int_{BZ} \frac{d^3\boldsymbol{k}}{(2\pi)^3} \delta(\varepsilon - \varepsilon(\boldsymbol{k})) \tag{1.13}$$

where the sum runs over all the band indices and the integration is performed on the irreducible Brillouin zone, with the factor 2 accounting for spin degeneracy. For the π electron system of graphene, due to the dimensionality and twofold valley degeneracy, Equation (1.13) reads as

$$\rho(\varepsilon) = 4 \int_{BZ} \frac{d^2\boldsymbol{k}}{(2\pi)^2} \delta(\varepsilon - \varepsilon(\boldsymbol{k}))$$

In the vicinity of the Dirac points, one can substitute the low-energy dispersion relation

$$\rho(\varepsilon) = 4 \int_0^{+\infty} \frac{1}{2\pi} |\boldsymbol{q}| \delta(\varepsilon - \varepsilon(|\boldsymbol{q}|)) d|\boldsymbol{q}|$$

and exploit its isotropy to easily carry out the integration, arriving at

$$\rho(\varepsilon) = \frac{2}{\pi} \frac{|\boldsymbol{q}|}{\left| \frac{\partial \varepsilon}{\partial |\boldsymbol{q}|} \right|} \tag{1.14}$$

[8] This is the reason why we use two different symbols, $\boldsymbol{\tau}$ and $\boldsymbol{\sigma}$ for the Pauli matrices.

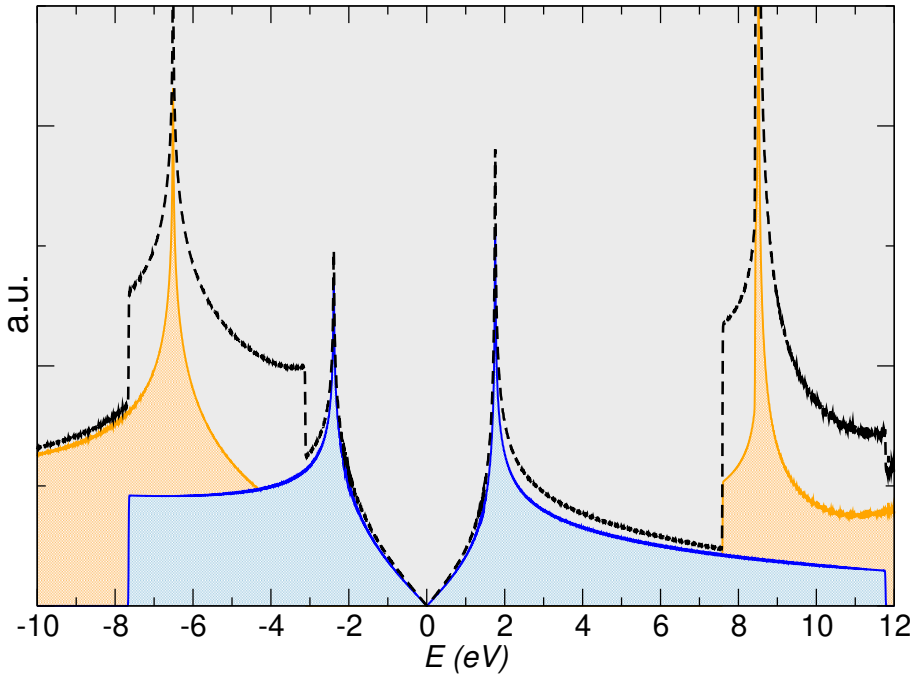

Figure 1.6. Total density of states (black) and projections on the π (blue) and σ (orange) systems. Calculations are performed with DFT-PBE as implemented in the SIESTA code[28], with a fine k-mesh and large mesh cut-off for the real-space integration.

as long as $\varepsilon \ll |t|$. By inverting the low energy dispersion, we then get

$$\boxed{\rho(\varepsilon) = \frac{2}{\pi}\frac{\varepsilon}{\hbar^2 v_F^2}} \tag{1.15}$$

We note that the density of states linearly vanishes for $\varepsilon \to 0$, *i.e.* close to the Dirac points. Noteworthy, graphene differs from standard 2D electron gases, for which the density of states is found to be constant. Yet, one can show that it is sufficient to consider two layers of graphene to get back a constant density of states.

For the sake of completeness, we report the analytical expression of the full density of states calculated by Hobson and Nierenberg (1953)[29]

$$\rho(\varepsilon) = \frac{4}{\pi^2}\frac{|\varepsilon|}{t^2}\frac{1}{\sqrt{Z_0}}\boldsymbol{F}\left(\frac{\pi}{2}, \sqrt{\frac{Z_1}{Z_0}}\right)$$

where

$$Z_0 = \begin{cases} \left(1 + \left|\frac{\varepsilon}{t}\right|\right)^2 - \frac{[(\varepsilon/t)^2 - 1]^2}{4} & -t \le \varepsilon \le t \\ 4\left|\frac{\varepsilon}{t}\right| & -3t \le \varepsilon \le -t \vee t \le \varepsilon \le 3t \end{cases}$$

$$Z_1 = \begin{cases} 4\left|\frac{\varepsilon}{t}\right| & -t \le \varepsilon \le t \\ \left(1 + \left|\frac{\varepsilon}{t}\right|\right)^2 - \frac{[(\varepsilon/t)^2 - 1]^2}{4} & -3t \le \varepsilon \le -t \vee t \le \varepsilon \le 3t \end{cases}$$

where $\boldsymbol{F}(\pi/2, x)$ is the complete elliptical integral of the first kind. Figure 1.6 displays the density of states as obtained by an AO-DFT calculation is shown: the electron-hole nature of the spectrum is approximately reproduced due to the rather small values of t'. The divergencies at $\pm t$ are known as *van-Hove singularities* and they are due to to

the saddle points of the energy dispersion at the M points at the borders of the first BZ. Such divergencies can be qualitatevely understood looking at Equation (1.14): they appear whenever the derivative of the energy dispersion vanishes, such as at the extrema or saddle points of the energy dispersion.

1.3 Hydrogen Sticking

In this Section, we describe the key aspects of the H sticking on graphene. The attention will be given here to the energetics of this process and of competing reactions that may occur at the gas-phase interface, such as the abstraction reactions, that are more relevant for this work. We will not go into the details of the sticking dynamics, for which the reader is referred to excellent review by Bonfanti et. al. (2008)[30] and related works[31, 32, 33, 34].

1.3.1 Diluted limit: physisorption and chemisorption

We start by considering the so-called diluted limit where H atoms can be considered quasi-isolated on the surface. In practice, only a few experiments are able to address this regime, since in most cases higher coverage conditions are employed[9]. In addition, as we shall describe in the following, dimerization and clustering of H adatoms occurs on graphene due to the electronic and structural modification induced by the single H adsorption itself. We first address the *physisorption* regime and then move to the relevant *chemisorption* regime.

The interaction potential relevant for the physisorption regime was characterized long ago by Ghio et. al. (1980)[35] who used low energy H atom beams ($50 - 65\,\text{meV}$) and first observed diffraction in the flux of scattered atoms off a graphite sample. From the position of the resonances, they estimated the well depth to be $43.3 \pm 0.5\,\text{meV}$ for graphite and extrapolated this value to a single graphene layer to obtain $39.2 \pm 0.5\,\text{meV}$. From the theoretical point of view, most simulations to compute the physisorption well depth have relied on model molecules, such as coronene, because of the difficulty in properly handling the long-range VdW interactions in periodic calculations. Accordingly, most studies found that the position of the H physisorbed species is a *hollow* position, *i.e.* at the center of the benzene ring. Standard quantum calculations such as Möller-Plesset perturbation theory on coronene using large basis-set and correcting for the Basis-Set Superposition Error (BSSE) (see Box "BSSE and the CP-correction on page 19") found a physisorption minimum at 2.93 Å with a depth of 39.7 meV (Bonfanti et. al. (2007)[36]), in good agreement with the experimental result. Because of the very small well depth, which is expected also on clean graphene surfaces, the H physisorption cannot be exploited for any *hydrogen storage* application. The problem remains, however, of some interest for the chemistry of the *ISM*, *i.e.* the mixture of gas and dust that fills the space between stars. The formation of H_2, which is still a puzzling question in astrochemistry, on dust grains may occur at temperatures that allow physisorbed species to be stable ($T \approx 10-20$ K in the so-called *diffuse clouds*) (see Chapter 2). At higher temperatures ($T > 50$ K), the desorption rate is instead so high that the refreshment of the surface is completed in a time-scale that is too short for astronomical standards.

[9] In this respect, it is worthy to add that most of the experiments in this field rely on graphite, rather than on graphene. On the other hand, theoretical modeling is most often performed on graphene, either because of the computational advantage or for real interest in the substrate. However, the experimental results on graphite can be translated with minor changes to graphene, since "graphene on graphite" can be considered effectively decoupled from the substrate[30].

Box 1.2: The BSSE and the CP-correction

The *Basis-Set Superposition Error* is one of the main truncation errors affecting *any* AO calculations. This error arises from the enlargement of the basis set experienced by two fragments, A and B, when they approach each other. In particular, fragment A can "borrow" basis functions from the other, thus its basis set is increased and its description improved. When computing, for instance, the H binding energy on graphene, the energy of the asymptote (the isolated graphene sheet and the H atom) results from unmixed basis sets while, in the binding geometry optimization (H+graphene), basis sets are mixed. Such mismatch is the source of the error and has to be removed when anytime AOs are employed. In this respect, *PW* are more convenient, being not affected by the BSSE. However, their main shortcoming is the much larger computational cost, which makes them out of reach for large systems.
The most popular method to get rid of the BSSE is the so-called *CP*-correction. The latter has the main advantage of being an *a posteriori* method, *i.e.* it only requires additional single-point calculations using the mixed basis sets - that can be realized by introducing "ghost orbitals" on the relevant atoms. For a reaction of the kind $A + B \rightarrow AB$, the CP-correction to the binding energy can be readily obtained through

$$E_{\mathrm{CP}} = (\tilde{E}_A^\star + \tilde{E}_B^\star) - (E_A + E_B)$$

where˜refers to the "final geometry" (*i.e.* that of the optimized AB structure), while $\star$ denotes the use of the *whole* basis set. Thus, $\tilde{E}_A^\star$ is the energy of the fragment A in the optimized geometry of AB and with the whole basis set (*i.e.* with ghost basis functions on B).
A less popular method is the so-called *chemical Hamiltonian approach (CHA)*[37, 38]. This is an *a priori* method in which basis set mixing is prevented by replacing the conventional Hamiltonian with one in which all the projector-containing terms that would allow mixing have been removed.

On the other hand, the chemisorption of H on graphene is a quite recent topic (15 years or so), since for some time H atoms were not believed to be able to bind to the substrate and early attempt to model the adsorption without relaxing the surface failed in finding the chemisorption minimum. The first to show that H binds to the surface if *substantially* surface reconstruction is allowed was Jeloaica and Sidis (1999)[31]. The value of the binding energy shows a sizable variability in the literature that can be ascribed to differences in the adopted DFT functionals and, more importantly, to the computational setup and the optimization strategy employed in the calculations[30]. Thanks to recent PW-DFT calculations the value of the chemisorption well converged to 0.85 eV[39, 40]. Atomic-orbital DFT results suggest a larger value (close to 0.97 eV, see Figure 1.7) likely because of BSSE and optimization strategy.

The chemisorption well on graphene is much smaller than that found on typical transition metal ($2-2.5$ eV) or the CH bond energy in hydrocarbons (≈ 4 eV). The main reason is that in the formation of the CH bond on graphene, a considerable fraction of the energy goes into the lattice, where it is stored indefinitely as deformation energy of the puckered surface. Such puckering consists in the out-of-plane displacement of the binding C and it is a consequence of the sp^2-sp^3 rehybridization of the valence C orbitals. The extent of such an out-of-plane movement is about 0.3-0.4 Å and extends several angstroms (≈ 10 Å) from the adsorption site[30].

The H chemisorption is an activated process that requires the overcome of barrier to occur, a.k.a. *sticking barrier*, to occur. From the experimental point of view, the presence of a barrier is undeniable. Indeed, as first recognized by Neumann et. al. (1992)[32],

hyperthermal beams ($T \approx 2300K$) are needed in order to deposit H atom on carbons surface. Without a barrier, cold atomic beams would be effective in depositing H atoms at room temperature and hydrogen deposition would be a random process, with estimated abundances of dimers and clusters much smaller than that observed. Nevertheless, the height of the barrier is yet unknown but current DFT results suggest a value close to 0.2 eV. In Chapter 5, we will return to this topic and present new DFT results about the H sticking barrier on graphene.

Concerning the sticking dynamics, most of the available theoretical investigations agree qualitatively on the classical, over-barrier regime where the energy transfer to the substrate is the only limiting factor[41, 42]. Few studies address the problem in the regime where tunneling plays a dominant role and, until recently, none of them considered tunneling in the presence of a true dissipative quantum bath, mimicking the surface. This has been long rather unpleasant since it was recognized long ago that the tunneling probabilities depend on strength of dissipative effects (Caldeira-Legget,1981[43]). The main problem hindering such studies is the so-called *dimensionality curse*, *i.e.* the exponential scaling affecting exact quantum approaches. Tremendous progress in this field has recently come from the so-called *Multi-Configuration Time-Dependent Hartree (MCTDH)* method[44] and its multilayer variant[45] (see Box 1.3 on pag. 20).

Box 1.3: The MCTDH approach

The MCTDH approach is an extension to the *time-dependent Hartree-Fock method* in which the wavefunction is written as a combination of products of single-particles functions $|\phi_{j_k}\rangle$

$$|\Psi\rangle = \sum_{j_1} ... \sum_{j_N} A_{j_1,j_2,...,j_N} |\phi^{(1)}_{j_1}\rangle |\phi^{(2)}_{j_2}\rangle ... |\phi^{(N)}_{j_N}\rangle$$

Exploiting the *Dirac-Frenkel* variational principle, the original N particle problem is reduced to N problems for each degree of freedom (DOF). With this method, one can treat up to tens of DOFs, but with a smart choice of each single-particle function, the number can be increased up to 100-150. Indeed, each $|\phi\rangle$ is not forced to represent just one DOF, but it can describe 2-4 DOFs, $|\phi^{(i)}_{j_i}(Q_i)\rangle$ with $Q_i = (q_1, ...q_n)$. In the multilayer variant, the dimension of each $|\phi^{(i)}_{j_i}(Q_i)\rangle$ is further enlarged and each function is itself written as a multiconfigurational product

$$|\phi^{(i)}_{j_i}(Q_i)\rangle = \sum_{k_1} ... \sum_{k_N} B_{k_1,k_2,...,k_N} \phi^{(1)}(\bar{Q}_1)\phi^{(2)}(\bar{Q}_2)...\phi^{(n)}(\bar{Q}_N)$$

In this way, one can arrive to treat up to 5000-10000 DOFs.

A key step in the investigation of the H sticking in the quantum regime was the formulation of a reliable model for chemisorption, due to Bonfanti et. al. (2015)[46]. The latter consists of a system-bath strategy that is based on the reliability of a generalized Langevin description of the C atom dynamics. With this assumption, the substrate is mapped into a surrogate bath of independent harmonic oscillators and the high-dimensionality problem is tackled with the MCTDH method in a numerically exact way. An accurate description of this method and the sticking dynamics is far beyond the scope of this work. The interested reader is referred to specific papers on the subject[30, 46].

1.3.2 Midgap states

From the electronic point of view, the chemisorption of H on graphene acts as a p_Z removal from the π-system of graphene, since the latter gets engaged in the strong covalent bond

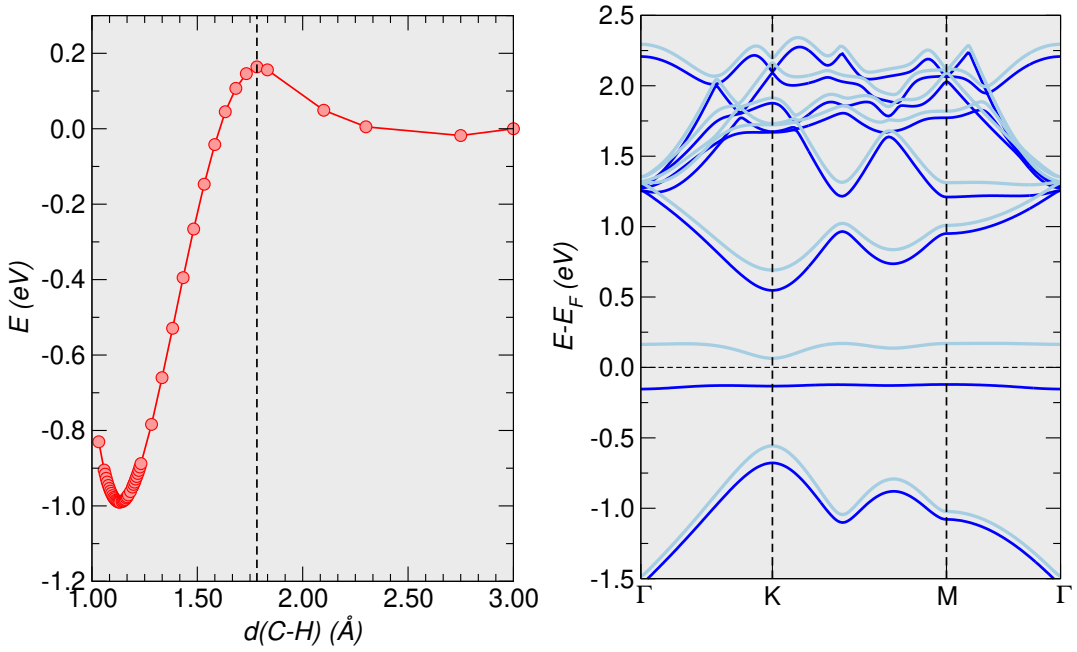

Figure 1.7. (Left) Energy path for the H chemisorption simulated on a 5×5 graphene superlattice, by keeping frozen at each step the C-H bond distance along the z-coordinate; (Right) Band structure for H on a 5×5 graphene superlattice. Spin-up and spin-down bands are respectively colored in black and red. Both simulations are performed with PBE density functional and DZP basis-set, as implemented in the SIESTA code[28].

with the incoming H. Such a removal creates an *imbalance* between the number of sites in the two sublattices and gives rise to the appearance of a single-occupied molecular orbital at the Fermi level dubbed *midgap state*. This zero-mode energy level is not strictly localized but it is found to decay from the adsorption site with a $1/r$ power law. At first glance, midgap states can be accounted for by considering that, if e-h symmetry (nn approximation) holds, the odd-numbered system has necessarily a zero-energy level. Due to the low value of the nnn hopping, while relaxing the nn approximation, the midgap state moves away from the Fermi level but remains very close to it.

From the chemical point of view, the appearance of semi-localized midgap states can be well understood in the resonance picture, familiar to chemists. Upon the formation of the C-H bond, the π-bond is broken and an unpaired electron is left on the neighboring C. This unpaired electron does not remain localized around the adsorption site but it delocalizes over the majority sublattice through well-known Pauli's resonance (in a sort of extended *ortho-para mesomeric effect*).

When bipartite lattices are concerned, interesting theorems can be formulated about zero-mode states, that allow understanding many properties of defective systems. Let consider the Hamiltonian of a bipartite system

$$H = -|t| \sum_{\langle i,j \rangle} a_i^\dagger b_j - |t| \sum_{\langle i,j \rangle} b_j^\dagger a_i \tag{1.16}$$

where $a_i^\dagger, b_j^\dagger$ (a_j, b_i) create (annihilate an electron respectively on site i of the A sublattice and j of the B sublattice[10]. We can formulate the following *zero-mode theorem*:

Theorem 1.3.1. *Whenever there is an imbalance in the number of atoms in the two*

[10]Here, we are using the terms "site" and "state" as synonyms, since A and B can be identified exactly with the subspaces spanned by the p_Z orbitals of the two sublattices

sublattices of a bipartite lattice, $\eta = N_B - N_A > 0$, there are η number of degenerate eigenfunctions of the Hamiltonian (1.16) *at zero energy, all with null amplitudes on the minority sublattice.*

The proof is straightforward[30]: let $N_A > N_B$ and

$$|\Psi\rangle = \sum_i \alpha_i |\alpha_i\rangle \tag{1.17}$$

a trial solution at zero-energy, with $|\alpha_i\rangle$ a complete set in A. Since, by definition, $H|\Psi\rangle = 0$, multiplying both sides of Equation (1.17) by $\langle\beta_j|H$ we get

$$\sum_i \langle\beta_j|H|\alpha_i\rangle\alpha_i = 0 \tag{1.18}$$

for $j = 1, 2, , ..N_B$. Equation (1.18) allows finding the α_i coefficients that define the trial solution. However, we have N_B equations to determine $N_A > N_B$ coefficients, meaning that the solution cannot be completely determined and we remain with $\eta = N_A - N_B$ linearly independent solutions. In addition, the above result also shows that the zero-energy states localize on the A sublattice, which is here the majority one. This theorem provide us with a counting rule, generally known as *imbalance rule*, which allows predicting the *minimum* number of midgap states in graphenic systems.

As we mentioned above, the midgap state describes an unpaired electron left by the breaking of the π-bond, hence the p_Z removal leads to a spin $1/2$ magnetic moment. When many-body phenomena such as magnetism are of interest, one needs to go beyond the TB description since the onset of magnetism originates from electron-electron interactions. The simplest way to improve the TB description and set up a correlated model is by including the following term in the Hamiltonian

$$H' = U \sum_i n_{i\uparrow} n_{i\downarrow}$$

describing a repulsive on-site Coulomb interaction, where $n_{i\sigma} = c^\dagger_{i\sigma} c_{i\sigma}$ is the spin-resolved electron density operator at site i and U the magnitude of the on-site repulsion (here $c^\dagger_i$ (c_i) creates (annihilates) an electron at site i indistinctly from the sublattice).The resulting total Hamiltonian, $H^{\mathrm{TB}} + H'$, constitutes the so-called *Hubbard model*. Despite its apparent simplicity, the Hubbard model is not analytically solvable for $N > 2$ electrons. In first approximation, one can assume that $n_{i\uparrow}$ and $n_{i\downarrow}$ slightly differ from their mean values. We introduce the two following operators

$$d_{i\uparrow} = n_{i\uparrow} - \langle n_{i\uparrow}\rangle$$
$$d_{i\downarrow} = n_{i\uparrow} - \langle n_{i\downarrow}\rangle$$

and re-write the interaction term as

$$H' = U \sum_i (d_{i\uparrow} + \langle n_{i\uparrow}\rangle)(d_{i\downarrow} + \langle n_{i\downarrow}\rangle)$$

Since $d_{i\sigma} \approx 0$ by hyphothesis, we can neglect the term $d_{i\uparrow} d_{i\downarrow}$ and we arrive at

$$H'_{\mathrm{mf}} = U \sum_i (n_{i\uparrow}\langle n_{i\downarrow}\rangle + \langle n_{i\uparrow}\rangle n_{i\downarrow} - \langle n_{i\uparrow}\rangle\langle n_{i\downarrow}\rangle)$$

This is the infamous *mean-field approximation*, which allows overcoming the main difficul-

ties of the full model[11]. Within the mean-field approximation, the Hubbard model can be self-consistently solved, starting from initial randomly chosen values of $\langle n_{i\sigma}\rangle$. Once the converged solutions are obtained, the total spin of the system S can be computed according to

$$S = \sum_i M_i = \sum_i \frac{1}{2}(\langle n_{i\uparrow} - n_{i\downarrow}\rangle$$

where M_i is the average magnetization on site i. In 1989, Lieb[47], working on the Hubbard model, established a fundamental theorem that allows characterizing the ground-state of bipartite systems:

Theorem 1.3.2 (Lieb)**.** *A bipartite system at half-filling described by a Hubbard model with repulsive electron-electron interactions ($U > 0$) has the ground state characterized by the total spin*

$$\boxed{S = \frac{1}{2}|N_A - N_B|} \tag{1.19}$$

where N_A and N_B are respectively the numbers of sites in sublattice A and B

This result holds in any dimension, regardless of the presence of a periodic structure. The application to the chemisorption of H on graphene is immediate: the adsorption of one H atom (say on the sublattice B) leads to the imbalance $N_A - N_B = 1$, resulting in a $S = 1/2$ ground-state. According to our previous discussion, this magnetic moment is due to an unpaired electron residing in the midgap state and localizing on the majority sublattice. These findings are confirmed by DFT calculations, as made evident from Figure 1.8 where the local and total density of states are displayed.

It is worth stressing that Lieb's theorem provides information on the total spin but it does not give the number of unpaired electrons. For instance, a $S = |N_A - N_B|/2 = 0$ ground state can be realized also with an *open-shell* configuration where two unpaired electrons have opposite spin. Correct counting of unpaired electrons can be realized by introducing the concept of *non-adjacent sites*. We say that two sites are non-adjacent if they are not connected by any transfer integral. In the nn approximation, two sites on different sublattice are then naturally non-adjacent. It always exists a maximal set of non-adjacent sites and we call α those sites belonging to such set and β the remaining ones. If N is the total number of sites of the bipartite lattice, then $N = N_\alpha + N_\beta$. Since each site α binds at least one site β and since we can arrange one electron per site, we can form, at most, N_β bonds. Then, we are left with $N_\alpha - N_\beta$ unpaired electrons or equivalently

$$\boxed{\eta = 2N_\alpha - N}$$

[11]Such approximation is at the heart of any *mean-field theory*: one neglects the detailed dynamics of the system and include the correlations between particles only "on the average". The method applies also to composite systems, with both fermions and bosons. If only the interactions between different particles are relevant, the Hamiltonian reads as

$$H = \sum_i \varepsilon_i^f f_i^\dagger f_i + \sum_j \varepsilon_j^b b_j^\dagger b_j + \sum_{ii'}\sum_{jj'} V_{ii'jj'} f_i^\dagger b_j^\dagger b_{j'} f_{i'}$$

where $f^\dagger, b^\dagger$ (f, b) are respectively the creation (annihilation) fermionic and bosonic operators. Introducing $d_{ii'} = f_i^\dagger f_{i'} - \langle f_i^\dagger f_{i'}\rangle$ (and the same for bosons), one gets the following mean-filed potential operator

$$V_{\rm MF} = \sum_{ii'}\sum_{jj'} V_{ii'jj'}(f_i^\dagger f_{i'}\langle b_j^\dagger b_{j'}\rangle + b_j^\dagger b_{j'}\langle f_i^\dagger f_{i'}\rangle) + \sum_{ii'}\sum_{jj'} V_{ii'jj'}\langle f_i^\dagger f_{i'}\rangle\langle b_j^\dagger b_{j'}\rangle$$

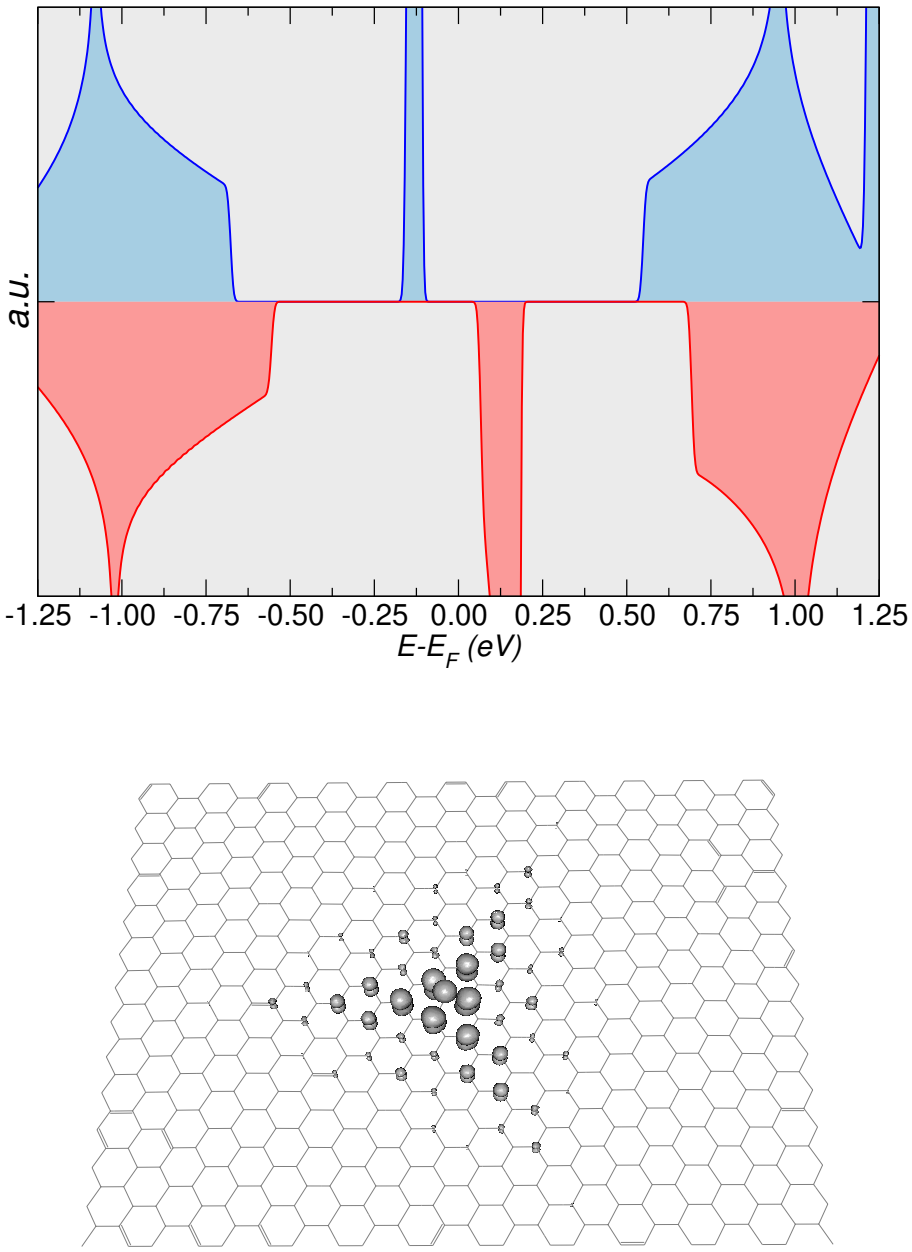

Figure 1.8. (Top) Spin-resolved density of states of H on 5×5 graphene superlattice. The spin-up and spin-down doss are respectively colored in blue and red. (Bottom) Difference between the spin-up and spin-down local density of states, showing the semi-localization of the midgap state. Both simulations are performed with PBE/DZP, as implemented in the SIESTA code[28].

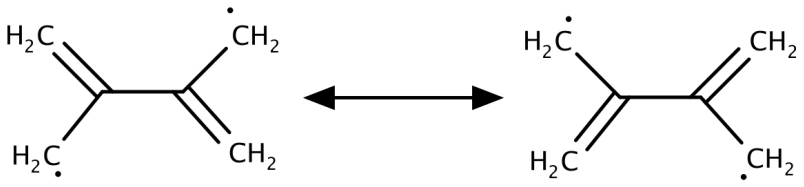

Figure 1.9. Structural formula of the 2,3-bis-methylene-1,4-butadiene, with its principal resonance structure.

Earlier, we have defined $\eta = |N_A - N_B|$ as the minimum number of midgap states. Here, we can redefine it as the total number of unpaired electrons in the Lewis structure with the maximum number of bonds, *i.e.* the total number of midgap states[12] localized on the maximal set of non-adjacent sites. Figure 1.9 shows an application of these concepts to a simple molecule: the maximal set of non-adjacent sites is given by the 4 sites at the edges of the molecule, hence one can realize at most $N_\beta = 6 - 4 = 2$ π-bonds and remains with $\eta = 4 - 2 = 2$ unpaired electrons. Note that $S = 0$ in this case.

1.3.3 Reactions at the gas-surface interface

Before moving to the high-coverage regime, it is worthy to discuss the reactions that may occur between an H already adsorbed (either physisorbed or chemisorbed) on the surface and one coming from the gas phase, since this is a typical situation characterizing the long-term exposure of a (pre-covered or not) surface to H flux.

The most important reaction is that leading to the formation of H_2, also known as *recombination*, which is characterized by large exothermicity and absence of any barrier. The huge amount of energy that is freed during the reaction goes into the product molecule though sometimes a considerable fraction can be left on the lattice, especially when chemisorbed H atoms are involved. The H_2 recombination on graphene can occur through three different mechanisms, that are operative at different thermodynamical conditions: the *Langmuir-Hinshelwood (LH)*, the *Hot-atom (HA)* and the *ER* mechanism.

In the LH mechanism, both reactants are physisorbed on the substrate and they diffuse until they meet each other and react. By definition, this mechanism is relevant only to the physisorption regime however it is not a standard since the thermalization of physisorbed H in stable adsorption sites is hampered by the zero-point fluctuations. In this process, the nascent product molecule either desorb immediately from the surface with a strong rotational excitation or stays trapped on the surface in a hot vibrational and rotational excited metastable state[48, 49].

In the HA mechanism, one of the reactants is trapped on the surface but not equilibrated. Typically, it diffuses hyper-thermally until it encounters a reaction partner to form H_2. The relevance of the HA recombination for hydrogen on graphene is yet unclear. It is probably operative when H atoms trap in the physisorbed well of a well-cleaned surface but it is expected to be rather sensitive to the surface temperature because of the great effect that the latter has on the hot-atom lifetime.

In the ER mechanism, one of the reactants is accommodated in stable chemisorption well. The second comes from the gas phase and the product molecule is formed through a direct collision with the adsorbed atom. The ER is recognized as the most important recombination mechanism since it is operative in a wide range of temperatures at which

[12]This result strictly holds for benzenoid systems. For a generic bipartite lattice, it gives only a lower bound to the total number of midgap states, namely $\eta \geq 2N_\alpha + 1$. There may exist further zero-energy states, known as *supernumerary modes*.

physisorbed species are known to be absent (50-300K at low coverage and up to 500 K at higher coverage)[30]. When the surface is exposed to hot H beams, the ER recombination generally competes with the H sticking (*i.e.* the formation of the dimer in this case). On the contrary, when cold atomic beams are used on a pre-covered surface, the incoming H is not able to overcome the sticking barrier and the abstraction dominates over the dimer formation[50]. A more detailed description of the ER reaction is left to Chapter 9, where we present new quantum dynamical simulations of this reaction on a very special surface, namely graphene on SiC.

1.3.4 High coverage

Chemisorption of hydrogen atoms is an activated process and thus any change in the height of the energy barrier to sticking reflects exponentially on the kinetics of the adsorption process. Without the presence of such a barrier, the sticking of atomic hydrogens would be a random process, in contrast to the experimental observations that find the formation of dimers and clusters. Since H are immobile on the surface when chemisorbed, the formation of dimers can be only due to a *preferentially sticking* that favors the adsorption of a second H atom on specific lattice positions around the defect[39]. Such preferential sticking can be understood by reminding the earlier discussion on midgap states. The first adsorption leaves an unpaired electron residing in a midgap state that semi-localizes around the defect, thus driving the second H addition on a neighboring site. The formation of *ortho* and *para* dimers is then an easy process since such an unpaired electron can be easily coupled to the electron of the incoming H with a small or even vanishing activation barrier. In this respect, theoretical results showed an expected preferential formation of "balanced" dimers, with para dimers being the most abundant ones[13].

After the formation of an AB dimer, there are no unpaired electrons to bias the adsorption of a third H in specific lattice positions. Nevertheless, there are still two effects to consider. First, some adsorption sites are more favored than others because the relaxation energy is lowered around sites that have already sp^3 character, *i.e.* that are already rehybridized and *pyramidalized* to some extent. This is a kind of substrate softening that occurs upon the adsorption of the first hydrogen atoms. Second, a dimer or a cluster on the surface introduces "edges" in the π-cloud and these are known to be more reactive than bulk lattice sites. We will have the occasion to discuss in more detail the rehybridization and pyramidalization effect in Part II when dealing with curved systems, and the second effect later in this Part I.

[13]Early thermal desorption experiments on hydrogenated graphene were puzzling because of a double peak structure for H_2 desorption (one at 445K and the other at 560K) that was incompatible with a monomer desorption barrier of 1 eV (the sum of adsorption energy 0.8 eV and adsorption barrier 0.2 eV), which was expected to give a single peak at 300K. It took some time before the formation of dimers was fully appreciated and thermal desorption spectra were correctly interpreted as the activated formation of H_2 from ortho and para dimers on the surface (Hornakaer et. al. 2006[51]). The temperature of the first peak is in agreement with the formation of H_2 out of the para dimer. Instead, at the temperature of the second peak, ortho dimers, which are more stable against thermal annealing, convert into para dimers and recombine.

Chapter 2

The role of PAHs in the Interstellar Chemistry

> *"Over the last 20 years, we have discovered that we live in a molecular universe: a universe where molecules are abundant and widespread; a universe with a rich organic inventory particularly in regions of star and planet formation; a universe where the formation of stars and the evolution of galaxies is driven in many ways by the presence of molecules; a universe where prebiotic interstellar molecules may represent the first steps toward life; a universe where molecules can be used as "dye" to trace important processes in the interstellar medium; a universe where molecules provide unique information on the physical conditions of a wide variety of regions; and a universe where molecules can work together to form such complex species species as you and me."*
>
> – A.G.G.M. Tielens, *The Molecular Universe*

In this Chapter, we introduce *polycyclic aromatic hydrocarbon*, a class of molecules that is strictly related to graphene, being graphene fragments with the edges saturated by H atoms. PAHs have sparked great interest in the last few years because of the role they might play in the *interstellar chemistry*. In particular, they have been demonstrated to act as catalysts for molecular hydrogen formation under interstellar conditions. Thus, they could provide a possible explanation for the relative abundancies of H_2 in those regions of the ISM where this molecule should be dissociated by ultraviolet (UV) photons and heat. In addition, being directly related to graphene, PAHs have been often adopted as a molecular model to investigate graphene properties and chemical reactivity.

This Chapter is organized as follows: in Section 1, we discuss the chemical reactivity of PAHs; in Section 2 we discuss their presence in the ISM and the recently proposed route to H_2 formation.

2.1 Structure and reactivity

PAHs are organic molecules formed by multiple benzenic rings fused. Their size can range from small unities (*e.g. napthalene*, which has just two benzenic rings) to very large islands, becoming graphene in the infinite limit. Even though they are characterized by aromatic motifs, not all PAHs satisfy the Hückel's rule. For instance, *coronene* ($C_{24}H_{12}$), one of the most studied molecules of this family, has 24 π-electrons, a number that does not satisfy the $4n + 2$ rule.

From a topological point of view, the π-system of PAHs constitutes a bipartite lattice, and therefore the theorems we introduced earlier (see Subsection 1.3.2) in discussing the appearance of midgap states in graphene apply also to these molecules. Considering again

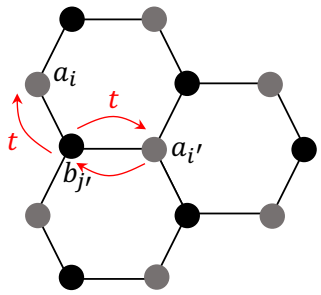

Figure 2.1. Pictorial representation of creation/annihilation process described by the operator $a_i^\dagger b_j^\dagger b_{j'} a_{i'}$.

coronene, its lattice is *balanced*, with $N_A = N_B = 12$. The maximal set of non-adjacent sites is realized by selecting all sites belonging to either one of the two sublattices. Therefore, $N_\alpha = 12$ and

$$\eta = 2N_\alpha - N = 0$$
$$S = \frac{1}{2}|N_A - N_B| = 0$$

The bare coronene molecule has then a *closed-shell* ground state with $S = 0$ and no midgap states.

From the chemical point of view, the reactivity of PAHs is closely related to that of graphene. However, in isolated systems, the presence of edges introduces additional electronic and geometrical effects. The latter can strongly affect the chemical reactivity, making some sites more likely than others to react with foreign species. Concerning the reactivity towards H atoms, several studies revealed a preference for addition at the edges of PAHs. One can argue that the sticking occurs at the edges because central C atoms of PAHs behave as "graphitic" sites so that the process requires there more energy due to the before-mentioned surface puckering. However, DFT calculations show that the reorganization energy, *i.e.* the difference between the energy of the bare molecule in the configuration in which it binds the H and the energy of the bare molecule in its equilibrium geometry, is higher for an edge site than for a central site. Therefore, electronic rather than geometrical effects are expected to play a major role in the preferential sticking at edges of PAHs. The origin of such electronic effect can be found in the *edge localization* of the (low-energy) frontier orbitals of the π-system, which enhances the reactivity of those sp^2 sites that have the smallest number of sp^2 neighbors. Sites at the edges of a PAH molecule, being undercoordinated in the π-system, are thus more reactive as if they present a sort of dangling bonds to be saturated.

2.1.1 π-coordination and π-hyperconjugation

The edge localization can be given a firmer ground already in a tight-binding model, by exploiting the bipartite structure of the Hamiltonian[52]. Let consider the following bipartite Hamiltonian in the nn approximation

$$H^{TB} = -t \sum_{\langle i,j \rangle} a_i^\dagger b_j + \text{h.c.} = H_{AB} + H_{BA} \tag{2.1}$$

where h.c. stands for "hermitean conjugate". By squaring Equation (2.1), we get the following renormalized Hamiltonian

$$\tilde{H} = t^2 \sum_{\langle i,j \rangle} \sum_{\langle i',j' \rangle} a_i^\dagger b_j b_{j'}^\dagger a_{i'} \tag{2.2}$$

The eigenspectrum of this renormalized lattice, $\{\tilde{\varepsilon}_i\}$, is related to the original through

$$\tilde{\varepsilon_i}^{\pm} = \pm\sqrt{\varepsilon_i} \tag{2.3}$$

In this way, the quadratic structure of H (in terms of annihilation/creation operators) is preserved: that is, one squares the matrix defining the form rather than the form itself. The ground-state of the renormalized lattice corresponds to the highest-occupied/lowest-unoccupied (HOMO/LUMO) molecular orbital pair of the original lattice. Through heuristical arguments, we can understand the meaning of the (non-trivial) four creation/annihilation product operator given in Equation (2.2). The first product, $b_{j'}^\dagger a_{i'}$ describes a process in which an electron is annihilated at site i' on sublattice A and created at the neighboring site j' on sublattice B (see Figure 2.1). The following b_j operator annihilates an electron at site j on sublattice B but this site must necessarily be occupied (otherwise $b_j|0\rangle = 0$), then it follows $j = j'$. The operator $a_i^\dagger$ can now create an electron at site i on sublattice A, which be either a nnn to i' or be i' itself, *i.e.* $i = i'$. Therefore, if Z_i is the *π-coordination number*[1] of site i in the A sublattice of the *original* lattice, the renormalized Hamiltonian looks like

$$\tilde{H} \approx t^2 \sum_i Z_i a_i^\dagger a_i + t^2 \sum_{\langle i,j \rangle} Z_i a_i^\dagger a_j \tag{2.4}$$

where $\langle i, j \rangle$ means now nns on the renormalized lattice. It follows that the renormalized lattice is a *triangular* lattice with hopping parameters $t' \equiv t^2$ and on-site energies equal to $t^2 Z_i$. Sites on the edges are undercoordinated in the π-systems, *i.e.* $Z = 2$ *vs.* $Z = 3$ of graphitic sites, therefore they present the lowest on-site energies. The HOMO/LUMO pair of the renormalized lattice is then naturally localized on the edge sites. From Equation (2.3), it follows that the same holds for the HOMO/LUMO pair of the original lattice. Notice that such localization does not involve all the edge sites in the same way. Indeed, in the renormalized lattice, we can expect that the low-energy orbitals mostly localize on those edge sites that have the *largest* number of nns with the same coordination to hybridize with. In the original lattice, such number corresponds to the number of nnns. This is a sort of an extended π-conjugation (of edge sites) involving nnns. For this reason, Bonfanti et. al. (2011)[52] coined the term *π-hyperconjugation*[2] and referred to the number of nnns with the same coordination as to the *hypercoordinaton number* (ξ). Hydrogen affinity is found to increase with this number, as exemplified, for instance by the cases of armchair edges (with $\xi = 0$) and zig-zag edges (with $\xi = 2$) (see Figure 2.2), which show markedly different H binding energies - 1.7 eV and 2.8 eV respectively[52].

In Chapter 4 we will have the occasion to see the π-coordination and the π-hyperconjugation in action in discussing the energetics of the step-wise hydrogenation reaction of the coronene molecule.

[1] Remind that we are working on the π-lattice, so the coordination number here refers to the number of C sp^2 neighbors, not to the "total" coordination number.

[2] This must not be confused with the *hyperconjugation* commonly introduced in organic chemistry courses. The latter is an interaction between electrons in a σ bond with an empty or partially filled adjacent non-bonding p orbital (or a σ/ π antibonding orbital or even a filled π orbital). On the contrary, π-hyperconjugation regards π-electrons only.

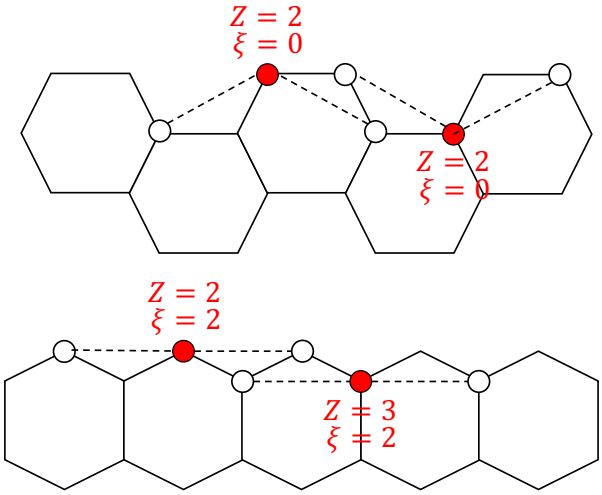

Figure 2.2. Armchair (top) and zigzag (bottom) edges with π-coordination (Z) and π-hypercoordination number (ξ) for different sites. White circles are used to denote the nnn*s*.

2.2 Interstellar Medium: too much H_2 ?

In the opening of this Chapter, we mentioned that PAHs have been the interest of the astronomy community because of the role they are supposed to play in the chemistry of the ISM. Since the work on coronene and coroannulene that we are going to discuss respectively in Chapter 4 and 7 was in part motivated by these arguments, we use this Section to provide the reader with a background on the interstellar chemistry concerning graphitic surfaces and PAHs. Of course, a complete treatment of this fascinating matter is far beyond the scope (and the knowledge) of the author. The interested reader is referred to the numerous groundbreaking works (*e.g.* those of Tielens and coworkers[53, 54, 55]) or the many excellent books written in this field[3].

According to the most recent astronomical observations, about the 95% of the *total* mass of the Universe is composed of dark matter and dark energy, and the contribution of the *baryonic* matter (*i.e.* the most familiar atoms and molecules) is only 5%[58]. Surprisingly, it is the existence of this tiny fraction of baryonic mass that generates the variety and complexity of our Universe, with the formation of planets, stars, and galaxies. Most interestingly, 98% of the baryonic mass is composed of H and He, while the total contribution of heavier elements such as C, N, or O, is only about 2%. The rich chemical world around us is then entirely based on such a small fraction of heavy elements. In astronomy, the exploration of the chemical evolution of matter in the Universe is of fundamental interest[56]. Understanding the molecular evolution will lead us to answer some fundamental questions such as "How are molecules formed in the ISM?", "How are molecules incorporated into planets or stars?" and eventually "What is the origin of our Solar System?".

Before addressing specifically the problem of H_2 formation in the ISM, it is worthy to briefly describe the composition of the interstellar matter and its circulation.

[3]For instance, the book of Yamamoto (2014)[56], "*Introduction to Astrochemistry*", that treats the chemical evolution from the interstellar clouds to planet formation, or the old but gold Duley (1984), "*Interstellar Chemistry*"[57].

2.2.1 Circulation of matter in the ISM

In the *Milky Way*, about 90% of the baryonic mass resides in stars, while the remaining 10% is found in the ISM[4]. The latter consists of gas and dust particles composed of silicate and various carbonaceous compounds, with sizes that are typically around 0.1 µm in diameter. The gas component is dominated by molecular hydrogen, which is the most abundant molecule in the ISM. The dust-to-gas ratio largely depends on the abundance of the heavier elements and varies among galaxies and even within our Galaxy, where its average value is around 0.01.

The interstellar matter is not uniformly distributed over the galaxy but is rather concentrated in *clouds*. Figure 2.3 shows the density (ρ) and the temperature (T) for some representative classes of clouds. *Diffuse clouds*, *intercloud gas*,*coronal gas* and some *molecular clouds* are extended clouds in pressure equilibrium (they lie along a straight line in Figure 2.3). Denser molecular clouds are instead gravitationally contracting and deviate from the line of constant pressure. *H II regions* are regions around high-mass stars, where the hydrogen exists mostly in the cationic form (H^+). The coronal and intercloud components of the ISM are both diffuse and ionized and they are generally classified into *hot ionized medium (HIM)* and *warm ionized medium (WIM)*. They evolve in diffuse clouds once their protons recombine with electrons. In diffuse clouds, hydrogen exists both in atomic and molecular forms. As the T decreases and ρ increases, diffuse clouds become gradually opaque to the *interstellar UV radiation*, and H_2 becomes the dominant form of hydrogen. The resulting clouds are the before-mentioned molecular clouds, which represent the formation site of new stars. Molecular clouds, due to their high density, are subjected to a gravitational contraction[5] which ultimately leads to the formation of *protostars*. These are the first stage of the so-called *main-sequence stars*. Stars remain in this phase of their evolution cycle for a relatively long time, which depends on their mass and chemical composition. For a $1M_\odot$ main-sequence star, the lifetime is around 10^{10} years, during which it continues to burn hydrogen. Once the hydrogen-burning is completed, main-sequence stars evolve into *late-type stars*. Some late-type stars lose a considerable fraction of their mass, thus supplying dust and gas to the interstellar environment. Massive stars ($> 8M_\odot$), instead, generally gives rise to *supernova explosions*, which are the most energetic events in the Universe. It is during these events that the heavy elements formed during *nucleosynthesis* in stars are spilled into the ISM. Thus, interstellar matter can circulate throughout the galaxy over and over the entire lifecycle of stars[56].

2.2.2 H_2 in diffuse and molecular clouds

Diffuse clouds are regions of relatively low density $n \approx 50\ \mathrm{cm}^{-3}$ and temperature $T \approx 80K$, corresponding to a thermal pressure of 4000 cm^{-3}K. Typical sizes and masses are ≈ 10 pc[6] and $\approx 500M_\odot$, but actually diffuse clouds show a broad mass and size distribution, which joins smoothly into those of molecular clouds[53].

In diffuse clouds, the typical H_2 (or H) density ranges from $10\,\mathrm{cm}^{-3}$ to $100\,\mathrm{cm}^{-3}$. Early observations of molecular hydrogen in this environment were puzzling because diffuse clouds are transparent to some extent to the interstellar UV radiation. The latter is able to penetrate deeply into diffuse clouds and determine the photodissociation of H_2 into atomic hydrogen. It has been estimated that 10% of all adsorption events of the interstellar UV radiation leads to the dissociation of H_2. As consequence, in a diffuse clouds, the

[4]The total mass of our galaxy is of the order of 10^{11} *solar masses* ($M_\odot$), while the interstellar matter is about $10^{10}M_\odot$.

[5]They are stable over time scales of 3×10^7 yrs, presumably due to a balance of magnetic or turbulent pressure and gravity[53]

[6]The *parsec* (pc) is a unit of length used to measure the large distances to astronomical objects outside the Solar System: 1 pc ≈ 3.26 light years $\approx 3.0857 \times 10^{16}$ m.

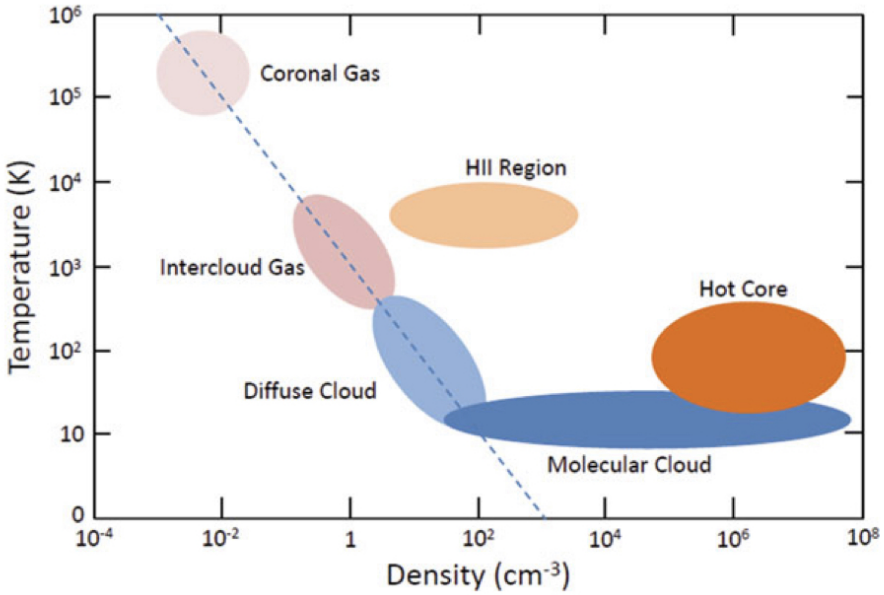

Figure 2.3. Temperature-density diagram of interstellar clouds taken from Yamamoto (2014)[56]. The dashed line indicate the constant-pressure line.

Figure 2.4. (Left) *Orion nebula*, a diffuse nebula situated in the Milky Way, south to the *Orion's Belt* in the Constellation of Orion; (Middle) *Eagle nebula*, a young open cluster of stars (a H II region) in the constellation Serpens; (Right) *"Pillars of Creation"*, a famous photograph taken by the *Hubble Space Telescope* of elephant trunks of interstellar gas and dust in the Eagle Nebula.

typical lifetime of a H_2 molecule is around 1000 years, which is an incredibly short time for astronomical standards[59]. Regions where photo processes are strongly active are for this reason called *photodissociation regions (PDRs)*, and they are generally found in the nearby of main-sequence stars[60, 61]. In PDRs, temperatures are generally higher since the UV radiation determines considerable heating of the environment. The debate about the presence of H_2 in the ISM arose from the consideration that, in both colder and hotter regions of diffuse clouds, H_2 could not form through gas-phase reactions since the radiative association (Equation (2.5)) would be rather inefficient at the density typical of such interstellar environment[53, 57].

$$H + H \longrightarrow H_2 + h\nu \tag{2.5}$$

Direct radiative association works in atmospheric conditions but at the pressures typical of the ISM, the contact time between H atoms is dramatically reduced. Consequently, there is not enough time for the forming H_2 molecule to radiate away the binding energy of 4.5 eV, which thus dissociates before reaching the equilibrium condition. Accordingly, it has been estimated that just one in 10^5 collisions would result in the formation of H_2 through this mechanism[7][57].

On the other hand, in opaque *molecular clouds*, where the H_2 density is as high as 10^2-10^6 cm^{-3}, photo processes can still occur due to the so-called *cosmic ray induced-UV radiation*[62]. Cosmic rays can penetrate through the cloud, ionize the surrounding H_2 gas and produce energetic electrons. These electrons can excite the H_2 molecules, resulting in UV emission. Much of the molecular gas in the Milky Way is localized in giant molecular clouds[8], with sizes up to 40 pc , masses of $4 \times 10^5 M_\odot$ and temperatures around 10 K. However, as diffuse clouds, also molecular clouds show a large range of these properties, which at the low end join smoothly with diffuse clouds[53].

Box 2.1: H_2 in the *Early Universe*

The first neutral H and He atoms formed from protons and electrons in a period of time of our Universe called the *Recombination Area*, started around 10^5 years after the *Big Bang*. The world "recombination" is somewhat misleading, since protons and electrons had not been combined before. This term is anyway still used for historical reasons, since it was introduced before the Big Bang hypothesis became the leading theory about the creation of our Universe. Our knowledge of both recombination and subsequent *post*-recombination era relies mainly on our current knowledge about non-equilibrium chemistry or cosmology, since, at present, we are not able to observe "objects" of this epoch of the Universe. At that time, the early Universe was still extremely hot, with temperatures much above 1000 K, but H atoms provided an important cooling mechanism, which was essential for the following formation of the first generation of stars (Population III or sometimes called PopIII)[57]. Indeed, once ionized, H atoms were able to radiate away part of the heat and allow gravitational collapse of gas to occur. H_2^+ and HD first formed from radiative reactions involving atomic hydrogen; then, neutral H_2 formed *via* ion-molecule exchange reactions involving protons and electrons:

$$H + H^+ \longrightarrow H_2^+ + h\nu$$
$$H_2^+ + H \longrightarrow H_2 + H^+$$

[7] A much more efficient mechanism is that involving a three-body collision, since the third body can remove the excess energy from the vibrationally excited H_2 molecule. A three-body collision, however, cannot be invoked in diffuse clouds, since the very low densities makes its probability negligible.

[8] In the galaxy, they are commonly traced through the typical CO $J = 1-0$ transition at 2.6 mm.

or

$$\mathrm{H} + e^- \longrightarrow \mathrm{H}^- + h\nu$$
$$\mathrm{H}^- + \mathrm{H} \longrightarrow \mathrm{H}_2 + e^-$$

Because of the high temperatures of the Early Universe, vibrational levels of H_2 were easily populated. The corresponding excited molecules could then emit radiation through vibrational relaxations and allow the gas to cool down. Excitation of H_2, followed by emission, could also occur through direct collision with H atoms. Such H_2 cooling mechanisms still occur today in the ISM and are of great importance for the interstellar chemistry.

In 1963, Gould and Salpeter were the first to propose that the formation of H_2 could be catalyzed on the surface of interstellar dust grains, thus providing a possible explanation for its relative high abundancies[63]. The H_2 formation rate on a grain surface can be estimated as

$$R_d(\mathrm{H}_2) = \frac{1}{2} S(T, T_d)\eta n_d \sigma_d n(H) v_H \tag{2.6}$$

where $S(T, T_d)$ is the sticking probability of a H atom with temperature T colliding with a grain of temperature T_d, η is the probability that an adsorbed H migrate over the grain surface, find another H atom and form an H_2 molecule, before evaporating from the grain surface, $n_d\sigma_d$ is the total grain-surface area per unit volume, n_H is the H-atom density, and $v_H = 1.5 \times 10^4 T^{1/2}$ is the thermal speed of the H atoms. For typical grain surfaces, $n_d\sigma_d \approx 10^{-21} n$ cm^{-1}, and

$$R_d(\mathrm{H}_2) \approx 5 \times 10^{-17} \sqrt{\left(\frac{T}{1000\mathrm{K}}\right)} S(T, T_d)\eta(T_d) \times n n_H \text{ cm}^{-3}\text{s}^{-1} \tag{2.7}$$

Hollenbach and Salpeter (1971)[64] found that at low temperatures, S and η are close to unity, and hence the above model for H_2 formation on grain surface can quantitatively explain the observed abundancies. Since then, a huge number of both theoretical and experimental works have been done on this topic, thus validating the earlier hypothesis of Gould and Salpeter[65, 66, 67]. Despite the consensus of the astronomy community, the detailed mechanisms behind the H_2 formation on the interstellar dust grains have however yet to be fully understood.

At temperatures typical of cold molecular clouds ($T < 40K$), mechanisms involving physisorbed H atoms can be invoked since the surface temperature is low enough to prevent desorption from the physisorption well. In this case, the H_2 may form either from a ER-HA or a LH pathway, since H atoms are very mobile at low temperatures[11]. Laboratory experiments have indeed shown that H_2 formation from weakly bound physisorbed hydrogen atoms is rather efficient at temperatures below 20 K[65]. At higher temperatures, typical of diffuse clouds, physisorbed species become unstable and the LH mechanism is ruled out. In such conditions, pathways involving strongly adsorbed species such as the ER have to be invoked. In this respect, recent experiments have shown that H_2formation on graphitic surfaces could be an efficient formation route[51], especially in the before-mentioned PDRs. However, at intermediate temperatures and low UV flux regions, a convincing route to H_2 formation is still missing and this is where PAHs come in[68].

Figure 2.5. The ρ Ophiuchi cloud complex: the main dark area on the left is the *Lynds 1688* nebula, at the center of the blue, yellow and red areas there are respectively the ρ Ophiuchi star, *Antares* e *Sigma Scorpii*.

2.2.3 The role of PAHs

PAHs are believed to look up 5-10% of the *all* carbon available in the ISM[53][9]. They are widely accepted to be the prime carriers of the infrared emissions at 3.3, 6.2, 7.7, 8.6, 11.3, and 12.7 µm in protoplanerary nebulae, reflection nebulae, H II regions, and the general interstellar medium, the so-called *Unidentified Infrared Emission (UIE)*[69, 70, 71]. In addition, they are suggested to be the cause of the *Diffuse Interstellar Band (DIB)*[72], absorption features seen in the spectra of astronomical objects in the Milky Way and other galaxies, which have not been assigned to transitions of any known molecules or solid particles.

Several studies have shown that the physical, chemical, and charge state of interstellar PAHs highly depends on the interstellar environment[55]. In diffuse clouds, PAHs are found mainly in the gas phase, while in dense molecular clouds they are expected to be in the condensed phase. Spectroscopical and photophysics studies have demonstrated that there is rich interstellar chemistry involving PAHs[73, 74, 75, 76]. Indeed, when they are included in the gas phase chemical reaction network of molecular clouds they are found to strongly affect the abundances of many molecular species[77].

In PDRs, PAHs are believed to play an important role in the photoelectric heating of the gas, through absorption of the stellar far-ultraviolet radiations[54]. The connection between PAHs and H_2 formation was proposed right during the investigation of PDRs. In particular, observations of the *ρ-Oph* PDR[10], show a correlation between PAHs emission and H_2 abundance leading to the proposal that PAHs might catalyze H_2 formation in these regions through addition and abstraction reactions on PAHs and very small grains[78].

The interaction between PAHs and hydrogen was investigated both theoretically[79]

[9]Their abundance can be estimated by comparing the intensity of their IR features to that of the dust and adopting the dust-to-gas abundance ratio measured for the ISM. Specifically, the fraction of the elemental carbon f_C locked up in a specific component is given by[53],

$$f_C = 0.23 \left(\frac{7 \times 10^{-18}\ \mathrm{cm}^{-2}}{\sigma_{\mathrm{UV}}} \right) \frac{f_{\mathrm{IR}}}{1 - f_{\mathrm{IR}}}$$

where σ_{UV} is the UV absorption cross section per C atom and f_{IR} is the fraction of the IR energy emitted in the vibrational bands of this component.

[10]The ρ-Ophiuchi is a multiple star system, displayed in Figure 2.5 in the constellation *Ophiuchus*, located about 360 light-years (110 pc) away.

Figure 2.6. The *Small* and *Large Magellanic Clouds*: two galaxies visible in the *Southern Celestial Hemisphere*, members of the Local Group and orbiting the Milky Way galaxy.

and experimentally[80, 81] first on PAH cations, which are supposed to represent the main charge state in intermediate UV flux regions. These studies showed that it is possible to super-hydrogenate PAH cations, with a clear preference for the addition of an odd number of H atoms, suggesting that PAH cations could act as a catalyst for H_2 formation. In addition, hydrogenation of PAH cations has been suggested to protect them from photo-induced fragmentation[82][11]. At low UV flux, PAHs are instead expected to be mainly neutral and possibly super-hydrogenated[55]. Theoretical investigations of PAH hydrogenation have shown that H_2 formation through abstraction reactions is possible. These results have been confirmed by experiments[85, 86, 87], which have shown that it is possible to add excess deuterium atoms (at 2300 K) to all sites on the coronene molecule, thus forming the fully super-hydrogenated species *perhydrocoronene* ($C_{24}H_{36}$). To date, spectral features attributed to the aliphatic content of PAHs have been identified at 3.4, 6.9, and 7.25 µm[88, 89], and some of these have been detected in a range of galactic and Magellanic cloud (shown in Figure 2.6) sources from young stellar objects over PDRs to the circumstellar environments of old stars[78, 90, 91]. These observations strongly suggest the presence of super-hydrogenated PAHs in the ISM, although conclusive evidence is still lacking.

In light of the present discussion, it is clear that PAHs are a *hot-topic* in current astrochemistry. The investigation of super-hydrogenated PAH species is the first fundamental step for their identification and the understanding of their role in interstellar chemistry. These reasons have motivated our work on the coronene molecule[92], which we are going to discuss in the next Chapters.

[11] This is still controversial since other studies suggested that the weakening of the carbon skeleton as a result of H atom addition might lead to hydrogenated PAHs being more prone to fragmentation[83, 84]

Chapter 3

Benchmarking DFT on PAH Chemistry

Published papers: P. A. Jensen, M. Leccese, F. D. S. Simonsen, A. W. Skov, M. Bonfanti, J. D. Thrower, R. Martinazzo and L. Hornekaer, *Identification of Stable Configurations in the Superhydrogenation Sequence of Polycyclic Aromatic Hydrocarbon Molecules*, MNRAS, 1-7, 2019

In the previous Chapter, we have delved into the properties of PAHs and the role they might play in the chemical composition of the ISM. As explained, there are convincing arguments for the catalytic H_2 formation on PAHs, which are expected to be neutral and possibly superhydrogenated especially in low UV flux areas of the ISM. To move a step forward in the understanding of the interstellar chemistry, the investigation of superhydrogenated PAHs is of preliminary importance. Motivated by these arguments and by a direct collaboration with the experimental group of Prof. L. Hornakaer from Aarhus University[1] (Denmark), we have focused on a small PAH, the *coronene molecule*($C_{24}H_{12}$), and studied with DFT the energetics of the stepwise hydrogenation, that ultimately leads to perhydrocoronene ($C_{24}H_{36}$).

Despite the continuous theoretical progress, the choice of the functional most appropriate for an application remains a key step to obtain accurate results from DFTelectronic-structure calculations. For the problem considered here, hydrogenation of a PAH, we have decided to use the so-called M06-2X[93] functional because of the indications we gained from a preparatory investigation of the system energetics, that is described in some detail in this Chapter. In particular, we have considered the adsorption of the first H atom on coronene, testing several *XC* functionals against the few data available for this process, in particular the results of accurate coupled-cluster (CCSD(T)) calculations extrapolated to the complete basis-set (CBS) limit[94]. However, since the system lacks of extensive data, further analysis was necessary to assess the quality of the functionals and make our choice robust. To this end, we have considered the thermochemistry of selected literature databases that seemed most appropriate to describe relevant aspects of the PAHs chemistry, and used them to compare the performance of the functionals.

This Chapter is organized as follows: in Section 1, we briefly describe the functional form of the XC functionals considered; in Section 2, we list the chemical processes considered within each of the selected databases and in Section 3, we discuss our results. The discussion of the stepwise hydrogenation of coronene is left to Chapter 4.

[1]Department of Physics and Astronomy and Interdisciplinary Nanoscience Center

Table 3.1. Functional form (M=meta, HM = hybrid-meta , MHF = meta (full) Hartree-Fock, RSHM = range-separated hybrid, CT=charge-transfer,TDDFT=time-dependent DFT), Hartree-Fock exchange percentage ($X\%$) and application area of the main Minnesota functionals (in paranthesis the year of development). [97, 96]

Functional	Type	$X\%$	Suggested use
MPW1B95 (2004)	HM	31	Covalent and non-covalent thermochemistry, hydrogen bonding, weak interactions, CT
MPWB1K (2004)	HM	44	Thermochemical kinetics, hydrogen bonding, weak interactions, CT
M06-L (2006)	M	0	Main-group thermochemistry, kinetics, non-covalent interactions
M06 (2008)	HM	26	Main-group thermochemistry, kinetics, metallochemical interactions non-covalent interactions
M06-2X (2008)	HM	52	Main-group thermochemistry, kinetics, non-covalent interactions
M06-HF (2006)	MHF	100	Long-range CT via TDDFT spectroscopic properties non-covalent interactions
M11 (2012)	RSHM	42.8-100	Replaces M06-2X, M06-HF, M06 best performance for CT via TDDFT

3.1 Exchange-Correlation functionals

The XC functional we have employed are listed in Table 3.1, along with B3LYP that represents a rather popular but often unsatisfactory choice. The functionals of Table 3.1 are considered to be among the best available nowadays and show outstanding perfomances for the application fields suggested by the developers (Thrular and coworkers)[95, 96] and given in the same Table 3.1. They are all of the *meta-hybrid* type and thus include the spin-labeled kinetic energy density in the set of fundamental variables, and a variable fraction of exact Hartree-Fock exchange (X%), in some cases dependent on the interelectronic separation (range-separated functionals). We describe with more details in the following.

B3LYP[98] is a standard, well-benchmarked, "hybrid" functional proposed by Becke. It relies on the correlation functional designed by Lee-Yang-Parr (LYP) while the exchange part is a three-parameter weighted average of the exact Hartree-Fock (HF) exchange, a local-density-approximation (LDA) exchange and a gradient correction (ΔE_X^B),

$$E_{XC}^{\mathrm{B3LYP}} = (1-a)E_X^{\mathrm{LDA}} + aE_X^{\mathrm{HF}} + b\Delta E_X^B + (1-c)E_C^{\mathrm{LDA}} + cE_C^{\mathrm{LYP}}$$

In practice, B3LYP depends on both the spin-labeled density and its reduced gradient (generalized gradient approximation, GGA).

MPW1B95, MPWB1K, M06, M06-2X and M06-HF are hybrid functionals of the general form

$$E_{XC}^{\mathrm{hyb}} = \frac{X}{100}E_X^{\mathrm{HF}} + \left(1 - \frac{X}{100}\right)E_X^{\mathrm{DFT}} + E_C^{\mathrm{DFT}}$$

similarly to B3LYP but, differently from GGA functionals, they include a functional dependence on the spin-labeled kinetic energy density. For this reason, they are commonly known as *meta-hybrid* functionals.

In MPW1B95 and MPWB1K[99], Adamo and Barone's mPW exchange functional is used for the gradient correction and Becke95 for the total correlation functional, both local and gradient-corrected. For MPW1B95, the percentage of Hartree-Fock exchange (31%) was optimized in order to minimize the root-mean-square error for a set of representative atomization energy (AE6), while for MPWB1K (44%) it was adjusted to minimize the RMSE in the Kinetic9 database[99]

In M06 the percentage of exact Hartree-Fock exchange is set to 26%, which increase to twice this value in M06-2X, while M06-HF is a full Hartree-Fock functional (in this sense, it cannot be considered a real hybrid). The DFT exchange functional for M06 reads as

$$E_X^{\mathrm{M06}} = \sum_\sigma \int dr[F_{X\sigma}^{\mathrm{PBE}}(n_\sigma, \nabla n_\sigma) + \epsilon_{X\sigma}^{\mathrm{LSDA}} h_X(x_\sigma, z_\sigma)]$$

where $F_{X\sigma}$ is the exchange energy density of the PBE model, $\epsilon_{X\sigma}$ the local spin-density approximation for exchange,

$$\epsilon_{X\sigma}^{\mathrm{LSDA}} = -\frac{3}{2}\left(\frac{3}{4\pi}\right)^{1/3} n_\sigma^{4/3}$$

and h_X is a working function depending on the reduced spin gradient ($x_\sigma = |\nabla n_\sigma|/n_\sigma^{4/3}$) and a working variable z_σ. The exchange energy in M06-2X has the same functional form but it corresponds to the special case in which $h_X = 0$. For all the functionals of the M06-suite[97], the opposite and parallel spin correlations are treated differently. The opposite-spin M06 correlation energy is expressed as

$$E_C^{\alpha\beta} = \int dr[e_{\alpha\beta}^{\mathrm{UEG}}(g_{\alpha\beta}(x_\alpha, x_\beta) + h_{\alpha\beta}(x_{\alpha\beta}, z_{\alpha\beta})]$$

where $e_{\alpha\beta}^{\mathrm{UEG}}$ is the uniform electron gas correlation energy density for the anti-parallel case, $g_{\alpha\beta}$ is a new working function depending on the reduced spin density gradient and on a certain number of parameters (c, γ) and $h_{\alpha\beta}$ is the previously mentioned working function depending on $x_{\alpha\beta} = (x_\alpha^2 + x_\beta^2)^{1/2}$ and $z_{\alpha\beta} = z_\alpha + z_\beta$. Similarly, the parallel-spin M06 correlation energy is defined as

$$E_C^{\sigma\sigma} = \int dr[e_{\sigma\sigma}^{\mathrm{UEG}}(g_{\sigma\sigma}(x_\sigma) + h_{\sigma\sigma}(x_\sigma, z_\sigma)]D_\sigma$$

where D_σ is a self-interaction correction factor depending on z_σ and the spin-labeled kinetic energy density τ_σ (clearly, this factor is defined such as it vanishes for any one-electron system)[97]. In these equations, the free parameters are determined upon fitting to the data in the training set.

In contrast, M11[96] is a "range-separated" meta-hybrid xc-functional, in which the admixture of HF exchange varies with the inter-electronic separation. Analytically, it is expressed as

$$E_{XC}^{\mathrm{M11}} = \frac{X}{100} E_X^{\mathrm{HF}} + \left(1 - \frac{X}{100}\right)(E_X^{\mathrm{LR,\ HF}} + E_X^{\mathrm{SR,M11}}) + E_C^{\mathrm{M11}}$$

where E_X^{HF} is the full-range non-local Hartree-Fock exchange, $E_X^{SR,M11}$ is a local exchange with the GGA enhancement factor given by PBE and RRPBE, and E_C^{M11} is a local cor-

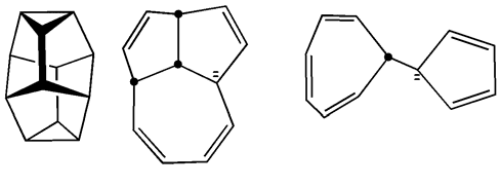

Figure 3.1. Some hydrocarbons considered in HC7.

relation energy. Thus, one sees that M11 contains a portion of short-range Hartree-Fock exchange equal to

$$\frac{X}{100}(E_X^{HF} - E_X^{LR,HF})$$

but at large electronic separation the portion is 100%.

3.2 Databases

Benchmarking of the functionals is usually performed w.r.t. several thermochemical and kinetic databases that gather key chemical-physical parameters of selected chemical processes (obtained either from experiments or high-quality electronic structure calculations). However, the results are typically application dependent and thus a careful choice of the databases that fit best to one,Äôs problem seems to be the best strategy for choosing the appropriate functional. For our problem we have considered the following databases:

πTC13 is a π-system database [100], comprising various reference values

i) proton affinities of conjugated polyenes
ii) proton affinities of conjugated Schiff bases
iii) energy separations between cumulenes and polyines
iv) torsional potentials of butadiene and styrene
v) bond length alternation in butadiene and octatetraene

PAH5 is a database of PAH isomerization energies [101], using CCSD(T) results with a CBS extrapolation as a reference. The isomerization reactions taken into account are the following:

i) phenanthrene → anthracene
ii) triphenylene → chrysene
iii) triphenylene → benzo[*a*]anthracene
iv) triphenylene → benzo[*c*]phenanthrene
v) triphenylene →naphthacene

HC7 is a database of hydrocarbon data that are sensitive to medium-range correlations energies [97], namely

i) isomerization of $(CH)_{12}$ into the three isomers of Fig. 3.1
ii) $(CH_3)_3CC(CH_3)_3 \rightarrow$ n-C_8H_{18}
iii) n-C_6H_{14} + 4 $CH_4 \rightarrow 5C_2H_6$
iv) n-C_8H_{18} + 6 $CH_4 \rightarrow 7C_2H_6$
v) adamantane + $3C_2H_4 \rightarrow 2C_2H_2$
vi) bicyclo[2.2.2]octane → $3C_2H_4$ + C_2H_2

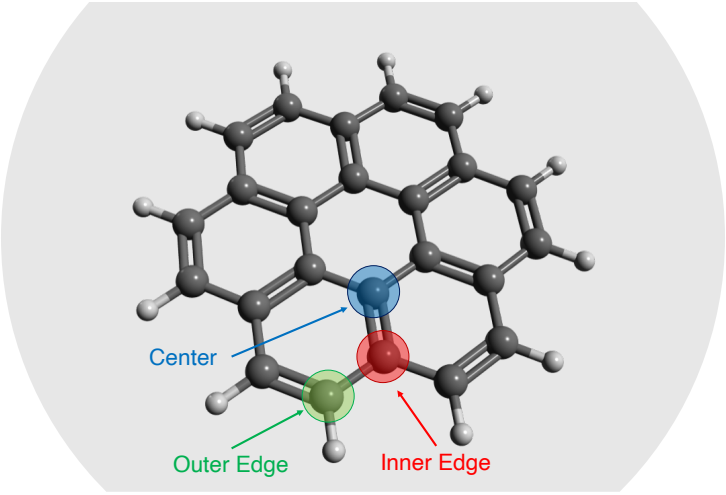

Figure 3.2. The three non-equivalent sites of coronene.

S22A is a database representing non-covalent interactions for some small to relatively large (30 atoms) complexes of common molecules with C,N,O and H, and single, double and triple bonds [102]. Here, the reference values are CCSD(T)/CBS results. The database is divided into three subsets

i) hydrogen bonded complexes: $(NH_3)_2$; $(H_2O)_2$; Formic acid dimer; Formamide dimer; Uracil dimer (C_{2h}); 2-pyridoxine·2-aminopyridine; Adenine·Tymine

ii) complexes with predominant dispersion stabilization: $(CH_4)_2$; $(C_2H_4)_2$; Benzene·CH_4; Benzene dimer; Pyrazine dimer; Uracil dimer (C_2); Indole·Benzene; Adenine·Tymine stack

iii) mixed complexes in which electrostatic and dispersion contributions are similar in magnitude: Ethene·ethine; Benzene·H_2O; Benzene-NH_3; Benzene·HCN; Benzene dimer; Indole·Benzene T-shape; Phenol dimer

3.3 Discussion

The performance of the functionals of Table 3.1 on the above datasets are given in Table 3.2 and Figures 3.3 and 3.4 as *MUE* (kcal/mol)[95, 101, 97, 102], along side the results of our benchmark calculations.

For the latter we have considered adsorption at the three physically distinct sites of the coronene molecule, namely the outer edge (o), the inner edge (e) and the central carbon (c) indicated schematically in Figure 3.2. We have computed the corresponding binding and barrier energies, employing the cheap but reasonably accurate Pople's 6-31+G(d,p) and using quasi second-order optimization algorithms (without constraints) and frequency calculation checks, as provided by the Gaussian16 suite[103].

We first discuss the hydrogenation of the central site, and in particular the performance of the functionals on sticking barriers (E_b). It is seen from Table 3.2 that exact exchange does affect the height of the barrier (cfr. the PW91 barrier with any of the hybrid results), but its exact value is not a simple increasing function of the HF percentage. The reason, we believe, is that HF exchange, in conjunction with different correlation functionals, modifies also the ability of the functional to describe weak non-covalent interactions, and these seem to play some role in determining the barrier height. Strictly speaking, M⋆ functionals are expected to correctly reproduce non-covalent interactions at geometrical separations close to the binding ones, because of their high flexibility (related to the high degree

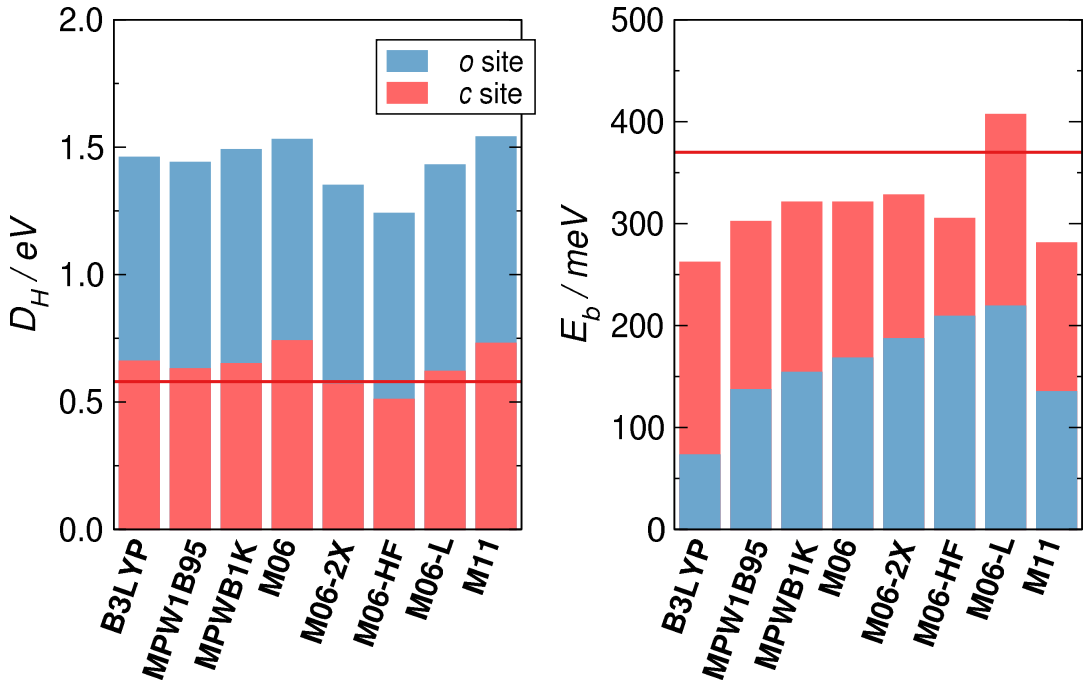

Figure 3.3. Binding energies (D_H, eV) and energy barriers (E_b, meV) for the outer edge (o, light blue) and center (c, light red) sites, with the XC functionals listed in Table 3.1. The red line indicates the CCSD(T)& CBS extrapolation[94].

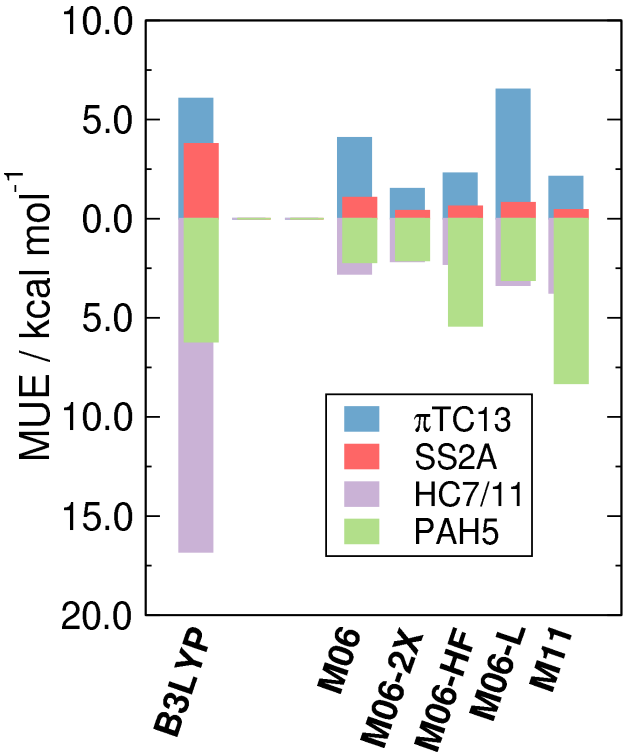

Figure 3.4. Perfomance (as MUE (kcal/mol^{-1}) of the XC functionals of Table 3.1 against the datasets described in the text

Table 3.2. Binding energies, D (eV) and sticking barriers, E_s (meV), for the hydrogen addition to three different sites of coronene, MUE (kcal/mol) for three different database, πTC13 (π-system thermochemistry), SS2A (Non covalent binding energies), HC7/11 (Medium-large correlation energies for hydrocarbons). All the values reported (this work and literature data) are not CP-corrected. "I" and "II" stands refer to two different basis set, respectively cc-pVDZ and cc-pVTZ. Ref. [a] Rauls. et. al.[68], Ref. [b] Kayanuma et. al. [104], Ref. [c] Wang et. al. [94].

					MUE			
		X%	D	E_b	πTC13	SS2A	HC7/11	PAH5
Outer Edge	B3LYP	20	1.46	73	6.06	3.77	16.8	6.2
	MPW1B95	31	1.44	137				
	MPWB1K	44	1.49	154				
	M06	26	1.53	168	4.08	1.06	2.78	2.2
	M06-2X	52	1.35	187	1.51	0.40	2.15	2.1
	M06-HF	100	1.24	209	2.29	0.62	2.29	5.4
	M06-L	0	1.43	219	6.52	0.80	3.35	3.1
	M11	42.8-100	1.54	135	2.12	0.44	3.74	8.3
	PW91[a]		1.45	60				
Center	B3LYP	20	0.66	262	6.06	3.77	16.8	6.2
	MPW1B95	31	0.63	302				
	MPWB1K	44	0.65	321				
	M06	26	0.74	321	4.08	1.06	2.78	2.2
	M06-2X	52	0.57	328	1.51	0.40	2.15	2.1
	M06-HF	100	0.51	305	2.29	0.62	2.29	5.4
	M06-L	0	0.62	407	6.52	0.80	3.35	3.1
	M11	42.8-100	0.73	281	2.12	0.44	3.74	8.3
	PW91[a]		~ 0.725	~ 180				
	B3LYP[b]	20	0.66	250				
	ROMP2/II [c]		0.29	400				
	ROCCSD(T)/I [c]		0.58	370				
Edge	B3LYP	20	0.71	279	6.06	3.77	16.8	6.2
	MPW1B95	31	0.67	342				
	MPWB1K	44	0.70	363				
	PW91[a]		~ 0.725	~ 180				

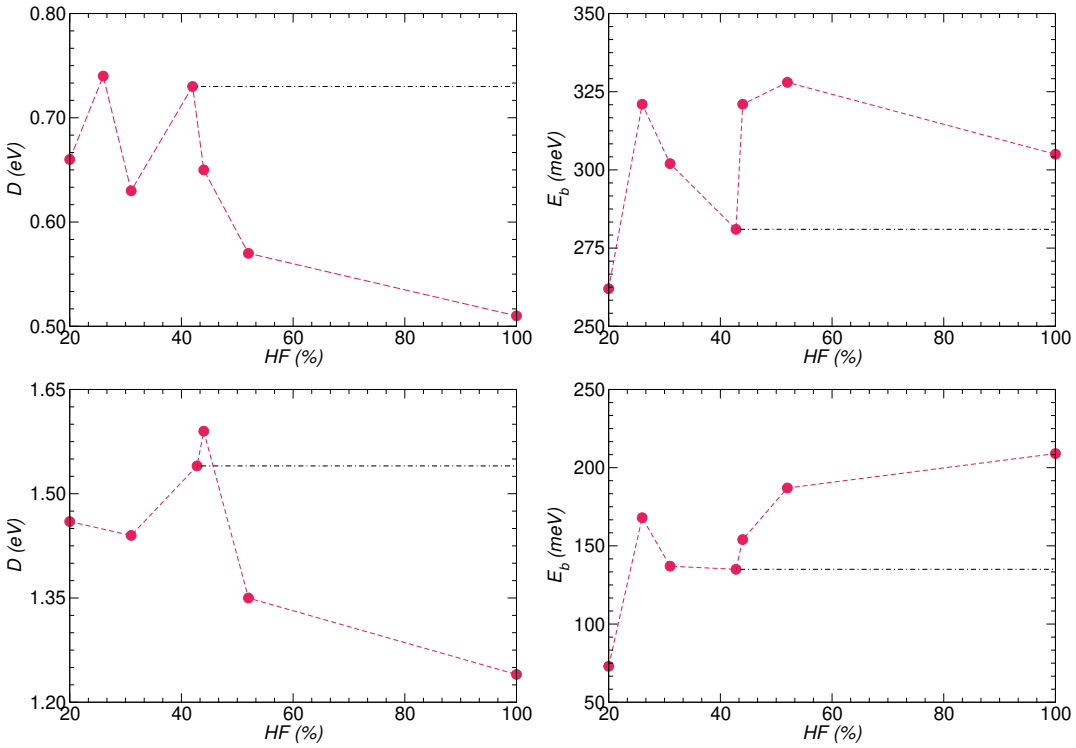

Figure 3.5. Binding energies (D, eV) and sticking barriers (E_b, meV) at different percentages of Hartree-Fock exchange (HF%) for both center (top row) and outer edge (bottom row) hydrogenation. The dash dot line is used to indicate the range of percentage of the M11 functional.

of parametrization) and to their dependence on the spin-labeled kinetic energy density. However, they do not properly reproduce the Vydrov and Van Voorhis (VV) interactions since they do not describe the characteristic $1/r^6$ asymptotic behavior of gas-phase pairs. On this basis, we consider the MUE relative to the SS2A database which is a measures of the performance of the functionals in reproducing non-covalent binding energies. Among the considered functionals, those of the Minnesota family effectively perform better than B3LYP, which thus gives rise to the lowest barrier. M06-2X, M06-HF and M11 seem to be much more accurate functionals in this respect, providing as small MUEs as 0.40, 0.63 and 0.44 kcal/mol, respectively. According to this, M11 should perform similarly to M06-2X, but it is found to give a much smaller sticking barrier. In this case, thus, other effects, likely connected to the range-separated form of M11, must play a role in lowering the barrier. Overall, we deem M06-2X to be the most accurate functional for our purposes since, in addition to the lowest MUE in SSA2, it gives a barrier height in good agreement with the Coupled-Cluster calculations of Y. Wang et. al.[94] (see Figure 3.3).

Moving to the outer edge hydrogenation, the trend is substantially reproduced, with the exception of M06-HF, which gives now the highest barrier to sticking (22 meV higher than M06-2X). However, for this site there exists a higher variability between values. For instance, M06 gives a sticking barrier of 19 meV lower than M06-2X, to be compared with 7 meV for hydrogenation on the central site.

For MPW1B95 and MPWB1K we do not have MUE to compare with. According to Truhlar and coworkers, MPWB1K was optimized for the kinetics, however the reference database (the above mentioned Kinetic9) do *not* really fit our problem, since it consists of three forward barrier heights, three reverse barrier heights and three energies of the reactions of quite different reactions, *i.e.* $OH+CH_4 \rightarrow CH_3 + H_2O$, $H + OH \rightarrow O + H_2$ and $H + H_2S \rightarrow H_2 + HS$.

As for the binding energies (D), the reference datasets are πTC13, PAH5 and HC7.

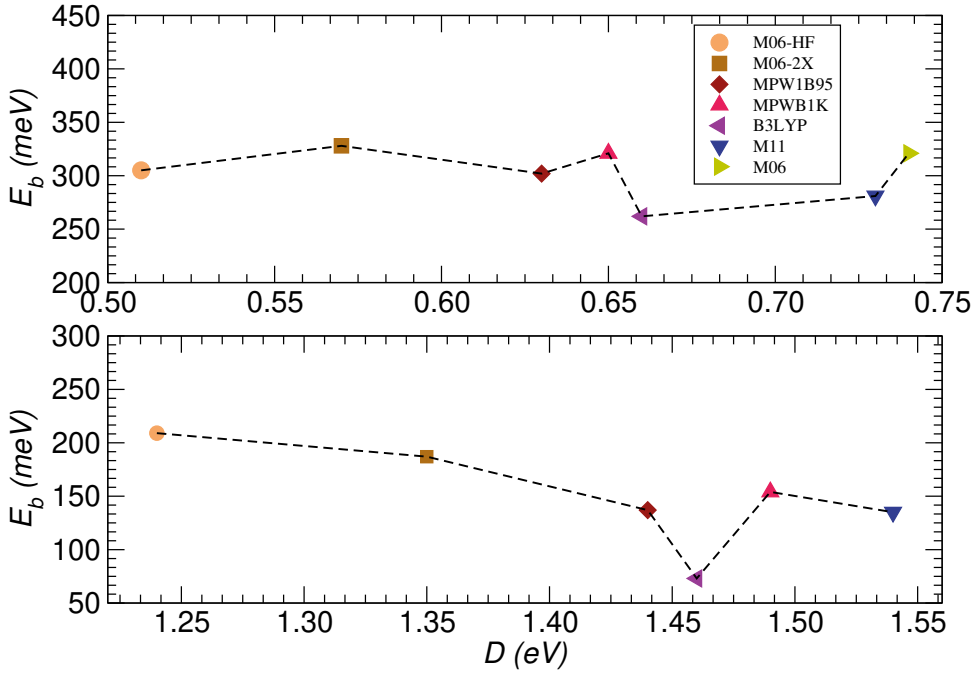

Figure 3.6. Binding energies plotted against sticking barriers for center (top row) and outer edge (bottom row) hydrogenation.

According to the MUEs for πTC13 and HC7, M06-2X and M06-HF are again the best performing functionals. They respectively give 0.57 and 0.51 eV for center hydrogenation, quite lower than the M06 and M11 values. This can be accounted for by the high non-locality of these functionals and the different effect that exact Hartree-Fock exchange has on pristine and hydrogenated coronene: the closed-shell pristine coronene is more stabilized by exchange effects than the open-shell hydrogenated one, thereby resulting in lower D. Here, it is worth noticing that the M06-2X value is, again, in perfect agreement with the above cited Coupled-Cluster calculations of Y.Wang[94]. For the outer edge hydrogenation, the trend is essentially the same. The PAH5 database is the only one concerning polycyclic aromatic hydrocarbons and M06-2X still has the lowest MUE. Overall, our results clearly indicate that M06-2X is the most appropriate functional for investigating coronene hydrogenation.

In Figure 3.5, the binding energies and the sticking barriers, for center and outer edge hydrogenation, are tentatively plotted against the percentage of Hartree-Fock exchange included in the functional. Clearly, this is not a real dependence of these energetic parameters on the HF exchange, since different percentages correspond also to different functionals. However, MPW1B95, MPWB1K, M06, M06-2X, M06-HF are all meta-hybrid GGA from the same family and should be comparable with each other to some extent. For comparative purposes, B3LYP and M11 are also included. Concerning the binding energies, we can see that, approaching the full Hartree-Fock limit, they get smaller and smaller, likely because of the above mentioned over-stabilization of the closed-shell bare molecule. However, there is not a monotonic decrease of D with respect to HF percentage, because other factors (*e.g.* the different parametrization in the transition between M06 (26%) and MPW1B95(31%)) can contribute.

The behavior of barrier energies is similar to that of D, because of the known correlation between the two quantities, which is made evident in Figure 3.6, for both the center (top row) and outer edge (bottom row) hydrogenation.

Table 3.3. CPU Time/Opt step (hour) and number of optimization step (#) for the optimization of pristine coronene with the computational setup described in the text.

Functional	CPU Time/Step	#
B3LYP	3.07	4
MPWB195	8.23	5
M06	26.17	3
M06-2X	26.06	3
M11	37.40	3

3.3.1 Computational cost

Because of their different parametrization, the functionals of Table 3.1 imply different computational cost. For a reasonable comparison, one can use the CPU time per optimization step by considering calculations carried out on the same system with the same setup. In this respect, we have considered the bare coronene molecule and its full internal geometry optimization, where the matrix of exact second derivative is computed at each step. The corresponding CPU time for some of the functionals employed are listed in Table 3.3. In Figure 3.7, the CPU time per optimization step is instead plotted against the MUE on the aformentioned datasets. Noteworthy, excluding B3LYP (3.07 h), we note that M06-2X has both the lowest MUEs and the smallest computational cost. Notice that the most "advanced" M11 functional has large MUEs in combination with great computational cost, likely because of the range-separation.

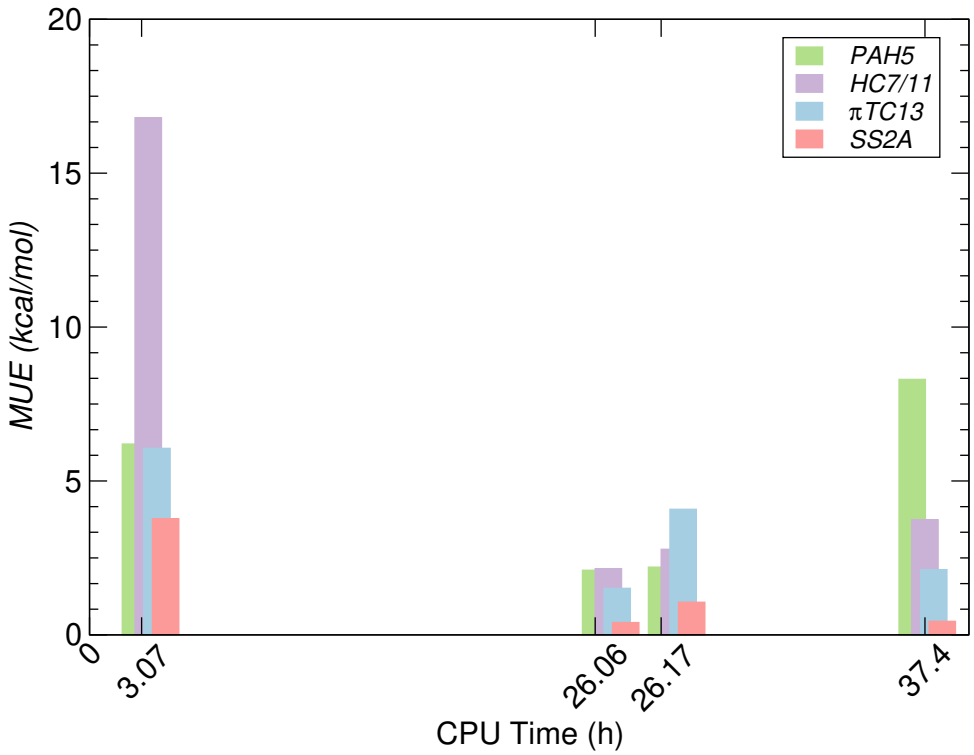

Figure 3.7. MUE (kcal/mol) for the selected databases at different CPU time/step (h): 3.07 (B3LYP), 26.06 (M06-2X), 26.17 (M06) and 37.40 (M11).

Chapter 4

The road to Superhydrogenated Coronene

Published papers: P. A. Jensen, M. Leccese, F. D. S. Simonsen, A. W. Skov, M. Bonfanti, J. D. Thrower, R. Martinazzo and L. Hornekaer, *Identification of Stable Configurations in the Superhydrogenation Sequence of Polycyclic Aromatic Hydrocarbon Molecules*, MNRAS, 1-7, 2019

In this Chapter we present a DFT investigation of the stepwise hydrogenation reaction of *coronene* ($C_{24}H_{12}$). The work was motivated by the arguments exposed in Chapter 2 and by a direct collaboration with the experimental surface science group of Prof. Liv Hornekær from Aarhus University. This Chapter is organized as follows: in Section 1, we briefly discuss the main experimental results[1], in Section 2, we summarize the computational details of our calculations, in Section 3 and 4 we present our results on two investigated pathways from bare to super-hydrogenated coronene ($C_{24}H_{12}$).

4.1 Experimental results

The results shown in this Section are provided by the experiments performed by Aarhus group of Prof. Liv Hornekær.

In the experiment, coronene films grown on a HOPG substrate were exposed to a beam of atomic hydrogen. The atoms were produced via thermal dissociation using a hot capillary source, operated at a temperature of 2300 K, at which H_2 dissociates. H atoms were then cooled down at 1000 K with a twisted quartz nozzle[2]. To identify the superhydrogenated structures, a *temperature-programmed desorption* experiment was carried out. Hence, the sample was heated in a controlled manner by 1 Ks^{-1}, using a PID controller. Then, the desorption products were measured by an Extrel CMS LLC quadrupole mass spectrometer. Singly ionized pristine coronene has mass-to-charge ratios (m/z) equal to 300 amu and singly ionized *perhydrocoronene* (fully super-hydrogenated coronene) has $m/z = 324$ amu. m/z in the range 280-330 amu were monitored. The lower limit was chosen to detect fragmentation products where applicable, and the upper limit was chosen to establish a baseline, as no products with such masses should be present.

Figure 4.1 shows mass distributions for hydrogen fluences ranging from zero to $\Phi_H = 2.8 \times 10^{19}\text{cm}^{-2}$. For the case of no hydrogen exposure (panel a) a large peak at 300 amu corresponding to pristine coronene is observed, with smaller peaks at slightly lower masses

[1]The reader is referred to the published paper[92] if he/she wishes more details about the experiment.
[2]The H atom flux at the sample position was determined to be $6(\pm 3) \times 10^{14}$atoms cm^{-2} s^{-1}

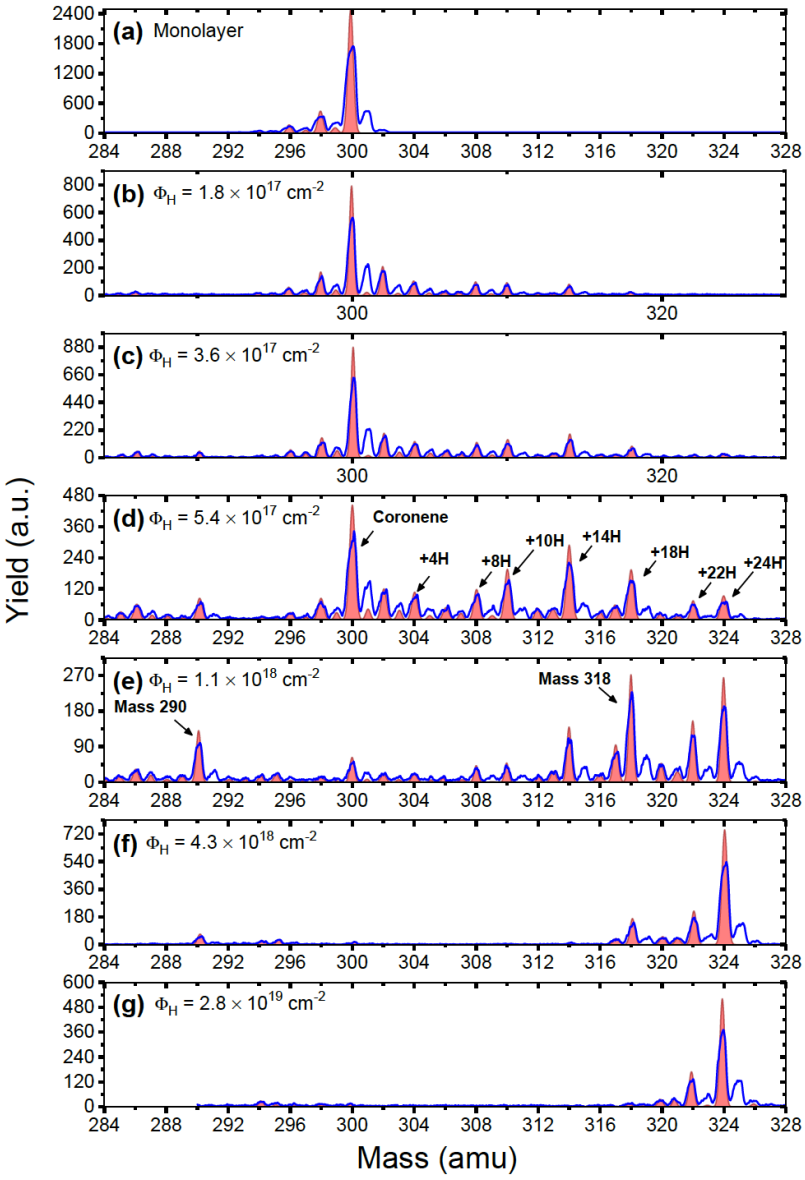

Figure 4.1. The blue lines show the mass distributions for coronene exposed to increasing atomic hydrogen fluences ranging from zero to $\Phi_H = 2.8 \times 10^{19}\text{cm}^{-2}$. The red shaded areas show how the peak structure would be in the abscence of the ^{13}C isotope, which has a natural abundance of 1.109%

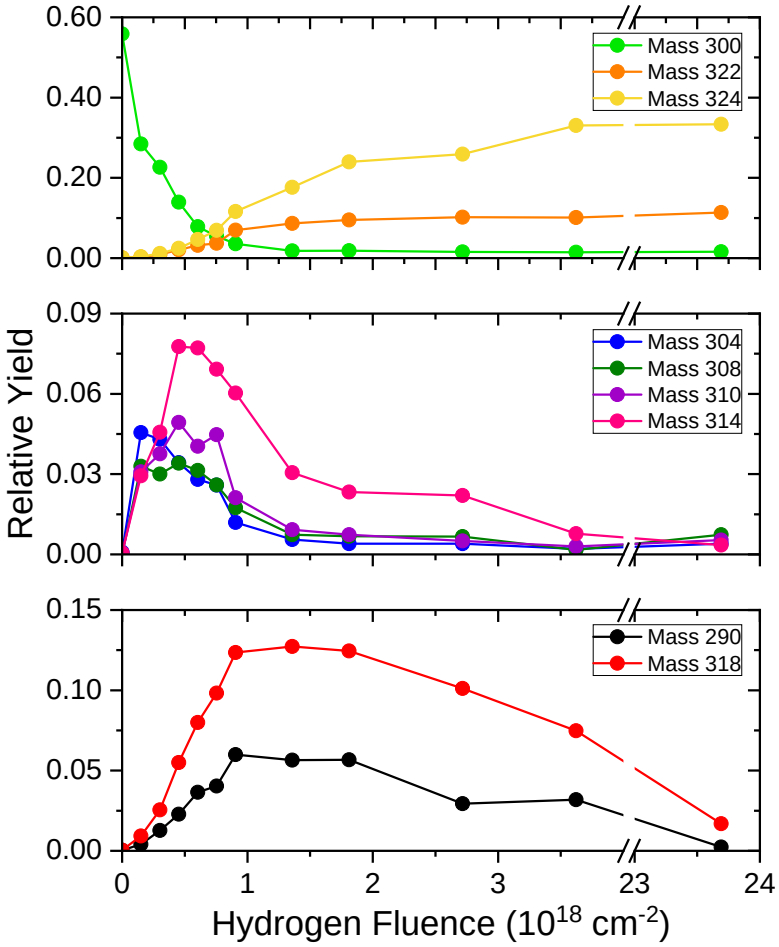

Figure 4.2. The relative yield of specific masses as a function of hydrogen fluence.

due to hydrogen loss during the ionization step in the mass spectrometer. A small peak at 301 amu is ascribed to the natural abundance of the heavier ^{13}C isotope in the coronene sample. At higher dose time, the peak at 300 amu becomes smaller and peaks at higher masses ascribed to super-hydrogenated coronene begin to appear. Especially prominent peaks are observed at 304, 308, 310, 314, 318, 322, and 324 amu suggesting increased stability for particular hydrogenation configurations. These correspond to the coronene molecule plus $n = 4, 8, 10, 14, 18, 22$ and 24 extra H atoms.

The red shaded areas in the mass spectra show how the peak structure would be if all ^{13}C isotopes (assuming an abundance equal to the natural abundance of 1.109%) are converted to ^{12}C. The main effect is apparent at small masses where the peak at 301 is drastically reduced. As a result, the mass 302 peak now also stands out as a prominent peak. We also note that a drop in total signal is observed with H fluence - i.e. compare graph a) and graph g) in Figure 4.1. This drop may be the result of fragmentation or chemical desorption, where the energy released in the hydrogen addition reaction leads to desorption of the super-hydrogenated molecule and/or potentially also neighbor molecules.

In Figure 4.2 the yield as a function of hydrogen exposure for the most prominent masses in Figure 4.1 is displayed. As the fluence is increased the yield of mass 300 amu

decreases exponentially, while masses 304, 308, 310, and 314 amu are observed to increase and then to subsequently decrease again at fluences above $\Phi_H = 1 \times 10^{18}\text{cm}^{-2}$, when even more highly super-hydrogenated species begin to appear. The yield in 318 amu slowly starts to decrease at fluences above $\Phi_H = 2 \times 10^{18}\text{cm}^{-2}$ and disappears completely at very high hydrogen exposures. The yields of mass 322 and 324 amu slowly increase and dominate the spectrum at fluences above $\Phi_H = 1 \times 10^{18}\text{cm}^{-2}$. For the longest hydrogen exposures only mass 322 and 324 amu show significant yields indicating almost complete super-hydrogenation. Furthermore, the evolution in the yields of masses 322 and 324 amu, follow the same trend and display similar thermal desorption behavior This indicates that the 322 amu peak may, at least in part, appear as a result of fragmentation of the fully super-hydrogenated molecule (perhydrocoronene) in the mass spectrometer, through loss of H_2.

4.2 Computational details

The appearance of peaks at specific masses indicates that certain superhydrogenation configurations are more stable than others and that when such stable configurations are reached, sizeable barriers for further additions exist. Therefore, to identify these stable hydrogenated structures, we have carried out an extensive DFT investigation of the step-wise hydrogenation of coronene.

The calculations described in the following were performed with the M06-2X hybrid-meta GGA[93], which was selected after the careful benchmark study on PAH chemistry discussed in Chapter 3. We employed the spin-unrestricted set-up, with the help of the Gaussian16 code[103] and the 6-311G(d,p) atom-centered basis set, with tight convergence criteria set on both the electronic and the structural optimizations. Optimized structures were checked with harmonic frequency calculations.

Binding energies for the addition of H atoms were computed for a number of sites i according to

$$D_i^{n+1} = E_\star^n + E_H - E_i^{n+1} \tag{4.1}$$

where $E_\star^n$ is the DFT energy of the most stable isomer with n extra hydrogens, E_H is the energy of a hydrogen atom and E_i^{n+1} is the energy of the structure with an additional H at site i (in the following, a star will be used to denote the most stable site, *i.e.* $D_\star^n \equiv \max_i\{D_i^n\}$). The plausible adsorption sites (typically 3-4 per step) were selected with the help of chemical intuition[52] and Fukui's analysis, and considered for adsorption at either side of the molecule, when meaningful. The sequence was continued by selecting at each step the structure with the largest binding energy[3], for a total of about 150 geometry optimizations[4]. Energy barriers were computed for the most relevant cases only, by performing a transition-state search and subsequent frequency analysis.

Before discussing the lowest energy pathway, we report a determination of the energetics of the first H addition to the outer edge site with a more accurate (but expensive)

[3]This does *not* guarantee that the structure is the lowest energy one for the given hydrogenation level. The reason is that it may well be possible (but hard to check or predict) that an "energetic" structural optimization changes the energetic order between isomers because of, *e.g.*, a conformational rearrangement, especially when they differ by few tenths of eV only. In a sense, the adopted procedure accounts for some possible kinetic impediments to the hydrogenation process

[4]A brute-force approach that considers all possible adsorption sites is yet out of reach nowadays even for a small-sized molecule like coronene with its only 24 hydrogenation sites (disregarding the possible difference between adsorption on one face or the other). The total number of sites N is several million, as a simple calculation shows. For, if the sites were distinguishable (i.e. in the absence of symmetry) this number would be given by

$$N = \sum_{n=0}^{24} \binom{24}{n} \equiv 2^{24}$$

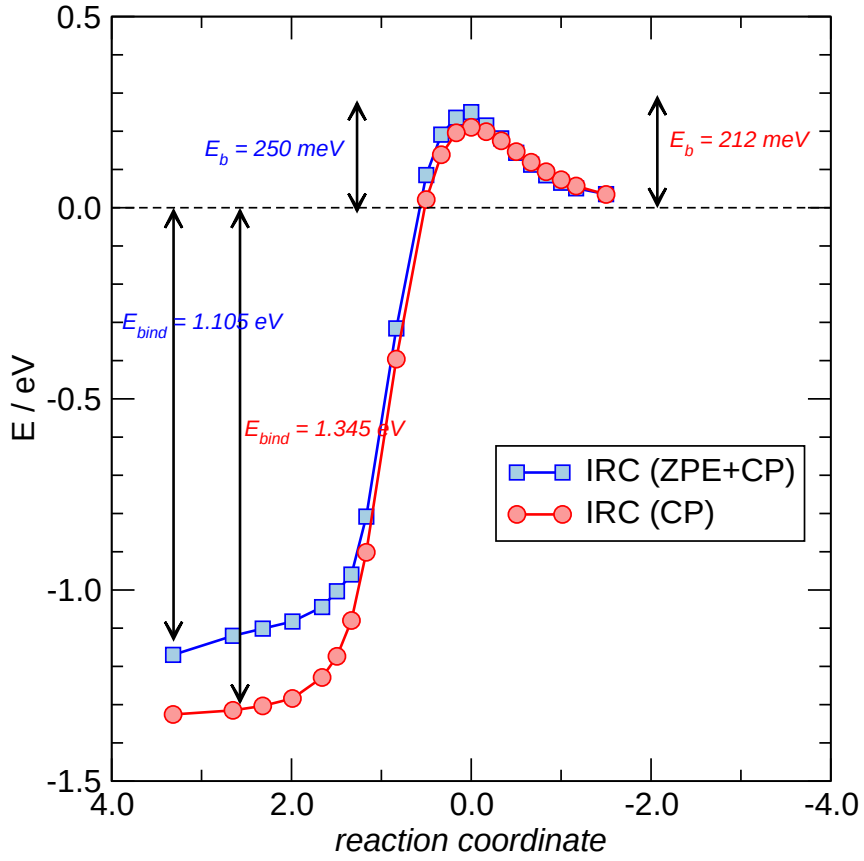

Figure 4.3. IRC for the H addition to the outer-edge sites with CP (Red) and CP+ZPE corrections (Blue).

computational setup (*unpublished result*). Figure 4.3 shows an IRC as obtained by a high-level DFT calculation, employing the before-mentioned M06-2X XC in combination with the DFT-optimized basis-set PCSEG-1. Both the IRC with the CP-correction (accounting for the BSSE) and with CP-correction plus the ZPE correction are reported. With this more accurate setup, the binding energy and energy barrier on the outer edge site of corenene are found to be 1.34 eV and 212 meV, respectively (*i.e.* they are resaonably close to the original values reported in Chapter 3, $D = 1.35$ eV and $E_b = 187$ meV for the original setup).

4.3 Main hydrogenation pathway

Figure 4.4 shows the lowest energy addition pathway, while the energetics along this path is shown in Figure 4.5. We note at first that the main hydrogenation sequence begins at an edge site before proceeding to center sites after a few H atom additions. From Figure, an even/odd alternation is also evident. The latter arises from the larger exothermicity of radical-radical reactions, *i.e.* those forming even-numbered $C_{24}H_{12+n}$ species. We remind, indeed, from Subsection 1.3.2, that coronene is a balanced bipartite lattice with a *singlet* ground state ($S = |N_A - N_B|/2 = 0$, $2S + 1 = 1$). Therefore, an odd number of extra H breaks this balance and leads to a doublet ground-state ($S = 1/2$, $2S + 1 = 2$). Provided

a number that should be divided by a symmetry factor of the order $\approx 6-8$ to account for the hexagonal symmetry of the substrate. More precisely, one should count the number of equivalent classes of configurations, *i.e.* only those configurations that cannot be superimposed by applying a symmetry operation of the pristine substrate. Thus, for instance, the symmetry number would be 8 for monomers, since out of the 24 possible configurations only 3 are distinct.

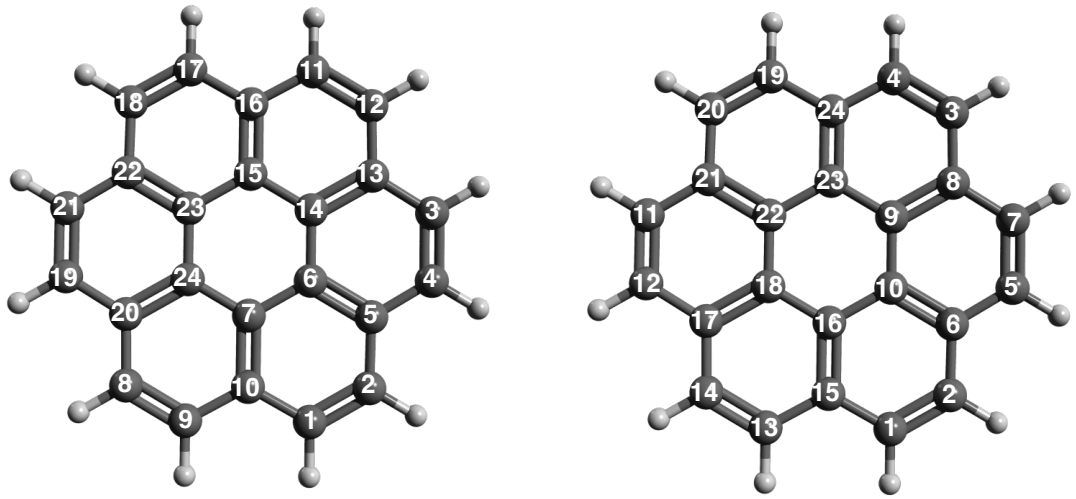

Figure 4.4. (Left) Main hydrogenation sequence of the coronene molecule. The numbers $j = 1, 2, ...n$ indicate schematically the lowest energy isomer with n extra hydrogen, $C_{24}H_{12+n}$. (Right) Alternative possible hydrogenation sequence of the coronene molecule. It uses the second most stable site at the 3rd step and the most stable sites onward.

that the molecules are in their ground state, the amplitude of the even-odd oscillation of the adsorption energy of 2.5 eV can be considered a rough measure of the π bond strength, since the breaking of a π bond is a necessary step only when forming odd-numbered species

Since the adsorption barrier correlates well with D_i^n - *i.e.*, the larger the binding energy the smaller the barrier - smaller binding energy is also indicative of a higher kinetic impediment to the addition reaction. The largest binding energies are found for coronene molecules with a specific number of extra hydrogens, $D_\star^n = 3.88, 4.10, 3.85, 3.72, 4.03, 3.71$ and 4.38 eV, for $n = 2, 10, 14, 16, 18, 22$ and 24 respectively.

To relate these findings to the experimentally observed abundances one may argue as follows. Since $D_\star^n$ is a measure of the stability of the species $C_{24}H_{12+n}$ against the desorption (or abstraction) of an H atom, and

$$\Delta D^n = D_\star^n - D_\star^{n+1} \tag{4.2}$$

is a measure of the stability against further hydrogenation (it is in fact the energy of the reaction $2C_{24}H_{12+n} \rightarrow C_{24}H_{12+n-1} + C_{24}H_{12+n+1}$), the combined index

$$\alpha = uD_\star^n + v\Delta D^n \tag{4.3}$$

should reflect the relative abundance of the species. Setting $u = v = 1/2$, we find that the structures with $n = 18, 10, 14$ and 2 extra H atoms (in decreasing order) are the most stable ones, with $\alpha = 3.44, 3.42, 3.16$ and 3.08 eV, respectively. Adding to these the case $n = 24$ - which has the largest $D_\star^n$ along the entire pathway and, being last in the sequence and indefinitely stable against further hydrogenation - we find a striking agreement with the thermal desorption spectra reported in Figure 4.1. These conclusions are further corroborated by the heights of the hydrogen adsorption barriers (the energy barrier of the reactions $C_{24}H_{12+n} + H \rightarrow C_{24}H_{12+n+1}$) that are found to be large for $n = 0, 2, 10, 14$ and 18, with a smaller, but still significant barrier for $n = 8$ and small (or even vanishing) barriers otherwise (see Figure 4.5 and 4.1 for exact values).

Table 4.1. Energy barriers (meV) for forming the n-times coronene superhydrogenated species ($C_{24}H_{12+n}$), along the two pathways depicted in Figures 4.5 and 4.9 (N.D. = not determined).

n	Main sequence	Secondary sequence
1	187	187
3	149	165
4	0.0	N.D.
5	3.8	159
7	47	0.0
9	90	74
10	0.0	0.0
11	170	178
12	0.0	N.D.
13	19	140
15	126	0.0
17	0.0	0.0
19	153	155
23	0.0	N.D.
24	0.0	0.0

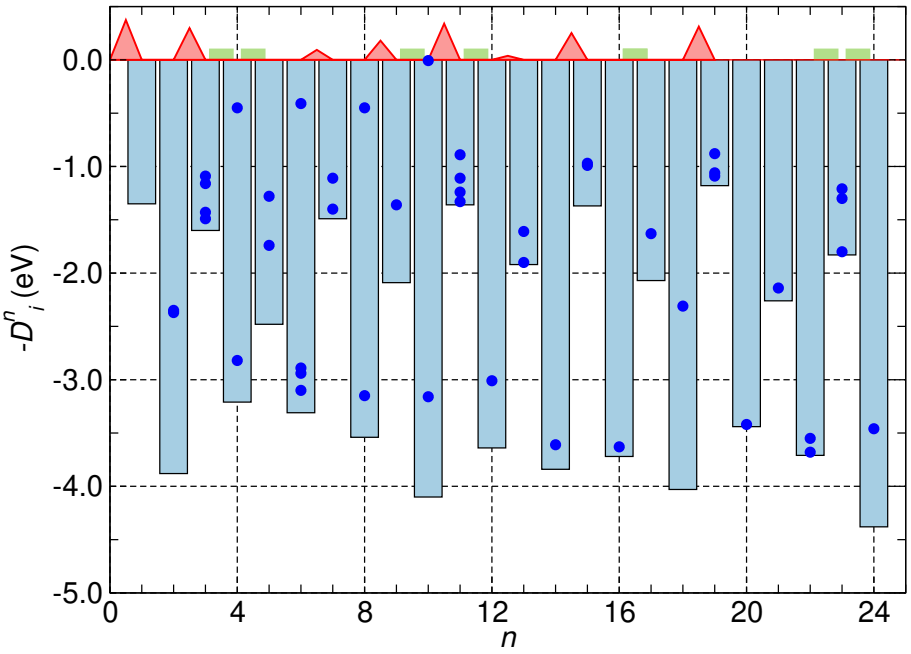

Figure 4.5. Hydrogen adsorption energy along the main sequence shown in Figure 4.4 (light blue bars). The energy for alternative, slightly less stable hydrogenation configurations with the same number of excess H atoms are shown as dots. A red triangle between n and $n+1$ represents the height of the barrier for sticking a H atom to the n-times hydrogenated coronene (multiplied by a factor of 2 to make it visible on the scale of the graph). Green bars denote situations where a barrierless adsorption path was found. A green bar is also used for the step $n = 4 \rightarrow 5$ which presents a too little barrier ($E_b = 3.8\,\text{meV}$) to be visible in the graph

.

4.3.1 Rationalizing the hydrogenation sequence

The hydrogen atom attachment to coronene can be rationalized with the help of some rules of thumb that should apply equally well to other PAHs. These rules follow from the discussion of Subsection 2.1.1. We can enunciate these rules as follow

Rule 1 (closed-shell molecules, *n even*)**.** *The factors driving the are the π-coordination and π-hyperconjugation. The former determines the localization of frontier orbitals at the edges of the electronic system, enhancing the reactivity of those sp^2 sites that have the smallest number of sp^2 neighbors. The latter, on the other hand, discriminates between sites with the same π-coordination but a different number of nnns in the π-lattice (ξ).*

Rule 2 (open-shell molecules, *n odd*)**.** *The addition is driven by the unpaired electron density and thus occurs at the so-called ortho and para positions where it mainly localizes through Pauli's resonance (again with a preference for sites with a small π-coordination)*

To elucidate the application of these rules and their usefulness in predicting the most reactive sites, let consider the first hydrogenation steps. To help us, Figure 4.6 displays the complete set of hydrogenation sites that have been considered during the investigation of the main hydrogenation pathway. Each hydrogenation level (nH) is pictorially represented as a molecular graph where black circles denote carbons that have already been hydrogenated in previous steps, and blue circles mark those positions that have been inspected at that specific step.

The first H addition occurs at an outer edge site, which has $Z = 2$ and $\xi = 1$. As seen for graphene, this hydrogenation leaves an unpaired electron (a midgap state) on the majority sublattice. The second H thus sticks on this sublattice, and, in particular, at an *ortho* position. In the resulting two-fold hydrogenated structure, site 1 has now the highest π-hypercoordination number ($\xi = 2$, among two π-coordinated sites) and it is then the third hydrogenation site. As the hydrogenation proceeds, edge sites are gradually removed from the π-systems, while inner sites (both graphitic (G) with three neighbors with $Z = 3$, and inner-edge with two (F_2) or one (F_1) three-coordinated neighbors) become progressively edge sites - *i.e.* their π-coordination is reduced and π-hypercoordination is increased. Correspondingly, their H affinity is increased and then the hydrogenation, once started at the edges, proceeds readily to these sites.

The good correlation between binding energies and π coordination/hyperconjugation numbers is shown in Figure 4.7, where the main results have been re-organized according to these numbers. The figure clearly shows the increase of the binding energy when decreasing Z and, for $Z = 2$, when increasing ξ (the correlation is even better if one limits the comparison to the energies for binding H to the different sites of the *same* structure, which is precisely the situation one addresses during the hydrogenation process).

Against this background, the exceptional stability of the hydrogenated species $C_{24}H_{12+n}$ with $n = 2, 10, 14$ and 18 extra hydrogen can be traced back to additional electronic effects, namely to a "residual aromaticity" that is left during the hydrogenation process. Indeed, as shown in Figure 4.8, when $n = 2, 10, 14$ and 18 the remaining sp^2 hybridized carbon atoms in the molecule still form a subsystem of three, two, or one aromatic rings, respectively, *i.e.* stable structural motifs that require extra energy for further hydrogen attachment to occur. The high stability of the structure with 24 extra H, on the other hand, is owed to the complete saturation of the π-system.

4.4 An alternative pathway

Figure 4.5 shows, for each degree of superhydrogenation, the binding energy of a number of less stable hydrogenation configurations. Some of these values are very close to $D^n_\star$, by less

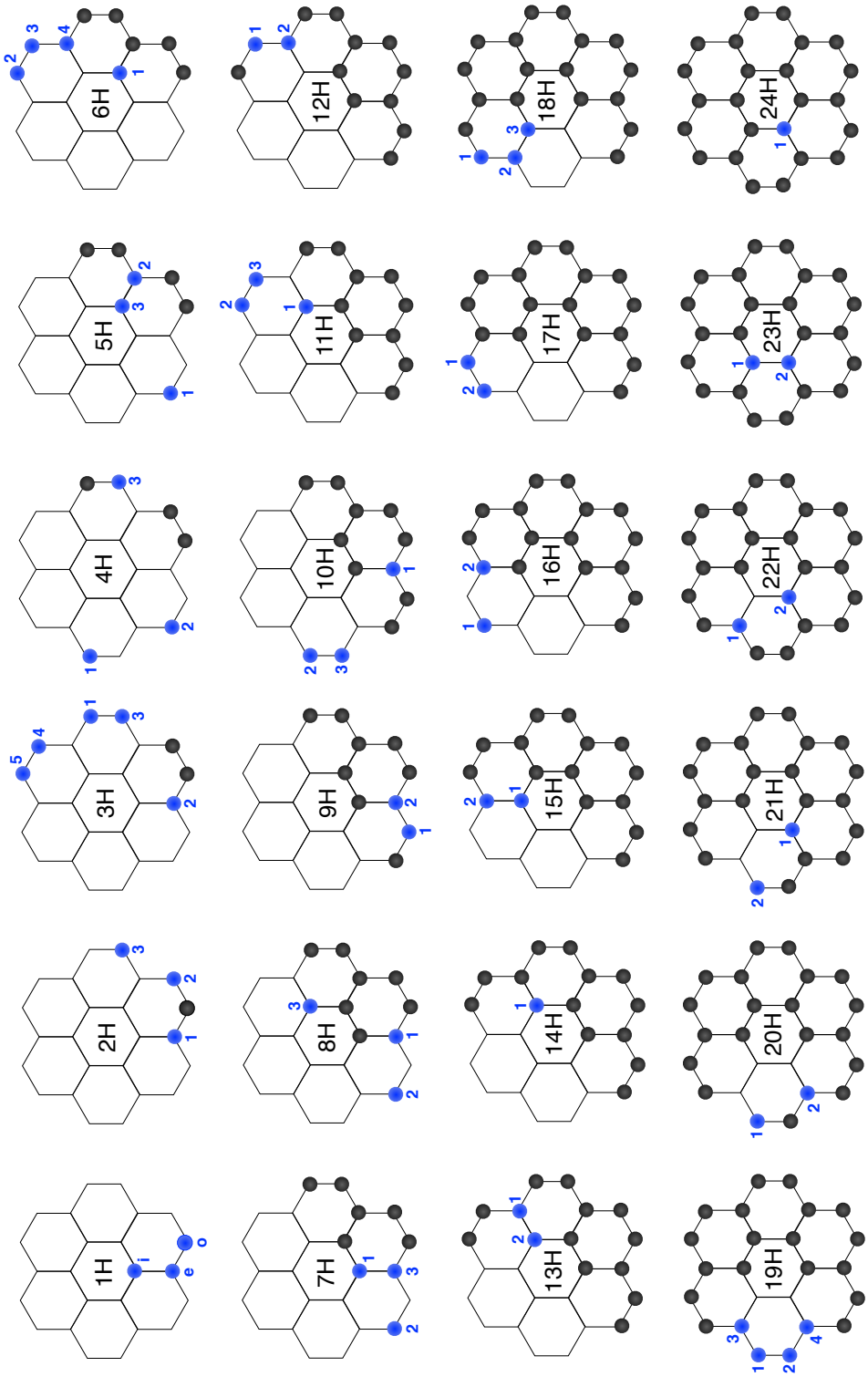

Figure 4.6. Black circles mark hydrogenated sp^3 carbons while blue circles mark sites whose binding energy has been computed at each hydrogenation level (nH).

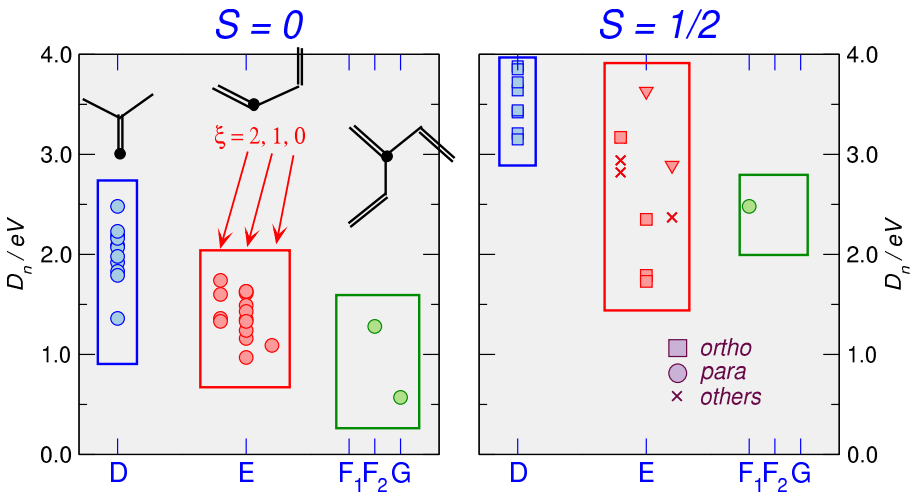

Figure 4.7. Correlation between hydrogen binding energy and coordination numbers. Left: H sticking on even numbered species (i.e., singlets), for different sites, $Z = 1, 2$ and 3 for D, E and F/G sites. Also indicated the hyperconjugation numbers. See text for details. Right: same as in the left panel for odd-numbered species (*i.e.*, doublets).

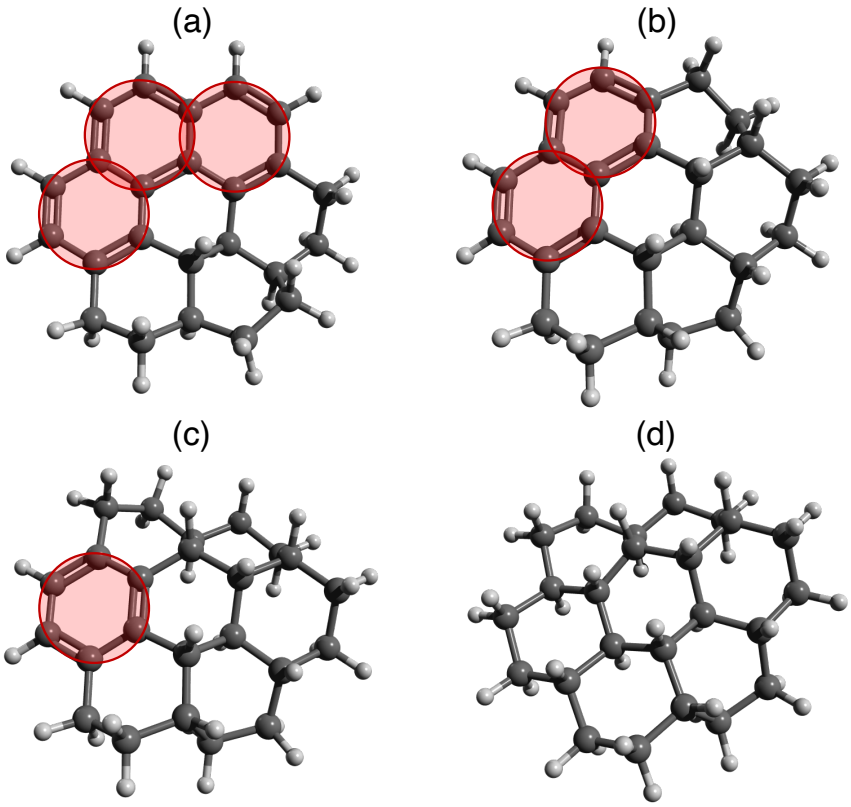

Figure 4.8. Superhydrogenated coronene molecule with 10,14,18 and 24 extra hydrogen atoms along the main sequence (panels a-d, respectively).

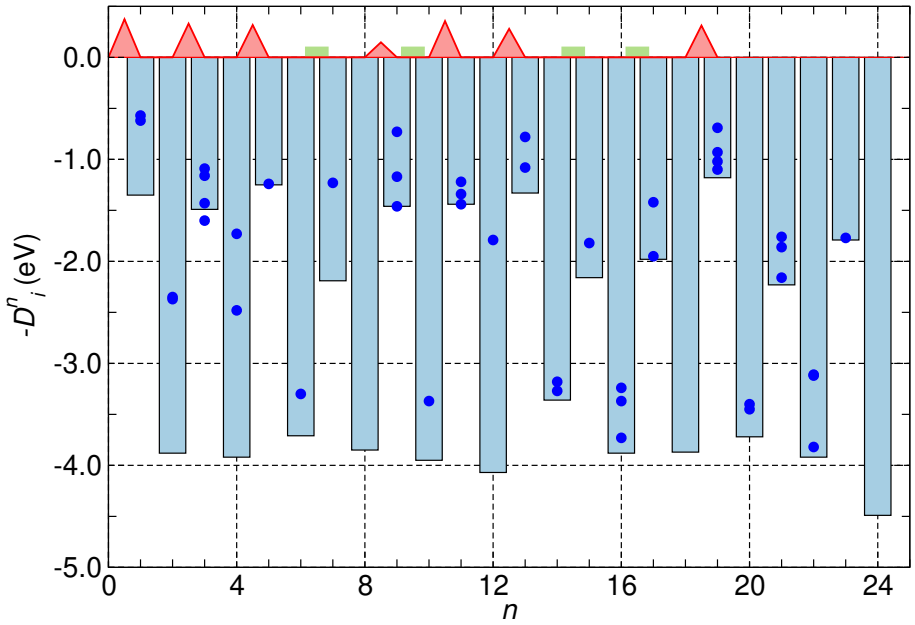

Figure 4.9. Hydrogen adsorption energy along the sequence shown in Figure 4.4 (right) (light blue bars). For each hydrogenation level, the energy for binding to alternative sites are shown as dots. Red triangles and green bars as in Figure 4.5.

.

than 20 meV - *e.g.* the ones relative to the 3rd, 6th, or 11th steps - thereby suggesting that these values of n may be branching points in the hydrogenation sequence. Therefore, an alternative hydrogenation pathway was investigated considering the second stable structure at the first branching point (3rd step), and keeping the lowest energy adsorption site onward. The resulting hydrogenation sequence is shown in Figure 4.4 (right), while the corresponding binding and barrier energies along the path are given in Figure 4.9. The results parallel those found for the main sequence and again identify $n = 10, 18$ and 24 as *magic numbers*. In addition, the structure with $n = 4$ is found to be more stable than in the previous path, in better agreement with the results of Figure 4.1. However, a remarkably smaller binding energy (and a non-detectable barrier for further hydrogenation) results for the structure with 14 extra hydrogens, at odds with the thermal desorption spectra which show $C_{24}H_{26}$ accumulating during exposure (see Figures 4.1 and 4.2). With the same token, Figure 4.9 also shows that the $n = 12$ structure should accumulate during the exposure, but this is not observed in the mass traces. In closing this section, we underline that the rules established in Subsection 4.3.1 can be equivalently applied to rationalize the alternative hydrogenation pathway.

Chapter 5

H adsorption on large clusters

The height of the H sticking barrier (E_b) on graphene is yet unknown with precision. In the literature, there is *zoo* of data, that witness the great sensitivity of E_b to the computational setup employed. Some authors, employing vdW-inclusive DFT calculations, have even claimed that such barrier should be vanishing[1][106, 107, 108], in direct contrast with the experimental results (see Section 1.3). At present, standard GGA-DFT calculations cluster around a value $\approx 0.2\,\text{eV}$[51, 40, 109]. However, more accurate calculations are needed to identify with better precision the H sticking barrier. In this respect, PAHs have been often employed as a molecular model of graphene to study the H adsorption energetics, because they allow a more refined computational setup, especially when small molecules such as coronene are considered. On the other hand, as discussed in Section 2.1, finite-size can introduce additional electronic effects that evidently influence the H adsorption energetics, undermining the extension to the infinite size limit.

In this Chapter, we present new DFT calculations on two large clusters, namely *circumcoronene* ($C_{54}H_{18}$) and *doublecircumcoronene* ($C_{96}H_{24}$ (see Figure 5.1), in order to minimize the finite-size effect while still employing a high-level of theory. This Chapter is organized as follows: in Section 1, we summarize the main computational details of our calculations; in Section 2 , we comment our results.

5.1 Methods

The calculations described in the following were performed with the set of XC functionals described in Chapter 3, again with the help of the Gaussian16 code[103]. We employed the 6-311G(d,p) atom-centered basis and tight convergence criteria on both the electronic and structural optimizations. For both the binding energy D and the energy barrier E_b, the BSSE was removed applying the standard CP correction (see Box on pag.19). Optimized structures were checked with harmonic frequency calculations.

5.2 Circumcoronene and Doublecircumcoronene

Figures 5.2 and 5.3 compare respectively the binding energies and energy barriers between coronene, circumcoronene and doublecircumcoronene. First, we note that the trend among different functionals observed for coronene is substantially reproduced also for larger clusters. Increasing the cluster size decreases the barrier height and, correspondingly, increases

[1] As highlighted by Bonfanti and Martinazzo (2018), some care is needed when a vdW-inclusive functional is combined with atomic-orbital basis-set. Indeed, the combination of an overbinding functional with the BSSE may lead to errors comparable to the estimated barrier height (*i.e.* 0.2-0.3 eV), thus making the latter vanishing[105]. We will return on this issue regarding the BSSE in Chapter 8, when discussing the bilayer binding energy in the C/Si interface.

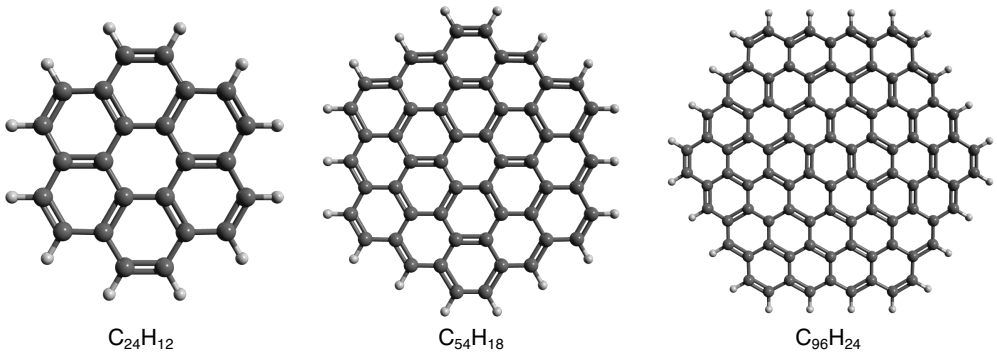

Figure 5.1. Geometrical structure of coronene ($C_{24}H_{12}$), circumcoronene ($C_{54}H_{18}$) and double-circumcoronene ($C_{96}H_{24}$).

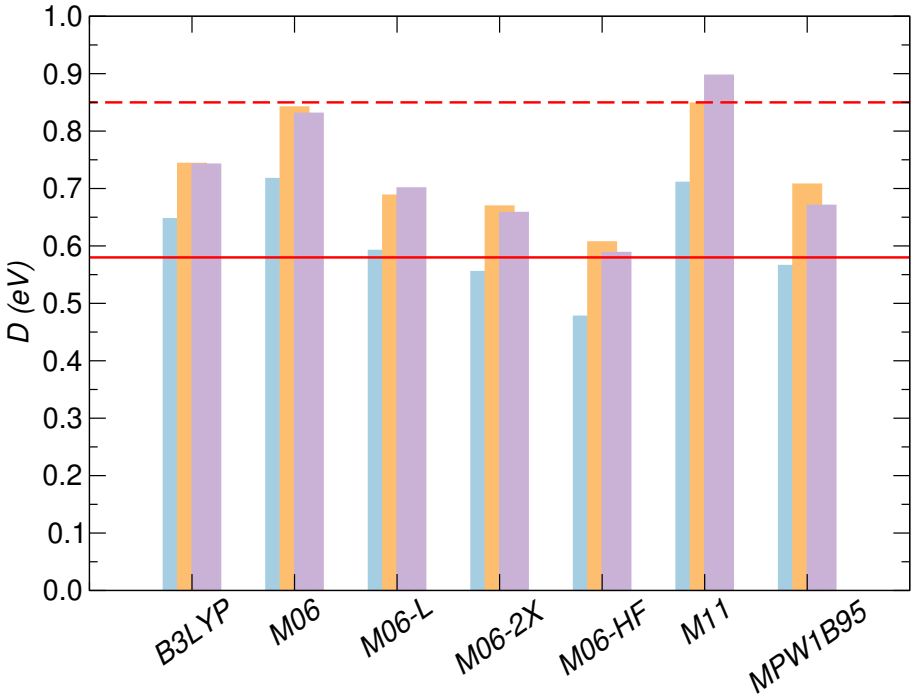

Figure 5.2. Binding energy (D, eV) for the H sticking on the center site of coronene ($C_{24}H_{12}$, light blue), circumcoronene ($C_{54}H_{18}$, light orange) and doublecircumcoronene ($C_{96}H_{24}$, light purple) for different XC functional. The dashed and dotted red lines denote respectively the CCSD(T)&CBS extrapolation on coronene[94] and a typical value of D given by periodic DFT calculations on graphene[39].

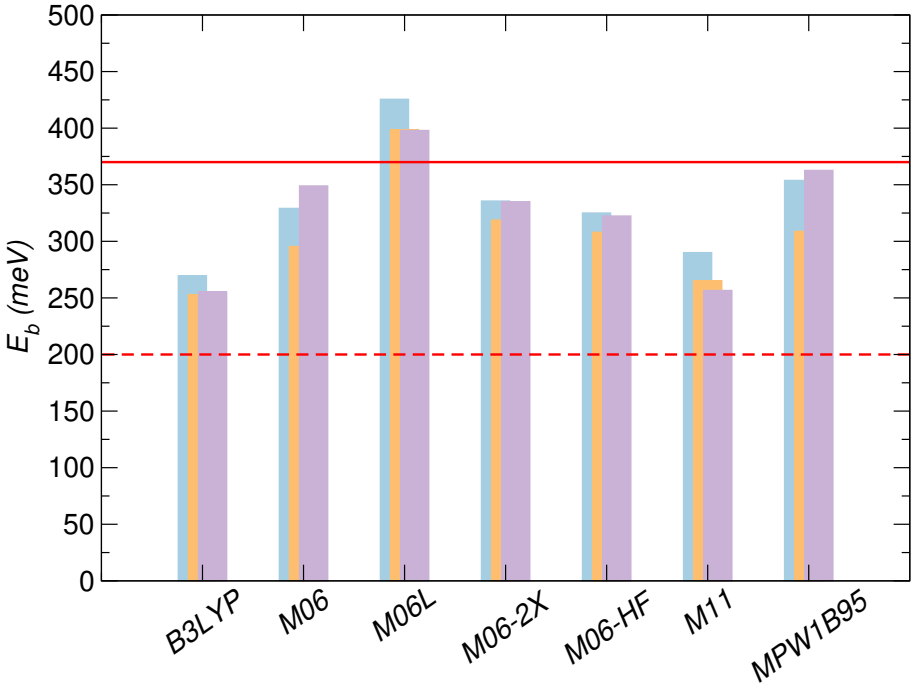

Figure 5.3. Barrier height (E_b, eV) for the H sticking on the center site of coronene ($C_{24}H_{12}$, light blue), circumcoronene ($C_{54}H_{18}$, light orange) and doublecircumcoronene ($C_{96}H_{24}$, light purple) for different XC functional. The dashed and dotted red lines denote respectively the CCSD(T)&CBS extrapolation on coronene[94] and a typical value of D given by periodic DFT calculations on graphene[39].

Table 5.1. Binding energy (D, eV) and barrier height (E_b, meV) as obtained by M06-2X/6-311++G(d,p) calculations on coronene ($C_{24}H_{12}$), circumcoronene ($C_{54}H_{18}$) and doublecircumcoronene ($C_{96}H_{24}$).

	D	E_b
$C_{24}H_{12}$	0.55	337
$C_{54}H_{18}$	0.67	319
$C_{96}H_{24}$	0.66	335

the binding energies (with few exceptions, such as M06 or MPW1B95). For the barrier height, this reduction is tough limited and it seems unlikely that its value attains ≈ 0.2 eV when extrapolated to the infinite size limit[30], as suggested by some authors. We can note that the M06-2X results on any cluster are quite larger than the "old" but still popular hybrid functional B3LYP. Interestingly, the meta-semilocal functional M06L, which has been finding increasing interest in the condensed matter community, provides even larger estimates for the barrier (*e.g.* 407 meV for coronene and 390 meV for circumcoronene). Nevertheless, as discussed in Chapter 3, this functional shows poor performances against those datasets that best fit our problem[92]. On the contrary, our M06-2X results compare reasonably well with coupled-cluster calculations on coronene[94, 92] (that found a barrier of about 370 meV), therefore suggesting a much larger barrier height for graphene than previously estimated[2] (335 meV for doublecircumcoronene). The M06-2X results are summarized in Table 5.1.

[2]In this regard, we should remind that GGA functionals underestimate (overestimate) the barrier (binding) energy especially when directional covalent bonds are formed. This is a known shortcoming of standard semilocal functionals.

Part II

Carbons in a *curved* world

Chapter 6

The rise of curvature in carbon nanostructures

In Part I, we had the occasion to see the concepts of π-conjugation and aromaticity in action in the context in which they were originally defined, that is for planar sp^2 systems. Every chemist knows, indeed, from the very first course in organic chemistry that π-conjugation arises from the mutual axial overlap of pure p orbitals orthogonal to a molecular plane that leads to the formation of π molecular orbitals that extend over the entire molecule (or π-bands for solid-state systems). Such long-range conjugation is responsible for the over-delocalized character of π-electrons, which yields many of the peculiar properties of the sp^2 carbon nanostructures. Likewise, since its formulation in 1930, the celebrated Hückel's rule [110] that attributes additional stability to "planar systems with $4n + 2$ π-electrons", has been a guiding principle in organic chemistry for decades.

During the past decades, the development of new synthetic routes has, however, allowed experimentalists to design and produce structures that seriously question the restriction of Hückel's theory and π-conjugation to planar systems. In this regard, we could mention different classes of aromatic compounds and low-dimensional nanostructures which are found to be characterized by an extended π-conjugation, even though their structure differs from the ideal planar. Without attempting to be exhaustive, we cite here carbon nanostructures such as nanotubes[111, 112, 113] or curved polycyclic aromatic hydrocarbons such as circulenes[114], coroannulenes[115, 116], and helicenes[117] or spheroidal aromatics as fullerenes[118, 119, 120]. Graphene sheets themselves are not strictly flat over long-range, instead, they are naturally characterized by corrugations in the form of frozen ripples and flexural phonons[121, 122]. In the past few years, attempts have been made to understand the effect of curvature on the physical and chemical properties of carbon nanostructures[123, 124, 125]. However, at present, a rationalization and quantitive description of curvature effects is still lacking, especially in the field of chemical reactivity. Indeed, this requires a deep theoretical investigation of how the overall curvature of the system affects both the π-conjugation and aromaticity, in terms of geometry and orbital characters. The very first issue to deal with lies at the basis of the topic: "how can we define the curvature of a carbon nanostructure?". Several authors have tried to answer this question[125, 126, 127] but a rigorous approach to the subject is still missing.

This Chapter sets then the beginning of our *journey* through the exotic world of curved carbon structures, that will be described in both Part II and Part III. Part II is organized into 4 Chapters. In this first Chapter, we *populate* the world of curved structures, that is we provide the reader with an overview of the major curved carbon systems (along with their properties) that have been designed and produced so far. In Chapter 2, we discuss the case of the step-wise hydrogenation of *coroannulene*, a molecule that can be considered as the curved analog of coronene. This Chapter is thus parallel to Chapter 3, but with

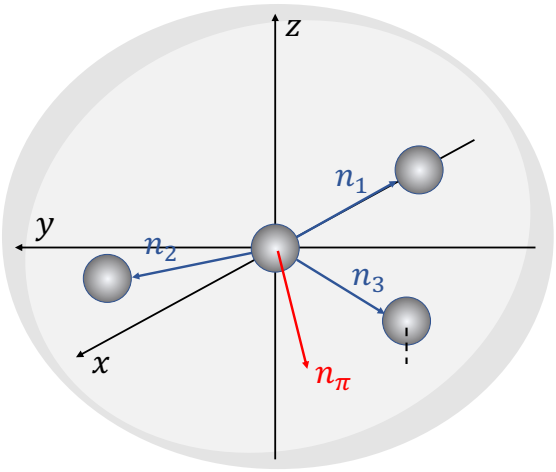

Figure 6.1. Reference system for the construction π-orbital axis vector. $\boldsymbol{n}_i$ are unit vectors directed along the σ-bonds, while $\boldsymbol{n}_\pi$ is the unit vector directed along the π-like orbital.

an additional element, namely the *curvature*. Chapter 3 and 4 are entirely dedicated to the investigation of graphene epitaxially grown on SiC (a.k.a. the C/Si interface). In this case, the curvature is of a different nature, since it is induced by the interaction with the substrate. We will see that, besides being an admitted "citizen" of the curved world, the C/Si interface may allow solving some current issues in the context of graphene technology[25].

While Part II approaches the topic from an applied perspective, in Part III we go back to the heart of the theory of curved systems and we try to answer the aforementioned question with a mathematically rigorous approach.

6.1 Pyramidalization and Rehybridization

Before discussing the most common curved structures, we need to introduce some consolidated concepts that date back to the early attempts to describe curved π-systems. In this field, Haddon[126, 127, 128] was one of the pioneers in providing a mathematical description of the effect of curvature on the atomic scale. In particular, he introduces the so-called *π-orbital vector analysis (POAV)* and the *pyramidalization angle* to quantify the degree of non-planarity at a conjugated carbon. To illustrate these concepts, let consider a C atom in the sp^2 orbital configuration and call $\hat{\boldsymbol{n}}_i$ $(i = 1, 3)$ the unit vectors defining the direction of the sp^2 orbitals. If the latter are directed towards the σ bonds (*i.e.* in case of non-bent bonds),

$$(\hat{\boldsymbol{n}}_1|\hat{\boldsymbol{n}}_2) = \cos\theta_{12} \tag{6.1}$$

defines the bond angle θ_{12} between the σ-bond 1 and 2 ($(\cdot|\cdot)$ denotes the standard scalar product in $\mathbb{R}^3$). For a true sp^2 carbon, $\theta_{12} = 120°$ and the fourth orbital, namely the pure p, makes an angle of 90° with each of $\hat{\boldsymbol{n}}_i$ $(i = 1, 3)$, being orthogonal to the molecular plane. Let consider now a carbon that lies on a generic curved surface, where something like a "molecular plane" no longer exists. Following Haddon (2001)[128], let define a coordinate system such that the relevant C atom is located at the origin, the first neighboring C lies along the $-x$ direction, the second in the xy plane, and the third lies out of the xy plane but with projection on this plane (see Figure 6.1). In this coordinate system,

$$\hat{\boldsymbol{n}}_i = x_i\boldsymbol{e}_x + y_i\boldsymbol{e}_y + z_i\boldsymbol{e}_z$$

From Equation 6.1 and simple geometrical arguments, it follows

$$\begin{array}{lll} x_1 = -1 & y_1 = 0 & z_1 = 0 \\ x_2 = -\cos(\theta_{12}) & y_2 = \sin(\theta_{12}) & z_2 = 0 \end{array} \tag{6.2}$$

and

$$x_3 = -\cos(\theta_{31}) \tag{6.3}$$

$$y_3 = \frac{\cos(\theta_{23} - \cos(\theta_{31})\cos(\theta_{12})}{\sin(\theta_{12})} \tag{6.4}$$

$$z_3 = \sqrt{1 - x_3^2 - y_3^2} = \sqrt{1 - \cos^2(\theta_{31}) - \left(\frac{\cos(\theta_{23} - \cos(\theta_{31})\cos(\theta_{12})}{\sin(\theta_{12})}\right)} \tag{6.5}$$

Assuming that the π-orbital makes an equal angle to the three σ-bonds also in non-planar structures, one can define a unique $\hat{\boldsymbol{n}}_\pi$ orbital vector (the before-mentioned π-orbital axis vector) making equal angles with $\hat{\boldsymbol{n}}_i$[1] taking the normalized cross-product of the two vectors $\hat{\boldsymbol{n}}_2 - \hat{\boldsymbol{n}}_1$ and $\hat{\boldsymbol{n}}_3 - \hat{\boldsymbol{n}}_1$, that is

$$\hat{\boldsymbol{n}}_\pi = \frac{(\hat{\boldsymbol{n}}_2 - \hat{\boldsymbol{n}}_1) \times (\hat{\boldsymbol{n}}_3 - \hat{\boldsymbol{n}}_1)}{||(\hat{\boldsymbol{n}}_2 - \hat{\boldsymbol{n}}_1) \times (\hat{\boldsymbol{n}}_3 - \hat{\boldsymbol{n}}_1)||}$$

With some algebra, one arrives at the following expression

$$\begin{aligned} \hat{\boldsymbol{n}}_\pi &= x_\pi \boldsymbol{e}_x + y_\pi \boldsymbol{e}_y + z_\pi \boldsymbol{e}_z \\ &= \frac{1}{\mathcal{N}} \left[(y_2 z_3)\boldsymbol{e}_x - z_3(x_2 - x_1)\boldsymbol{e}_y + [y_3(x_2 - x_1) - y_2(x_3 - x_1)]\boldsymbol{e}_z\right] \end{aligned}$$

where $\mathcal{N}$ is a normalization constant, namely

$$\mathcal{N} = \sqrt{x_\pi^2 + y_\pi^2 + z_\pi^2}$$

The angle $\theta_{\sigma\pi}$ is then given by[2]

$$\boxed{\cos(\theta_{\sigma\pi}) = (\hat{\boldsymbol{n}}_1 | \hat{\boldsymbol{n}}_\pi) = \frac{1}{\mathcal{N}}(x_1 y_2 z_3)} \tag{6.6}$$

From $\theta_{\sigma\pi}$, one usually defines the angle $\theta_P := \theta_{\sigma\pi} - 90°$, called *pyramidalization angle*[3], so that $\theta_P \equiv 0$ for sp^2 C atoms. For an sp^3 C, σ bonds make an angle of about 109.5° with each other, hence $\theta_P \approx 19.5°$. Pyramidalization angle in the range $0 < \theta_P < 19.5°$ thus indicate mixed sp^2-sp^3 orbital configuration. The latter manifests itself through a change in the balance between the σ (sp^2) and π (p) hybridization. In particular, π-orbitals acquire a fractional s component while sp^2 orbitals deviate from such "purely" integer hybridization.

The extent of such *rehybridization* can be determined in the hypothesis of non-bent bonds by resorting to the so-called *Coulson's directionality theorem*. Let consider a C atom using some kind of sp^τ hybrids to form σ bonds with the neighboring substituents.

[1] In other words, $\boldsymbol{n}_\pi$ is the *pyramid axis* of the pyramid whose basis is delimited by the three C atoms bonded to the central C at the origin.

[2] This is a general formula for a C_1 symmetry. For a C_{2h} symmetry, *i.e.* $\theta_{12} = \theta_{23} = \theta$ and $\theta_{13} = \theta'$, the formula reduces to

$$\cos(\theta_{\sigma\pi}) = -\sqrt{1 - \frac{4\sin^4(\theta/2)}{4\sin^2(\theta/2) - \sin^2(\theta'/2)}}$$

[3] This is at times called *pyramid angle*, see footnote 1 on pag. 67.

The (unnormalized) hybrids can be represented in the form

$$|\psi_i\rangle = |s\rangle + \sqrt{\tau_i}|p\rangle$$

where $|s\rangle$ describes a (total-symmetric) s orbital and $|p\rangle$ a directional p-orbital[4], while τ_i is the fraction of p character of the hybrid, a.k.a. the *hybridization index*. Assuming orthogonality w.r.t. to the scalar product defined in the Hilbert space $\mathcal{H}$ spanned by the hybrids[5], we have

$$\begin{aligned}\langle\psi_i|\psi_j\rangle = \delta_{ij} &= 1 + \sqrt{\tau_i\tau_j}\langle p|p'\rangle \\ &= 1 + \sqrt{\tau_i\tau_j}\cos(\theta_{ij})\end{aligned}$$

where θ_{ij} is the corresponding bond angle. Therefore, the hybridization indexes are given by the geometry around the C atom through

$$\boxed{\cos(\theta_{ij}) = -\frac{1}{\sqrt{\tau_i\tau_j}}} \tag{6.7}$$

Equation 6.7 defines a system of three equations in three unknowns (namely, τ_i with $i = 1, 3$), which can be easily solved to give

$$\boxed{\tau_i = -\frac{\cos(\theta_{jk})}{\cos(\theta_{ij})\cos(\theta_{ik})}} \tag{6.8}$$

Note that for the π-like orbital, we may write

$$|\psi_\pi\rangle = |s\rangle + \sqrt{\tau_\pi}|p\rangle$$

and thus defining three additional Equations of type 6.7 involving the angles $(\theta_{1\pi}, \theta_{2\pi}, \theta_{3\pi})$. The problem is only apparently overdetermined because the orientation of the fourth orbital actually follows from orthogonality once the orientation of the first three is given (a consequence of having a 4-dimensional function space in 3-dimensional Euclidean space). The hybridization index λ for the π-like orbital can thus be obtained by the conservation of p (or s) weights upon hybridization. The latter simply follows from the condition

$$\sum_{i=1}^{3} ||\psi_i||^2 + ||\psi_\pi||^2 = 1$$

that leads to

$$\boxed{\lambda = \frac{1}{1 - \sum_i (1+\tau_i)^{-1}} - 1} \tag{6.9}$$

which is singular ($\lambda \to \infty$) for co-planar σ-bonds, *i.e.* when $\tau_i = 2$, for $i = 1, 3$. In case of a C_{2h} symmetry, *i.e.* when the C atom, say X, has two equal substituents, say Y, the above Equations simplify, since one has just two different bond angles, namely $\theta_{12} = \theta_{23} = \theta$ and $\theta_{13} = \theta'$ (see Figure 6.2). In this case, a convenient measure of the "distortion" of the

[4] $|s\rangle, |p\rangle$ represent a basis in which the hybrid orbital is expanded. $|p\rangle$, being a directional orbital, can be further expanded in the local basis $|p_x\rangle, |p_y\rangle, |p_z\rangle$.

[5] Such condition ensures separability and non-zero overlap.

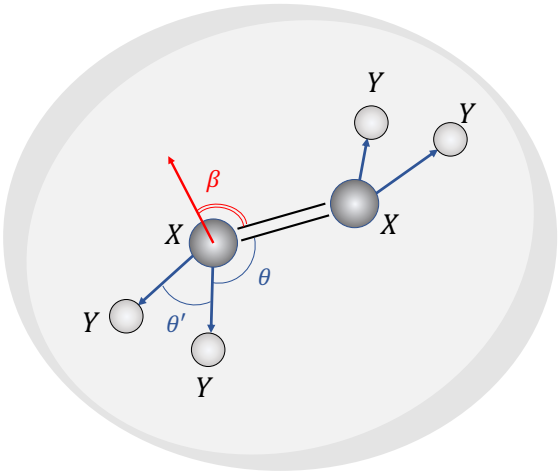

Figure 6.2. Pictorial representation of a C_{2v} molecule. θ and θ' are respectively the YXX and YXY bond angles. β is the angle between the π-like orbital and the XX bond direction and it represents a good measure of "distortion" for a C_{2v} molecule.

π-axis is provided by the angle that the fourth hybrid makes with the XX bond[129]

$$\beta = \arccos\left(\cos\theta\sqrt{-\frac{1}{\lambda\cos\theta'}}\right) \tag{6.10}$$

Pyramidalization and rehybridization are thus two powerful concepts that apply to a rather generic curved molecule to describe the effect of curvature at the atomic scale.

6.2 Curved aromatics

The first *big* class of curved structures that we discuss is that of curved aromatic (or π-conjugated) molecules. In the current literature, it is custom to categorize curved sp^2 systems according to their *Gaussian curvature*, K. In Part III, we give a rigorous definition of Gaussian curvature in its original mathematical context. For the present discussion, it suffices to know that the Gaussian curvature is an intrinsic measure of curvature at a point P of a surface: at dome-like points, such as on ellipsoids or spheres, $K > 0$ and the point P is said to be an *elliptic point*; at saddles, $K < 0$ and the point P is referred to as *hyperbolic point*; if one can find a curve through P that is not "curved"[6], like the generatrix of a cylindrical surface (see Figure 6.3), then $K = 0$ and the point P is said to be a *parabolic point*.

When dealing with a molecule or material surface, from the geometrical point of view we have *discrete* object, that roughly speaking are made of balls and sticks, that is they are bi- or tridimensional polyhedra, where C atoms are the *vertexes* and σ-bonds are the *edges*. The above definition of Gaussian curvature still applies to discrete surfaces, and, in its discrete formulation, K can be computed as

$$K = 2\pi - \sum_{i=1}^{3}\theta_i \tag{6.11}$$

where θ_i are the bond angles (or the angles at the vertexes). The discrete Gaussian curvature represents then an *angular defect*: it is the missing angle when comparing a

[6]Rigorously, we are referring to the *normal curvature* of a curve defined on the surface, see Part III, Subsection 10.4.1 at pag. 157.

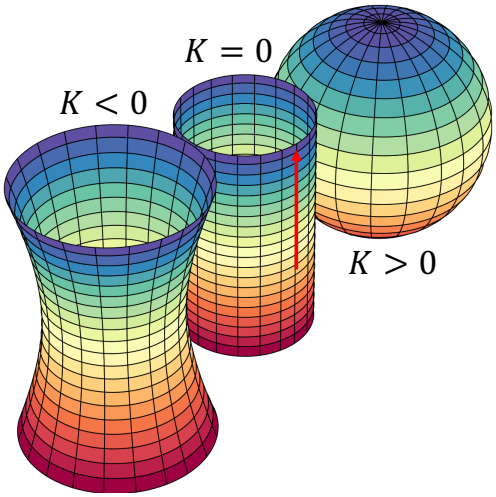

Figure 6.3. Prototypical surfaces of negative, zero and positive Gaussian curvature, K. For the $K = 0$ case, the direction of vanishing (normal) curvature is indicated by a red arrow. On a cylinder, this direction is *any* direction parallel to the cylinder axis.

Table 6.1. Symmetry, Pyramidalization angle (θ_P), Gaussian curvature (K) and hybridization of the π-like orbital for C_{20}, C_{50}, C_{50}, C_{60} and C_{70}. Fullerenes are here identified as aromatic or not on the basis of the electron number (Hirsch's rule). It is worth noticing that C_{50} has not equivalent carbons, despite being aromatic.

	Symmetry	Aromaticity	θ_P	K	$\|\psi_\pi\rangle$
C_{20}	I_h	No	19.0°-22.0°	33.7°-43.8°	$sp^{2.1}$-$sp^{3.2}$
C_{50}	D_{5h}	Yes	10.7°-15.6°	11.4°-23.4°	$sp^{5.7}$-$sp^{13.7}$
C_{60}	I_h	No	11.6°	12.0°	$sp^{11.4}$
C_{70}	D_{5h}	No	8.6°-11.9°	7.4°-14.0°	$sp^{10.7}$-$sp^{20.6}$

circumference of a circle 2π (with unitary radius) on a plane to that on a surface[7].

A well-known example of positive Gaussian curvature at *any* points are *fullerenes*, spheroidal molecules with formula C_n[119, 120, 130]. Table 6.1 reports the hybridization and local curvature information of four known fullerenes (C_{20} the smallest fullerene, C_{50}, C_{60} and C_{70}, whose geometrical structure is shown in Figure 6.4). Buckminsterfullerene[8] (C_{60}) is by far the most famous member of the family, because of its shape that resembles that of a soccer ball[9]. C_{60} was originally conjectured independently by Osawa[131] in 1970, and Stankevich[132], Bochvar, and Galpern[133] in 1973, and then discovered accidentally by mass spectrometry in 1985 by Kroto et al.[118] through laser evaporation of graphite. Later in 1990, it was first synthesized in larger amounts by Krätschmer et al.[134].

Fullerenes occur in nature and they have been detected in the interstellar medium like PAHs, albeit in minute amounts (10^{-4} of the interstellar carbon in various environments[135]). C_{60} was first identified in young planetary nebulae in 2010[136], and it is the only fullerene that is widely detected from its weak mid-IR features[135, 137]. At present, how fullerenes and in particular C_{60} can form in the ISM is still a debated question[138]. The most convincing route is through bending and subsequent closure of graphene sheets with a number

[7]In polyhedra, such angular defect is zero along the edges and for any point on the faces. Therefore, the Gaussian curvature is all "concentrated" at the vertex. On the other hand, we are interested in K at vertexes, since they represent the conjugated carbon in the present context.

[8]It was named after Richard Buckminster Fuller (1895-1983), a celebrated architect who designed the *geodesic dome*, a hemispherical thin-shell structure that topologically resembles a fullerene.

[9]Indeed, they are informally called *buckyballs*.

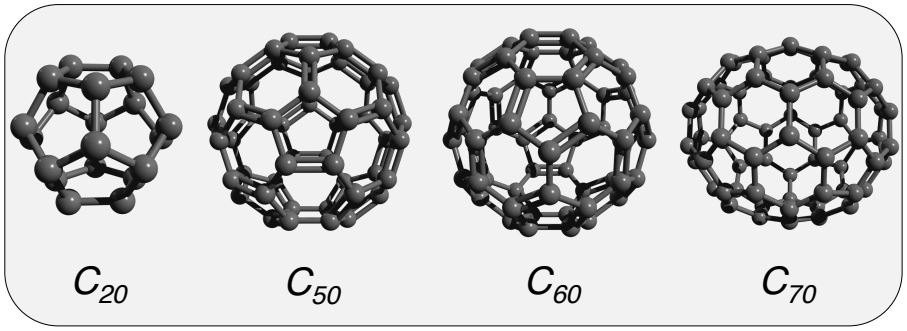

Figure 6.4. Optimized geometrical structures for some of the most common fullerenes: C_{20}, C_{50}, C_{60} and C_{70}.

of C atoms slightly larger than 60 heated under UVphotons[135, 139] or from the surface decomposition of SiC grains in hydrogen-dominated gas[140].

From a more applied perspective, one of the most studied applications of fullerenes in the past few years regards their use as an encapsulating agent, in drug delivery or cancer treatment[141, 142].

In the context of aromaticity, some members of the family behave similarly to aromatic molecules in terms of structural properties (uniform bond length), magnetic properties (the existence of ring currents) or resonance stabilization energy, and this has thus motivated the introduction of the term *spherical aromaticity* or *superaromaticity*. In 2000, Hirsch et. al.[143] suggested an extended version of the Hückel's rule to account for aromaticity in fullerenes. In particular, they observed that fullerenes are aromatic when they have $2(N+1)^2$ π-electrons so that the π-density is totally symmetric, in full analogy with planar aromatic molecules[10]. According to this definition, C_{60} should not be aromatic since it does not satisfy the Hirsch's rule. However, its aromatic character has been the source of some controversy in the literature, since in some experiments it has shown to displays a certain of degree of aromaticity[144].

Fullerenes have been widely investigated also from the topological point of view and, truthfully, they represent one of the most successful applications of *mathematical chemistry*[11]. A comprehensive introduction to this fascinating matter can be found in the work of Schwerdtfeger et. al.[130].

Another class of curved molecules is represented by *polycyclic aromatic hydrocarbons* (PAHs). In Part I, we largely discuss this class of molecules restricting our attention to planar structures. However, PAHs can display a curvature, that can be intrinsic, because of their size or their skeleton itself, or induced by partial hydrogenation[12]. Intrinsic curvatures are induced by a topological modification of the PAH. For instance, if one replaces the inner 6-membered ring of coronene with a 5-membered ring, the resulting structure, called *coroannulene*, is curved (see Figure 6.5 (a))[116]. The reason for such bending can be understood from topological arguments if one recognizes that coroannulene is a "section" of C_{60} fullerene, that cannot be realized with just hexagons. This result is the consequence

[10]This implies that every set of orbitals than span an irreducible representation of the point group of the molecule is either filled or empty. We should remind, however, that this argument is valid for non-interacting electrons only. In more general situations, the symmetry of the *global* wavefunction seems to dictate the aromaticity.

[11]Graph theory and topology are two fields of maths that have found important applications in chemistry-related problems.

[12]As seen for coronene, when few atomic positions are hydrogenated, partly disturbing the aromaticity, PAHs undergo a structural distortion which often appears as a surface bending.

of the so-called *Euler's formula*, which establishes that the quantity

$$\chi = V - E + F = 2 \tag{6.12}$$

is a *topological invariant*[13] in convex polyhedra[14], called *Euler's characteristic*. V are the vertexes of the polyhedron, E the edges and F the faces. Since each edge is shared by two faces and each vertex V is shared by a certain number of faces, that we call the degree of V ($\deg(V)$), it follows that

$$\sum_{i=1}^{V} (deg)(V) = 2E \tag{6.13}$$

In fullerenes, $(deg)(V) = 3$, and therefore the following relatioships hold

$$E = \frac{3}{2}V \tag{6.14}$$

$$F = 2 - V + E = \frac{1}{2}V + 1 \tag{6.15}$$

$$V = 2F - 4 \tag{6.16}$$

From Equations 6.12 and 6.16, we have $E = 3F-6 = 3F_5+3F_6-6$, since $F = F_5+F_6$ where F_5 (F_6) is the number of pentagonal (hexagonal) faces. Since each pentagonal (hexagonal) face has 5 (6) edges and each edge is shared by two faces, for the total number of edge we also have $E = (5/2)F_5 + (6/2)F_6$. This result combined with $E = 3F_5 + 3F_6 - 6$, gives

$$3F_5 + 3F_6 - 6 = \frac{5}{2}F_5 + 3F_6 \Longrightarrow F_5 = 12 \tag{6.17}$$

which is usually known as the *12 Pentagon theorem for fullerenes*. As a main corollary to this theorem, it follows that $F_6 = (V - 20)/2$ with $V = n \geq 20$ and n the number of C atoms, and the general formula for fullerenes C_{20+2F_6}. Roughly speaking, this theorem suggests that pentagons are the source of a positive Gaussian curvature, which characterize polyhedra (or closed surfaces) with $\chi = 2$, *i.e.* topologically equivalent to a sphere (no holes).

On the other hand, theoretical investigations have shown that also coronenes ($C_{6N^2}H_{6N}$) bend as $N \leq 9 - 12$ (according to the method used), that is flatness is removed at increasing size of the PAH[15] Such bending signals that the curvature has a fundamental role in determining the structure of large PAHs and, at the same time, contrasts with the usual chemical intuition, which instead recognizes additional stability in extended (planar) π-conjugated systems[145].

Like their flat relatives, curved PAHs are under investigation for the role they might play in the ISM. For instance, it has been recently suggested that the inclusion of non-planar components in aromatic structures induces spectral patterns similar to the UIE[146, 147]. In addition, super-hydrogenated forms of curved PAHs may too act catalysts of the H_2 formation in photodissociation regions. In this respect, coroannulene is again one of the most interesting members of the family. Although it has not been uniquely identified so far,

[13]The result can be extended to any topological space. Generally speaking, χ is a number that uniquely defines the shape of a topological space, *regardless of the way it is bent*. For example, for a sphere $\chi = 2$ while for a disk $\chi = 0$. Therefore, one cannot find a "continuous" deformation that converts a disk into a sphere. In differential geometry, χ is defined in the context of the Gauss-Bonnet theorem, which is a fundamental result that relates the geometry of a surface (through the Gaussian curvature and the so-called geodesic curvature) with its topology (see Part III, Theorem 10.6.2 in Section 10.6, at pag,. 171).

[14]χ is 1 or 2 for any convex polyhedron in two or three dimensions, respectively. However, it can take different values in more complicated objects, *e.g.* 0 in *octahemioctahedron* or -6 in the *small stellated dodecahedron*.

[15]This implies that also graphene is not strictly flat, see below.

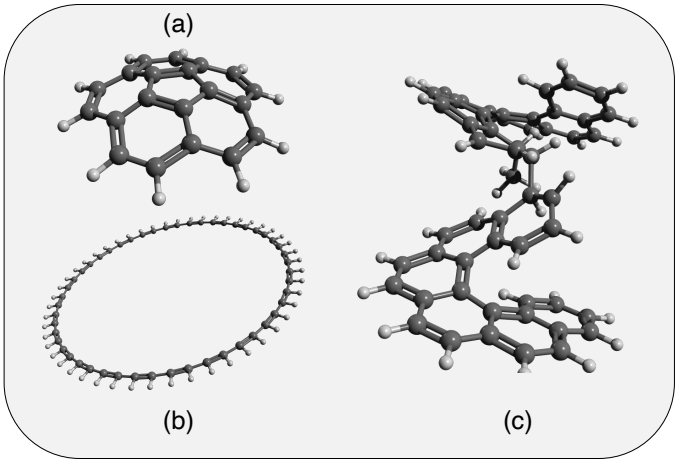

Figure 6.5. Geometrical structures of (a) coroannulne, (b) a [n]-annulene and (c) an helicene.

both terrestrial laboratory experiments[148] and astronomical observations of the diffuse interstellar bands suggest its presence in the ISM[149]. Furthermore, it is the simplest molecule on which one can study the influence of curvature on the structural and chemical properties, with the possibility of a direct comparison with the flat analog (coronene). These characteristics of coroannulene have thus motivated part of this work. In particular, in parallel to what was done on coronene in Chapter 7, we present a DFT investigation of the step-wise hydrogenation reaction of coroannulene.

Another class of curved π-conjugated molecules that is worth citing here is that of *helicenes*, which are polycyclic aromatic molecules with a helical shape[117] (see Figure 6.5 (c)). The topology and chiral properties of these molecules have sparked a great interest in the field of magnetism, magnetotransport, and spintronics. In particular, helicenes represent a suitable molecular model to study a recently observed phenomenology, namely the so-called *chiral-induced spin selectivity*[150]. With this term, one refers to the capability of chiral molecules to act as electron spin filters at room temperature, a property that is typical of inorganic ferromagnetic materials. The field of spin-selectivity effect in chiral aromatic molecules is still unexplored. Its comprehension, in relation to chemical properties such as π-conjugation, may open the possibility of designing and using this class of molecules for modern spintronics applications.

Last but not least, we cite one-dimensional systems like ring-closed polyacetylene chains, a.k.a. [n]-*annulenes* (se Figure 6.5 (b)). In the past, they served as a basic model to study the charge conduction and the optical properties in organic polymers. Even though there are no relevant technological applications of these systems, they represent a suitable model to study the local and global effects on electronic states. Moreover, since in these systems the curvature is restricted in one dimension, a connection between curvature, rehybridization, and eventually, their physical and chemical properties[151, 152, 153], can be established with less effort from the mathematical point of view. [n]-annulenes will be discussed in detail in Chapter 11 (Part III).

6.3 Graphene: flat or curved?

In the opening of Chapter 1, we mentioned the so-called Mermin's theorem[2] (see box 1.1 on pag. 4), which extended what was originally theorized by Landau[16] and Pierels[15], namely that strictly bi-dimensional crystals should be thermodynamically unstable and not exist. As discussed earlier, at first the discovery of graphene[3] in 2004 questioned the foundation of such fundamental result of Statistical Mechanics. Later, the experimental

observation of graphene, together with the discovery of other bi-dimensional materials, was reconciled with the theory, by recognizing that such crystals, being extracted from a 3D material, are quenched in a metastable state, where the strong interatomic forces assure that thermal fluctuations do not lead to disruptive atom displacements. Also, graphene samples are rarely "free-standing", rather they are at most suspended.

A complementary fact that explains the existence of graphene is that graphene is not flat at all! As a matter of fact, in many experimental setups, graphene displays a curvature in the form of *ripples*[25, 121, 154, 155, 156], which can be static or dynamical according to the experimental conditions. The extent of rippling is generally characterized through the h/l ratio, where h is the height of the ripple and l its lateral extension. According to the entity of rippling, graphene can display electronic structure or physical and chemical properties that strongly differs from planar graphene. From the chemical point of view, the first modification induced by the presence of rippling is the aforementioned pyramidalization and rehybridization. In Chapter 1, we saw that part of the chemisorption energy involved in the H adsorption process is due to the sp^2-sp^3 rehybridization of the binding C atom. Such rehybridization is associated with a change of the local geometry, from planar to tetrahedral, leading to surface puckering. On a curved system (like rippled graphene but also curved PAHs), part of the puckering energy is converted into chemisorption energy because of the curvature itself (the surface is already "prepared" to accommodate the incoming hydrogen). In addition, the overlap between neighboring p-orbitals is reduced and the π-bonds weaken so that breaking the π-bond is less expensive. Consequently, surface curvature leads to an enhancement of chemical reactivity. Boukhalov and Katnelson[157] were among the first to investigate theoretically this issue on rippled graphene. They introduced an artificial ripple on a graphene sheet by a smooth out-of-plane distortion of a group of carbon atoms, following the geometric shape of an isotropic semi-sphere. By means of DFT, they investigated the energetics of the H_2 adsorption as a function of the h/R ratio, where h is the height of the ripple and R the radius of the semi-sphere. Interestingly, they found that the regions of stable hydrogenated ripples are characterized approximately by integer numbers of the ratio $h/R = 0.04$, which is the right value of the ratio between the height of out-of-plane atomic distortion and radius of the distorted region for a pair of hydrogen atoms on flat graphene. In addition, it turns out that the H_2 will spontaneously decompose and bind at ripples with a large enough stabilizing curvature.

Such spontaneous decomposition of H_2 at ripples has been recently taken into account to explain the rather singular (and experimentally detected) permeability of graphene to molecular hydrogen[158]. Graphene is, indeed, recognized to be one of the most impermeable materials to gas. For instance, for helium, which is the most permeating of all gases, the permeability of graphene is estimated to be of no more than a few atoms over one month of exposure. To put this into perspective, defect-free graphene is less permeable than 1km-thick quartz glass[158]. The transparency of graphene to H_2 is therefore striking since it should be completely forbidden. Because of the estimated energy barrier ($\approx 10\,\text{eV}$), it would take longer than the lifetime of the Universe for a single H atom to pierce a defect-free membrane of graphene. To account for such unexpected behavior, P.Z. Sun et. al.[158] proposed a scenario where molecular hydrogen decomposes and binds at ripples[16]. The resulting adatoms then flip to the other side of graphene in a transport process similar to that previously reported for proton transport.

Similar investigations were conducted for the single H addition on rippled graphene, revealing that H preferentially chemisorbs on convex areas of the ripple. By exploiting the tunability of the H binding energy at different local curvatures, Tozzini and Pellegrini[159]

[16]It is still not clear whether the decomposition of H_2 is determined by static or dynamical ripples. A possible factor limiting the contribution of dynamical ripples is their relatively short lifetime, which, according to simulations, should be of the same order as the timescale of hydrogen permeation (few femtoseconds).

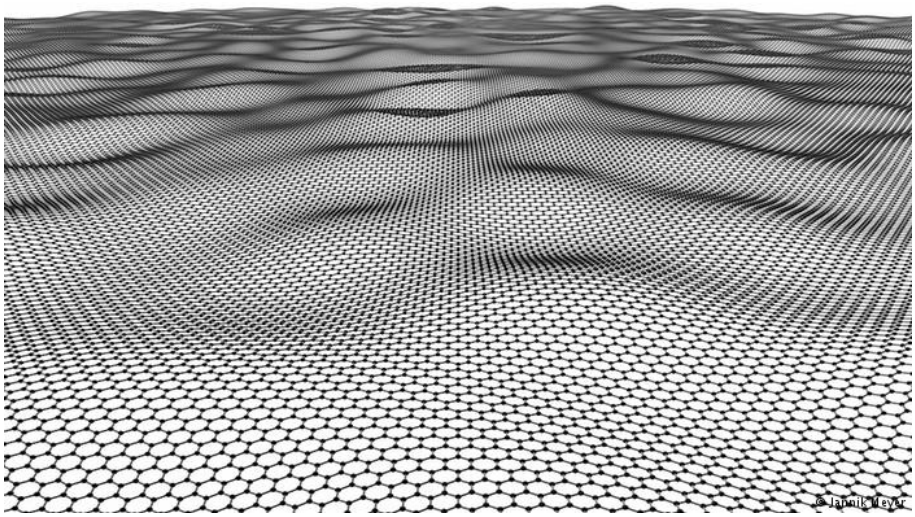

Figure 6.6. Geometrical structure of a rippled graphene sheet.

interestingly proposed a mechanism where hydrogen is stored on rippled graphene and then released by a curvature inversion, thus suggesting a new kind of hydrogen storage device based on curved graphene.

The curvature-induced enhancement of chemical reactivity has been also proven experimentally, on both suspended and epitaxially grown graphene. In suspended graphene, which is generally obtained transferring graphene sheets on TEM grids, the curvature is usually due to intrinsic rippling of the surface[154]. Instead, when graphene grows on a substrate such as SiC (Balog and coworkers[160], Riedl and coworkers[161]), a stable curvature can be obtained, because of the Moiré pattern modulation that the so-called buffer layer forms on graphene itself. The case of graphene grown on SiC deserves a special mention and we will discuss it in detail in Section 6.4.

The introduction of ripples on graphene affects also the electronic structure as well as its physical properties. In particular, ripples come with a modulation of the hopping parameter (Δt) and therefore of the Fermi velocity (v_F). These fluctuations of the hopping parameter give rise to an effective magnetic flux through the hexagon of the order $\Delta\Phi \approx \Delta t/t$ (in units of eh/c)[162]. If the hopping varies smoothly over a distance l, then $\Delta t \approx \delta t(a/l)$, where $a = 1.41\,\text{Å}$ is the C-C bond length and δt the overall modulation of t. Hence, the total flux through a region of area l^2 is $\Phi \approx (\delta t/t)(l/a)$. When the modulation δt comes solely from the presence of a ripple of height h and length l, then

$$\delta t \approx \frac{\partial \log(t)}{\partial \log(a)} \frac{h^2}{al}$$

Considering that in graphene, $t \approx 2.7\,\text{eV}$, the parameter $\beta = \partial \log(t)/\partial \log(a)$ is approximately equal to 2-3. The resulting flux per ripples in quantum units is

$$\Phi \approx \beta \frac{h^2}{la}$$

For realistic ripples, $h \approx 1{-}2\,\text{nm}$ and $l \approx 50\,\text{nm}$, then $\delta t/t \approx \delta v_F/v_F \approx 10^{-2}{-}10^{-1}$ and $\Phi \gtrapprox 1$. Guinea et. al.[162] demonstrated that Φ, which is to all effects the flux of a *pseudomagnetic field* threading an area of the size of the ripple, lead to the formation of midgap states, which are known to affect the chemical property of graphene (see Subsection 1.3.2). These midgap states are comparable to Landau levels at the Dirac energy induced by an external magnetic field.

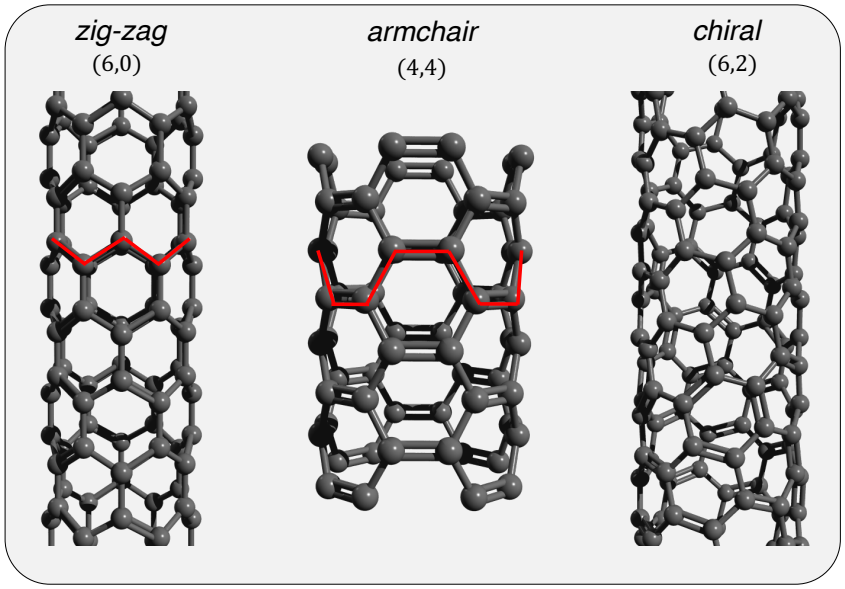

Figure 6.7. Geometrical structure of a zig-zag, armchair and chiral nanotube. In red, the zigzag and armchair path along the circumference that form when cutting and rolling a graphene sheet along the direction $(n, 0)$ and (n, n), respectively.

6.3.1 Rolling graphene: carbon nanotubes

Another important class of curved structures that originates directly from graphene is that of *carbon nanotubes (CNTs)*. Carbon nanotubes are cylindrical structures that form by rolling a graphene sheet in a given direction. They were firstly discovered by Ijima in 1991[111]. They can be *single-walled* or *multi-walled* according to the number of layers rolled. One further distinguishes from *zig-zag* $(n, 0)$[17], *armchair* (n, n) or *chiral* (n, m) (with $n \neq m$) nanotubes, according to the type of path along the circumference of the tube that results from the rolling (see Figure 6.7).

Box 6.1: The (n, m) notation

The (n, m) notation is used to distinguish from the zigzag, armchair (also known as *achiral* nanotubes), and generic chiral nanotubes. To understand the meaning of this notation, let imagine cutting the nanotubes along a direction parallel to its cylindrical axis starting from some atom X, and then unrolling the nanotube flat on the plane. Once unrolled, let suppose that atoms of the original nanotube coincide with those of an imaginary graphene sheet. The resulting two halves of the atom X will end up over two atoms $X1$ and $X2$.

[17] This is the so-called (n, m)-notation for the classification of different nanotubes (see the box 6.1, on page 76).

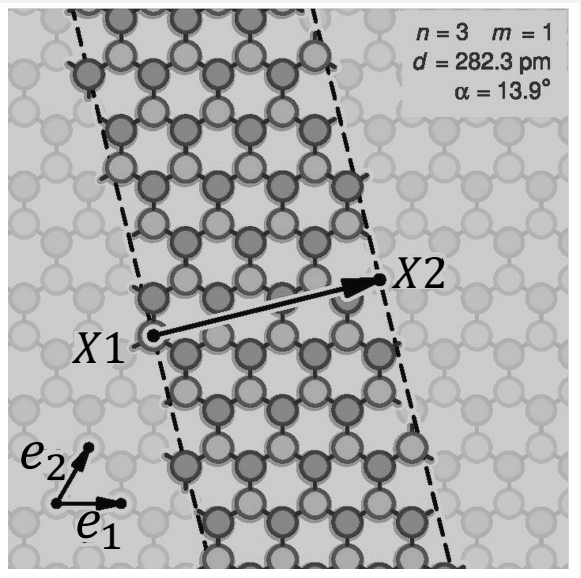

Let $\boldsymbol{e}_1$ and $\boldsymbol{e}_2$ be two linearly independent vectors connecting $X1$ to two of its nnn, *i.e.* two C atoms belonging to the same sublattice. Since $X2$ must be on the same sublattice of $X1$, the vector connecting $X1$ to $X2$ must be a linear combination of $\boldsymbol{e}_1$ and $\boldsymbol{e}_2$, that is $n\boldsymbol{e}_1 + m\boldsymbol{e}_2$. Therefore, the integers (n, m) define uniquely a possible position of $X2$. The argument can be reversed, that is one can define a vector $\boldsymbol{C} = n\boldsymbol{e}_1 + m\boldsymbol{e}_2$ that connects two C atoms ($X1$ and $X2$) on a graphene sheet. Then, cutting a strip along lines perpendicular to $\boldsymbol{C}$ through $X1$ and $X2$ and rolling the strip into a cylinder, one obtains the corresponding (n, m) nanotube. If such a procedure is applied to the pair $(n, 0)$, the result is a zigzag nanotube, with a closed zigzag path of $2n$ atoms. For a (n, n) pair, one obtains instead an armchair nanotube, with a closed path of $4n$ atoms. From the above argument, it follows that $|\boldsymbol{C}|$ represents the circumference of the nanotube, hence

$$|\boldsymbol{C}| = |\boldsymbol{e}_1|\sqrt{n^2 + nm + m^2} = d\sqrt{3(n^2 + nm + m^2)}$$

where d is the CC bond lenght. The diamater D of the nanotube is then given by $|\boldsymbol{C}|/\pi$, *i.e.*

$$D = \frac{d}{\pi}\sqrt{3(n^2 + nm + m^2)} \tag{6.18}$$

The angle θ formed between $\boldsymbol{C}$ and $\boldsymbol{e}_1$ is called *chiral angle*, and it is an important quantity strictly related to the electronic properties of the nanotube. Such angle is defined through

$$\cos(\theta) = \frac{(\boldsymbol{C}|\boldsymbol{e}_1)}{|\boldsymbol{C}||\boldsymbol{e}_1|} = \frac{2n + m}{2\sqrt{n^2 + nm + m^2}} \tag{6.19}$$

In any case, the Gaussian curvature is strictly zero on each point of the nanotube since any point on a cylinder is a parabolic point[18].

In the present context, Park and coworkers[123] developed a simple model tested on CNTs that relates the chemisorption energy of an atom X to the optimized value of the pyramidalization angle ($\theta_P^{\min}$). They broke the formation of the CX bond into three steps - preparation (strain), binding, and relaxation - and expressed their energies in terms of $\theta_P^{\min}$

$$E_{\text{total}} = E_{\text{strain}}(\theta_P^{\min}) + E_{C-X}(\theta_P^{\min}) + E_{\text{relax}}$$

[18]By rolling a flat paper sheet into a cylinder, the Euler's characteristic must be conserved!

The strain energy was defined as the excess energy left on the system when the binding C is pulled out of the surface and the remaining atoms are kept fixed. E_{strain} is thus represented as elastic Hook's terms describing the pulling of the C and the bond-stretching energy of the three nns, *i.e.*

$$E_{\text{strain}} = \frac{1}{2}k_b \sum_{i=0}^{3}(\theta_P^i - \theta_0^1)^2 + \frac{1}{2}k_s \sum_{i=0}^{3}(a_P^i - a_0^i)^2$$

where a^i is the bond lenght with the nearest-neighbor i and the subscript 0 refers to initial equilibrium values. k_b and k_s are force constants obtained through a fitting of DFT data. The CX binding energy comprises two terms: the breaking of the π-bond into a free π orbital and the binding of the latter with the atom X. In this model, it reads as

$$E_{\text{CX}} = (E_{\text{graphite}} - \alpha\theta_0^2) + (\sqrt{2}\tan(\theta_P)E_{sx} + \sqrt{1 - 2\tan^2(\theta_P)}E_{px})$$

where E_{graphite} is the π-bond breaking energy of graphite taken as a reference. $\alpha\theta_0^2$ is an energy shift due to the inherent curvature of nanotubes, where the constanst α is obtained through a fitting of the formation energy difference between CNTs and graphene. The second term in bracket represents the bond energy between the state $|\psi_\pi\rangle$[19] (describing the free π- orbital) and a state $|x\rangle$ of X, with $E_{sx} = \langle s|H|x\rangle$ and $E_{px} = \langle p|H|x\rangle$. Note that E_{sx} and E_{px} depend only on the atom X and therefore they can be treated as constants. According to DFT calculations, Park et. al.[123] found that $E_{relax} \approx -0.2\,\text{eV}$ regardless of the initial structure. By validating and applying this model on CNT, they observed that curvature affects the first and the second steps, respectively by reducing the strain and the π-energy. Moreover, the model revealed that the local chemical reactivity can be controlled by a proper mechanical deformation, as mentioned earlier for graphene.

6.3.2 Exotic curved nanostructures

In closing this Section, we mention two other interesting examples of curved nanostructures. The first is a carbon nanostructure devised by Yakobson and coworkers[163] and displayed in Figure 6.8 (a), where the curvature is induced by a screw dislocation. Essentially, this nanostructure consists of a graphene layer spiraling continuously around the line perpendicular to the basal plane, thus mimicking the topology of a $log(z)$ *Riemann surface*[20]. Interestingly, Yakobson et. al. have shown that, if the voltage is applied to such

[19] In terms of θ_P only, this state reads as

$$|\psi_\pi\rangle = \sqrt{2}\tan(\theta_P)|s\rangle + \sqrt{1 - 2\tan^2(\theta_P)}|p\rangle$$

[20] Riemann surfaces are complex topological manifold introduced to represent *multi-valued* function. Consider for instance the function $w = \sqrt{z}$, which in polar coordinates reads as $w = \sqrt{r}e^{i\theta/2}$. For $r = 1$ and $\theta = 0$, $w(z) = 1$, but walking around the origin and going back to the original point with $r = 1$ and $\theta = 2\pi$, $w(z) = -1$. To get back to $w(z) = 1$ in the w-plane we need to make another closed path of 2π in the z-plane. The idea is thus to represent the second path on a different z-plane, thus building up a surface called the Riemann surface. If the function has a singular point z_0 and, starting from a point z_1 in the z-plane we need to take an angle greater than 2π to get back to the original value, then z_0 is called *branch point* and the "cut" originating from such point called *branch cut*. Similar considerations apply to $\log(z)$, which is a complex-valued function, defined on some subset U of $\mathbb{C}^\star$, the set of nonzero complex numbers, satisfying

$$\log : U \to \mathcal{C}^\star \quad e^{\log z} = z \quad \forall z \in U$$

In polar coordinates, $z = re^{i\theta}$, and $\log(z) = \ln(r) + i\theta$, where θ is again defined module 2π. $z = 0$ is a singular point for $\log z$, which then has a jump discontinuity of $2\pi i$ when crossing the corresponding branch cut. The logarithm can be made continuous by gluing together countably many copies, called *sheets*, of the complex plane along with the branch cut.

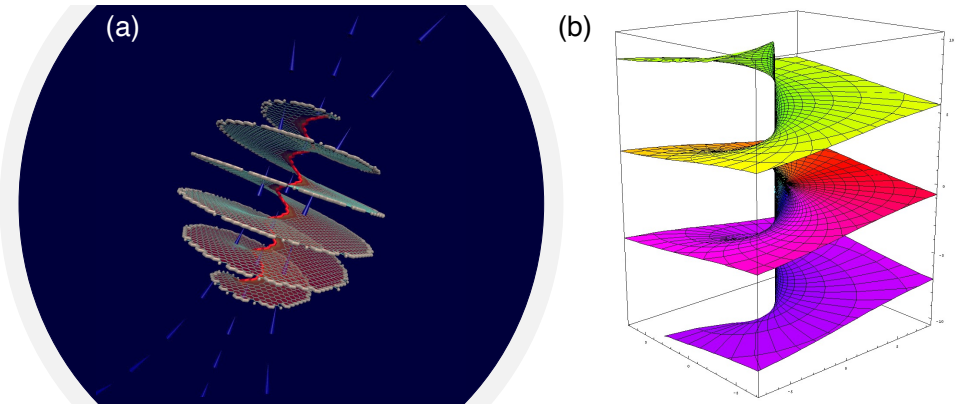

Figure 6.8. (a) Geometrical structure of the carbon nanostructure with helicoidal shape devised by Yakobson and coworkers; (b) $\log z$ Riemann surface.

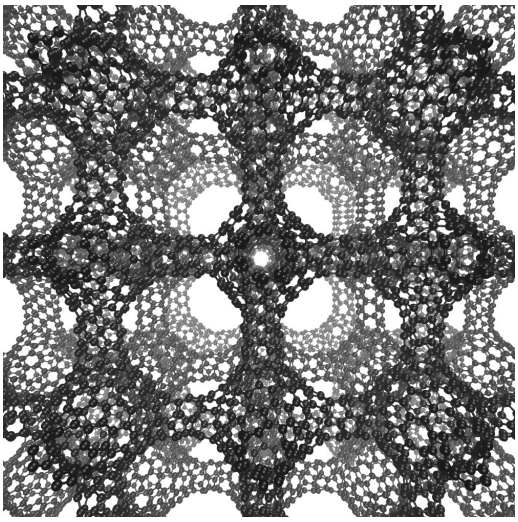

Figure 6.9. Geometrical structure of schwarzite.

a dislocation, a significant electrical current arises, thanks to the full covalent continuity, accompanied by a large magnetic field that originates from the helical current trajectory. For large diameters, the behavior approaches that of a classical ohmic helicoid, with a magnetic field B in the cavity proportional to $\log(R/R')$ (where R and R' are respectively the exterior and core radii) and an inductance increasing with the core cavity size. Due to their high winding density, the magnetic fields and the inductance generated are several orders larger than any achievable in recent microelectronics.

Other curious curved carbon structures are the recently discovered *schwarzites*. These have sparked great interest in recent years because of their singular topology and geometrical shape, which is expected to translate into unique physical properties[164]. First, as shown in Figure 6.9, schwarzites have the peculiar feature to display a negative Gaussian curvature[165]. The latter has been recently related to a suppression of thermal conductivity with a monotonic dependence on curvature[166]. From the electronic point of view, first-principles calculations predict that these structures can exhibit semimetal Dirac-like points, like the ones present in graphene[167]. In addition, schwarzites have also been predicted to present a net magnetic moment in their electronic ground state[168]. Yet, their synthesis remains elusive[21], and further theoretical and experimental investigations are needed to understand their applicability in modern technology.

[21] At present, the most convincing synthetic route is through zeolite templating[169].

6.4 The C/Si interface

In previous Section, we have thoroughly discussed the rich *plethora* of curved structures originating from graphene and the appearance of rippling, which makes it deviating from the idealized bi-dimensional arrangement. An additional example with uncountable experimental evidence comes from the field of supported and epitaxially grown graphene. Indeed, when graphene is supported or is grown on a substrate, interactions of different strengths at the interface may give rise to a curvature across the carbon lattice. The case of epitaxial graphene on silicon-carbide (SiC) deserves a rather special mention, not only in the context of curved carbon-based structures but also from a technological perspective[25, 170, 171].

SiC has sparked a great interest in the last few years because of the possibility of growing single (or few-layers) graphene by simple thermal annealing. The first investigation of the graphitization of SiC dates back to 1975, by Van Bommel *et. al.*[172], but, at that time, in a "pre-graphene era", it was not possible to recognize the capability of this system to give access to pure two-dimensional crystals, with the excellent physical properties of graphene. When SiC is annealed at high temperatures (around 1100°C), Si atoms desorbs from the Si-terminated (0001) surface, leaving a carbon-rich layer that undergoes surface reconstruction (the $(6\sqrt{3} \times 6\sqrt{3})R30°$[25, 170, 161, 173], see the box "Wood's Notation" 6.2 on pag. 80).

Box 6.2: Wood's Notation

The Wood's Notation is the most frequently used for defining the surface lattice vectors when the bulk and the surface unit cell have the same or closely-related symmetries. It involves specifying the surface lattice vectors $\boldsymbol{s}_1$ and $\boldsymbol{s}_2$, in terms of the bulk vectors $\boldsymbol{b}_1$ and $\boldsymbol{b}_2$, and the rotation angle of the surface unit cell w.r.t. the bulk unit cell. For instance, in the following structure

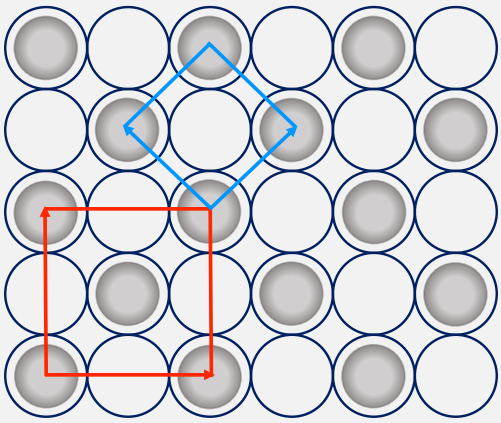

we can identify a non-primitive unit cell (red) where the surface lattice vectors are two times larger than the bulk ones, leading to a 2×2 structure in Wood's notation. Otherwise, we can specify a primitive unit cell (blue) $(\sqrt{2} \times \sqrt{2})R45°$, with the surface lattice vectors a factor of $\sqrt{2}$ larger than the bulk ones and the unit cell rotated by 45° *w.r.t.* the bulk unit cell.

The latter consists of a graphene layer - usually called the *buffer layer graphene (BLG)* - which is still bonded to the SiC substrate through strong C-Si covalent bonds. Further annealing at temperatures above 1350°C determines additional Si-atoms desorption at the C/Si interface that results in the decoupling of the BLG, which then becomes *quasi-freestanding monolayer graphene (QFMLG)* - the before-mentioned *epitaxial monolayer graphene (EMLG)* or simply called *monolayer graphene* - and the formation of another BLG

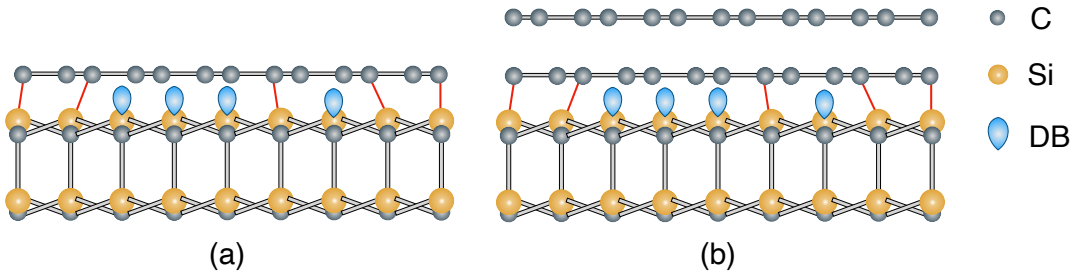

Figure 6.10. A pictorial representation of the C/Si interface: (a) Buffer layer graphene on top of SiC, where red segments are used to indicate the C-Si covalent bonds; (b) the full interface with both the buffer and the monolayer graphene.

reconstructed surface underneath [25, 174](see Figure 6.10). The outlined experimental procedure allows producing graphene samples of extremely high quality and could soon enable mass production of graphene, contrary to standard techniques such as mechanical exfoliation from HOPG or chemical derivation[25, 161]. As outlined in Chapter 1, large-scale production of graphene is already feasible on various metallic substrates by CVD but the metallic contact at the interface, in most cases, strongly influences the electronic structure of graphene, preventing the integration in electronic devices[175, 176, 177, 178, 179]. As a major drawback of CVD methods there is therefore the need to transfer graphene onto a different substrate. On SiC, in contrast, graphene is grown directly on top of a semiconducting material, namely SiC, making such a C/Si interface compatible with the modern Si wafers based electronic industry[180]. As we are going to discuss in the following, the buffer layer does not retain the typical band structure of graphene and hence it looses most of its peculiar transport properties[181, 182]. Similarly, although EMLG is to some extent already decoupled from the substrate, residual interactions at the interface remain - determining, for instance, an intrinsic n-doping which results in the shift of the graphene Dirac points downwards *w.r.t.* the Fermi level[25, 181, 182]. Therefore, for a concrete wide-spread application of the C/Si interface, the graphene layers needs to be completely decoupled from the underneath structure. In this respect, one possible strategy that has been widely documented in the literature is provided by the intercalation of hydrogen beneath the buffer layer. It was indeed shown that the H intercalation saturates the Si dangling bonds on the (0001) face, transforming the buffer itself into a quasi-free standing graphene[183, 184, 185, 186, 187] or the buffer plus the overhead monolayer into a bilayer graphene[188]. Although poorly documented in the literature, the passivation of the buffer layer, *e.g* by extensive hydrogenation[189, 183, 184], may play an equivalent role in decoupling just the monolayer graphene from the interface and transforming it into a truly free-standing graphene.

Besides the valuable technological implications, the C/Si interface finds its place in the panorama of corrugated or curved structures because both the buffer layer and the graphene layer are curved. In particular, the former is strongly corrugated because the C-lattice forms a *moiré pattern* (see the box "Moiré pattern" 6.3 on pag. 82). on the SiC(0001) (the aforementioned surface reconstruction) that displays C-Si interactions of rather different strengths at the various lattice positions. Such *moiré pattern* modulates also the morphology of the overhead graphene layer, which displays a wavy profile[173, 190]. Therefore, the C/Si interface can be undoubtedly added to the list of the "inhabitants" of the curved world, that we are describing in this Chapter, and stands out as a model system to study the impact of curvature on the chemical reactivity. Furthermore, as highlighted above, the investigation of the H sticking on the buffer layer (and the graphene layer, as we shall see later) is still less documented in the literature, despite the prospect of relevant technological applications in the context of graphene production.

In this Section, we provide the reader with a bird's eye view of the state-of-the-art of epitaxial graphene on SiC[22]. After a brief discussion about the extraordinary properties of SiC, which makes this material rather unique, we first recap the long debate in the literature about the structure of the surface reconstruction that leads to the BLG. Next, we briefly describe the growth process and the experimental techniques that allow controlling the number of layers. Then, we end this Section with a review of the main theoretical and experimental works about the passivation of the buffer layer and related techniques to decouple both the buffer and the graphene layer. It is worth noticing that, in the literature, the buffer layer is at times called *zero layer graphene (ZLG)* or *interface layer graphene (ILG)*. In the following, we will mostly use the term "buffer layer". As for the second (quasi-freestanding) graphene layer, we will use the term "monolayer graphene", as it is custom in the literature.

Box 6.3: Moiré pattern

According to the Encyclopedia Britannica[191], the definition of the *moiré pattern* is the geometrical design that results when a set of straight or curved lines are superimposed onto another set. Its etymology can be found in the French word *moire*, which is a type of textile with a rippled or "watered" appearance. A *moiré pattern* emerges because of an interference between two patterns that are not completely identical, but rather rotated, displaced or with slightly different pitch. Some examples are provided below:

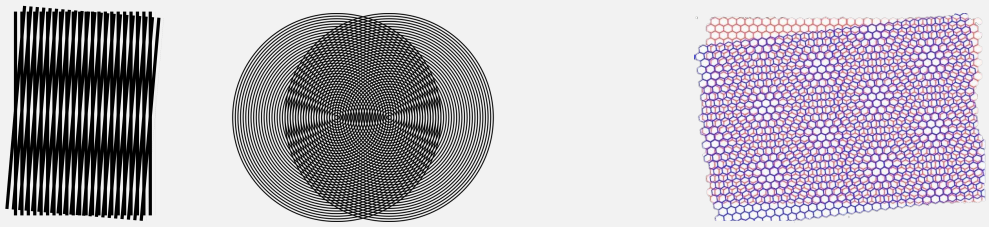

(a) (b) (c)

Picture (a) displays the *moiré pattern* arising from the superimposition of two set of parallel lines, with one set rotated by an angle of 5° *w.r.t.* other. Picture (b) displays the *moiré pattern* created by the overlapping of two sets of concentric circles. As a more relevant example, Picture (c) displays the *moiré pattern* that emerges in *twisted bilayer graphene*, a bilayer graphene with one layer rotated by a given angle *w.r.t.* the other layer. For the buffer layer graphene on SiC, the *moiré pattern* is a consequence of the lattice mismatch between SiC (with lattice parameter 3.07 Å) and graphene (with lattice parameter 2.46 Å)[161].

6.4.1 SiC: synthesis, properties and applications

The research into SiC has witnessed explosive growth during the past few decades thanks to its outstanding physical and chemical properties[192]. The wide band-gap, the high thermal and electrical conductivity under high-power/high-temperature/high-voltage, or the extraordinary chemical inertness are just some of these appealing properties which have opened the door for uncountable applications. There is vast modern literature on SiC and comprehensive analysis of the topic is clearly far beyond the scope of the present work. Here, we will limit to give an overview on the subject and refer the interested reader to the detailed book *Fundamentals of Silicon Carbide Technology* by T. Kimoto and J.A.

[22] see J. Hass et. al.(2008)[170], Riedl et. al(2010)[25] and N. Mishra et. al. (2016)[171] for three extensive reviews on the topic.

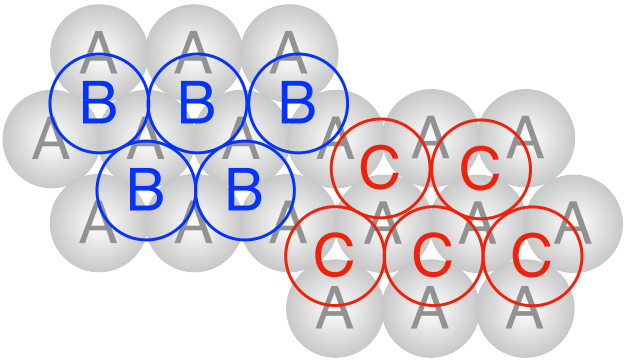

Figure 6.11. Possible occupation sites (A, B or C) in the hexagonal close-packed (hcp) system.

Cooper(2014)[193] or to the extensive reviews by M. Xu et. al.(2021)[192] and R. Wu et. al.(2015)[194].

SiC is a compound of silicon and carbon with a rigid 1:1 stoichiometry. In mineralogy, SiC is generally called *moissanite*, from Henri Moissan[23], who was the first to investigate this material as a mineral found in meteorites of Canyon Diablo[195], Arizona. Nevertheless, natural SiC is extremely rare in nature and, indeed, its discovery was reported later than its first synthesis. The latter dates back to 1892 by Acheson[196], who was able to produce powders of SiC from silica and carbon. The use of SiC powders produced by the *Acheson process* for cutting, grinding, and polishing was the first industrial application of SiC.

In the bulk structure of SiC, both Si and C are sp^3-hybridized, hence each Si atom is bonded to four C and *viceversa*. From the structural point of view, a unique feature of SiC is the so-called *polytypism*. Polytypism occurs when a material can adopt several crystal structures which vary only in the stacking sequences, without any changes in the chemical composition (Kimoto(2014)[193]). Different crystal structures or *polytypes* are the results of a different occupation of sites along the c-axis in a hexagonal close-packed (hcp) system. There are three sites, which are usually denoted as "A", "B" and "C", as shown in Figure 6.11. For any stacking sequence, two layers cannot successively occupy the same sites, *i.e.* "AA..", "BB..", etc. are not allowed. Despite the existence of an infinite number of possible stacking sequences, most materials are stable only in one type of stacking, which is usually the zincblende or the wurtzite structure. In contrast, for SiC there have been reported more than 200 different polytypes. To distinguish all of these structures, *Ramsdell's notation* is commonly employed, which labels each polytype with a code "nX", where n is the number of Si-C bilayer in the unit cell and X is the crystal system (C for cubic, H for hexagonal and R for rhombohedral). The most common polytypes for SiC are 3C-SiC (often called β-SiC), 4H-SiC, 6H-SiC, and 15R-SiC (which are generally all referred to as α-SiC). For instance, 4H-SiC is characterized by a hexagonal unit cell with four Si-C bilayers and the stacking sequence "ABCB..." (see Figure 6.12). 4H and 6H-SiC have become the most popular polytypes for SiC applications since S. Yoshida et. al.(1987)[197] showed the possibility of growing high-quality samples homoepitaxially by CVD at relatively low temperatures on off-axis substrates. 3C-SiC is also popular and can be grown heteroepitaxially on Si substrates.

In both surface science and crystallography, one generally needs to refer to specific directions or crystal planes. For hexagonal SiC polytypes, the latter are commonly ex-

[23]In 1906, Henry Moissan won the Nobel Prize in Chemistry for being the first to isolate fluorine.

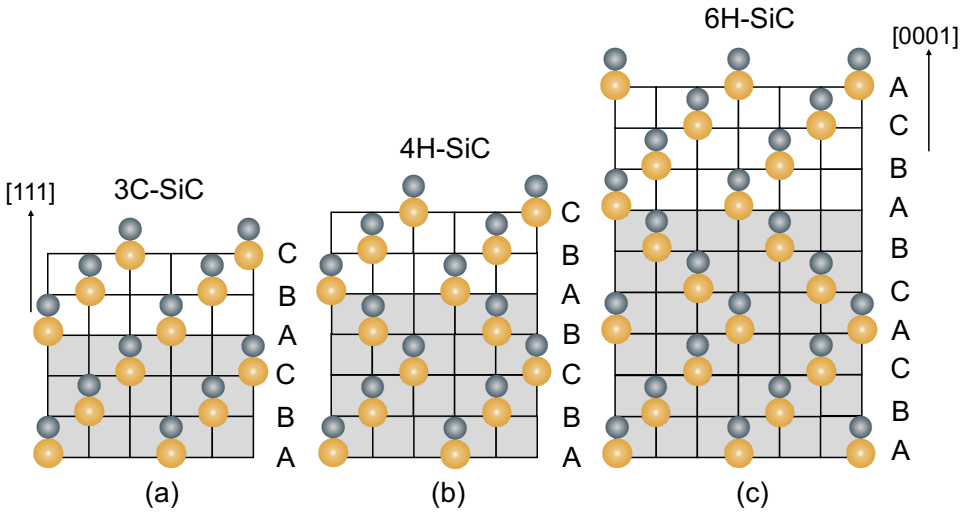

Figure 6.12. Schematic representation of the structure of the more common SiC polytytpes: (a) 3C-SiC, (b) 4H-SiC and (c) 6H-SiC. Gold and grey circles denotes Si and C atoms, respectively. The [111] for cubic and [0001] directions for hexagonal systems are also indicated.

pressed using four Miller-Bravais indices, $(h_1h_2h_3l_h)$. The equivalence between a crystal plane $(h_1h_2h_3l_h)$ and the three Miller indices (hkl) is given by the following relationships (Kimoto(2014)[193]):

$$h_1 = h \quad h_2 = k \quad h_3 = -(h+k) \quad l_h = l$$

Similarly, a crystal direction $[u_1u_2u_3w_h]$ is equivalent to a direction $[uvw]$ defined by three Miller indices when the following relationships are satisfied:

$$u_1 = (2u - v)/3 \quad u_2 = (2v - u)/3 \quad u_3 = -(u + v)/3 \quad w_h = w$$

Figure 6.13 displays a schematic illustration of the bonding pattern in hexagonal SiC, with the indication of the (0001) crystal-plane -also called "Si-face" - and $(000\bar{1})$ - also called "C-face" [24].

The first excellent properties of SiC that are worth mentioning are the mechanical ones, which are the direct consequence of its structure and the strong Si-C bond (4.6 eV vs 2.3 eV of a Si-Si bond[198]). SiC is one of the hardest known materials, with Young's modulus that reaches 700 GPa for the 6H polytype[25][193, 201].Furthermore, SiC retains its high hardness and elasticity even at very high temperatures. For instance, the yield strength, *i.e.* the tendency to fracture, is estimated to decrease from 21 GPa at room temperature to 0.3 GPa at 1000°C, while for Si the yield strength drops to 0.05 GPa already at 500°C[193]. Such intriguing mechanical properties are accompanied by a rather unique behavior at high temperatures. For example, SiC has been shown to melt incongruently at ambient pressure, *i.e.* with the Si fraction coming out as liquid and C remaining in the solid phase. Such decomposition starts at around 2600°C in the experiments[202]. Congruent melting has been also reported at high pressure (around 5-7 GPa) but some confusion persists in the literature about the nature of this phase transition[203].

Figure 6.14 shows the theoretical band structure of the 4H-SiC polytype from Ref.[204]

[24] In cubic polytypes, such as 3C-SiC, the (111) and $(1\bar{1}1)$ faces correspond to the Si and C face, respectively

[25] For comparison, Young's modulus of the diamond is 1050 GPa[199] while that of Si is just 160 GPa[200].

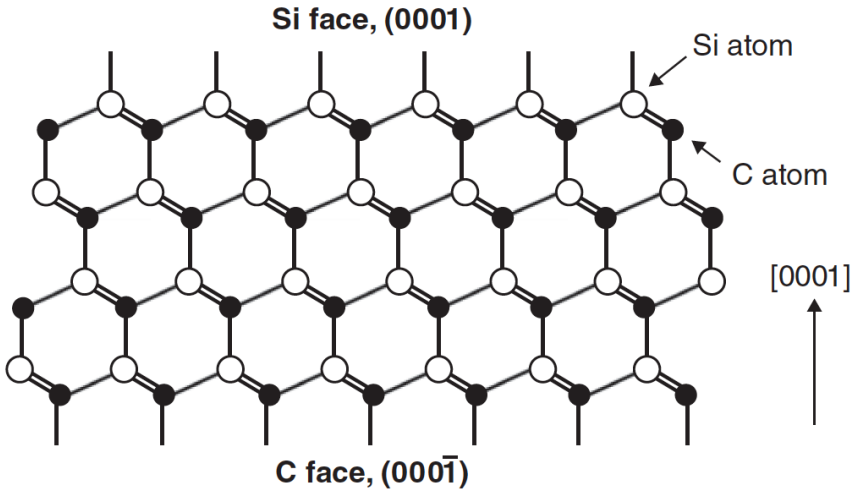

Figure 6.13. Schematic representation of the bond configuration in hexagonal SiC polytypes taken from Kimoto(2014)[193]. Si and C-face are indicated.

, as obtained with GGA-PBE calculations plus a GW correction. It is seen that SiC is a wide band-gap semiconductor with an *indirect band-structure*. The indirect band-gap ($\mathbf{\Gamma}$-$\boldsymbol{M}$) predicted theoretically by GW is 3.26 eV and agrees well with the experimental value, 3.29 eV. For the two other more common polytypes, 3C and 6H, the band-gap is smaller (2.36 and 3.02 eV respectively)[193]. The band-gap is known to decrease at increasing temperatures but the large value for SiC (compared to 1.12 eV for Si[205] or 1.4 for GaAs[206], for instance) makes it able to operate at high temperatures without suffering from intrinsic conduction effects. In addition, SiC has a breakdown electric field strength much larger than that of Si (2.4×10^6 MV/cm vs 0.2×10^6 MV/cm), meaning that it can withstand a large electric field or voltage gradient without suddenly becoming an electrical conductor[207]. Last but not least, SiC is characterized by a high thermal conductivity (4.9 W/cm·K for 4H-SiC[193, 208] vs 1.5 for Si[209]).

The excellent properties of SiC (the most relevant are summarized in Table 6.2) open the possibility for a great variety of applications. Some of them are already exploited in modern industry, others are still under scrutiny[192, 194]. For instance, SiC is already used as an abrasive or structural material, for high-performance brake disks in automobiles, as a fuel in steel production, as catalyst support, in membrane technology, medical implants (thanks to its biocompatibility), and, more recently, in electronic devices such as Schottky diodes[192, 194]. Nevertheless, further investigations are needed to "unlock" all the potentialities of SiC (*e.g.* the role of defects). Because of its superior quality to Si, SiC has especially attracted the attention of modern research into semiconductors and it is expected to play a game-changing role in the field of high-power/high-voltage/high-temperature devices. Finally, SiC may soon enable the large-scale production of graphene, which is indeed the main point of this Section.

6.4.2 The $(6\sqrt{3} \times 6\sqrt{3})R30°$ Surface Reconstruction

The buffer layer graphene is grown on the Si-terminated (0001) face[26] by thermal annealing of 4H or 6H-SiC(0001) samples, which are previously thermally etched with hydrogen to

[26]Growth of the buffer layer has been reported also on the C-terminated (000$\bar{1}$) face. In this case, the graphene formation starts at lower annealing temperatures and it is much faster than on the Si-terminated face, making more difficult the precise control of the number of layers grown.[171, 210]

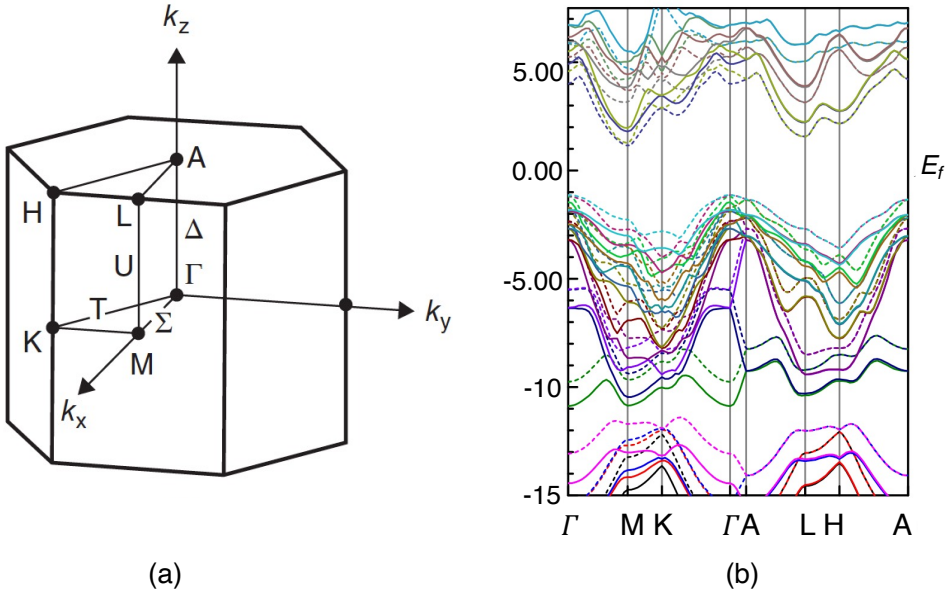

Figure 6.14. (a) Representation of the Brillouin zone of hexagonal SiC polytypes taken from Kimoto(2014)[193]; (b) Electronic band structure of 4H-SiC, obtained by GGA-PBE+GW correction from Ref.[204]

Table 6.2. Main mechanical, electrical and thermal properties of the two more popular SiC polytytpes (4H and 6H) compared to Si. Unless specified differently, all data are at room temperature.

	Property	4H-SiC (6H-SiC)	Si
Mechanical[193]	Density (g/cm^3)	3.21	2.33
	Young's modulus (GPa)	390 (690)	160
	Poisson's ratio	0.21	0.22
	Fracture strength (GPa)	21	7
Electrical	Bandgap[204] (eV)	3.26 (3.09)	1.12
	Breakdown electric field[193] (MV/cm)	$2.4 \cdot 10^6$	$0.2 \cdot 10^6$
	Electron mobility[192] (cm^2/(V·s))	1000 (400)	1400
	Intrinsic carrier concentration (at 300K (cm^{-3}))[192]	$5 \cdot 10^{-9}(1.6 \cdot 10^{-9})$	$1.0 \cdot 10^{10}$
	Saturated electron drift velocity (cm/sec)[192]	$2.0 \cdot 10^7$	$1.0 \cdot 10^7$
Thermal[193]	Thermal conductivity (W/(cm·K))	3.3 (4.9)	1.4-1.5
	Specific heat (J/(g·K)	0.69	0.7

remove any polishing damage[25]. This treatment allows obtaining atomically flat terraces where graphitization can occur. The thermal annealing can be then performed either in Ultra High Vacuum (UHV) conditions or under a controlled Ar atmosphere in a radio-frequency induction furnace[27][25, 171, 161, 212]. When UHV conditions are employed, the optimum preparation process can be divided into three main steps[161]:

(i) The sample is annealed at 850°C under Si flux, leading to the formation of a Si-rich 3×3 reconstruction;

(ii) Further annealing at around 950°C-1000°C leads to a $(\sqrt{3} \times \sqrt{3})R30°$ phase;

(iii) If the temperature is further increased to 1100-1150°C, the well-ordered $(6\sqrt{3} \times 6\sqrt{3})R30°$ phase is formed. Between 1100°C and 1200°C, $(\sqrt{3} \times \sqrt{3})R30°$ still coexists with the $(6\sqrt{3} \times 6\sqrt{3})R30°$ phase, until 1250°C is reached, where the smaller periodicity disappears.

One can directly go from step (i) to step (iii) by reaching directly the target temperature, without the formation of the intermediate $(\sqrt{3} \times \sqrt{3})R30°$ reconstruction. Heating is generally conducted by electron bombardment.

The controversial debate about the exact periodicity of the surface reconstruction has arisen from different interpretations of the LEED pattern and STM images. Indeed, the $(6\sqrt{3} \times 6\sqrt{3})R30°$ phase, which we call $6R3$ henceforth, actually comprises different periodicities, with the 6×6 and 5×5 the most commonly observed in the experiments[25]. These periodicities are a consequence of the relationships between graphene and SiC lattice constants, that can give rise to a large number of commensurate structures. Following J. Hass et. al.(2008)[170], if we define $\boldsymbol{a}_G, \boldsymbol{b}_G$ ($\boldsymbol{a}_{\mathrm{SiC}}, \boldsymbol{b}_{\mathrm{SiC}}$) the lattice vectors of graphene (SiC) , the commensurate phases can be calculated by setting:

$$|n'\boldsymbol{a}_{\mathrm{SiC}} + m'\boldsymbol{b}_{\mathrm{SiC}}| \approx |n\boldsymbol{a}_G + \boldsymbol{b}_G|$$

where n', m', n, m are integer numbers. In terms of the SiC unit vectors and employing Wood's notation, both $l \times l$ and $(l\sqrt{3} \times l\sqrt{3})R30°$surface reconstructions can give rise to commensurate structures, provided that

$$l = \begin{cases} \left\lfloor \frac{a_G}{a_{\mathrm{SiC}}} R_G \right\rfloor & (l \times l) \\ \\ \left\lfloor \frac{a_G}{a_{\mathrm{SiC}}\sqrt{3}} R_G \right\rfloor & (l\sqrt{3} \times l\sqrt{3})R30° \end{cases}$$

where $\lfloor ... \rfloor$ is the floor function, $a_G = 2.46\,\text{Å}$ ($a_{\mathrm{SiC}} = 3.08\,\text{Å}$) is the lattice constant of graphene (SiC) and $R_G = \sqrt{n^2 + m^2 - nm}$ is a dimensionless distance. The rotation angles of the graphene sheets w.r.t. to the SiC $n'\boldsymbol{a}_{\mathrm{SiC}}$ are given by[170]:

$$\theta(\mathrm{mod}\ 60°) = \begin{cases} \cos^{-1}\left(\frac{2m-n}{R_G}\right) & (l \times l) \\ \cos^{-1}\left(\frac{2m-n}{R_G}\right) - 30 & (l\sqrt{3} \times l\sqrt{3})R30° \end{cases}$$

[27]Historically, the thermal decomposition in UHV conditions was the first method employed for the fabrication of graphene on SiC[172]. Afterwards, in 2009, Emtsev et. al.[211] report the possibility of growing graphene on SiC also in Ar atmosphere. The use of Ar environment has shown to be better than UHV in producing graphene samples of high-quality morphology. Such improvement has been related to the slowing down of the Si evaporation process promoted by the reflection back to the surface of desorbed Si atoms after colliding with Ar atoms[171]. Later, other fabrication techniques have been proposed. Nowadays, one of the most used fabrication method is the annealing in the presence of an external Si-flux, in either UHV conditions or Ar atmosphere. In this Si-flux method, the quality of the graphene samples is determined by the control of Si vapour pressure using disilane gas.

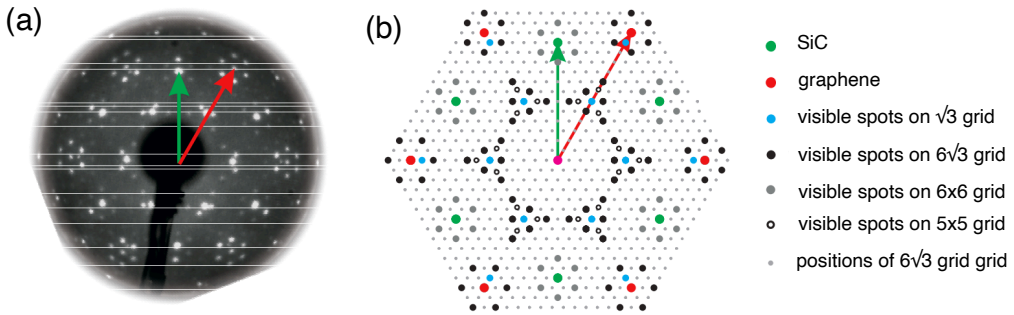

Figure 6.15. (a) LEED pattern of the $(6\sqrt{3}\times 6\sqrt{3})R30°$ reconstruction at 140 eV, with reciprocal unit vectors of SiC (green) and graphene (red); (b) Sketch of the different diffraction spots seen within the $6R3$ LEED pattern taken from Ref.[25], originating from four grids: 5×5, 6×6, $(3\sqrt{3}\times 3\sqrt{3})$-$R30°$, $(6\sqrt{3}\times 6\sqrt{3})R30°$.

Table 6.3. A short of list of commensurate graphene/SiC structures taken from Ref. [170]. The strain $\Delta l/l$ is defined as $(1-l)/l$.

Commensurate SiC unit cell	Graphene angle relative to SiC	$\Delta l/l$ (%)
$(6\sqrt{3}\times 6\sqrt{3})R30°$	30°	0.15
(quasi 6×6)		
9×9	$30°\pm 2.543°$	0.05
(quasi $3\sqrt{3}\times 3\sqrt{3}$)		
5×5	$\pm 16.10°$	-0.30
$(2\sqrt{3}\times 2\sqrt{3})R30°$	$\pm 6.59°$	0.44
(quasi 2×2)		

A LEED pattern and a sketch of the different diffraction spots taken from the review of C. Riedl et. al. (2010)[25] are displayed in Figure 6.15. On this LEED image, spots corresponding to the 5×5 periodicity are hardly visible. Indeed, as shown by Riedl. et. al.(2007)[161], the appearance of the 5×5 domains highly depends on the preparation process, with more intense spots appearing when an ex-situ prepared $(\sqrt{3}\times\sqrt{3})R30°$(R3) phase is annealed without Si deposition. Lately, the 5×5 periodicity has been rarely reported since it has become a common practice the use of Si-flux throughout the preparation procedure (see footnote 27 on pag. 87). Spots on the $\sqrt{3}$ grid are residual of the intermediate surface reconstruction and disappear as the annealing temperature is increased. On the other hand, the 6×6 periodicity has been the main source of misunderstanding[28], since a 6×6 corrugation is often imaged by STM[213, 214, 215, 216]. However, this periodicity has been proved to be pronounced only at high tunneling bias. When a low tunneling bias is used (around 0.2 eV) $6R3$ periodicity is resolved and a clear *moiré pattern* with irregular hexagons emerge[173]. Indeed, as shown in Figure 6.16, on the STM image two types of rings of different sizes can be identified. In addition, in the larger rings three protrusions - which are part of a diamond of four atoms - are visible[25, 161]. The latter are not repeated within the 6×6 periodicity, rather they are compatible with the $6R3$. The latter is thus the only structure that can account for both the LEED pattern and the STM images. For completeness, we report in Table 6.3 a short list of the commensurate graphene/SiC structures taken from Ref.[170].

[28] On the $6R3$ reconstruction there are some high-symmetry points, where a C atom of the buffer layer sits directly above an atom of the SiC or where an atom of the SiC lies below the center of an hexagon of the overhead buffer layer. These high-symmetry points are those that define a (quasi)-6x6 unit cell (see Fig. 6.16 (a))

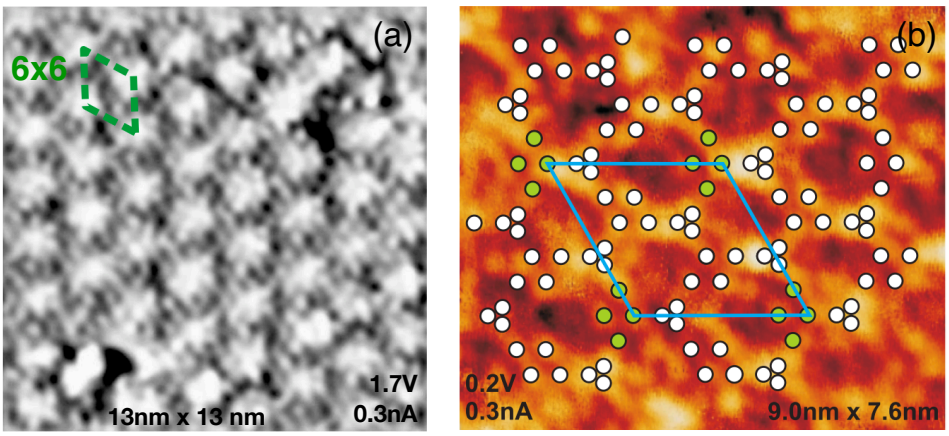

Figure 6.16. (a) Atomically resolved STM micrograph at $U_{\text{tip}} = 1.7$ V, showing the 6×6 unit cell taken from Ref.[161]; (b) Atomically resolved STM micrograph at $U_{\text{tip}} = 0.2$ eV, showing the $(6\sqrt{3} \times 6\sqrt{3})R30°$ periodicity taken from Ref. [25].

We should mention that some authors have suggested a different interpretation of the LEED pattern. For instance, in the original work of Von Bommel et. al.(1975)[172], the diffraction spots were assigned to a "pure" *moiré pattern*, *i.e.* formed by the SiC 1×1 unit cell and graphite (without any reconstruction). Indeed, the $6R3$ periodicity is the result of the lattice mismatch between graphene (2.46 Å) and SiC (3.08 Å). However, as indicated by the different intensities of the spots in the LEED pattern, the atoms on the $6R3$ surface are buckled, because of the different strengths of the C-Si bonds that we mentioned at the beginning. Furthermore, the band structure of the $6R3$ reconstruction - that we are going to discuss shortly - is incompatible with such interpretation.

From the theoretical standpoint, even though the formation of the $6R3$ phase has been confirmed, few works in the literature report the modeling of such periodicity. The main difficulties arise from the exceptionally large size of its unit cell. The latter has a 32 Å side length ($= (3.08 \times 6 \times \sqrt{3})$ with 3.08 Å the SiC 1×1 lattice parameter), resulting in 108 Si atoms and 108 C atoms per SiC bilayer and 338 atoms in a graphene layer (corresponding to a 13×13 graphene superlattice). For the 4H-SiC polytype, the total number of atoms in the cell amounts to 1310 (= 338 atoms of the graphene layer + [(108 Si atoms + 108 C atoms) $\times$ 4] atoms of the SiC substrate + 108 H atoms to saturate the danglings bonds on the C-face), thus posing a great obstacle from the computational point of view.

Having established the role of the $6R3$ periodicity, we shall comment on its electronic structure. As shown by ARPES measurements[25, 188] and theoretical band structure[181, 217] calculations, the buffer layer preserves the σ-band structure of graphene but the linear band crossing around the Fermi level typical of Dirac fermions is absent (see Figure 6.17 (a) and 6.18 (a)). This is consistent with the breaking of the π-network due to the formation of CSi bonds between the BLG and the SiC substrate. In particular, according to the area ratio between peaks of three-coordinated and four-coordinated (*i.e.* Si-bonded) C atoms in the Core-Level PhotoElectron Spectroscopy (CLPES) spectrum, around 30% of C atoms are bonded to SiC (see Figure 6.17)[25]. Lacking the π-band structure of graphene and being a precursor of the epitaxial monolayer, the term "zero-layer" graphene has then been often used to refer to the 63R phase[25, 188, 218, 219, 220].

6.4.3 Few-layers graphene on SiC

When the $6R3$ structure is annealed at $T > 1350$°C, true epitaxial graphene layers are formed on top of the surface reconstruction[174, 182], with the number of layers depending

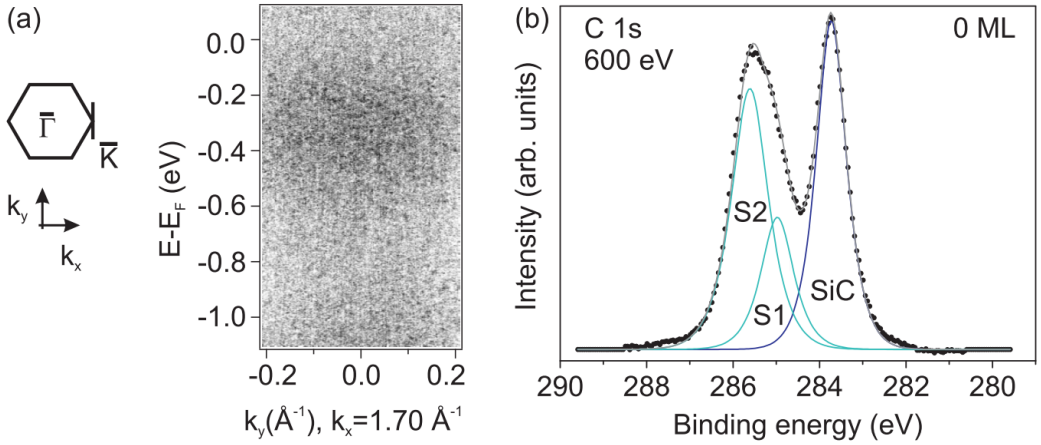

Figure 6.17. (a) Inverse grayscale plot of the band structure of the $(6\sqrt{3} \times 6\sqrt{3})R30°$ surface reconstruction near the **K** point obtained by an ARPES experiment perpendicular to the **ΓK**-direction taken from Ref. [188]; (b) C 1s spectrum of the $(6\sqrt{3} \times 6\sqrt{3})R30°$ surface reconstruction (incident photon energy of 600 eV) and its decomposition into different carbon components taken from Ref. [25]: the $S1$ peak result from four-coordinated carbons, *i.e.* carbons that are directly bonded to one Si atom of the underneath SiC, the $S2$ peak result from three-coordinated carbons of the buffer layer while the "SiC" peak refers to carbons of the SiC structure.

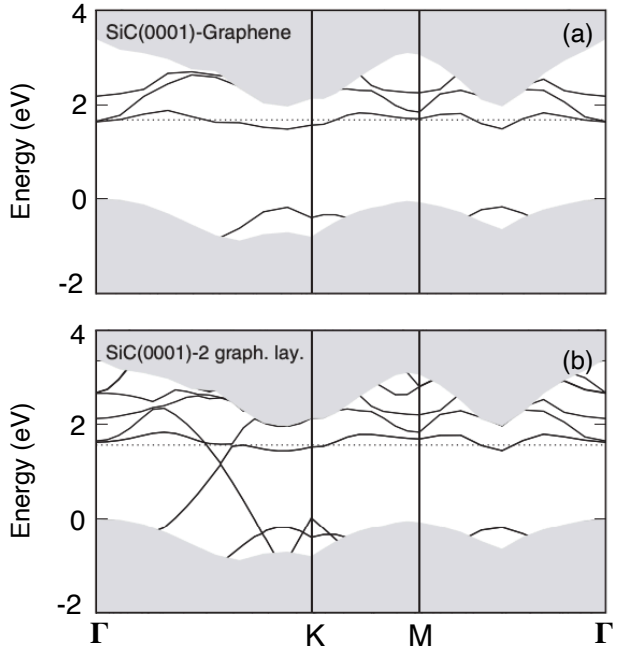

Figure 6.18. (a) Band structure of the buffer layer in the $(\sqrt{3} \times \sqrt{3})R30°$ surface reconstruction on SiC(0001) and (b) of the monolayer graphene as obtained by plane-wave DFT calculations, taken from Ref. [217].The shaded energy regions are the projected energy bands of SiC.

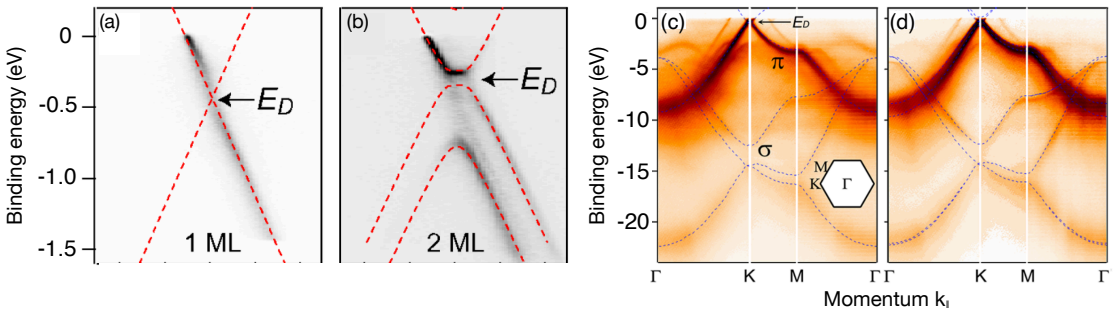

Figure 6.19. The π and $\pi^\star$ bands near the Fermi level for 1 (a) and 2 (b) graphene layers; Photoemission images of 1(c) and 2 (d) graphene layers along the symmetry direction **Γ**-***K***-***M***-**Γ**. The dashed lines are scaled DFT band structure of freestanding films. Both images are taken from Ref. [182].

on the annealing temperature[210, 221, 222]. Again, the experiment can be performed in a UHV chamber or Ar atmosphere. Interestingly, it was also demonstrated that the growth of the graphene layer can also be accomplished at a lower temperature (950°C) if additional carbon atoms are supplied like in molecular beam epitaxy[223]. Anyway, the formation of the graphene layers is mediated by the 63R reconstruction, regardless of the preparation procedure[174]. The covalent bonds between the buffer layer and the substrate break and the Si atoms at the interface desorb. Accordingly, the buffer layer is released and thus transformed into a true graphene layer. Simultaneously, the $6R3$ phase is reformed underneath, as it has been confirmed experimentally by CLPES spectra[25]. Since each graphene layer comprises 338 atoms, it is clear that three bulk SiC bilayers (108 C atoms times 3) are needed to form each graphene layer. Such a growth process, with the unaltered presence of the $6R3$ phase, forces the graphene layers above to be rotated by the same angle (30°) w.r.t. the SiC substrate. The stacking that is commonly observed experimentally is the Bernal stacking (ABAB...)[29]

One of the most compelling features of the C/Si interface is that it allows precise control and counting of the number of layers grown[25, 170]. ARPES and LEED are again suitable experimental techniques for this purpose. The first relies on the modification of the electronic band structure that occurs when the number of layers is increased. Indeed, in contrast to the buffer layer[226], the monolayer graphene displays the typical linear band crossing. Yet, the Dirac point (E_D) is not located at the Fermi energy, but it is shifted 420 meV downwards, leading to a strong n-doping ($n \approx 10^{13}\text{cm}^{-2}$)[25, 181, 226] (see Figure 6.18 (b) and 6.19 (a)), regardless of the preparation procedure or SiC polytype[25]. As shown by both experimental and theoretical simulations, a close inspection of the band structure reveals the presence of a band gap ($\approx$ 200 meV) with a midgap state (see Subsection 1.3.2) in the middle[181, 227]. This midgap state has been ascribed to the sublattice symmetry breaking determined by the interlayer coupling. When an additional layer forms on top of the graphene layer (*i.e.* bilayer graphene on SiC), two parabolic π-bands are observed in the ARPES measurements. The bands are still shifted by the n-doping, albeit less than in monolayer graphene ($E_D \approx -300$ meV). Still, a band gap of 100 meV is observed (see Figure 6.19)[25, 182, 222, 228]. By a straightforward counting of π-branches, ARPES can be then used to control the number of layers.

ARPES is an accurate techinque but, as it often happens in science, it is a complex experiment that is not always available. A convenient alternative is provided by the LEED

[29]The rhombohedral stacking (ABC...) is also common in graphene, being energetically close to the Bernal one (see for instance Ref. [224]). It characterizes about the 14% of all natural graphite (vs 80% for the Bernal and <6% for the least common hexagonal, AA, stacking)[225].

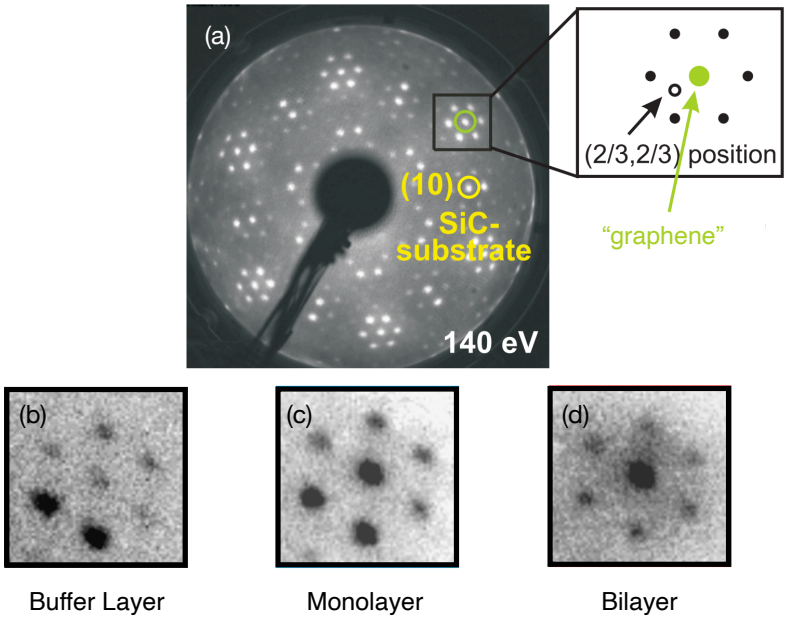

Figure 6.20. (a) LEED pattern from Ref. [25] of the $(6\sqrt{3} \times 6\sqrt{3})R30°$ surface reconstruction. In the inset, the graphene (10) spot is marked in green; (b), (c) and (d) the graphene (10) LEED spots for the different numbers of epitaxial graphene layers grown on 4H-SiC obtained at 126 eV.

experiment. Indeed, during the graphitization process, the LEED pattern undergoes visible variations[25, 161]. Figure 6.20 displays three LEED patterns at different annealing temperatures showing the (10) graphene spot with the surrounding spots of the $6R3$ phase. We note that for the buffer layer the graphene spot is weaker than its surrounding spots, for the monolayer they have approximately the same intensity, whereas for the bilayer the graphene spot is brighter than the surrounding spots. Thus, LEED can be used as a qualitative but practical, *in-situ* technique to distinguish, at least, from the buffer, the mono, or the bilayer graphene on SiC.

6.4.4 Hydrogen intercalation and adsorption

The buffer layer graphene does not have the same electronic properties as free-standing graphene because of the strong interactions with the SiC substrate. Therefore, it is electronically inactive. In addition, as previously discussed, the buffer layer also affects the electronic band structure of the overhead layer, which is n-doped. For a practical application, such an n-doping has then to be reversed. A possible approach is represented, for example, by the deposition of organic molecules with strong electron-acceptor groups, such as F4-TCNQ[229, 230]. However, this reverse doping does not change the nature of the interface layer.

In contrast, the use of molecular hydrogen has drawn great attention in the last few years because it allows the transformation of the inactive buffer layer into a true graphene layer[183, 184, 185, 186, 187, 188, 231, 232].

When the $6R3$ phase is exposed to H_2 (with a partial pressure of about 950 mbar) at 600°C, H atoms intercalate into the buffer/SiC interface and saturates the Si atoms in the uppermost SiC layer[30]. Accordingly, the buffer layer decouples from the interface and transforms into a quasi-free standing layer. Once decoupled, this layer shows the typical linear dispersing π-bands but the Fermi level is shifted below the Dirac point by about 100

[30] According to theoretical simulations, hydrogen cannot penetrate the buffer layer at 600°C. Therefore, it has been suggested that hydrogen penetration occurs through defects, such as vacancies, grain boundaries, or open-core screw dislocation[232]

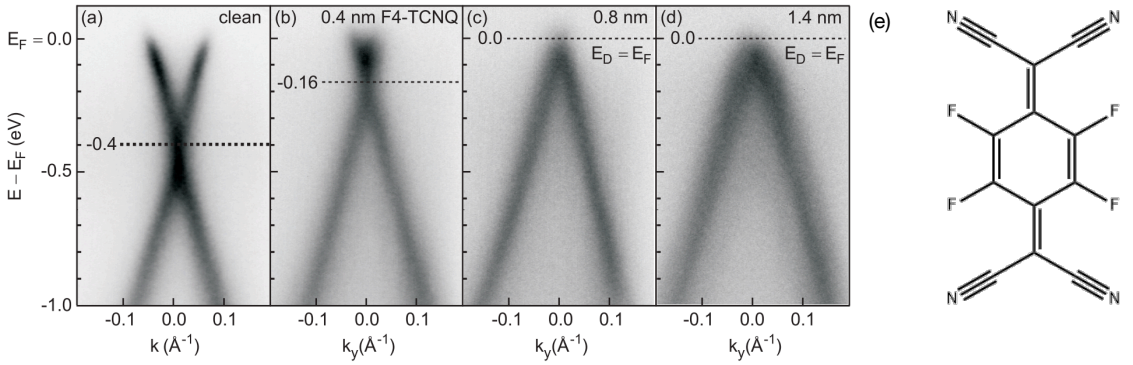

Figure 6.21. π-bands measured with ARPES at the $\boldsymbol{K}$ point for (a) monolayer graphene on SiC(0001), (b) after deposition of a partial F4-TCNQ film, (c) after saturation with F4-TCNQ molecules and (d) after further growth of a second layer of F4-TCNQ, taken from Ref. [229]; (e) molecular formula of F4-TCNQ.

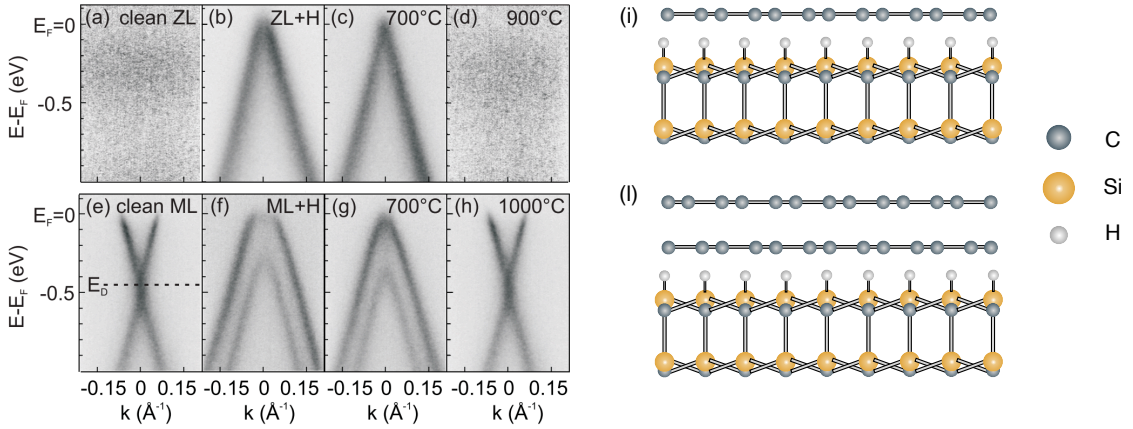

Figure 6.22. π-band dispersion measured with ARPES perpendicular to the **ΓK**-direction for (a) buffer layer (zero-layer, ZL) graphene, (b) after H intercalation, (c) after subsequent annealing to 700°C and (d) to 900° taken from Ref. [25]. π-band dispersion for (e) monolayer graphene (ML), (f) after H intercalation, (g) after annealing to 700°C and (d) to 1000°C. (i) Pictorial representation of the buffer layer graphene and (l) monolayer graphene after H treatment.

meV, resulting in a slight *p*-doping[188, 233]. To eliminate the *p*-doping, the sample has to be heated to 700°C, thus leading to the original band structure of graphene (see Figure 6.22). An additional advantage of hydrogen intercalation is its complete reversibility[25, 188]. Indeed, the heating of the sample at 900°C determines the breaking of Si-H bonds and progressive desorption of H atoms, which ultimately re-establish the buffer layer structure.

When the hydrogen treatment is applied to the monolayer graphene, bilayer graphene is formed as a consequence of the buffer layer decoupling[25, 188, 234]. Again, the π-bands show *p*-doping which can be removed by heating to 700°C. The structure with the inactive buffer layer and the graphene layer on top can be re-formed by increasing the temperature to 1000°C[25, 188].

While the hydrogen intercalation has been addressed by several experimental and theoretical works, the hydrogenation of the buffer layer has been poorly investigated in the literature. Furthermore, at present, modeling of the C/Si interface has been limited to systems with a reduced dimensionality - *i.e.* with surface reconstruction that differs from the experimental $6R3$ phase. Experimentally, at lower temperatures (< 750°C) hydrogen atoms have been shown to covalently bind to carbons of the buffer layer instead of intercalating[189]. Pioneering works in this field are those of F. C. Bocquet and coworkers[183, 184]. Ex-

posing buffer layer sample to hydrogen at room temperature and performing LEED and HREELS measurements as function of annealing temperature, they showed that H atoms bind to the buffer layer and are remarkably stable up to $\approx$ 750 K[183, 184]. These findings determines a narrow temperature window ($\approx$ 750-1100) for the preparation of quasi-free standing graphene on SiC by H intercalation, because the latter is expected to compete with H chemisorption on the buffer layer and H desorption from the intercalation site ($\gtrapprox$ 1100 K)[183, 184].

The H binding energies are expected to be considerably larger on the buffer layer than on free-standing graphene, because of the strong sp^2-sp^3 rehybridization induced by the surface reconstruction[184, 235]. For instance, a plane-wave DFT investigation with a $(4\sqrt{3} \times 4\sqrt{3})R30°$ reconstruction, with graphene uniformly stretched by about 1.4%, have provided H binding energies up to 3.5 eV[236]. Furthermore, experiments indicate that the buffer layer is drastically modified upon hydrogenation, as evidenced by the transformation of the $(6\sqrt{3} \times 6\sqrt{3})R30°$ LEED pattern into a quasi-(1×1)[184]. Yet, the esteem of H binding energies on the experimental 63R phase is still lacking in the literature.

Hydrogenation of hydrogen (deuterium) intercalated quasi-free standing graphene on SiC have also been addressed and its stability confirmed in vacuum up to 550 K[183]. The latter can be obtained in a two step procedure, as shown by F.C. Boquet at. al.[183]: first, the intercalation of deuterium below graphene at 950 K and, second, the hydrogen adsorption on graphene at 300 K. The observation of SiD oscillators confirms the nature of the intercalation used to obtain quasi-free-standing graphene on SiC, *i.e.*, the intercalated D is covalently bound to the silicon atoms of the SiC substrate. Likewise, the observation of CH oscillators proves the successful hydrogenation of quasi-free-standing graphene on SiC and is consistent with the observation of a drastically reduced DOS near the Fermi level[183].

As for the graphene layer hydrogenation, there is still little knowledge in the literature. As we mentioned earlier, the graphene layer is not flat over long-range, but its morphology is modulated by the underneath surface reconstruction. Goler et. al.[237] showed that when the graphene layer is exposed *in-situ* to atomic hydrogen, H atoms preferentially stick on the maximally convex areas of the C-lattice, forming ortho and para dimers and even tetramers. These C-H bonds have shown to be chemically stable up to 650°C. On the contrary, H atoms did not attach to locally concave parts of the surface. As discussed for rippled graphene, this preferential sticking combined with the known flexibility of graphene may be exploited in a future generation of hydrogen storage devices[237]. However, further studies are needed on this front. In particular, investigation of the graphene layer hydrogenation is still missing.

The curvature features of the C/Si interface combined with its incredibly technological value have motivated part of the present work. Chapter 8 and 9 are entirely dedicated to the C/Si interface. In these Chapters, the hydrogenation of the buffer and graphene layers on the experimentally observed $6R3$ reconstruction is addressed, thus bridging the gap in the current literature.

Chapter 7

Bending the rules of PAHs hydrogenation: the case of Coroannulene

The first curved system that we present and discuss is *coroannulene* ($C_{20}H_{10}$). In Section 6.2, we have introduced this molecule as one of the simplest structures among the family of curved aromatics, which results from the substitution of the inner 6-membered ring of coronene with a 5-membered ring. In this Chapter, we discuss in particular the result of a DFT investigation of the step-wise hydrogenation reaction of coroannulene ($C_{20}H_{10+n}$, with $n = 1-20$) . The work is parallel to that presented in Chapter 4 for coronene[92] and was motivated again by a collaboration with the experimental group of Prof. L. Hornæker from the Aarhus University. They exposed coroannulene films grown on a HOPG substrate to a beam of atomic hydrogen. Next, they carried out a temperature-programmed desorption experiment and monitored the desorption (super hydrogenated) products with a quadrupole mass spectrometer. The resulting mass distributions, shown in Figure 7.1, display the appearance of prominent peaks at specific mass-to-charge (m/z) ratios, indicating the accumulation of hydrogenated species more stable than others. A theoretical investigation of the step-wise hydrogenation of coroannulene was then conducted to identify such configurations and explain their particular stability. Moreover, through a direct comparison with coronene, the system is suited to the study of curvature effect on the H adsorption, thus fitting the main purpose of the present work. This Chapter is organized as follows: in Section 1, we briefly summarize the computational details of our calculations; in Section 2, we compare the first H addition in coronene and coroannulene; in Section 3, we discuss the main hydrogenation pathway leading to perhydrocoroannulene (fully superhydrogenated coroannulene); in Section 4, we discuss a proposed alternative pathway and in Section 5, we comment on some features of the thermal desorption spectra of coroannulene.

7.1 Method

The calculations were performed with the M06-2X[93] exchange-correlation[1] functional in the spin-unrestricted set-up, with the help of the Gaussian16 code[103]. The 6-311G(d,p) atom-centered basis set was adopted throughout and tight convergence criteria were set on both the electronic and the structural optimizations. Optimized structures were checked with harmonic frequency calculations. Binding energies for the addition of H atoms were

[1]This is the same hybrid-meta GGA functional employed for coronene and selected after the careful benchmark study on PAH chemistry discussed in Chapter 3.

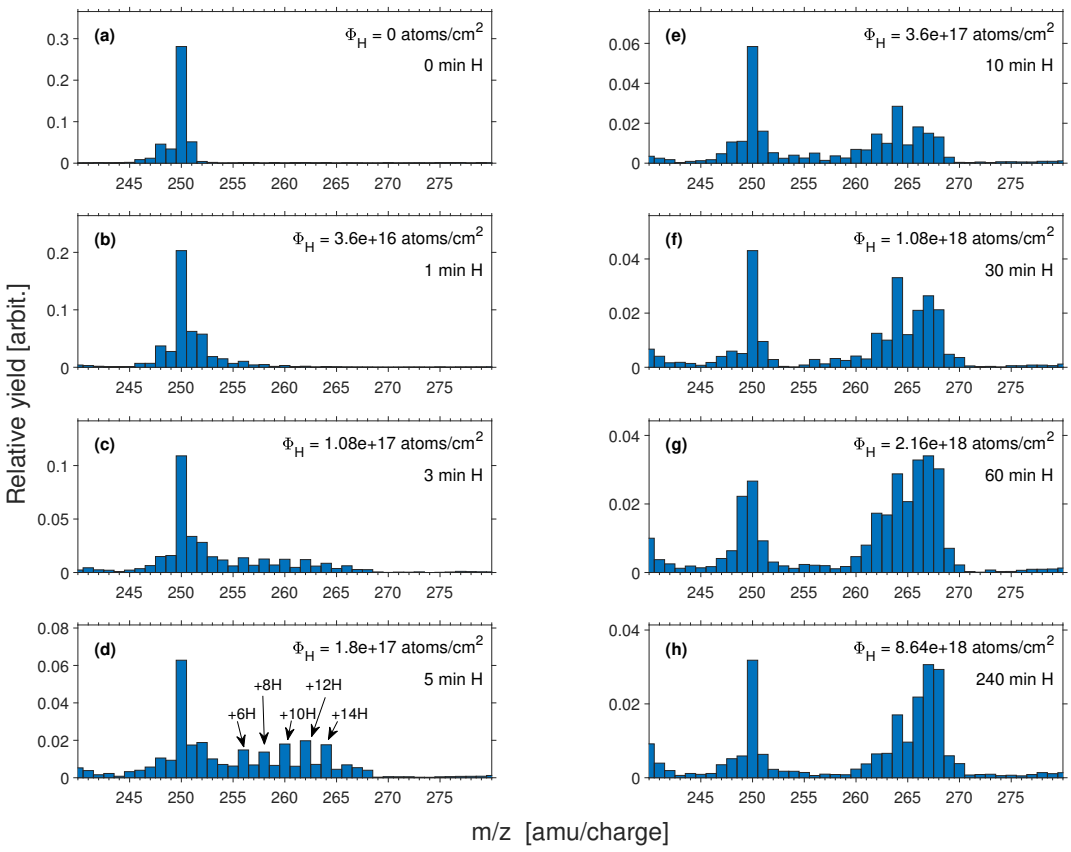

Figure 7.1. Mass distributions at different hydrogen exposure time. (Dr. R. Jaganathan and L. Hornæker, *private communication*).

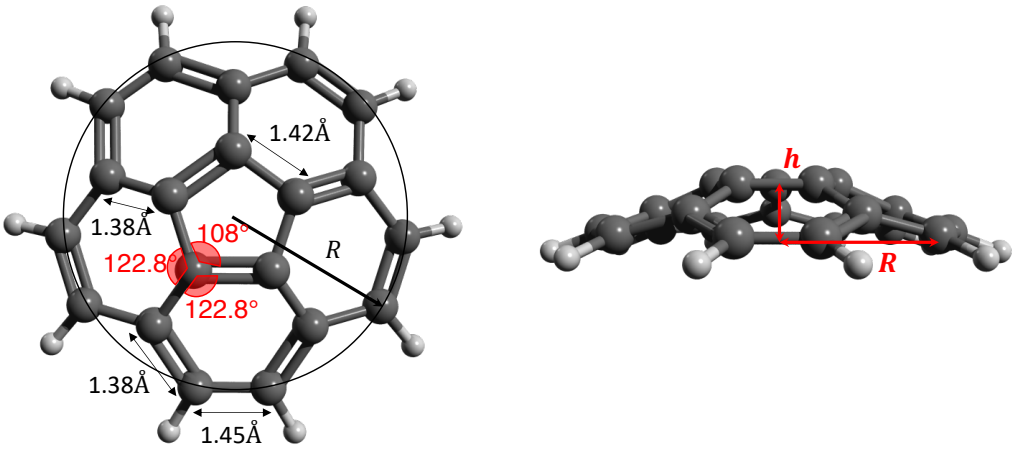

Figure 7.2. Main geometrical parameters of the coroannulene molecules.

computed for a number of sites i according to the following expression

$$D_i^{n+1} = E_\star^n + E_{\mathrm{H}} - E_i^{n+1} \tag{7.1}$$

where $E_\star^n$ is the DFT energy of the most stable isomer with n extra hydrogens, E_{H} is the energy of a hydrogen atom and E_i^{n+1} is the energy of the structure with an additional H at site i. Keeping the same notation introduced for coronene, a star ($\star$) is used to denote the most stable site, *i.e.* $D_\star^n \equiv \max_i\{D_i^n\}$. The plausible adsorption sites (typically 3-4 per step) were selected with the help of chemical intuition and at first guided by the rules established for coronene (see Subsection 4.3.1), even though, as we shall see later, the presence of curvature and the 5-membered ring introduces some striking differences. The hydrogenation sequence was continued by selecting at each step the structure with the largest binding energy[2]. Energy barriers were computed for the most relevant cases only, by performing a transition-state search and subsequent frequency analysis.

7.2 First H addition: coroannulene *vs.* coronene

We begin by briefly describing the geometrical structure of coroannulene. Coroannulene is a bowl-shaped molecule consisting of a central 5-membered ring surrounded by five fused 6-membered rings. Figure 7.2 summarizes the main geometrical parameters. As for coronene, all CC bonds in coroannulene display a bond length that is intermediate between a single CC (sp^2) (1.48 Å) and a double CC (1.34 Å) bond. On the edges, short (1.38 Å) and long (1.45 Å) bonds alternate. These bonds are slightly elongated with respect to those at the edges of coronene, displaying a bond-length alternation (BLA) of 0.07 Å (*vs.* 0.05 Å for coronene). Bonds of the 5-membered ring have a length of 1.42 Å. Bond angles at a central C are 122.8°, 122.8° and 108.0°, that is the *discrete Gaussian curvature* (the angular defect, see Section 6.2) at C in the 5-membered ring is 6.4° (about the average of K in C_{60} fullerene). The h/R ratio, where h is the height of the bowl and R its radius is ≈ 0.24[3] Overall, these geometrical parameters are in good agreement with available experimental and theoretical data[238].

Table 7.1 summarizes the results for the first hydrogenation of both coroannulene and

[2]Notice that, again, this does not guarantee that the structure is the lowest energy one for the given hydrogenation level, see footnote 3 on pag. 50.

[3]Here, h is calculated as the distance between the centroid of the 5-memebred ring (or equivalently any of the C atoms in the ring) and the plane containing the outer edge carbons. Then, R is calculated as the distance between the centroid projected on the plane and one of the outer edge site (see Figure 7.2).

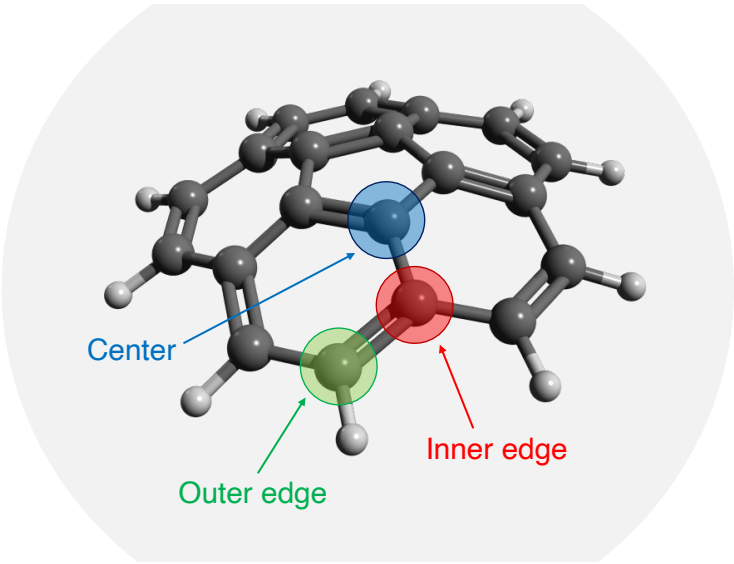

Figure 7.3. The three non-equivalent sites of coroannulene.

coronene. Both molecules are characterized by three non-equivalent sites: two-coordinated sites in the π-system ($Z = 2$) on the edge, three-coordinated ($Z = 3$) sites on the edge, and three-coordinated sites ($Z = 3$) in the inner ring, which we again refer to as outer edge, inner edge, and center sites, respectively (see Fig.7.3).

Table 7.1. Binding energies, D (eV), and sticking barriers, E_s (meV) for the hydrogenation on the three non-equivalent sites of coronene ($C_{24}H_{12}$) and coroannulene ($C_{20}H_{10}$). These values are zero-point energy corrected.

	$C_{24}H_{12}$		$C_{20}H_{10}$	
	D	E_b	D	E_b
Outer edge	1.11	235	1.37	180
Inner edge	0.37	446	0.76	296
Center	0.30	423	1.23	155

The 5-membered ring determines two important features of coroannulene:

(i) From the topological point of view, it breaks the bipartite nature which is instead a characteristic of coronene. In Section 2.1.1, we have seen that in bipartite lattice (like graphene or some PAHs) we can define the concept of π-*hyperconjugation*[52]. The highest is the π-hyperconjugation of a C in the lattice, the largest is its hydrogen affinity. Therefore, this concept can help identifying the most reactive site during an H addition[92]. In this case, π-hyperconjugation can no longer be invoked to explain the hydrogenation at specific lattice positions;

(ii) As discussed in Section 6.2, the presence of a 5-membered ring is a sufficient condition for the structure to bend, thus forming a bowl-shaped molecule.

From a chemical point of view, the presence of curvature determines at first the pyramidalization and rehybridization of C atoms. Table 7.2 reports the rehybridized "sp^2" hybrids and the pyramidalization angles, computed through Equations 6.1, 6.2 and 6.5. The curvature determines a substantial pyramidalization of carbon atoms of the inner ring, that displays $\theta_P \approx 8.36°$. Outer and inner edge sites, with θ_P respectively of 1.63° and 3.81°,

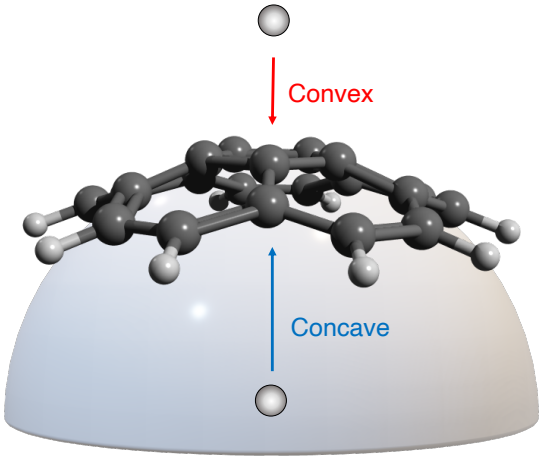

Figure 7.4. Representation of the hydrogen sticking on a center site on the convex and concave face of the molecule.

are instead less affected by the rehybridization. Center sites are found in a configuration that most closely resembles the sp^3 ($\theta_P = 19.5°$), therefore, from a geometrical perspective, they are expected to be more "prepared" to accept an incoming H. This should translate into higher binding energy and a reduced barrier to sticking.

Table 7.2. s-weights and corresponding hybridization (in brackets) of the σ-like orbitals, s-weight of the π-like orbital and pyramidalization angles θ_P at each of the three non-equivalent sites of coroannulene.

	σ-like			π-like	θ_P
Outer edge	0.31 ($sp^{2.26}$)	0.34 ($sp^{1.95}$)	0.35 ($sp^{1.84}$)	0.0016	1.63
Inner edge	0.21 ($sp^{3.71}$)	0.39 ($sp^{1.57}$)	0.39 ($sp^{1.57}$)	0.0088	3.81
Center	0.49 ($sp^{1.05}$)	0.24 ($sp^{3.24}$)	0.24 ($sp^{3.24}$)	0.041	8.36

Indeed, from a direct comparison of the H adsorption energetics on the two molecules (see Table 7.1), we note that center and outer edge sites of coroannulene display a comparable hydrogen affinity. In particular, the rehybridization increases the binding energy of center sites by 310% and reduces the barrier by 64% with respect to coronene. Planarity and bipartitism of coronene determine a strong edge localization of frontier orbitals, which translates into very large D and small E_b for H addition on outer edge sites ($Z = 2, \xi = 2$). Here, the curvature "breaks" in a sense such a strong edge localization, and, through pyramidalization, contributes to considerably increasing the reactivity of center sites. The undercoordination ($Z = 2$) typical of outer edge sites still determine a great reactivity of these lattice positions but it no longer represents a net driving force of the reaction. Noteworthy, the barrier to stick the H on the center site is smaller (by ≈ 25 meV) than on the outer edge, because the surface is to some extent already puckered around this lattice positions[4].

For the center hydrogenation, one may distinguish between a sticking from the convex

[4]Remind that the activation barrier for the H adsorption on graphene is mainly due to the puckering of the surface (see Section 1.3).

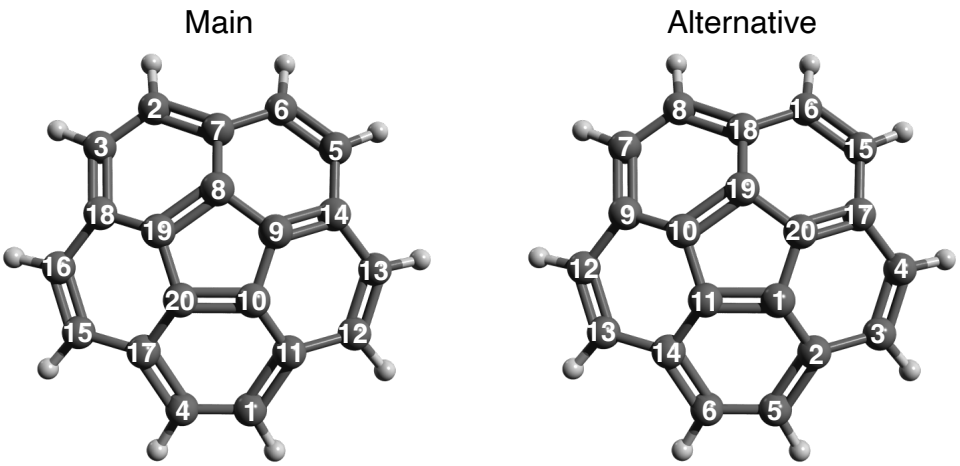

Figure 7.5. Main (Left) and Alternative (Right) hydrogenation sequence.

face (whose energetics is the one reported in Table 1) and from the concave face[5](see Figure 7.4). When considering the concave hydrogenation, an inversion of the molecule occurs during the optimization process. Such inversion restores the orientation with the H on the convex face. This is a consequence of the great flexibility of the coroannulene molecule, as indicated by its small bowl-to-bowl inversion barrier (≈ 442 meV at 209 K[239]).

7.3 Main hydrogenation pathway

The lowest energy addition pathway is displayed in Figure 7.5 (Left). We remind that this sequence is obtained by selecting at each hydrogenation step the structure i with the largest binding energy ($D^n_\star$). The energetics along this path is displayed in Figure 7.6, which reports the sequential H adsorption energy (D^n_i) as vertical bars. As we have discussed for coronene, even-numbered species are in a closed-shell (singlet) ground-state, while odd-numbered species are in an open-shell (double) ground-state. The energetics shows again an evident even-odd alternation, arising from the larger binding energies resulting from radical-radical reactions, *i.e.* those forming even-numbered $C_{20}H_{10+n}$ species. The amplitude of the oscillation is rather irregular in this case, but, on average, its value (≈ 1.8 eV) is smaller than that found for coronene (≈ 2.5 eV). This is indicative of a reduced π-bond strength[6] w.r.t. to the flat case, as expected by the reduced overlap between p orbitals induced upon bending.

The largest binding energies are found for coroannulene with a specific number of extra H, namely $D^n_\star = 3.63, 3.33, 3.38, 3, 28, 3.47, 3.75, 3.29$ and 3.37 eV for $n = 4, 6, 8, 10, 12, 14, 16$ and 18, respectively[7]. The stability of these species is further corroborated by the appearance of sizeable barriers to further sticking E_b (reported in Table 7.3), which are known to correlate well with D (*i.e.*, the larger the binding energy the smaller the barrier[240]).

The largest adsorption barrier (for the reaction $C_{20}H_{10+n} + H \rightarrow C_{20}H_{10+n+1}$) are

[5]The terms *concave* and *convex* may create some confusion in this context. When referring to surfaces of separation, convex or concave refers to the type of set enclosed by the surface itself considered as an *external* face. For instance, the external face of a sphere is a *convex face* because it encloses a topologically convex space region. With this definition, in a *convex (concave) hydrogenation* the hydrogen is stuck on the *convex (concave) face*, *i.e.* it approaches the coroannulene molecule from a region that is topologically *concave (convex).*

[6]As seen in coronene, the breaking of the π-bond is a step required only when forming odd-numbered species. Then, the even-odd alternation of binding energies can be considered as a rough measure of the π-bond strength, provided that each species is in its ground-state.

[7]For all the other species, $D^n_\star \leq 3.0$ eV.

Table 7.3. Energy barriers (meV) for forming the n-times coroannulene superhydrogenated species ($C_{20}H_{10+n}$) along the two pathways depicted in Figure 7.5 (N.D. = not determined).

n	Main sequence	Secondary sequence
1	180	155
3	49	161
5	152	120
7	23	175
9	155	155
11	0.0	41
13	80	112
15	199	207
17	0.0	0.0
19	125	49

found for $n = 4, 8, 12, 14, 18$, thus indicating a great stability for such hydrogenated species. Overall, these results are in good agreement with the thermal desorption spectra, but some differences between theory and experiment appear.

For instance, $n = 4$ is not found to accumulate in the mass traces, although, according to our findings, this should be a rather stable structure. The stability of $n = 4$ is, after all, supported by an electronic effect. In coroannulene, the maximal number of benzenic rings that one can draw with six delocalized π-electrons, a.k.a. *Clar's number*[241] (C), is 2. The set of six delocalized π-electrons that form a benzenic cycle is usually referred to as *Clar's sextet*. In bare coroannulene, one can realize up to 5 resonance structures with two Clar's sextets ($r_C = 5$), also called *Clar's structures*. (see Figure 7.8). As H atoms are attached to the molecule, the number of possibile resonance structures involving 2 Clar's sextets (that is, the maximal Clar's number) is progressively reduced. In particular, for $n = 4$, one can draw just two resonance structures preserving this maximal Clar's number. As soon as a 5th H is stuck on the molecule, regardless of its position, such a resonance is fully removed and one can draw just a single Clar's structure with two benzenic rings. Therefore, at least in the gas phase, $n = 4$ is expected to be a first "obstacle" to the full hydrogenation of coroannulene, as corroborated by the large barrier ($\approx 152\,\text{meV}$) resulting from our DFT calculations. The absence of a peak corresponding to this specie in the thermal desorption spectra may be due to interaction with the substrate, which may facilitate the addition of the next H atom[8].

For $n = 6$ and $n = 10$, the situation is somewhat reversed. These structures are found to accumulate during the experimental hydrogen exposure, even though the computed small or even vanishing adsorption barriers indicate a small kinetic impediment to the next H attachment.

In the region of high superhydrogenated structures, the mass distributions show prominent and persistent peaks at $n = 14, 16, 17$ and 18. The accumulation of $n = 14$ is in perfect agreement with our findings: $n = 14$ has both the largest $D^n_\star$ (3.74 eV) and E_b to further sticking (200 meV) along the entire pathway. Note, indeed, that, when 14 H atoms are attached to coroannulene, the molecule is left with one 6-membered aromatic ring, *i.e.* a stable structural motif that requires extra energy for next hydrogenation to occur.

The presence of a peak corresponding to $n = 17$ is undoubtedly the most singular feature of the thermal desorption spectra of coroannulene. Odd-numbered species should not accumulate during the hydrogen exposure because their hydrogenation is expected to

[8]In this respect, it is worth noticing that the exact orientation of the coroannulene molecule on the substrate is not known.

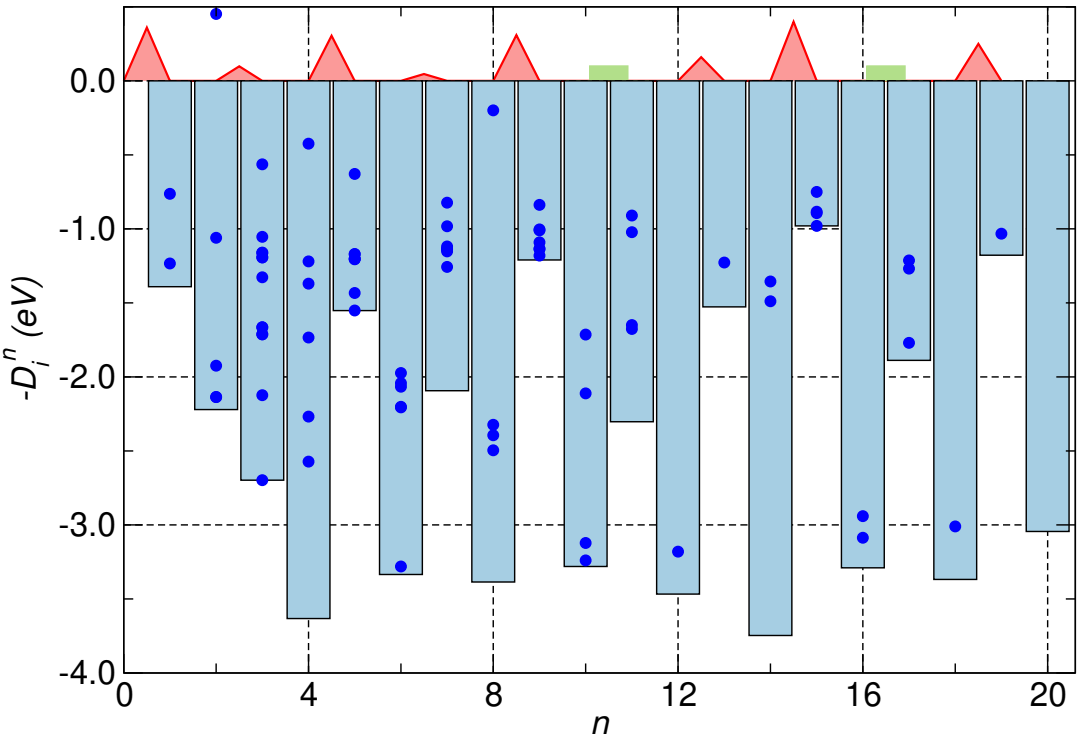

Figure 7.6. Energetics along the main hydrogenation pathway. Vertical bars indicates (minus) the binding energy of the nth hydrogen, grey triangles indicates the barrier of the $n \rightarrow n+1$ (meV, multiplied by 2), while black dots marks the binding energies of additional sites considered at each hydrogenation step. All values are zero-point energy corrected.

be barrier-less. In Section 7.5, we expand our discussion on this hydrogenation step and comment on additional calculations we have performed to understand the origin of this peak.

7.3.1 New rules for the hydrogenation?

For coronene, we were able to rationalize the hydrogenation sequence using very simple rules of thumb that should apply equally well to any other PAH. It is worthy to briefly recall these rules[92]:

(i) When *closed-shell* ($S = 0$) molecules are involved, the H attachment at specific lattice positions is dictated by the *π-coordination* and *π-hyperconjugation*. In particular, the H preferentially sticks to undercoordinated sites ($Z = 2$ or $Z = 1$ when available) in the π-system; when more than one undercoordinated site is available, the H preferentially sticks to the carbon with the highest π-hypercoodination number (ξ), *i.e.* with the highest number of next-to-nearest neighbors in the lattice with the same coordination to hybridize with;

(ii) When *open-shell* molecules are involved ($S = 1/2$), the reaction is driven by the position of the unpaired electron. The latter resides in a midgap state that semilocalizes from the defect position with a $1/r$ decay, thus making the *ortho* and *para* positions the most reactive towards the H sticking (again with a preference for sites with small π-coordination).

As mentioned earlier, the concept of π-hyperconjugation cannot be applied in this case because the π-network of coroannulene does not constitute a bipartite lattice. On

the other hand, looking at the hydrogenation sequence shown in Figure 7.5, we observe that π-coordination[9] and semilocalization of the unpaired electron are still good guiding principles of the hydrogenation reaction. The only step violating these rules is the 2nd hydrogenation, where the H attaches to a carbon that is distant from the 1st hydrogenated site (but still on the other sublattice), rather than preferring a closer *ortho* position. It is worth noticing that, consequently, the 3rd hydrogenation occurs on an undercoordinated site ($Z = 1$) with a relatively large binding energy for an odd addition. The latter, in conjunction with small binding energy for the 2nd addition, breaks initially the even-odd alternation.

One may wonder if a new rule involving pyramidalization or rehybridization can be established to rationalize the hydrogenation sequence of coroannulene. In general, there is no clear-cut correlation between the pyramidalization angle and the H binding energy. The reason is that, in a molecule, both the pyramidalization and the presence of edges contribute, to different extent, to increase the reactivity and their effects cannot be separated in a trivial way. Nevertheless, a close inspection of each hydrogenation level reveals that large pyramidalization angles (typically higher than 6°) in conjuction with small π-coordination determines larger hydrogen affinity. When comparing sites with same π-coordination and comparable pyramidalization ($\Delta\theta_P < 2{-}3°$), as it happens for outer edge and inner edge[10], the H addition occurs preferentially on outer edge sites. This is well illustrated, for instance, by the 5th or 9th step (see Figure 7.7). At the 5th hydrogenation, the most pyramidalized sites are central C atoms[11] which though have π-coordination $Z = 3$. Among inner edge, there are four sites with $Z = 2$, those close to the previously hydrogenated positions. Because of the smaller π-coordination, these sites display greater binding energies ($D = 1.43\,\text{eV}$) than inner edge with $Z = 3$ ($D = 0.63\,\text{eV}$). However, the pyramidalization of these sites is still limited ($\approx 4.2°$), and the reaction occurs on an outer edge site (as for the first H addition). Noteworthy, the H attaches to the most pyramidalized site among outer edge. On the other hand, at the 9th step, sites on the inner 5-membered ring with $Z = 2$ and $\theta_P > 6$ are available and the H sticks indeed on the C with the largest pyramidalization angle. Overall, the H attachment on specific lattice positions is thus determined by a delicate interplay between coordination and pyramidalization.

Besides, an additional concept that allows understanding the hydrogenation sequence is the aforementioned *Clar's number*. The maximal Clar's number (C) is the number of circles that one can draw with six delocalized electrons in a cycle of a resonance structure. For coroannulene, the maximal Clar's number is 2, while for coronene is 3. Looking at the hydrogenation sequence, we note that, up to the 8th step, the reaction proceeds in such a way that the maximal Clar's number is preserved (see Figure 7.8). The sticking of the 9th H atom, regardless of the position, determines the reduction of such a number from 2 to 1. Therefore, as indicated above for $n = 4$, also $n = 8$ should represent another "stop" on the road to perhydrocoroannulene, as indeed indicated by the large barrier to further sticking (155 meV). The validity of Clar's number in determining the reactivity of the coroannulene molecule underlines how the concept of aromaticity, which is originally defined for planar structures, can still play a crucial role also in curved systems.

[9]Strictly speaking, π-coordination is also a result of the bipartite nature, because it relies on (actually determines) the on-site energies of the renormalized lattice (see Subsection 2.1.1). However, in this context it is still useful to use π-coordination to generally refer to the number of "sp^2-neighbors (*i.e.* unsaturared) of a C in the lattice.

[10]Here, an outer edge site is intended as a site on the edge that binds two C atoms. Therefore, during the hydrogenation, an outer edge site remains so, regardless of the presence of hydrogenated nearest-neighbors. The same apply to inner edge sites.

[11]Note that, as for the first H addition, these sites are still characterized by relatively large binding energies, when compared to outer edge sites.

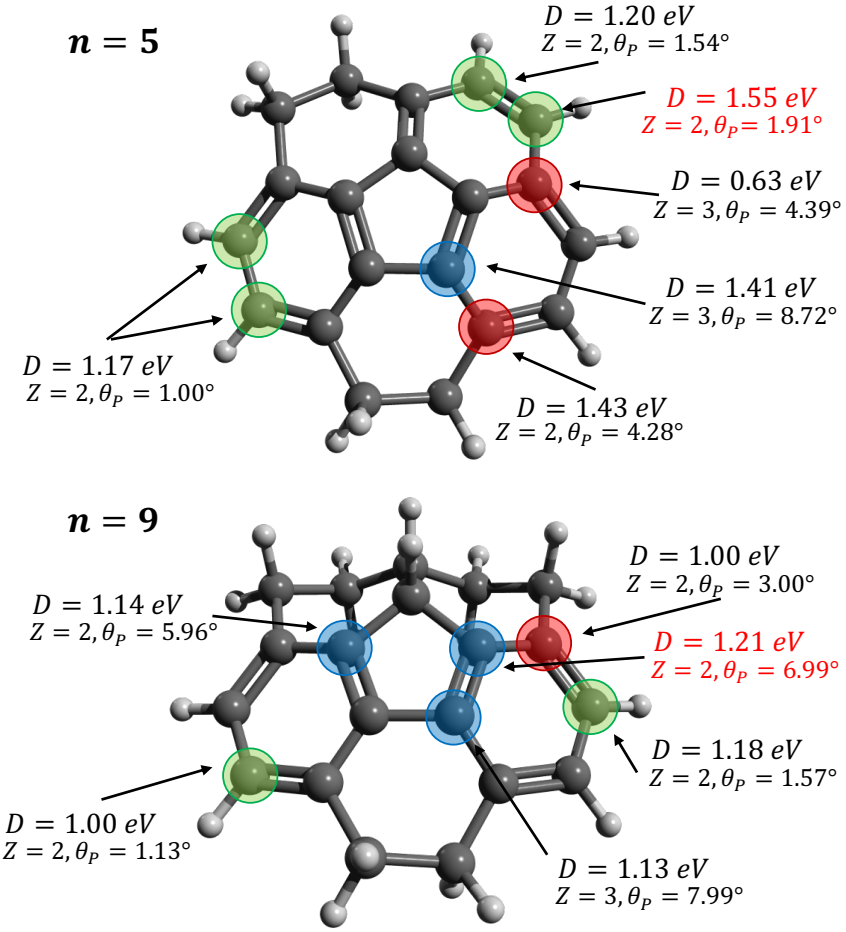

Figure 7.7. Binding energies for some sites that were checked at the 5th ($n = 5$) and 9th ($n = 9$) hydrogenation levels. For each site, the π-coordination (Z) and the pyramidalization angle θ_P is reported. Green, red and blue circle mark outer edge, inner edge and center sites, respectively.

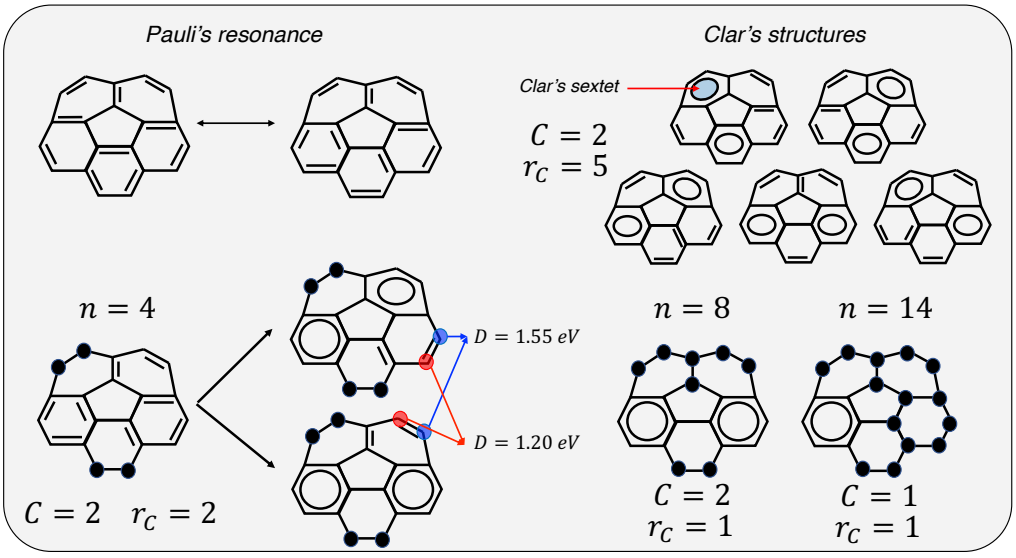

Figure 7.8. Pictorial representation of coroannulene Clar's structures. C is the maximal Clar's number, r_C is the number of resonance structures with the maximal Clar's number that one can draw.

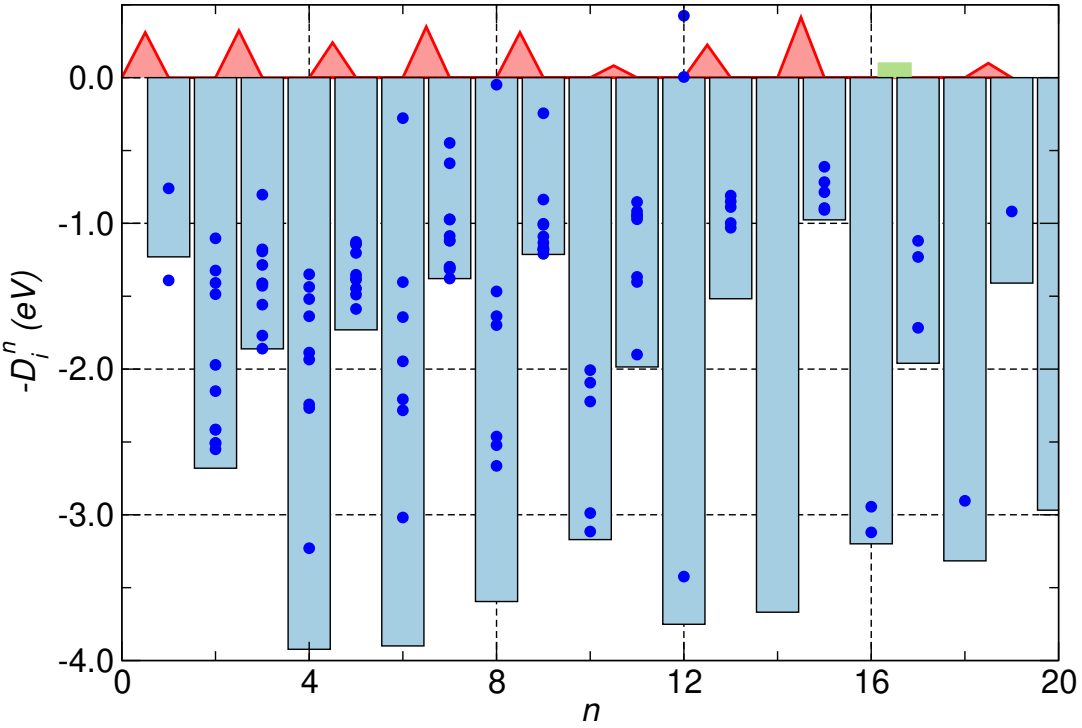

Figure 7.9. Energetics along the alternative hydrogenation pathway. Vertical bars indicates (minus) the binding energy of the nth hydrogen, grey triangles indicates the barrier of the $n \to n+1$ (meV, multiplied by 2), while black dots marks the binding energies of additional sites considered at each hydrogenation step. All values are zero-point energy corrected.

7.4 An alternative path to perhydrocoroannulene

Figure 7.6 also shows the binding energies of less stable hydrogenated configurations (blu dots). Again, some of these values are close to $D_\star^n$, thereby suggesting the possibility of branching points also in the hydrogenation sequence of coroannulene. However, in considering an alternative pathway, we have decided to start from the very first step, guided by the fact the hydrogenation on the center site has the smallest barrier height. The resulting sequence is shown in Figure 7.5, while the corresponding energetics along this path is displayed in Figure 7.9. Overall, the results are parallel to those for the main pathway. The most relevant difference is that a sizeable barrier is detected for the hydrogenation of $n = 6$, indicating great stability of this structure, in better agreement with the experimental result. By the same token, in contrast to the main path, a barrier is found to hydrogenate $n = 10$, though still small (41 meV). However, a remarkably smaller barrier (49 meV *vs.* 125 meV) is found to hydrogenate $n = 18$, at odds with the experimental data that show the accumulation of this structure. Noteworthy, $n = 4$ is again a very stable structure, while $n = 17$ is not.

7.5 Build-up of $n = 16, 17, 18$

A remarkable feature of the thermal desorption spectra shown in Figure 7.1 is the accumulation of the species $n = 16, 17, 18$, together with the absence of a strong peak for the fully hydrogenated molecule ($n = 20$), contrary to what observed for coronene. While the large binding energy and a large barrier to further sticking confirm the stability of $n = 18$, the energetics of both the main and the alternative pathway cannot account for the peaks $n = 16$ and 17. The lower stability of $n = 20$ w.r.t. $n = 18$ and the large barrier to add the 19th H atom may instead partly prevent the formation of perhydrocoroannulene. Notice,

Table 7.4. Energies (ΔE, eV) and barriers (E_{ab}, meV) for the abstraction reaction ($C_{20}H_{10+n}$ + H $\rightarrow$ $C_{20}H_{10+n-1}$ + H_2) and (minus) binding energies ($D^n_\star$, eV) and barriers (E_b, meV) for the H addition ($C_{20}H_{10+n}$ + H $\rightarrow$ $C_{20}H_{10+n+1}$).

n	+H $\rightarrow$ $(n-1)$ + H_2		+H $\rightarrow$ $(n+1)$	
	ΔE	E_{ab}	$-D^n_\star$	E_b
16	-1.08	161	-1.89	0.0
17	-2.48	0.0	-3.37	0.0
18	-1.00	120	-1.18	125
19	-3.20	0.0	-3.04	0.0

indeed, that coronene does not show any barrier for the H addition at high hydrogenated degrees (see Chapter 4).

The case $n = 17$ is undoubtedly the most singular in the mass distributions since odd-numbered species are unstable against further hydrogenation and should not accumulate. In an attempt to understand the presence of such a peak, we have then investigated other mechanisms that may lead to the formation of the 17th hydrogenated structure. However, it is worth saying at the outset that none of them provided an unquestionable and satisfactory explanation of this peak. In the following, we discuss them in detail.

The first alternative reaction that one may invoke is the abstraction through the *Eley-Rideal* mechanism, which we have discussed in the context of graphene in Subsection 1.3.3. In general, the H sticking and the Eley-Rideal reaction competes with each other on a graphitic surface, but this could not be the case on a small PAH. If energetically easier, the abstraction on $n = 19$, $n = 18$ and $n = 17$ (*e.g.* $C_{20}H_{18}$ + H $\rightarrow$ $C_{20}H_{17}$ + H_2) may indeed explain the build-up of $n = 16, 17, 18$. Table 7.4 reports the computed abstraction energies and barrier (together with the sticking barriers) for the relevant steps (on the main pathway). Overall, the emerging picture is that of abstraction and H addition competing with each other as in graphene since the abstraction barrier matches (or differs by a few meV) the sticking barrier. The only noticeable exception is for $n = 16$, where the abstraction has a sizeable barrier while the further hydrogenation is barrier-less. This, in conjunction with the slightly larger ΔE than $-D_\star$ for n=19, may partially explain the accumulation of the species in the range $n = 16-18$.

Another mechanism we considered is the formation of $n = 17$ through the addition of a H_2 molecule to $n = 15$. Indeed, the sum of the binding energies for $n = 16$ and $n = 17$ is 5.2 eV, that is it exceeds by 0.7 eV the bond dissociation energy of H_2 (≈ 4.5 eV). The feasibility of this process has been confirmed by DFT calculations. Placing an H_2 molecule in the vicinity of an unsaturated bond, the HH bond dissociates and the structure $n = 17$ is formed. Nevertheless, looking at the energetics profile displayed in Figure 7.6, the same argument may be applied to other odd-numbered species. For instance, the sum of $D^{10}_\star$ and $D^{11}_\star$ gives 5.6 eV, thereby suggesting the possibility for the specie $n = 9$ to bind a H_2. Therefore, if the above arguments were employed to account for the stability of $n = 17$, one should equally expect intense peaks for other odd-numbered species, such as $n = 11$.

Another process that may explain the formation of $n = 17$ is the desorption of a H_2 from $n = 19$. In this case, in removing two H atoms, one should consider different dimer configurations, since there is no guarantee that the backward pathway, going from the perhydrogenated to the bare molecule, follows the same steps of the onward. The total number of H dimers that we can remove from a 19-fold hydrogenated structure is evidently too big and out of reach to be tested. Indeed, the first H can be removed from 19 different positions, while the second from 18, leading to $19 \cdot 18 = 324$ possible configurations, a

number that cannot be reduced by any symmetrical argument since the molecule has lost every symmetry after the addition of 19 H atoms. We have then restricted our attention to just a few configurations. Following chemical intuition, we have considered four *ortho* dimers, classified on the basis of the type of binding C atoms (*e.g. o-o* means that the two H atoms desorb from two ortho outer edge sites.). In addition, for the sake of comparison, we also considered a *para* dimer and a configuration in which the two H atoms desorb from two distant sites. The energy to desorb the dimer in a given configuration i (ΔE^i) were computed according to

$$\Delta E^i = (E^i_{n=17} + E_{H_2}) - E_{n=19}$$

where $E^i_{n=17}$ is the DFT energy of the structure with $n = 17$ after the desorption of the H_2 in the dimer configuration i, $E_{n=19}$ is the energy of the structure with $n = 19$ and E_{H_2} is the energy of the H_2 molecule. The results are listed in Table 7.5.

Table 7.5. Desorption energies (ΔE, eV) for different dimer configuration: *i-c* (inner-center), *o-o* (outer edge-outer edge), *i-o* (inner-outer edge), *c-c* (center-center) and *para*.

Configuration	ΔE
i-c	0.17
o-o	4.01
i-o	1.00
c-c	0.93
para	0.29

The lowest reaction energy is found for the $i-c$ dimer configuration, whose desorption leads to the structure $n = 17$ that forms during the onward hydrogenation pathway. However, we note that the reaction is endoergic for any configuration considered[12], thereby indicating that the desorption of H_2 from $n = 19$ is not an energetically convenient road to $n = 17$.

Other mechanisms may be taken into account to explain the abundance of $n = 17$, such as a fragmentation of higher hydrogenated species or structural rearrangements, which are however hardly captured by a DFT structural optimization. The substrate, that is the HOPG, may too play a relevant role in this case, by stabilizing the allyl radical that characterize $n = 17$. Further experimental and theoretical investigations are then required to shed light on these still unclear aspects of the coroannulene superhydrogenation.

7.6 Summary and concluding remarks

In this Chapter, we have discussed two possible pathways from bare to superhydrogenated coroannulene. It may be worth keeping in mind that, in the experiment, it is rather unlikely that each coroannulene molecule follows the same hydrogenation pathway. Our analysis has revealed that several alternative paths are feasible, as indicated by some values of the binding energies to secondary sites along both pathways. It is the sum of all of these possible ramifications to give rise to the mass traces captured by the experiment. The theoretical investigation of *all* of these pathways is clearly out of reach for DFT calculations. The main and alternative paths discussed here are merely the photograph of two of these, even though they are expected to have the largest statistical weight. Overall, our results compare well with the experimental data, but some noticeable differences appear. The

[12]The reaction energy for the removal of two H from distant sites is not reported because such removal led to a rearranged structure with the breaking of a CC bond and the opening of a decagonal ring (which is anyway less stable than $n = 17$ of the forward pathway.)

most striking ones are the absence of a peak at $n = 4$, together with the presence of an intense peak at $n = 17$, which seems to prevent the formation of perhydrocoroannulene. There are convincing theoretical arguments that support the (in)stability of the species ($n = 17$) $n = 4$, at least in the *gas phase*, in contrast with the experimental observation. Therefore, we deem the absence/accumulation of these species in the mixture to be due to the specific experimental setting, *e.g.* an interaction with the HOPG substrate or fragmentation patterns that exist under laboratory conditions, rather than being due to specific features of the gas-phase hydrogenated species. There is also the possibility that different hydrogenated coroannulene molecules interact with each other on the substrate. The coverage conditions could support this possibility.

Chapter 8

The C/Si interface: H adsorption energetics

Throughout this work, we have repeatedly emphasized the unique properties of graphene which have attracted the interest of both experimentalists and theoreticians. In the same way, we have also marked some of its limitations that have hindered the widespread diffusion of this material, together with some aspects that still need to be fully understood. The C/Si interface introduced in Chapter 6 finds a key place in this context. From a more applied perspective, it may allow a practical and large-scale production of high-quality graphene samples, thus solving the issues of currently available fabrication techniques. From a fundamental point of view, the C/Si interface lends itself to the study of the curvature effects on the chemical reactivity of graphene, which is still a hot topic in modern graphene literature.

We have ended Section 6.4 by pointing out some lacks in the current research about the C/Si interface. In particular, we have highlighted that the modeling of the interface in the experimental surface reconstruction ($6R3$) and the theoretical investigation of the buffer and monolayer hydrogenation are still missing in the literature, despite their fundamental and technological interest, supported by existing experimental evidences provided by the works of F.C. Bocquet and coworkers[183, 184].

The present Chapter aims to fill such a gap, by showing a DFT investigation of the H adsorption on the C/Si interface. In particular, the latter has been modeled in the experimental $6R3$ reconstruction, in order to take into account the long-range features of the interface - *i.e.* its curvature - on the H adsorption energetics.

The Chapter is organized as follows: Section 1 describes the methods and the computational setup employed in our calculations; Section 2 presents our results on the structure of the buffer layer and its hydrogenation; Section 3 addresses the H adsorption on the monolayer graphene. In this chapter, we keep using the nomenclature introduced in Chapter 6: the first graphene layer, which is still bonded to SiC, is called "buffer layer" while the second layer on top is referred to as "monolayer".

8.1 Methods

The calculations were performed within density functional theory as implemented in the SIESTA package. The method is based on the self-consistent Kohn-Sham approach, using standard norm-conserving pseudopotentials and linear combinations of atomic orbitals as a basis set, thus allowing fast and very accurate simulations of systems with a relatively high number of atoms. The details of the SIESTA method will not be covered here; the interested reader is referred to the reviews by its developers (Soler et. al.(2002)[28] and Garcia et. al.(2020)[242]. In our calculations, the exchange and correlations were treated

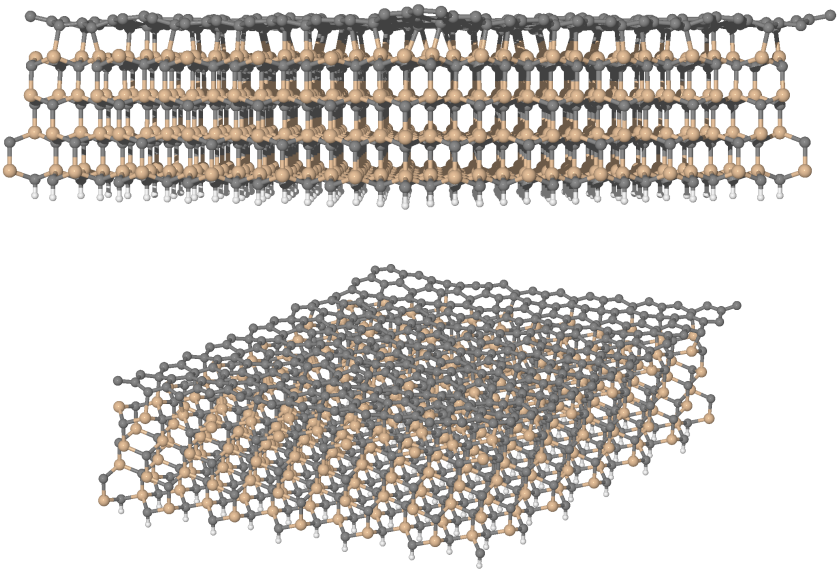

Figure 8.1. Unit cell of a minimal structure consisting of four SiC bilayers and a buffer layer graphene. The bottom C termination of SiC are saturated by H atoms.

within the *generalized gradient approximation* (GGA), employing the popular PBE xc-functional[243] which is a good compromise between accuracy and computational cost. Additional calculations with a Van der Waals inclusive functional, the Vydrov and Van Voorhis (VV)[244], were also performed for the monolayer graphene. In both cases, a double-ζ plus polarization (DZP) basis set was used. The unit cell for the modeled $6R3$ reconstruction consists of four SiC bilayers (864 atoms), with the bottom C terminations saturated by H atoms (108 atoms), plus a buffer layer graphene (338 atoms). The total number of atoms in the unit cell amounts to 1310, rising to 1648 when a second (monolayer) graphene is added on top. The internal geometry relaxation was performed with the *conjugate gradients* algorithm while keeping fixed the unit cell (optimized lattice constant $a = 32.6\,\text{Å}$) until tight-convergence criteria were met (max force tolerance 0.01 eV/Å). Thanks to the large size of the system, only the $\mathbf{\Gamma}$ point was sampled in the reciprocal space.

8.2 Buffer layer graphene

We begin by discussing a minimal structure consisting of just the SiC plus the buffer layer graphene in the experimental surface reconstruction. We remind that the latter is the $(6\sqrt{3}\times 6\sqrt{3})R30°$[1], meaning that the lattice vectors defining the graphene superlattice are $6\sqrt{3}$ times larger than the SiC bulk lattice vectors and rotated by 30° w.r.t. them. The relaxed unit cell is displayed in Figure 8.1. During the structural optimization, just the buffer layer and the first (uppermost) SiC bilayer were let free to relax.

8.2.1 Structure

The morphology of the buffer layer graphene on SiC is rather unique if compared to graphene epitaxially grown on other substrates such as metal surfaces. Indeed, graphene C atoms can form strong covalent bonds with Si atoms of the underneath SiC(0001) face. Since these CSi interactions have different strengths across the lattice, the buffer layer displays a pronounced corrugation, which in turn reflects the peculiar $6R3$ reconstruction.

[1] See the box 6.2 on pag. 80

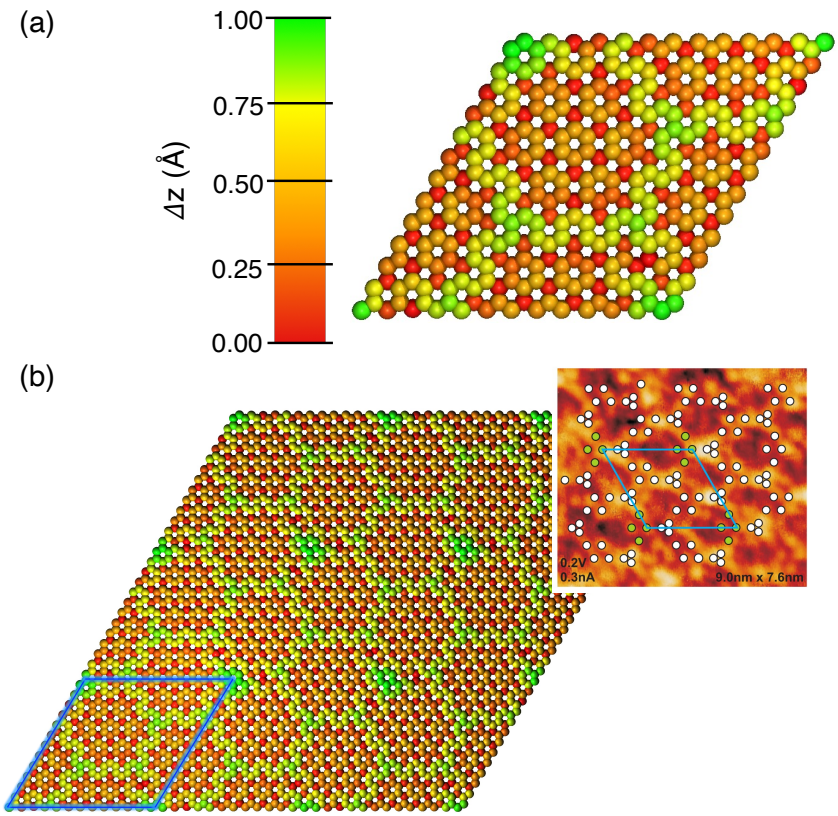

Figure 8.2. (a) Height map of the buffer layer where different colors referred to different heights from the minimum of the buffer layer (Δz). The legend of colors is reported on the left side: green/yellow and red/orange shades indicate more and less puckered carbons respectively. (b) Repetition of the color map displaying the *moiré* pattern formed by the C-lattice on the SiC surface; on the right side, an STM image taken from Ref. [25] is reported for comparison.

Figure 8.2 (a) shows a color map of the buffer layer in the unit cell, where different colors referred to different heights (z coordinate) (w.r.t. a common reference that here is taken to be the minimum of the buffer layer, *i.e.* the C with the lowest z coordinate). By the repetition of this color map, a (quasi) honeycomb superstructure with hexagons of two different sizes emerges (shown in Figure 8.2 (b)). The latter is the *moiré pattern* that the C-lattice forms on the SiC surface and it is an direct manifestation of the $63R$ surface reconstruction. Interestingly, such a simple color map shows the same symmetry properties of the surface density of states mapped by the STM experiments[25].

In Figure 8.3, the cross-sectional views of the corrugation along the two diagonals of the $63R$ unit cell are reported. We can identify the alternation of crests and troughs of different amplitudes. The maximal corrugation is reached at the vertexes of the unit cell, where $\Delta z \approx 1$ Å, in agreement with available experimental data[173]. The local structure of the buffer layer has been unknown for a long time. However, the combination of experimental and theoretical works in the past years has allowed gaining more detailed information about the nature of the buffer layer. In our model, a close inspection of the C-lattice reveals the presence of four different types of C atoms (see Figure 8.4):

(i) "graphene-like" carbons, *i.e.* three-coordinated carbons characterized by an (almost) flat local neighborhood, like in planar graphene;

(ii) three-coordinated carbons with 1 Si-bonded nn;

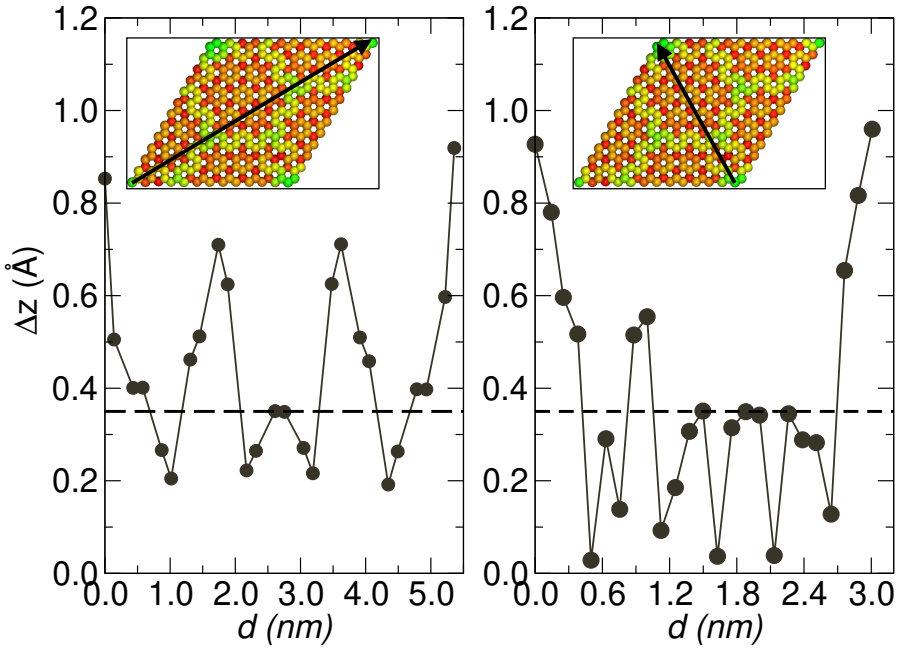

Figure 8.3. Cross-sectional views of the corrugation along the two diagonals of the $6R3$ unit cell. The black dotted line indicates the average puckering (≈ 0.35 Å) that occurs when H is adsorbed on planar graphene. In the two insets, the arrows indicate the directions of the cross-sections considered.

(iii) three-coordinated carbons with 2 Si-bonded nns;

(iv) four-coordinated carbons, *i.e.* those directly bonded to Si.

The same variety of C atoms has been identified also on a different modeled surface reconstruction, namely the $(4\sqrt{3} \times 4\sqrt{3})R30°$ by Sclauzero et. al.[236][2]. In the following, to distinguish between these different C atoms, we use the notation C_m^n where n refers to the coordination and m to the number of Si-bonded nns[3]. Hence, C_0^3 are "graphene-like" carbons, C_1^3 are three-coordinated carbons with 1 Si-bonded nn, etc. Four-coordinated carbons are labeled as C^4.

C^4 carbons represent about 25% of the total number of C atoms in the unit cell, in agreement with CLPES data[25]. The covalent bonds between C and Si induce a strong re-hybridization also on the neighboring C atoms, which are then pyramidalized in the opposite direction (see Figure 8.4). Therefore, C_1^3 and C_2^3 are those responsible for the more corrugated areas of the buffer layer (*i.e.* they are those surrounded by visibly different shades on the color map of Figure 8.2). Figure 8.5 reports the occurrence of each of these C atoms in the unit cell. It is interesting to note that about 70% of C atoms are C_1^3, while C_2^3 represents less than 2% of the total number of C in the cell.

The presence of strong CSi covalent bonds between graphene and the underneath SiC induces a sizeable re-hybridization across the whole C-lattice, whose atoms are then found in a mixed sp^2-sp^3 hybridization. To grasp the extent of such re-hybridization, one can look at the percentage of s weight of the π-like orbitals. As discussed in Section 6.1, when the geometry slightly deviates from planar, the π-like orbital - which is a pure p for a true

[2]The same authors also report the modeling of a $(2\sqrt{3} \times 2\sqrt{3})R30°$ periodicity, where configurations with 3 Si-bonded nearest-neighbors are possible.

[3]CSi bonded pairs are defined whether their distance is less than 2.3 Å, which is the average bond distance in an elongated CSi bond.

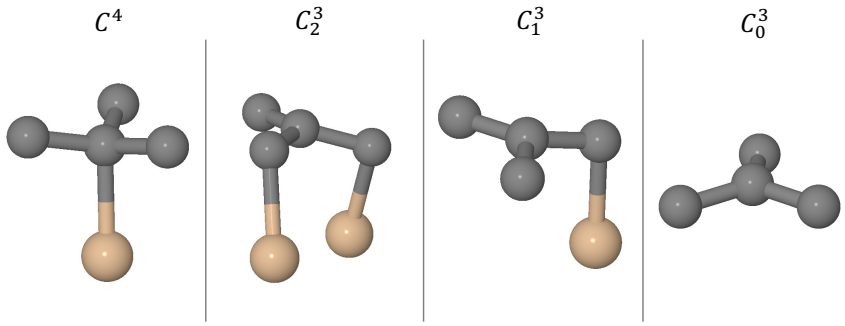

Figure 8.4. Four different types of C atoms that can be identified across the buffer layer: three-coordinated C atoms with 0,1 or 2 Si-bonded nns (C_0^3, C_1^3, C_2^3, respectively) and four-coordinated, *i.e.* Si-bonded (C^4).

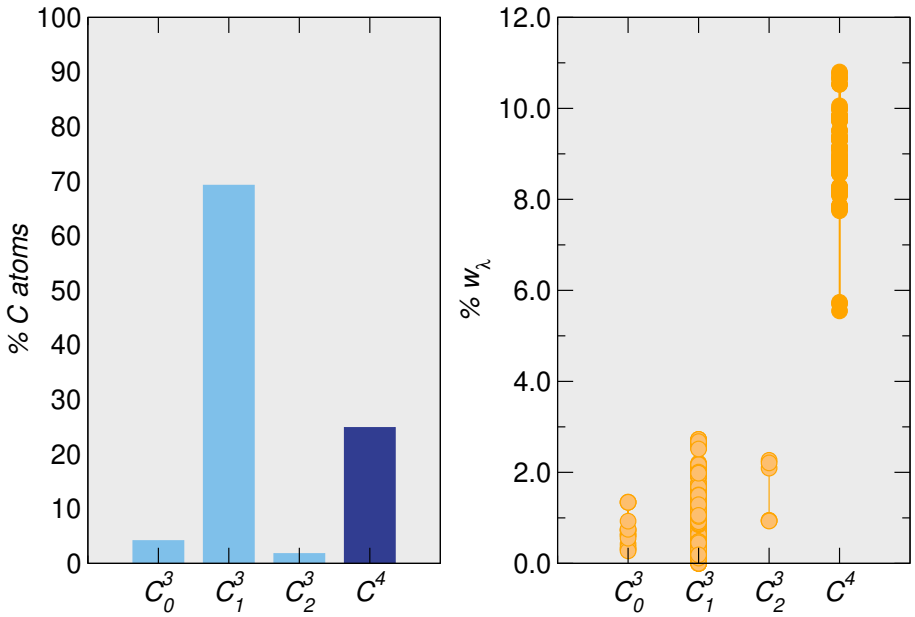

Figure 8.5. (Left) Occurrence of each type of C atoms in the unit cell (338 C atoms for the buffer layer graphene); (Right) Dispersion of the percentage of s fraction of the π-like orbital ($\%w_\lambda$) for each type of C atoms.

sp^2 configuration - acquires a fraction of s character. In the same way, the three hybrids involved in the σ-bonds deviate from the ideal sp^2. We have seen that, in the hypothesis of non-bent bonds, *Coulson's theorem* allows computing the p hybridization indexes (τ_i, $i = 1, 3$ and λ for the π-like orbital) or the s weights (w_{τ_i}, $i = 1, 3$ and w_λ for the π-like orbital) from simple geometrical information:

$$\cos(\theta_{\tau_i\tau_j}) = -\frac{1}{\sqrt{\tau_i\tau_j}} \tag{8.1}$$

$$\lambda = \frac{1}{1 - \sum_i (1-\tau_i)^{-1}} - 1 \tag{8.2}$$

where $\cos(\theta_{\tau_i\tau_j})$ is the angle between two hybrids τ_i and τ_j (*i.e.* a bond angle in the hypothesis of non-bent bonds). Exploiting Equations (8.1) and (8.2), we have computed the percentage of s character of the π-like orbitals (% $w_\lambda = (1/(1+\lambda))\cdot 100$) for each C atoms of the lattice. Results are reported in Figure 8.5 (left). The strongest rehybridization occurs in four-coordinated C^4 carbons because of the covalent bond formed with the underneath Si atoms. For these carbons, $\%w_\lambda$ can reach $\approx 11\%$ (*vs.* 25% for a pure sp^3)[4]. Three-coordinated C atoms are less hybridized, with $\%w_\lambda$ that does not exceed 3%. Overall, the s weights of the π-like orbitals are widely dispersed on a large range of values for each type of C, reflecting the great variability across the lattice of CSi interactions. On average, C_0^3 carbons are the least re-hybridized but they are not strictly in an sp^2 configuration. C_1^3 and C_2^3 are instead more rehybridized because of the neighboring CSi bonds. Nevertheless, among C_1^3, which are the most abundant on the buffer layer, also "true" sp^2 C atoms can be identified. Note that one can equivalently look at the *pyramidalization angle*, θ_p, introduced in Section 6.1 and defined by the relationship $\theta_P = \theta_{\sigma\pi} - 90°$ with $\cos(\theta_{\sigma\pi}) = \boldsymbol{k}_\pi\hat{\boldsymbol{n}}_1 = \boldsymbol{k}_\pi\hat{\boldsymbol{n}}_2 = \boldsymbol{k}_\pi\hat{\boldsymbol{n}}_3$, where $\hat{\boldsymbol{n}}_i$ are normal vectors directed along the σ-bonds and $\boldsymbol{k}_\pi$ is the pyramid "vector" (or π-orbital axis vector). The distribution of the pyramid angles across the buffer layer, computed through the Equations (6.2)-(6.5), is displayed in Figure 8.11.

Overall, the emerging picture from the above analysis is that of a strongly corrugated C-lattice with a substantial rehybridization of C atoms, that partly correlates with the number of Si-bonded nearest neighbors. From the structural point of view, the buffer layer thus differs a lot from planar free-standing graphene. Therefore, its peculiar *geography* is expected to have a significant influence on its chemical reactivity.

8.2.2 H adsorption

In Section 6.4, we have mentioned the H adsorption of the buffer layer as a possible strategy to decouple the monolayer graphene. Moreover, we have highlighted that, at present, the H adsorption has been poorly investigated in the literature, especially from the theoretical side, and thus there is little knowledge about the influence of the buffer layer corrugation on the H adsorption energetics.

As we have mentioned in 6.4.4, pioneering works by F.C. Bocquet et. al. have shown that, at low temperatures, H atoms bind to the buffer layer graphene rather than intercalating, and do not desorb from the surface up to annealing temperatures of about 750 K[183, 184]. In addition, the buffer layer appears to be drastically modified upon hydrogenation, as evidenced by the transformation of the $(6\sqrt{3}\times 6\sqrt{3})R30°$ LEED pattern into a quasi-(1×1)[184].

In light of these experimental works and in order to fill the gap in current theoretical literature, we have scrutinized the H adsorption on the buffer layer by computing the H

[4]Most often, in chemistry one refers to the hybrid orbitals using the p hybridization indexes. Correspondingly, for the most rehybridized C^4 atoms the set of hybrid orbitals is $\{sp^{2.3}, sp^{2.3}, sp^{2.5}, sp^{8.4}\}$.

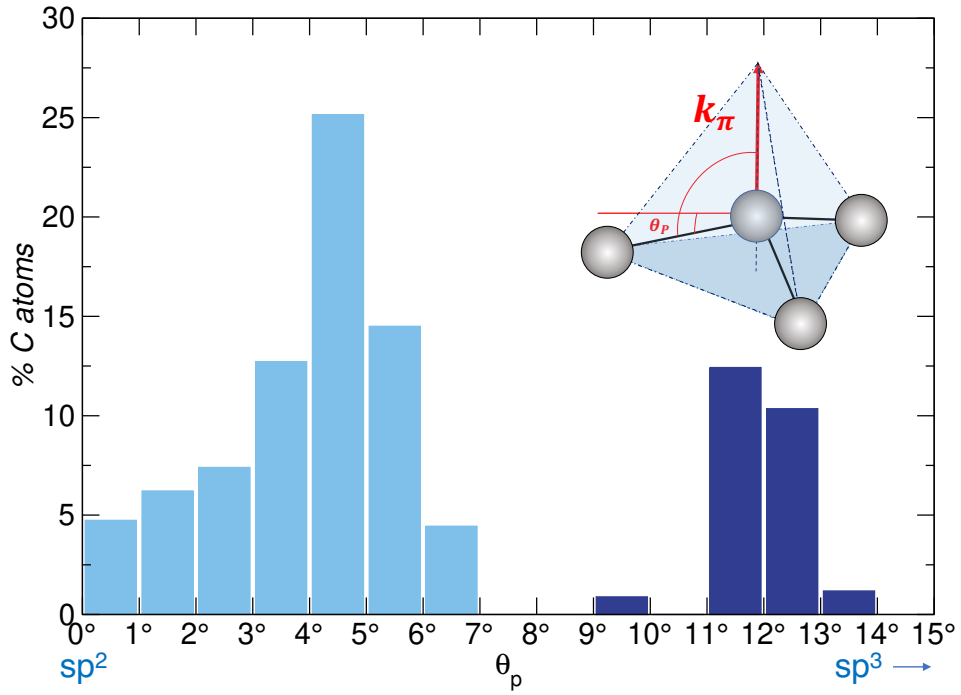

Figure 8.6. Distribution of the pyramid angles (θ_p) across the buffer layer. Light and dark blue bars refers to three-coordinated and four-coordinated C atoms, respectively. The inset shows a sketch of the local neighborhood of a C atom, along with the definition of the pyramidalization angle.

binding energy on some representative sites. Binding energies were computed according to the usual formula

$$D = E_{\mathrm{SiC+BLG+H}} - (E_{\mathrm{SiC+BLG}} + E_{\mathrm{H}})$$

where $E_{\mathrm{SiC+BLG+H}}$ is the DFT energy of the hydrogenated interface, $E_{\mathrm{SiC+BLG}}$ is the DFT energy of the bare interface and E_{H} the DFT energy of an isolated H atom. In the following, we use the subscript SiC+BLG to refer to the system SiC (with H saturated termination) plus the buffer layer and the subscript SiC+BLG+MLG when also the (second) monolayer graphene is present. The optimization of the hydrogenated system was performed in two steps: first, by relaxing just the buffer layer (opt (1) in Table 8.1), and second, by letting to relax also the first SiC bilayer (opt (2) in Table 8.1). D for the two cases are reported in Table 8.1.

One can immediately note that the binding energies are much larger than on planar freestanding graphene ($\approx$ 0.8 eV), ranging from 2.49 eV to 3.22 eV[5], for the two-steps optimization procedure, consistent with the large desorption temperatures indicated by the experiments[183]. Note that these values include the BSSE arising from the use of AOs. To remove this error, it is common practice to use CP correction (see box 1.2 on pag. 19). In the present case, the scheme consists in properly re-defining the asymptotic situation when computing the H binding energy. Namely,

$$D = E_{\mathrm{SiC+BLG_H}} - (E'_{\mathrm{SiC+BLG}} + E'_{\mathrm{H}}) \tag{8.3}$$

[5]These binding energies are comparable to those computed by Sclauzero et. al.([236]) for the H adsorption on $(4\sqrt{3} \times 4\sqrt{3})R30°$ and $(2\sqrt{3} \times 2\sqrt{3})R30°$ surface reconstructions

Table 8.1. H binding energy (not CP-corrected, eV) on the buffer layer graphene and percentage of s-character of the π-like orbital of the binding carbon ($\%w_\lambda$) for different types of C (C_0^3, C_1^3, C_2^3). opt (1): relaxation of the buffer layer; opt(2): relaxation of the buffer layer and the topmost SiC bilayer. $C_1^3 \rightarrow C_2^3$ denotes the change of the C type after the relaxation.

	D (eV)		
Type	opt (1)	opt (2)	$\%w_\lambda$
C_0^3	2.33	2.49	0.63
C_0^3	2.53	2.55	0.75
C_1^3		2.68	2.66
C_1^3	2.68	2.71	2.72
C_1^3	2.69	2.73	1.98
C_1^3	2.70	2.75	1.90
$C_1^3 \rightarrow C_2^3$	2.66	2.88	1.46
C_2^3	3.05	3.09	2.21
C_2^3	3.04	3.09	2.26
$C_1^3 \rightarrow C_2^3$	2.93	3.22	0.00

where

$$E'_{\mathrm{H}} = E^{\star}_{\mathrm{H}} \tag{8.4}$$

$$E'_{\mathrm{SiC+BLG}} = E_{\mathrm{SiC+BLG}} + \tilde{E}^{\star}_{\mathrm{SiC+BLG}} - \tilde{E}_{\mathrm{SiC+BLG}} \tag{8.5}$$

where $E_{\mathrm{SiC+BLG_H}}$ is the DFT energy of the hydrogenated buffer layer, $\tilde{}$ indicates that the calculation is performed in the "final geometry", *i.e.* that of the hydrogenated structure, while $\star$ denotes the use of the whole basis set[6]. When such a scheme is applied, the binding energy range shifts to 2.22-2.95 eV.

Anyway, the corrugation of the buffer layer has a considerable effect on the chemical reactivity towards H atoms. Furthermore, from Table 8.1, it is seen that binding energies can increase by more than 0.15 eV when the first SiC bilayer is free to relax, compared to the case where it is kept frozen. Indeed, upon H adsorption, additional CSi bonds with the underneath Si Dangling Bonds (DB) can form[7], thus making the first SiC bilayer playing an "active" role during the hydrogenation process[8].

A correlation of binding energies with the number of Si-bonded nn can be spotted: the reactivity follows the order $C_0^3 < C_1^3 < C_2^3$. Such a trend indicates that the presence of nearby CSi bonds plays a primary role in determining the reactivity towards H. On average, C_2^3, being more rehybridized among three-coordinated C, are more puckered out of the surface and thus more "prepared" to accept the incoming H, but, as discussed for coroannulene, there is again no clear-cut correlation between D and the degree of rehybridization. In addition, one should consider that the type of the binding C can change after hydrogenation because additional CSi bonds can form, thus further affecting the H adsorption energetics (in Table 8.1, this situation is indicated as, *e.g.* $C_1^3 \rightarrow C_2^3$)).

Yet, the increased reactivity of the buffer layer is not just the by-product of its corru-

[6]For instance, $\tilde{E}^{\star}_{\mathrm{SiC+BLG}}$ is the energy obtained by a single-point calculation of the buffer layer in the hydrogenated geometry and with the full basis set, *i.e.* with a ghost atom on the H

[7]When occurring, the total number of CSi bonds increase at most by one for a single H adsorption event. The bond formation occurs on a nn or nnn to the H binding C.

[8]Experimentally, quenching in the Inverse Photo-Emission Spectroscopy (IPES) spectra of the DB-related peak upon hydrogenation has been observed[189]

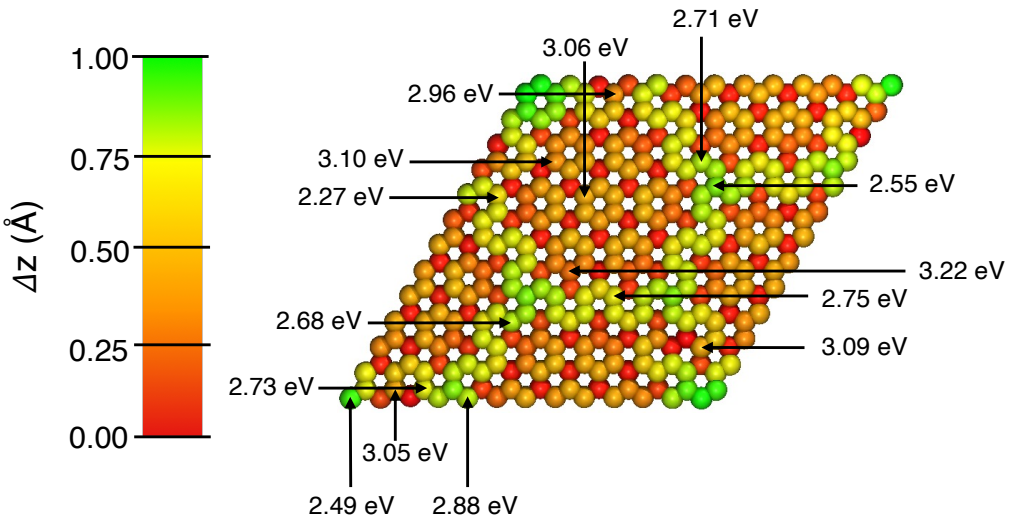

Figure 8.7. Distribution of binding energies (not CP-corrected) mapped on the Δz profile of the C-lattice.

gation. The breaking of the π-bonds due to the CSi interactions determines an increase of the local spin density on the neighboring carbons - like the introduction of p_z defects in free-standing graphene. Such electronic effect contributes to the increase of the binding energies[9]. C^4 carbons are not listed in Table 8.1 because they are not reactive. When an H is attached to these sites, it moves to a neighboring three-coordinated carbon during the relaxation procedure. Indeed, being already in maximal coordination, C^4 carbons just contribute to the stability of the overall interface.

Figure 8.7 provides immediate visualization of the distribution of binding energies across the C-lattice. One can note that, in general, on "green-yellow areas", D varies in the range 2.5-2.7 eV while the most reactive are "orange sites" surrounded by strongly "red-shifted" sites. Even if they are characterized by small Δz, these are C_2^3 carbons, for which the presence of nearby Si-bonded C increases the local corrugation and spin density, thus leading to increased reactivity.

8.3 Monolayer graphene

After the characterization of the structure and reactivity of the buffer layer graphene, we discuss the case of a full interface with monolayer graphene on top of the buffer layer. The dimensionality of the system, with a total number of atoms in the unit cell amounting to 1648, is exceptionally large, and, to the author's knowledge, no modeling of such a system has been reported in the literature so far. The relaxation procedure was performed by placing a second graphene layer on top of the buffer layer at the interlayer distance of about 3.3 Å, with the same orientation. Just the internal coordinates of the monolayer and the buffer layer were let to free to relax. After the geometrical optimization, the stacking of the bilayer resulted to be the Bernal AB stacking, in agreement with the experimental evidence[25].

[9]The effect is analog to what is observed in even hydrogenations of coronene and coroannulene, where the radical-radical character of the reaction determines higher binding energies and vanishing sticking barriers.

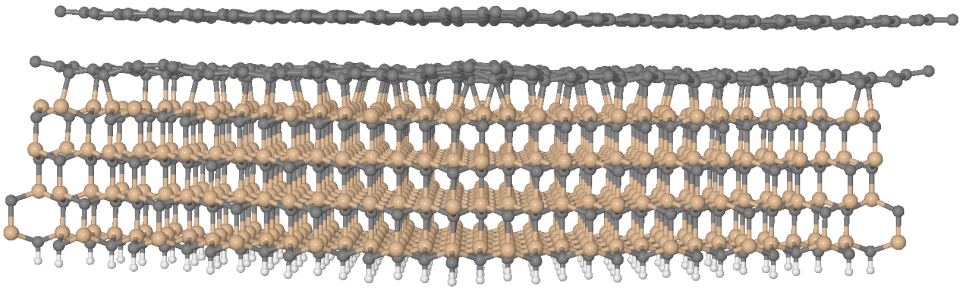

Figure 8.8. Relaxed unit cell of the full C/Si interface (total number of atom amounting to 1648).

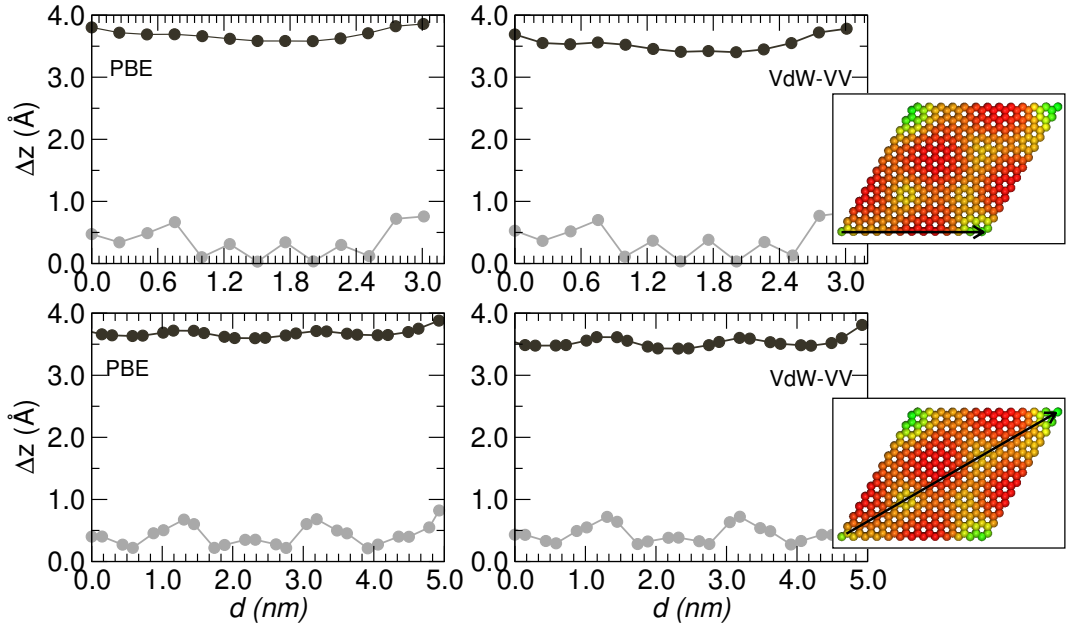

Figure 8.9. Cross-sectional views of the interface corrugation along the x-side and one diagonal of the unit cell, as obtained by PBE (left) and vdW-VV (right) optimizations. Δz is calculated *w.r.t.* the minimum of the buffer layer. The insets show the height color map of the monolayer graphene, with the black arrow indicating the directions of the cross-sectional views on the left.

8.3.1 Structure

Figure 8.8 displays the unit cell of the full interface, as obtained by a PBE calculation. The interlayer distance, d_{int} after the optimization is 3.33 Å, comparable with that of graphite (3.35 Å). d_{int} reduces to 3.14 Å when a van der Walls (vdW)-inclusive functional, such as VV, is employed. It might be surprising that a semilocal functional, such as PBE, results to be binding, with a reasonable d_{int} for this system with long-range interactions between the two layers. In the next section, we show that the explanation of such an unexpected binding can be found in the computational setup employed, and in particular in the use of AOs. Figure 8.9 shows the cross-sectional views of the interface along one diagonal and one side of the unit cell. We note that, in contrast to the strong corrugation of the buffer layer, the monolayer graphene displays a wavy profile like in rippled graphene, with a less pronounced curvature that is barely "visible" from the optimized structure in Figure 8.8. From the insets in Figure 8.9, showing the height color maps for the monolayer graphene, one can note a correspondence between these 2D-ripples in monolayer and the underneath surface reconstruction. Figure 8.10 displays the cross-sectional views of the monolayer graphene along the two diagonals. We note that the maximal Δz for the monolayer is

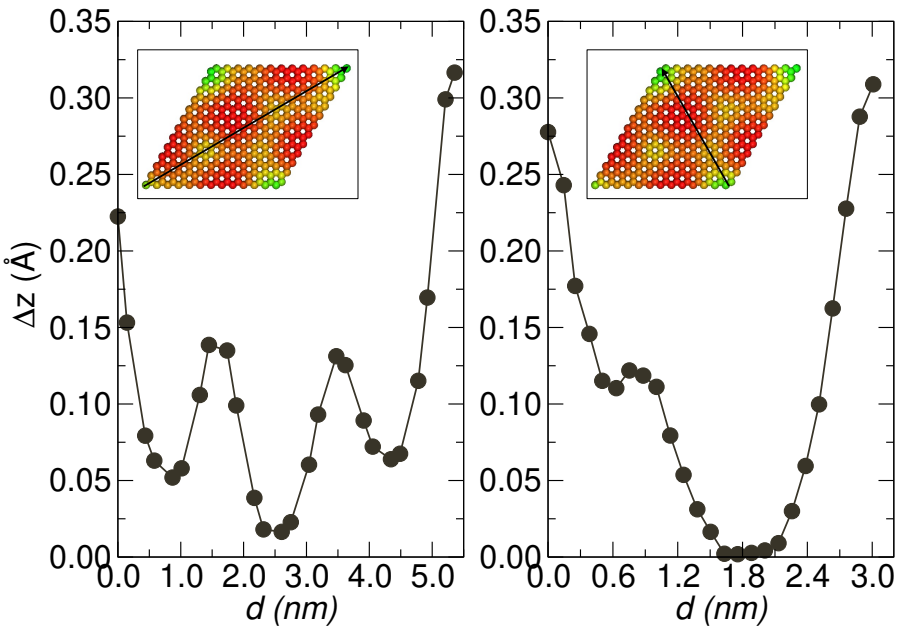

Figure 8.10. Cross-sectional views of the corrugation of the monolayer graphene along the diagonals of the unit cell. The insets show the height color map of the monolayer graphene, with the black arrow indicating the directions of such cross-sectional views.

about 1/3 of that of the buffer layer graphene (0.32 Å, in agreement with experimental data[190, 237]). Due to the curvature, a rehybridization of C atoms is expected to occur also across the monolayer graphene, albeit to a less extent than seen for the buffer layer. As a matter of fact, the local curvature is so small that the percentage of s-weight of the π-like orbital ($\%w_\lambda$) hardly deviates from 0% (the maximal value it reaches is about 0.03%). By the same token, the pyramidalization angles across the lattice are very small, not even exceeding 1° (see Figure 8.11). Therefore, the curvature of the monolayer is so small that its structural properties are locally very similar to those of free-standing graphene[10].

8.3.2 Bilayer binding energies

To estimate the binding between the graphene layers, bilayer binding energy (per C atom in one layer) (E_{bil}) was computed according to the following formula

$$E_{\text{bil}} = [E_{\text{SiC+BLG+MLG}} - (E_{\text{SiC+BLG}} + E_{\text{graphene}})]/338$$

where $E_{\text{SiC+BLG+MLG}}$ is the DFT energy of the full interface, $E_{\text{SiC+BLG+MLG}}$ is the DFT energy of the SiC+BLG and E_{graphene} is the DFT energy of a single graphene layer (with 338 atoms). Our results are reported in Table 8.2. The experimental value of the binding energy in (bare) bilayer graphene is not known. Its value is bound from above by the cohesive energy of graphite, which is about 52 ± 5 meV[105]. For this system, the computed binding energy is slightly larger, around 74 meV/atom with a PBE calculation. Such value increases to 185 meV/atom with a vdW-inclusive functional.

As we have pointed out above, it might be surprising that a semilocal functional such as PBE, which lacks any non-local electron correlation, turns out to be binding for a system dominated by the vdW interactions. Such binding was indeed observed also for bare bilayer graphene, where PBE in combination with AOs predicts a minimum at a correct interlayer distance and with a reasonable depth[105]. The origin of such unexpected binding lies in the

[10]This is in clear contrast with the buffer layer, where the presence of the CSi bonds induces a local strong corrugation.

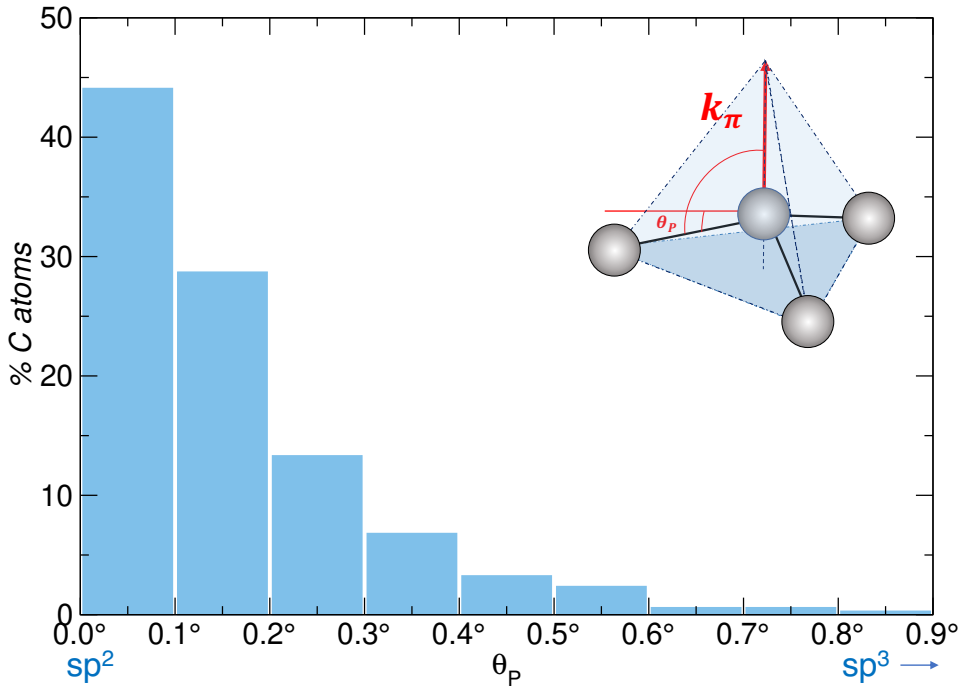

Figure 8.11. Distribution of the pyramid angles (θ_p) across the monolayer graphene. The inset shows a sketch of the local neighborhood of a C atom, along with the definition of the pyramidalization angle.

use of AOs. Indeed, AOs calculations are always plagued by the BSSE, as we mentioned multiple times in this work. It is worthwhile to briefly recall again the origin of such error: it arises from the enlargement of the basis set experienced by two fragments when they approach each other. In particular, one fragment can "borrow" basis functions from the other, thus its basis set is increased and its description improved. In computing the binding energy, the energy of the asymptote (isolated SiC+BLG and isolated graphene) results from unmixed basis sets while, in the SiC+BLG+MLG optimization, basis sets are mixed. Such mismatch is the source of the error and has to be removed when AOs calculations are employed[11]. We repeatedly mentioned the usefulness of the popular CP correction to properly remove the BSSE. For the system at our hands, the CP correction reads as

$$E_{\mathrm{CP}} = (\tilde{E}^{\star}_{\mathrm{SiC+BLG}} + \tilde{E}^{\star}_{\mathrm{graphene}}) - (\tilde{E}_{\mathrm{SiC+BLG}} + \tilde{E}_{\mathrm{graphene}})$$

where, again, $\tilde{}$ means that the calculation is performed in the *final* geometry (that of SiC+BLG+MLG), while $\star$ denotes the use of the whole basis set. The CP correction amounts to ≈ 92 meV/atom for PBE and 124 meV/atom for vdW-VV. The CP-corrected bilayer binding energies are reported in Table 8.2. When the BSSE is properly accounted for, we note that PBE is no longer binding, as expected by standard semilocal DFT. If instead the BSSE is not removed, the PBE binding energy is comparable to the vdW calculation with the proper CP-correction applied. To understand such a result, we remind that the BSSE acts as an overbinding effect, which adds to the long-range features of the vdW-inclusive functionals, clearly determining largely overestimated binding energies. Therefore, such error has to be properly taken into account when vdW interactions are of concern. On the contrary, the overbinding induced by the BSSE can balance out the lacking of long-range features typical of semilocal functionals. Our results suggest therefore that a pragmatical way to overcome these known shortcomings of semilocal DFT is to include the

[11]This error can be minimized - but not removed - by employing a large basis set, such as TZP. However, an enlarged basis set considerably increases the computational cost of the calculation.

Table 8.2. Bilayer binding energies, E_{bil} (meV / atom), for the C/Si interface for different setups, compared with bare bilayer graphene values. Both not CP-corrected (BSSE included) and CP-corrected (BSSE removed) are reported. For bilayer graphene, the bilayer binding energy as obtained by a PW calculation with vdW-VV taken from Ref. [105] , is also reported.

		E_{bil}	
System	Method	BSSE included	BSSE removed
C/Si interface	PBE/DZP	74	-18
	vdW-VV/DZP	185	61
Bilayer graphene	PBE/DZP	66	-21
	vdW/DZP	163	58
	vdW-VV/PW[105]	/	47

BSSE in combination with semilocal exchange-correlation functionals when dealing with systems with long-range interactions. In this regard, PWs calculations, being not affected by the BSSE, are superior to AOs, but they are known to be much more computationally demanding. For the system at hand, AOs are the only viable investigation method but, at the same time, our results highlight the need of taking care of truncation errors such as the BSSE in this type of DFT calculations.

8.3.3 H adsorption

The corrugation of the buffer layer has a strong influence on its chemical reactivity, determining large H binding energies. On the contrary, the monolayer graphene is just weakly curved, but still, its reactivity is expected to differ from that of planar free-standing graphene. To understand the effect of curvature on the reactivity of the monolayer graphene, H binding energies (D) were computed for several representative sites across the lattice. As a first optimization, just the monolayer and the adsorbed H were let free to relax.

The binding energies computed with PBE range from 1.44 eV to 1.71 eV. Hydrogenated sites are indicated on the height color map of Figure 8.12, together with the corresponding binding energy. We note a correlation with the relative Δz (which is again calculated w.r.t. to the minimum z of the monolayer graphene): concave areas (red) of the monolayer are characterized on average by lower binding energies than convex areas (green-yellow). This behavior contrasts with that observed on the buffer layer, where the local corrugation is more irregular and the reactivity is ruled by the nearby presence of the CSi interactions. Notice that, the greater reactivity of convex areas was observed also experimentally on the monolayer graphene on SiC[237] and previously predicted also for rippled graphene[157, 159].

To understand the role of the underneath buffer layer and SiC, one further relaxation was performed for some of the sites previously considered, namely by letting to relax both the buffer layer and the topmost SiC bilayer during the optimization of the hydrogenated interface. As the result of such "full" optimization, the binding energy range shifts to 1.56 eV - 1.71 eV. In particular, the energetics of the hydrogenation on concave areas, *i.e.* those closer to the underneath structure, appear to be more influenced by the relaxation of the topmost SiC bilayer.

Given the small curvature of the monolayer, the computed binding energies might

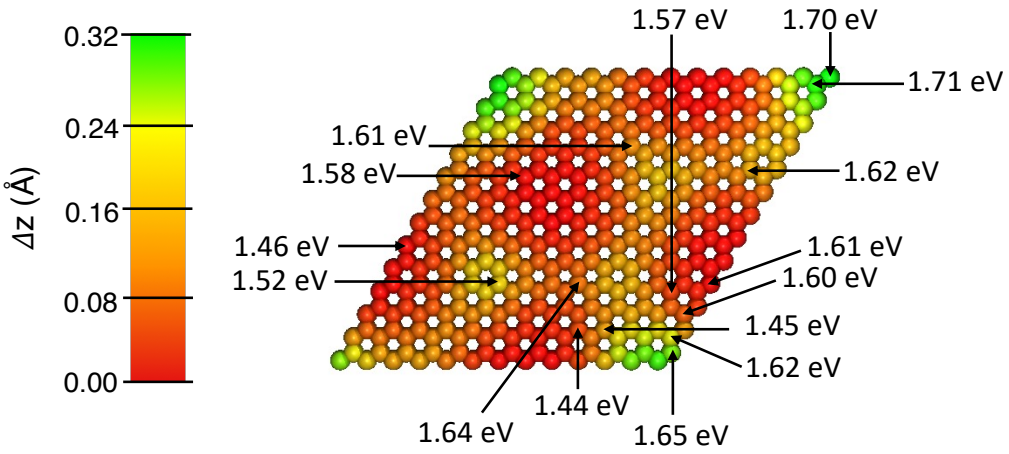

Figure 8.12. Distribution of binding energies mapped on the Δz profile of the C-lattice.

appear unexpectedly large if compared to 0.8-0.9 eV[12] typical of planar free-standing graphene. However, our AOs calculations are again affected by some errors:

(i) the enlargement of the basis set experienced by the H and the puckered interface that results from their proximity;

(ii) the overbinding due to the bilayer structure mentioned in the previous Section.

The first error can be accounted for by applying again the standard CP-correction, following Equations (8.3), (8.4) and (8.5). The CP correction in this case amounts to 0.24 eV[13], thus shifting the range of the binding energies to 1.20-1.47 eV.

When applying the above correction, we are not taking into account the BSSE resulting from the bilayer structure, the second aforementioned source of error. Indeed, since the CP-correction is an *a posteriori* method, it uses geometries that are optimized with such BSSE already included. Therefore, the overbinding arising from the bilayer structure cannot be corrected trivially while computing the H adsorption energetics. Nonetheless, in the previous Section, we noted that a better estimate of the bilayer binding energy with a semilocal functional is provided by including this BSSE, which can play the role of the missing long-range interactions. Therefore, these arguments suggest not to further correct the computed binding energies, *i.e.* including the BSSE of the bilayer structure to improve the description of the binding between the two layers with the employed semilocal functional.

8.3.4 Limits of the AOs

The above considerations evidently demonstrate the limits of the AO calculations and the need for careful control of the ubiquitous BSSE. Yet, AO-based methods allow handling systems that are much larger than those allowed by PW methods and therefore remain a powerful tool in the context of DFT calculations. Because of the exceptional dimension of the system, the estimate of the H binding energy on the monolayer graphene with PWs is out of reach. Accordingly, to get to a deeper understanding of the H adsorption energetics,

[12] In Chapter 1, we mentioned that the H binding energy on graphene slightly changes according to the type of calculation employed. With AO-PBE calculation on a 6×6 superlattice and the BSSE included, the H binding energy is 0.9 eV

[13] Being an *a posteriori* correction, such value is indipendent of the relaxation procedure employed, *i.e.* it is the same whether the buffer layer and the topmost SiC bilayer are let to relax during the optimization of the hydrogenated monolayer or not.

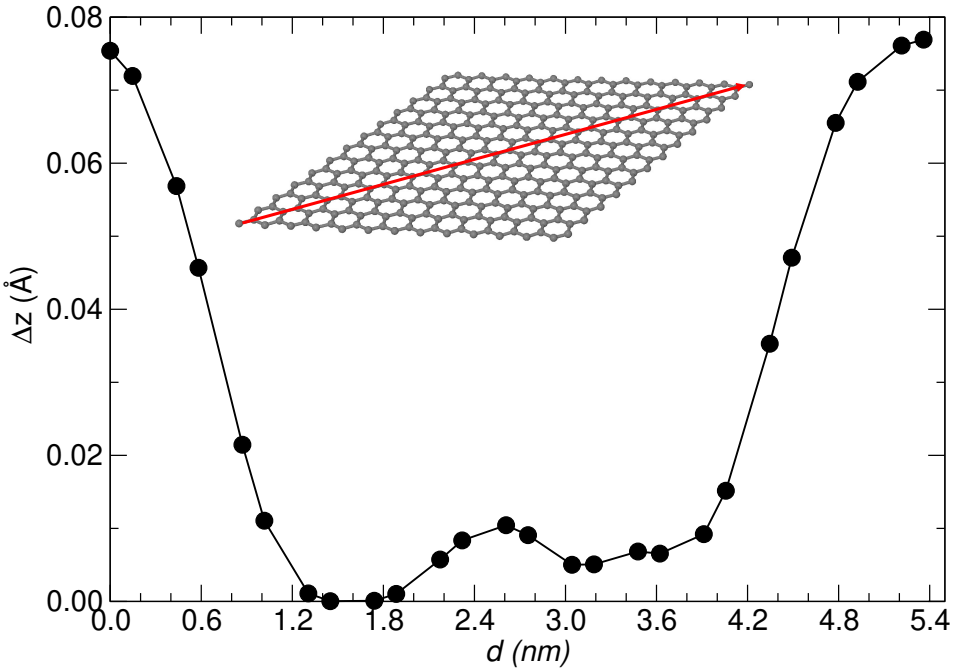

Figure 8.13. The cross-sectional views of the corrugation along the diagonal of a 13×13 graphene superlattice. The inset shows the optimized structure of the superlattice and an arrow indicating the direction of the cross-section considered.

other model systems were considered, with the main aim of identifying what contributes to the large values (1.20-1.47 eV) resulting from our PBE calculations. In particular, four major characteristics of the C/Si interface were further analyzed, namely:

(i) the large size of the graphene superlattice;

(ii) the presence of a bilayer structure;

(iii) the presence of a substrate (SiC) under the bilayer;

(iv) the n-doping experimentally observed for the monolayer graphene.

Let consider the large size of the graphene superlattice. Due to the $63R$ surface reconstruction, the unit cell accommodates a 13×13 graphene superlattice. The H binding energy is influenced by the size of the unit cell because, when relaxing such a large cell, graphene is not forced to remain flat over the long-range. Geometric perturbations that break the two-dimensional character of the sheet can set in. Despite being relatively small, such perturbations can affect the H binding energy. Figure 8.13 reports the corrugation profile of the 13×13 graphene superlattice, as obtained by a PBE geometry optimization with the same computational setup employed for the C/Si interface. Although the corrugation is 4 times smaller than that observed on the monolayer graphene on SiC, the H binding energy is around 1.11 eV (not CP-corrected), *i.e.* ≈ 0.2 eV larger than what found on 6×6 superlattice (a smaller unit cell, but reasonably large to minimize defect-defect interactions). Therefore, the relaxation of a large graphene sheet can considerably impact the H adsorption energetics.

The second feature of the C/Si interface that is worthwhile to inspect is the bilayer structure. As discussed above, a pragmatic approach to overcome the deficiency of the PBE

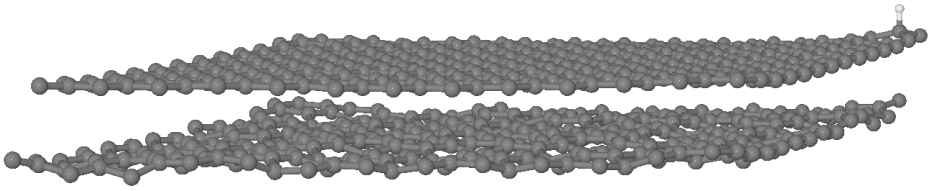

Figure 8.14. The hydrogenated structure of the model bilayer graphene, with one layer kept frozen in the buffer layer structure.

functional is to include the overbinding arising from the BSSE between the two layers. Nevertheless, one may argue that a wrong assessment of such overbinding may be the source of the large D obtained. An evaluation of such overbinding effect can thus help us understand its contribution to the H binding energy. An artificial way to capture the extent of such effect is to minimize the BSSE by relaxing just the nearest neighbors to the binding C atom and keeping the remaining atoms in their initial position. A comparison between the H binding energy with full relaxation of the monolayer versus that obtained with this "constrained" relaxation should provide us with an estimate of the bilayer overbinding, though approximated. Looking at the most reactive site (1.71 eV), D reduces to 1.63 eV. Therefore, such infamous overbinding resulting from AOs is likely to count less than 0.1 eV on the H binding energy. This result suggests that the computed binding energies are feasible and not too much overestimated.

Moving along to point (iii), we may ask how the underneath SiC affects the reactivity of the monolayer graphene on top. A very rough and - again - artificial way of looking at this contribution is provided by the removal of the SiC from the system. In other words, one can look at the H adsorption on bilayer graphene where the bottom layer is kept frozen in the buffer layer geometry, thus simulating the absence of the SiC substrate (see Figure 8.14). For the most reactive site on the full system (1.71 eV), the binding energy on this model bilayer is reduced to 1.21 eV. Hence, there is half an eV that comes just from the presence of the SiC substrate. Again, this is due to a combination of both "geometrical" and "electronic" effects. The vdW or pseudo-vdW vary largely across the whole unit cell and a tiny fraction of energy gained in some interaction could account for some tenths of eV. In addition, the unpaired electron can strengthen some interaction with the buffer layer.

Last but not least, as discussed in Chapter 6, the substrate with the buffer layer induces an n-doping on the monolayer graphene, shifting the Fermi level by about 0.42 eV[25]. The excess charge density on the graphene sheet due to such n-doping (or p-doping) can strongly affect the H chemisorption energy, as proved on B (or N)-doped graphene[245]. Indeed, charge doping populates the $\pi^\star$ states (and correspondingly depopulates the π state), thus weakening the π-bonds. Consequently, the H chemisorption is made easier and the binding energy increases, with a quasi quadratic scaling w.r.t. to the excess charge density[245]. The Fermi level shift in graphene due to charge doping can be related to the excess charge density n by the following relationship

$$\varepsilon_f = \hbar v_f \sqrt{\pi n}$$

where v_F is the Fermi velocity of graphene ($\approx 10^6$ m/s). The Fermi level shift in monolayer graphene on SiC corresponds to $n \approx 10^{13}$ cm^{-2}, as verified experimentally[25, 181]. Such doping level is anyway less efficient in promoting the reactivity towards H atoms, whose binding energy is expected to increase by just one-tenth of eV w.r.t. to the undoped case, according to previous works on doped graphene[245, 246]. Therefore, that n-doping of the

monolayer has little influence on the H adsorption energetics.

In light of the present discussion, we can conclude that the large energies released when binding H on the monolayer graphene can be ascribed to two main factors: the large dimensionality of the system, which introduces a curvature on the monolayer, though weak, and the presence of the underneath SiC. The BSSE arising from the bilayer structure and n-doping seem to play a marginal role, in this regard. Nevertheless, as already pointed out by some authors in the literature[105], this work restates some of the limitations of the AO calculations and the need for an *a priori* scheme to correct the BSSE.

8.4 Summary and Concluding Remarks

In this Chapter, we have shown an in-depth DFT investigation of the C/Si interface modeled in the experimental surface reconstruction. Such work was motivated by the great interest sparked by this interface and, in particular, by its hydrogenation, in solving some of the existing issues in graphene technology, such as large-scale production. In addition, because of its structure, the C/Si interface represented an interesting milestone in our *journey* through curved carbon-based systems. Thus, we have scrutinized the H adsorption energetics on both the buffer and monolayer graphene, to understand the role of their unique surface properties on their chemical reactivity. According to our DFT calculations, the H binding energy on the buffer layer can reach values as large as 3.0 eV. The latter are the result of a geometric effect (the corrugation) and an electronic effect (the breaking of the π-bonds across the lattice), both governed by the presence of interactions between C atoms and the underneath Si dangling bonds. For the monolayer graphene, the less pronounced curvature comes with H binding energies that are smaller than those found on the buffer layer (not exceeding 1.5 eV) but still large when compared to free-standing graphene. Once taken into account the truncation errors arising from the use of AOs and the more relevant properties of the interface, such large binding energies have been ascribed to the large dimensionality of the system (and the corresponding curvature) and the presence of the underneath SiC.

In Chapter 1, we have discussed that the H adsorption is not the only process that can occur when a graphene sheet is exposed to an H flux. H atoms can recombine over the surface, thus forming molecular hydrogen, especially when cold beams are employed on the pre-covered surfaces and incoming H do not have enough energy to overcome the barrier to sticking. We have mentioned that the most common abstraction mechanism is the *Eley-Rideal*, which is operative in a large range of temperatures. Since the Eley-Rideal recombination is barrier-less, its rate is determined by the exothermicity of the reaction, *i.e.* by the H binding energy. The H adsorption and the Eley-Rideal recombination can, in general, compete with each other, and therefore their competition will rule the hydrogenation of the buffer layer (and that of the monolayer), that lies at the heart of the monolayer decoupling strategy outlined in Chapter 6. To integrate further our understanding of the C/Si interface and its behavior under H exposure, we have then combined our DFT investigation with a quantum-dynamical (QD) study of the Eley-Rideal recombination on both the buffer and monolayer graphene. The results of such a DFT-QD study are presented in the following Chapter.

Chapter 9

The C/Si interface: quantum dynamics of the Eley-Rideal reaction

The buffer layer graphene on SiC is more reactive towards H than planar graphene, with binding energies (D) that can reach 3.0 eV. In the previous Chapters, we have pointed out that binding energies and adsorption barriers are correlated, that is the larger the binding energy the smaller is the barrier to sticking (the so-called *Bell-Evans-Polany principle*). Therefore, while the hydrogenation of planar free-standing graphene proceeds through the formation of dimers and clusters - because of the *preferential sticking* discussed in Subsection 1.3.4 - the H adsorption on the buffer layer graphene is likely to occur randomly, since negligibly small or vanishing adsorption barriers are expected across the whole C-lattice. Yet, at the gas-surface interface, several processes can compete with the H adsorption, thus affecting the final state of long-term hydrogen exposure of the C/Si interface. In Chapter 6 we have mentioned that the passivation of the buffer layer with H atoms could be a strategy to decouple the monolayer graphene, especially at low temperatures ($\approx 500°$) where H atoms do not intercalate underneath the buffer layer. Hence, it is crucial to investigate the dynamics of H atoms above the buffer layer in order to properly understand how its passivation works.

The most relevant competing reaction at the temperatures of interest is H_2 recombination through the *Eley-Rideal* mechanism. In this reaction, a H atom coming from the gas phase feels the interaction potential of one hydrogen already adsorbed on the surface. The H is thus captured by such interaction potential and collides with the chemisorbed H, thus forming a H_2 molecule that leaves the surface. The ER recombination is barrier-less, then its rate is governed by its exothermicity, *i.e.* the depth of the chemisorption well.

The question that naturally arises is the following: how does the peculiar *geography* of the buffer layer, which results in very large D, affect the rate of the competing Eley-Rideal reaction? To answer this question and further integrate our understanding of the C/Si interface upon hydrogenation, we have combined our DFT data on the buffer layer with a fully quantum-dynamical investigation of the ER reaction. For this purpose, we have employed a time-dependent wave packet method that was already tested and successfully applied in the literature to study the ER recombination on metal surfaces and graphite.

In Section 1, we briefly describe this method and we present some preliminary calculations on graphite to better illustrate it and some basic features of the ER reaction. Section 2 and 3 are dedicated to the discussion of our results on the ER reaction on the buffer layer and the monolayer graphene on SiC, respectively. An overview on classical and quantum scattering theory is left to Appendix B.

9.1 A time-dependent wave packet method

In this Section, we provide the reader with a quick description of the method employed for the computation of ER cross-sections on graphene. Such method was developed by Persson and Jackson (1994)[247] for the theoretical investigation of the ER recombination dynamics on metal surfaces. The interest in modeling such gas-phase reaction was originally inspired by a series of groundbreaking experiments on the matter conducted in the late 1980s. In this regard, we could note cite the works of Hall et. al.[248] and Eeshustra et. al.[249]. On H_2 recombination of W, the molecular beam study by Rettner et. al.[250] examining the isotopic effect in H_2 recombination on Cu(111) or the work by Lykke and Kay[251] on the reaction between gas phase H and Cl adsorbed on Au(111). Such experimental works shed light on some features of the ER dynamics, like the sensitivity to the initial state of the gas-phase species or the large internal excitation of the desorbing product molecule. Later, the experiments were extended to graphite, PAHs and realistic analogs of the interstellar dust grains for the recognized role of the ER reaction in the interstellar chemistry (see Chapter 2).

In a nutshell, the method consists in solving a time-dependent Schrödinger's equation describing the evolution of heights and the lateral separation of the two H atoms, applying a flat-rigid surface approximation in the nearby of the target (that is, disregarding the lattice motion) and modeling the interaction between the two H with a potential of the London-Eyring-Polany-Sato (LEPS) form[252]. In the following we outline such approach and illustrate some of the features of the ER reaction with preliminary calculations on graphene. For a comprehensive description of the method, the reader is referred to the original papers[253, 254, 255].

The flat-rigid surface approximation allows reducing the dimensionality of the problem from six to three, by introducing three constants of motion. Indeed, beside the rotationally invariance around the surface normal, such approximation makes the interaction between the atoms and the surface translationally invariant, thus introducing an additional axial symmetry. In the center-of-mass (CM) frame, such symmetries makes the potential $V(\boldsymbol{x}_1, \boldsymbol{x}_2)$ (with $\boldsymbol{x}_1$ ($\boldsymbol{x}_2$) position vector of the target (projectile)) assuming the form $V(\rho, z, Z)$, where ρ is the interatomic distance projected on the surface plane, z is the relative separation along the surface normal and Z the center-of-mass height. The lateral momentum of the center-of-mass and the z-component of the angular momentum of the relative motion become conserved quantity, and one can then apply a *partial-wave expansion* to the initial state vector[255]

$$|\Psi\rangle = \sum_{m=-\infty}^{+\infty} c_m |\psi^m\rangle |m\rangle \tag{9.1}$$

where $|m\rangle$ is an eigenstate of the center-of-mass angular momentum ($\langle\phi|m\rangle = e^{im\phi}/\sqrt{2\pi}$ with ϕ being the azimuthal angle of the diatomic), while $|\psi_m\rangle$ are vectors of the remaining degrees of freedoms. The latter evolve independently according to the Hamiltonian

$$H^m = T_\perp + T_\parallel^m + V \tag{9.2}$$

$T_\perp$ is the kinetic energy operator for the motion along the surface normal and reads as (in coordinate representation)

$$T_\perp = -\frac{1}{2M}\frac{\partial^2}{\partial Z^2}$$

with $M = m_1 + m_2$ the total mass. $T_\parallel^m$ is the kinetic energy operator for the relative

motion and reads as (in coordinate representation)

$$T_{\parallel}^{m} = -\frac{1}{2\mu}\left[\frac{1}{\rho}\frac{\partial}{\partial\rho}\left(\rho\frac{\partial}{\partial\rho}\right)\right] + \frac{m^2}{2\mu\rho^2}$$

where $\mu = (1/m_1 + 1/m_2)^{-1}$ is the reduced mass. Note that such operator contains a centrifugal term, namely $m^2/2\mu\rho^2$. $V = V(\rho, z, Z)$ is the potential energy in the flat-rigid approximation.

The interaction between the surface and the atoms is assumed to be governed by a single electronically adiabatic potential energy surface. The latter is modeled in the LEPS form, namely

$$\begin{aligned} V(\rho, z, Z) = U_a(z_i) + U_a(z_t) + U_m(r) + \\ - \left[Q_m(r)^2 + (Q_a(z_i) + Q_a(z_t))^2 - Q_m(r)(Q_a(z_i) + Q_a(z_t))\right]^2 \end{aligned} \tag{9.3}$$

where

$$\begin{aligned} U_i(x) = \frac{D_i}{4(1+\Delta_i)}[(3+\Delta_i)e^{-2\alpha_i(x-x_i)} + \\ - (2+6\Delta_i)e^{-\alpha_i(x-x_i)}] \end{aligned} \tag{9.4}$$

and

$$\begin{aligned} Q_i(x) = \frac{D_i}{4(1+\Delta_i)}[(1+3\Delta_i)e^{-2\alpha_i(x-x_i)} + \\ - (6+2\Delta_i)e^{-\alpha_i(x-x_i)}] \end{aligned} \tag{9.5}$$

In Equations (9.3)-(9.5), $i = a, m$ where a denotes an atomic term and m a molecular term while r is the internuclear separation, namely $r^2 = z^2 + \rho^2$. The parameters describing gas-phase H_2 are the binding energy $D_m = 4.745\,\text{eV}$, $\alpha_m = 1.943\,\text{Å}^{-1}$ and $x_m = r_m = 0.741\,\text{Å}$. D_a is the depth of the H-substrate chemisorption well. The remaining parameters such as the *Sato parameters* Δ_a and Δ_m can be tuned to modify the reactivity and model various substrates. They are obtained by fitting the potential with *first-principle* data. For the problem at our interest, such parameters were fitted to periodic DFT calculations of the interaction of two H atoms with a (0001) graphite surface. It is worthy to emphasize that in this potential model, the carbon atom beneath the adsorbed H (*i.e.* the target) is held fixed at a puckered configuration. The incoming H (*i.e.* the projectile) experiences a physisorption interaction with the substrate. This is the "diabatic" model of Ref. [254] denoted as Case A. The resulting dynamics is then a *fast dynamics*, that is the binding carbon has no time to relax and the incoming H has no time to chemisorb. Such dynamical process occurs at high collision energies of the projectile, which suggests that the results provided by the method in such regime should be more consistent with the potential. However, we should keep in mind that the method employed here disregards any quantum lattice motion, which may play a relevant role in such regime[1]. On the other hand, one may also consider the "adiabatic" model, where the H from the gas phase reacts with the chemisorbed H but the substrate is allowed to fully relax for every configuration of the two H atoms. This is denoted as Case B in Ref. [254]. The *real* dynamics should lie somewhere

[1]The lattice motion has been included in the work of Pasquini et. al.[256]

between these two limiting situations[254][2].

The initial wave packet should represent an adsorbate atom 1 (the target) in a given vibrational eigenstate of $V_a(z_1)$ and an atom 2 (the projectile) far away from the surface, with a given angle of incidence θ and kinetic energy E_i. The target has a zero lateral momentum, $\boldsymbol{p}_{1\parallel} = 0$, while the projectile is represented by a plane wave parallel to the surface with lateral wave vector $\boldsymbol{k}_{2\parallel} = \sqrt{2m_2 E_i}$ and a Gaussian wave function normal to the surface. Therefore, in the flat-rigid approximation, $|\psi^m\rangle$ of Equation (9.1) reads as

$$\psi^m(\rho, z, Z; t = 0) = \frac{1}{\sqrt{\rho}} \nu_n(z_1) G(z_2) J_{|m|}(k_\parallel \rho) F(\rho) \quad \rho > 0 \tag{9.6}$$

where $J_{|m|}$ is a *cylindrical Bessel function*, $k_\parallel = \mu k_{2\parallel}/m_2$ is the lateral wave vector for the relative motion, $\nu_n(z_1)$ is an eigenstate wavefunction of $V_a(z_1)$ while $G(z_2)$ is a Gaussian function

$$G(z_2) = \frac{1}{\sqrt{\pi \Delta z}} \exp\left[-ik_z(z_2 - z_1) - \frac{(z_2 - z_i)^2}{2\Delta z^2}\right] \tag{9.7}$$

k_z is the average momentum of the target normal to the surface, z_i is the average initial position and δz is its position spread with a corresponding normal kinetic energy spread $\Delta E_z \approx \sqrt{E_z/(2m)}/\Delta z.k_z$ is given by $k_z = \sqrt{2m_2(E_{iz} - \langle V \rangle}$, where $E_{iz} = E_i \cos^2\theta_i$ is the average incident energy at infinity and $\langle V \rangle$ is the average of the potential over the initial wave packet. $F(\rho)$ is a cut-off function introduced in order to localize the lateral extension of the wave packet within the grid. It is chosen to be in the form

$$F(\rho) = \sqrt{\frac{\pi}{A^{\text{eff}} c(m; k_\parallel)}} \begin{cases} 1 & \text{if} \quad |\rho| < \rho_c \\ \exp\left[-\left(\frac{|\rho| - \rho_c}{\lambda}\right)^2\right] & \text{otherwise} \end{cases} \tag{9.8}$$

where A^{eff} is the effective area of the lateral spatial extension of the initial wave function, $c(m; k_\parallel)$ is a relative contribution from component m. In a more compact notation, the wave packet $|\psi^m\rangle$ is then chosen in the form $|\nu\rangle|z_i k_z; \Delta z\rangle|k^m\rangle$, where it is intended that $|\nu\rangle$ is the adsorbate vibrational eigenstate, $|z_i k_z; \Delta z\rangle$ the state describing the vertical motion of the incident atom, while $|k^m\rangle$ that describing the motion along the surface. The time-propagation of $|\psi^m\rangle$ is performed by applying a short-time *split-operator approximation* to the full time-evolution operator corresponding to H^m (Equation (9.2)). The latter is based on the *Trotter formula*

$$e^{-iH\delta t} \approx e^{-iV\frac{\delta t}{2}} e^{-i(H_1 + H_2)\delta t} e^{-iV\frac{\delta t}{2}}$$

where δt is an infinitesimal time-step and $H = H_1 + H_2 + V$.

In the original approach described above, the set of coordinates adopted is the center-of-mass (Z) and the relative motion z of the two atoms[257, 258, 259]. Later, the method was extended by Martinazzo et. al.[255] to allow for the use of the heights of the two atoms (z_i and z_t) as a set of coordinates. The first choice is better suited for the computation of rovibrational distributions of the ER product molecule and for such reason it is referred to as "product" set of coordinates. The second is better suited to compute different exit channel probabilities, such as the exchange, $P + TS \to T + PS$, or the two-atom trapping, $P + TS \to PS + TS$, where P is the projectile and T the target atom.

For the computation of energy-resolved reaction probabilities, a flux-operator approach

[2]Sha. et. al. have shown that the resulting reaction probabilities in the two cases are very similar, because it is the strong HH interaction to dominate the reaction dynamics. The notable difference is that, in the relaxed case, the lattice begins to "unpucker" as soon as the HH bond forms, making the entrance channel more attractive. As a result, in the relaxed case the reaction cross-sections in the low energy regime are larger w.r.t. the rigid-puckered case[254].

applied to the time-energy mapping of the wavefunction is employed[255]. To elucidate such procedure, let consider an initial state $|\psi_0\rangle$ corresponding to an incoming asymptotic state $|\phi_\alpha\rangle$ in channel α, that is $|\psi_0\rangle = \Omega_+^\alpha|\phi_\alpha\rangle$, with Ω_+^α the appropriate Möller operator (see Appendix B). Let P be an operator such that $\lim_{t\to\pm\infty}\langle\psi_t|P|\psi_t\rangle$ exists. Then, the change of P due to collision will be given by[255]

$$\Delta P = \int_{-\infty}^{+\infty}\langle\psi_t|\dot{P}|\psi_t\rangle dt \tag{9.9}$$

where $\dot{P}$ is the *dynamical derivative* of P, namely $\dot{P} = i[H, P]$. Using

$$\begin{aligned}|\psi_0\rangle &= \int dE|E\alpha+\rangle\langle E\alpha+|\psi_0\rangle \\ &= \int dE|E\alpha+\rangle\langle E\alpha|\phi_\alpha\rangle\end{aligned} \tag{9.10}$$

we may rewrite Equation (9.9) as

$$\Delta P(\infty) = \int dEP(E)|a(E)|^2 \tag{9.11}$$

where $a(E) = \langle E\alpha+|\psi_0\rangle = \langle E\alpha|\phi_\alpha\rangle$ and $P(E) = 2\pi\langle E\alpha+|F|E\alpha+\rangle$, where the *flux-operator* $F = \dot{P}$ has been introduced. $P(E)$ represents the energy-resolve change of P. Since we are interested in product projection operators and the initial wavepacket is localized in the asymptotic reaction region, we have to follow only the forward time evolution and the energy weights are simply given by $a(E) \approx \langle E\alpha|\psi_0\rangle$ and $P(t) = 0$ for $t < 0$ with $|\psi_0 \approx |\phi_\alpha\rangle$.

For the problem at our hand, the energy-resolved probabilities, $P_{i\leftarrow f}$, are then computed from

$$P_{i\to f} = 2\pi\langle Ei+|F_f|Ei+\rangle \tag{9.12}$$

where F_f is the flux-operator for products into states f given by $F_f = \dot{P}_f$. P_f is a projector onto the final internal states f times a projector onto the asymptotic region of the relevant scattering coordinate, $P_f = h_{R_\infty}|f\rangle\langle f|$, with h_{R_∞} an Heavised operator projecting onto $R > R_\infty$. $|Ei+\rangle$ in Equation (9.12) is an energy normalized scattering eigenvector for the initial condition i

$$|Ei+\rangle = \frac{1}{2\pi}\frac{1}{\langle Ei|\psi_0\rangle}\int_0^\infty e^{iEt}|\psi_t\rangle dt$$

where the coefficients $\langle Ei|\psi_0\rangle$ are related to the momentum representation of the initial wavepacket.

Adsorbing potentials are used as boundary conditions to avoid unphysical reflection at the edge of the three-dimensional grid. They are started at Z_s, z_s^-,z_s^+,ρ_s in product coordinates (+ and − denotes the left and right edges of the z grid respectively) and $z_{i,s}^+$, $z_{i,s}^-$ in reagent coordinates and implicitly define the flux lines. The adopted adsorbing potential is the transmission-free of Manolopoulus, which is defined in terms of the minimum kinetic energy for which reflection is less than 1%.

To illustrate some general features of the ER reaction, we begin by showing some calculations on the H_2 recombination on graphitic surface ($D_i = 0.68\,\text{eV}$)[3]. Figure 9.1 displays the *cross-sections* ($\sigma(\text{Å}^2)$) in a large range of collision energies of the incident atom and for different vibrational eigenstate of the adsorbate. Note that the reported σ

[3]These are *known* results, that the interested reader can find in the paper by R. Martinazzo et. al. (2006)[255].

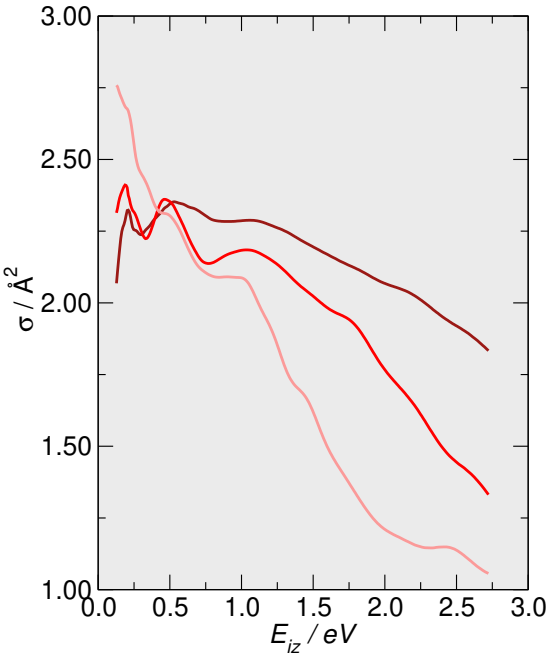

Figure 9.1. Cross-sections (σ, Å^2) of the ER reaction on graphite ($D_i = 0.68\,\text{eV}$) as functions of the collision energy (E_{iz}, eV) of the incident H atom. Dark to light red denotes respectively $\nu = 0, 1, 2$ vibrational eigenstate of the target atom.

are scaled by a factor 1/4 w.r.t. the *total* cross-sections. Indeed, in contrast to H on metals, the magnetic moment of the chemisorbed H is not quenched on graphite and therefore such scaling factor is a spin-statistical factor that accounts for the fact that only 1/4 of the H couples are the right spin-configuration[40].

In spite of the scaling, cross-sections on graphite remain larger when compared to metals. This behavior is due to the fact that H on graphite experiences a much weaker substrate attraction, that allows for steering of the incoming projectile. Moreover, the stronger interaction of H on metals ($D_i = 2{-}2.5\,\text{eV}$) puts the target closer to the surface (0.5 Å vs 1.54 Å), thereby leading to smaller cross-sections.

Vibrational excitation of the target atom promotes, as expected, the reaction in the low energy regime, as indicated by the larger cross-sections, but acts as an inhibiting factor at larger values, in particular as soon as the so-called *collision induced desorption (CID)* channel opens. CID refers to the process $P + TS \rightarrow P + T + S$, where the target desorbs in consequence of the collision and becomes a relevant mechanism as the projectile collision energy overcomes the target binding energy (not shown).

Figure 9.2 displays the average vibrational and rotational states of the product molecule (H_2) at different vibrational eigenstates of the target atom. The vibrational excitation, and the internal energy (not displayed), decrease with the increase of the collision energy of the projectile. Correspondingly, this indicates an increase of the translational energy of the product and therefore an efficient conversion of the relative kinetic energy into center-of-mass kinetic energy due to the collision, especially when the target is in low-lying vibrational states. The rotational excitation is instead a monotonically increasing function of the collision energy. Higher-energy calculations have shown that above 2 eV, the average vibrational excitation and the internal energy become an increasing function of the collision energy, while the rotational excitation levels off.

One may wonder why we are applying a full *quantum* approach to investigate a barrierless reaction such as the Eley-Rideal, where *classical* methods should be rather adequate in describing its dynamical features. Besides the fact that reaction at our interest involves

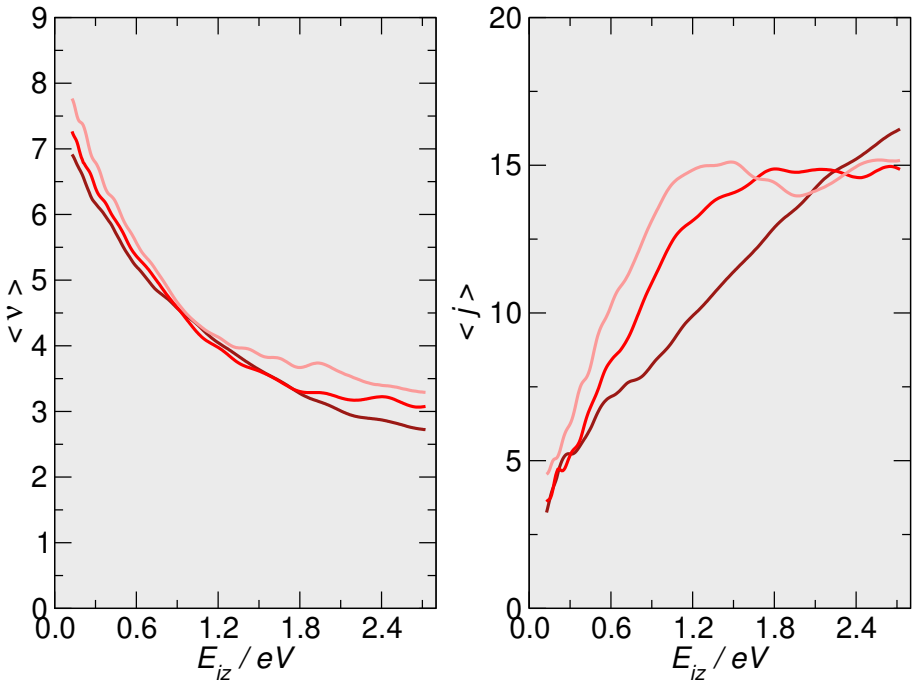

Figure 9.2. Vibrational (ν) and Rotational (j) excitation of the product molecule (H_2) as functions of the collision energy (E_{iz}, eV) of the incident H atom. Dark to light red denotes respectively $\nu = 0, 1, 2$ vibrational eigenstate of the target atom.

light atoms, Martinazzo et. al.[255] showed that *oscillations* appearing in the cross-sections displayed in Figure 9.1 cannot be reproduced by classical and quasi-classical trajectory calculations. They are due to a *selective* population of the low-lying vibrational eigenstates of the product molecule, that is they are not due to any particular feature of the potential but they arise from the obvious quantization of the product states[4], which is able to manifest itself in a global observable such as the reaction cross-section. In parallel, the quantum CID cross-sections display a peak structure that may be assigned to the population of *metastable* states of a rotationally excited transient H_2 molecule.

9.2 ER recombination on the buffer layer

Employing the time-dependent wave packet method described above, we have investigated the ER reaction on the buffer layer graphene. As mentioned in the introduction to this Chapter, the purpose was to understand the influence of corrugation on the rate of the abstraction process. The ER reaction cross-sections were then computed by tuning the depth of the chemisorption well of the target atom (D_i) in the range of the H binding energies found with DFT calculations. We shall highlight that our calculations are of model type, also because they assume normal incidence only.

The target atom was left in its vibrational ground state. For the incident atom, a large range of collision energies was considered. Its average energy was set to $E_{i0} = 1.0\,\text{eV}$ and the average height at $z_{i0} = 9.5\,\text{Å}$. The time-step δ_t of the time propagation was set to 0.25 fs and the propagation was performed until the wave packet was completely adsorbed by the adsorbing potentials. The calculation was performed in the "product" coordinate sets. The optimized grid parameters are summarized in Table 9.1.

The ER reaction cross-sections (σ) computed in our simulations are displayed in Figure

[4]Clearly, also the correct prediction of the rovibrational populations appears straightforward in a quantum calculation and (though possible, to some degree) rather involved in the QCT case.

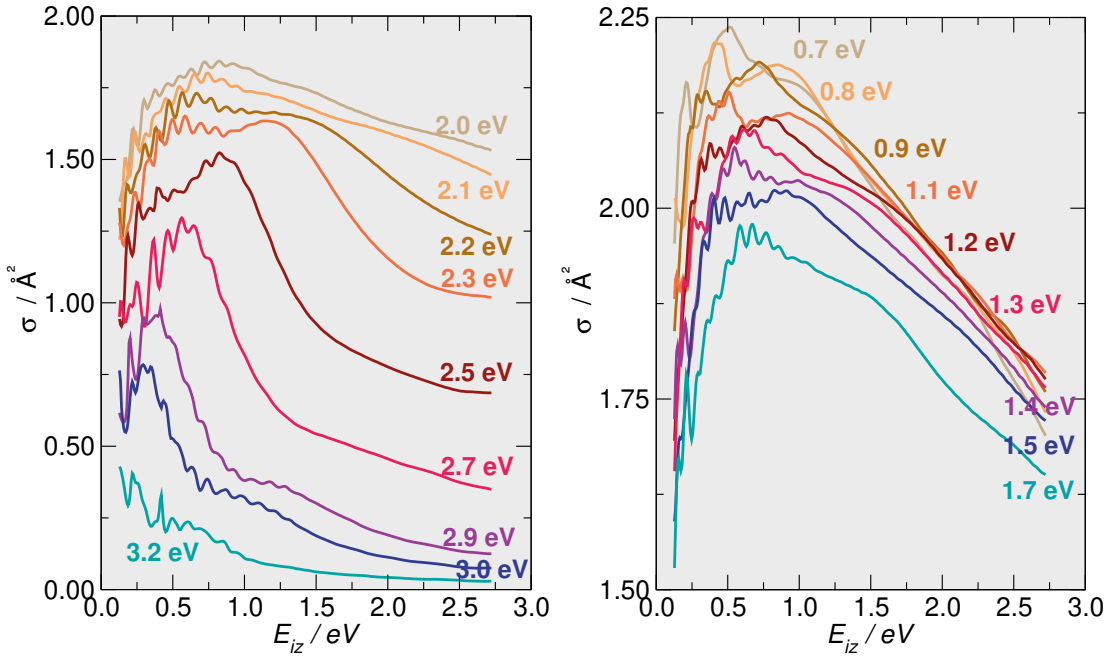

Figure 9.3. Eley-Rideal reaction cross-sections, σ, (Å^2), as functions of the incident atom collision energies, E_{iz} (eV), at target binding energies (different colors) typical of the buffer (Left) and monolayer graphene (Right) on SiC.

9.3 (left). These σ already include the spin-statistical factor of 1/4. Earlier classical and quasiclassical trajectory analysis on graphite by R.Martinazzo et. al.[255] have shed light on the details of the scattering mechanism and the resulting cross-sections. For the system at hand, in the range of 2.0-2.7 eV, the behavior of the ER cross-sections is parallel to that observed on graphite, hence we can reasonably assume that the underlying scattering mechanism is the same. Namely, In the low energy regime, a slight increase of E_{iz} results in an increase of σ, because the target is able to capture projectiles with higher impact parameters. A further increase of E_{iz} determines a loss of reactivity and a reduction of σ because other mechanisms can set it (for instance, the projectile can be scattered away or collide multiple times with the target). The effect of deepening the chemisorption well of the target is clear: σ starts to steeply decrease at collision energies that are smaller and smaller as D increases. Yet, σ are still large, and, contrary to what observed on metal surfaces[5], they exceed 1 Å^2 up to $D \leq 2.7$ eV and $E_{iz} \leq 1.0$ eV.

The situation dramatically changes at larger D. Above 2.9 eV, σ keeps decreasing over the entire range of E_{iz} considered and they become even vanishing at the largest values when the collision energy exceeds ≈ 1.75 eV. On the buffer layer graphene, binding energies close to 3.0-3.2 eV are typical of C^{32} atoms, *i.e.* carbons with 2 Si-bonded nearest neighbor. Because of the vanishing reaction cross-sections, one can then expect that the ER reaction hardly occurs on these sites. The picture that emerges from the combination of our DFT and QM calculations may be described as follows. When the C/Si interface is exposed to an H flux, the hydrogenation may, in principle, proceed randomly, since H atoms should not find any barrier to sticking, by virtue of the large D. However, most of the sites are still characterized by sizeable ER cross-section and, once hydrogenated, can undergo abstraction reaction. In contrast, the small fraction of C atoms represented by C^{32} with the largest binding energies, is expected to remain populated by H throughout the entire H exposure, because of a vanishing (or negligibly small) cross-section.

[5]Note that the H binding energies on typical metal surface are comparable, ranging from 2.0 to 2.5 eV.

Table 9.1. Grid parameters for the quantum calculations, where P stands for "product" coordinate set; $(x, z) = (Z, z)$; N_i is the number of grid points along the coordinate i and Δx_i is the grid spacing. Distances are in angstrom.$Z_s, z_s^-, z_s^+, \rho_s$ define the coordinates where the absorbing potentials are started.

	P
$Z_{\min}$	0.00
Δ_Z	0.035
N_Z	216
$z_{\min}$	-5.00
Δ_z	0.070
N_z	225
L_ρ	13.0
N_ρ	190
Z_s	6.00
$(z_s^-)z_s^+$	(-3.10)8.0
ρ_s	12.0

9.2.1 Vibrational and rotational excitations

Figure 9.4 displays the behavior of vibrational and rotational excitations of the product molecule as a function of the collision energies, at different D of the target. The vibrational and rotational state of the product depends on the scattering mechanism followed during the reaction. For the problem at hand, the investigation of the reaction mechanism was out of scope. Nevertheless, the description of Figure 9.4 can be again guided by the quasiclassical picture of the scattering mechanism provided by earlier works on graphite.

At low binding energies and in the low collision energy regime, a hot vibrational and cold rotational product is formed. The latter arises from a collinear or quasi-collinear scattering mechanism, where the projectile directly impinges on the target and most of the translational energy is thus converted into internal vibrations. In this regime, an initial increase of the projectile collision energy determines a reduction of the vibrational excitation and a corresponding more efficient conversion of incident kinetic energy into product translational energy (see above). As mentioned earlier, a further increase of the collision energy determines a loss of reactivity, because the projectile can scatter away or regain its energy after colliding with the target. Then, the reaction generally occurs through *glancing collisions* by H with high impact parameters, leading to rotationally hot and vibrationally cold molecules. Noticeably, the trend is reversed as the binding energy exceeds 2.7 eV: when the target atom is strongly bound to the surface, both the vibrational and rotational excitation increases with the collision energy.

9.3 ER recombination on the monolayer graphene

The H_2 recombination have been investigated also on the monolayer graphene, again by tuning the depth of the chemisorption well of the target atom in the range of values found with DFT calculations. The resulting spin-statistics corrected cross-sections are displayed in Figure 9.3 (right), while the vibrational and rotational states of the product molecule are displayed in Figure 9.5.

At the relevant values, the behavior of σ is parallel to that observed for the low binding energy regime on the buffer layer: the reactivity is initially promoted by an increase of the projectile collision energy, but then, at larger E_{iz}, the recombination mechanism becomes

Figure 9.4. Vibrational (Left) and Rotational (Right) excitations of the product molecule (H_2), as functions of the collision energy of the incident atom, E_{iz} (eV), at binding energies of the target (different colors) typical of the buffer layer graphene on SiC

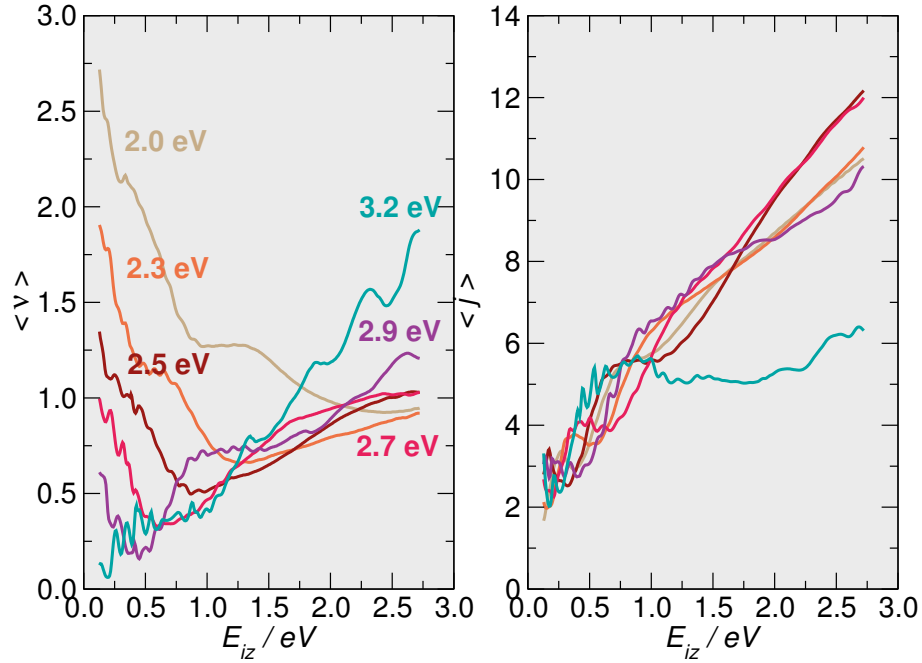

Figure 9.5. Vibrational (Left) and Rotational (Right) excitations of the product molecule (H_2), as functions of the collision energy of the incident atom, E_{iz} (eV), at binding energies of the target (different colors) typical of the monolayer graphene on SiC

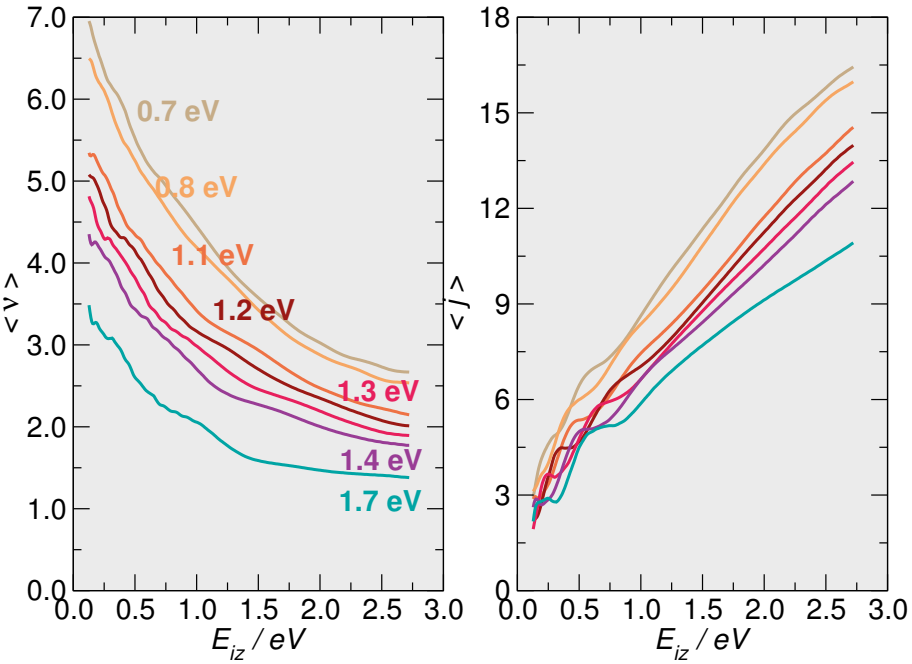

gradually rather inefficient[6]. Nevertheless, we note that σ still exceeds $1\,\text{Å}^2$ on the whole range of collision energies, and therefore, also for the monolayer, the rate of the ER reaction remains quite large (*e.g.* larger than on typical metal surfaces).

Similar considerations apply to Figure 9.5. Vibrational and rotational excitations are steeply decreasing and increasing functions of E_{iz}, respectively, as for the H_2 recombination on graphitic surfaces[255].

[6]We should also remind that as E_{iz} exceeds the target binding energy, the CID channel opens, thus leading to a further fall of the ER cross-sections

Part III

Towards a *curved* theory of π-conjugation

Chapter 10

The mathematics of the *curved* world

In this Chapter we introduce some mathematical concepts that are instrumental for the later development of a mathematical description of curved π-systems, which is left to Chapter 11. During his Ph.D. course, the author has spent a great amount of time on the study of *differential geometry*, a wide field of maths that, roughly speaking, applies the theory of differential calculus to the study of arbitrary "curved" spaces. This Chapter represents then a summary of part of the knowledge acquired on this topic. The expert reader will notice that we will not talk about *connections* or *covariant derivative*, fundamental concepts that lie at the heart of the subject and, in particular, of the general theory of tensors on differentiable manifolds[1]. The reason is that the author has decided to give here more emphasis to the classical theory of *surfaces* (2-dimensional Riemannian manifold emdedded in a 3-dimensional Euclidean space (E_3)), which is more relevant to this work[2] . In a sense, such approach follows the historical development of the topic. Indeed, Riemannian manifolds[261] were first introduced, namely differentiable manifolds endowed with a $(0,2)$ covariant tensor field, g_{ij}, called **metric tensor**. The latter allows measuring arc lengths of curves, angles between vectors on manifolds, curvature properties, and therefore guarantees a rich geometrical structure. However, it was later realized that the metrics is not necessary for a self-contained theory of curvature: one just needs a set of coefficients following a specific transformation law, called *affine connection*. If the reader is interested in this second general approach to the subject, (s)he is referred to the wonderful book *Tensors, Differential forms and Variational Principles*, by D. Lovelock and H. Rund (1989)[262], which the author discovered by chance but that was fundamental for his comprehension of the matter.

This Chapter is organized as follows: in Section 1 we review some basic concepts about the theory of curves and surfaces; in Section 2, we introduce the *first fundamental form*; in Section 3 we will see how the first fundamental form enables us to measure distances, angles and area elements on a generic surface; in Section 4, thanks to the introduction of the *second fundamental form*, we will begin to talk about the concept of "curvature"; in Section 5, we introduce the *principal curvatures* and the related *mean* and *Gaussian curvature* - this is the most important Section for the purposes of Chapter 11; finally, in

[1] In this context, it is suffices to know that a *manifold* is a topological space that *locally* resembles an Euclidean space, but globally may look completely different. More precisely, a manifold ($\mathcal{M}$) is a separable Hausdorff topological space that can be *covered* by an *atlas*, that is a collection of *charts* $\{U_\alpha, h_\alpha\}$ with α a set of indexes, where U_α are open sets of a point $p \in \mathcal{M}$ and h_α are homeomorphisms to $\mathbb{R}^n$, *i.e.* $h_\alpha : U_\alpha \to \mathbb{R}^n$. A manifold is said to be *differentiable* if it is endowed with a *differentiable structure*, *i.e.* an atlas such that each of its charts are C^∞-compatible with each other.

[2] The interested reader is referred to the book of Kreyszig (1991)[260], that specifically deals with the differential geometry of surfaces.

Section 6 we present the theory of curvature of Riemannian spaces. Connections with the general theory of "affinely connected spaces" will be made throughout when possible.

10.1 Introduction: curves and surfaces

As we shall see later in this Chapter, in many investigations of geometrical properties (such as the curvature itself), one looks at special classes of curves to extract relevant information on the surface under examination. Therefore, the study of curves on surfaces is at the heart of classical differential geometry and needs to be treated in detail for our subsequent discussion. In this Section, we begin by reviewing some basic concepts about curve in E_3. Next, we give a formal definition of a surface and its representation.

10.1.1 Curves in E_3

Let consider an Euclidean space E_3 and introduce a Cartesian coordinate system x_i (with $i = 1, 3$) so that any point $q \in E_3$ can be represented as $\boldsymbol{x} = (x_1, x_2, x_3)$. A curve C is defined by a *one-parameter* representation $\boldsymbol{x} = \boldsymbol{x}(t)$, with t defined in the interval $I : a \leq t \leq b$, such that $x_i(t)$ are of class C^r, with $r \geq 1$, and $\forall t \in I$, at least one of the three functions $x_i'(t) = dx_i(t)/dt$ is different from zero.

Among all allowable parametric representation for a curve, a special role is played by the representation in terms of the *arc length*, s, also called "natural parameter", defined according to

$$s = \int_a^b \sqrt{\sum_{i=1}^{3} \left(\frac{dx_i}{dt}\right)^2} dt = \int_a^b \sqrt{(\boldsymbol{x}'|\boldsymbol{x}')} dt$$

where $(\cdot|\cdot)$ is the standard scalar product in E_3 and $'$ denotes the derivative w.r.t. t. The reasons is that many results of the theory of curves in E_3 are simplified in such representation. We introduce the *element of arc* or *line element* of C, ds^2, symbolically defined as

$$ds^2 = \sum_{i}^{3} dx_i^2 = (d\boldsymbol{x}|d\boldsymbol{x}) \tag{10.1}$$

A curve with allowable parametric representation $\boldsymbol{x}(s)$ can be characterized through the definition of a number of vectors. First, one define the **unit tangent vector**, $\boldsymbol{T}(s)$ to the curve C at the point $\boldsymbol{x}(s)$ as

$$\boldsymbol{T}(s) = \lim_{h \to 0} \frac{\boldsymbol{x}(s+h) - \boldsymbol{x}(s)}{h} = \frac{d\boldsymbol{x}}{ds} = \dot{\boldsymbol{x}}(s) \tag{10.2}$$

Being $\boldsymbol{T}$ a unit vector, by differentiating the relation $(\boldsymbol{T}|\boldsymbol{T}) = 1$, we get $(\boldsymbol{T}|\dot{\boldsymbol{T}}) = 0$. Hence, if the vector $\dot{\boldsymbol{T}} = \ddot{\boldsymbol{x}}$ is not the null vector, it has to be orthogonal to the unit tangent vector - in other words it lies on the plane *normal* to the curve C at the point under consideration. The corresponding unit vector

$$\boldsymbol{P}(s) = \frac{\dot{\boldsymbol{T}}(s)}{|\dot{\boldsymbol{T}}(s)|} \tag{10.3}$$

is referred to as **unit principal normal** to the curve C. The vectors $\boldsymbol{T}$ and $\boldsymbol{P}$ together span a plane called *osculating plane*. Since $\boldsymbol{P}$ belongs to both the osculating and the normal plane, it follows that this vector is actually the intersection between these planes. The absolute value of $\boldsymbol{P}$,

$$\kappa(s) = |\boldsymbol{P}(s)| = \sqrt{(\ddot{\boldsymbol{x}}(s)|\ddot{\boldsymbol{x}}(s))} \geq 0 \tag{10.4}$$

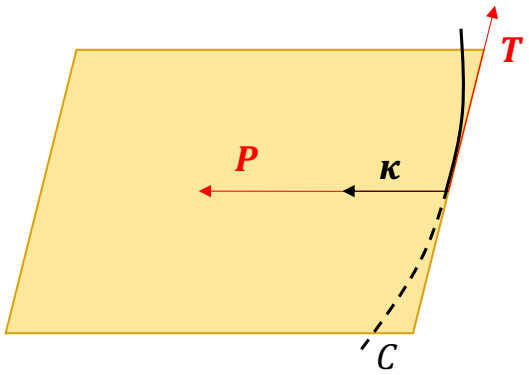

Figure 10.1. A curve C with the tangent vector $\boldsymbol{T}$, the principal normal vector $\boldsymbol{P}$ and the curvature vector $\boldsymbol{k}$ at a given point.

is called the **curvature** of the curve C at the point $\boldsymbol{x}(s)$[3]. This name is justified upon considering that $\kappa(s)$ is related to the rate of change of the unit tangent vector; therefore, for a straight line, $\dot{\boldsymbol{x}}(s) \equiv k$ with k a constant, everywhere on C, and $\kappa(s) \equiv 0$. One also define the reciprocal of the curvature

$$\rho(s) = \frac{1}{\kappa(s)} \tag{10.5}$$

that is called the *radius of curvature* of the curve C at the point $\boldsymbol{x}(s)$. It is advantageous for our later development of the theory to introduce the notation $\boldsymbol{k}(s) = \dot{\boldsymbol{T}}$ and call this vector the *curvature vector* of the curve C.

Remark 1. *Notice that, while the sense of the unit tangent vector to a curve depends on the orientation of the curve resulting from the choice of a certain representation, the unit principal normal vector is independent of the orientation of the curve.*

With the above definition, the unit principal normal is given by $\boldsymbol{P}(s) = \rho(s)\ddot{\boldsymbol{x}}(s)$. Since the latter and the unit tangent vector are orthogonal, one can uniquely introduce the following vector

$$\boldsymbol{B}(s) = \boldsymbol{T}(s) \times \boldsymbol{P}(s) \tag{10.6}$$

which is orthogonal to both $\boldsymbol{T}$ and $\boldsymbol{P}$ and is called the **unit binormal vector** of the curve C at the point $\boldsymbol{x}(s)$. From this definition, we have that $\boldsymbol{T}, \boldsymbol{P}, \boldsymbol{B}$ in this order define a right-handed local frame which is generally referred to as *moving trihedron*. Let now consider the two following scalar products, $(\boldsymbol{B}|\boldsymbol{B}) = 1$ and $(\boldsymbol{B}|\boldsymbol{T}) = 0$. By differentiation, we obtain

$$(\boldsymbol{B}|\dot{\boldsymbol{B}}) = 0 \quad \text{and} \quad (\dot{\boldsymbol{B}}|\boldsymbol{T}) + (\boldsymbol{B}|\dot{\boldsymbol{T}}) = 0$$

Since $\dot{\boldsymbol{T}} = \kappa\boldsymbol{P}$, we find that

$$(\dot{\boldsymbol{B}}|\boldsymbol{T}) = -(\boldsymbol{B}|\dot{\boldsymbol{T}}) = -\kappa(\boldsymbol{B}|\boldsymbol{P}) = 0$$

Hence, if the vector $\dot{\boldsymbol{B}}$ is not null, it has to be orthogonal to both $\boldsymbol{T}$ and $\boldsymbol{P}$, *i.e.* it is parallel to the unit principal normal. We may set then

$$\dot{\boldsymbol{B}}(s) = -\tau(s)\boldsymbol{P}(s) \tag{10.7}$$

[3]For a generic allowable parametric representation $\boldsymbol{x}(t)$, the analytic expression of the curvature reads as

$$\kappa = \frac{\sqrt{(\boldsymbol{x}'|\boldsymbol{x}')(\boldsymbol{x}''|\boldsymbol{x}'') - (\boldsymbol{x}'|\boldsymbol{x}'')^2}}{(\boldsymbol{x}'|\boldsymbol{x})^{3/2}}$$

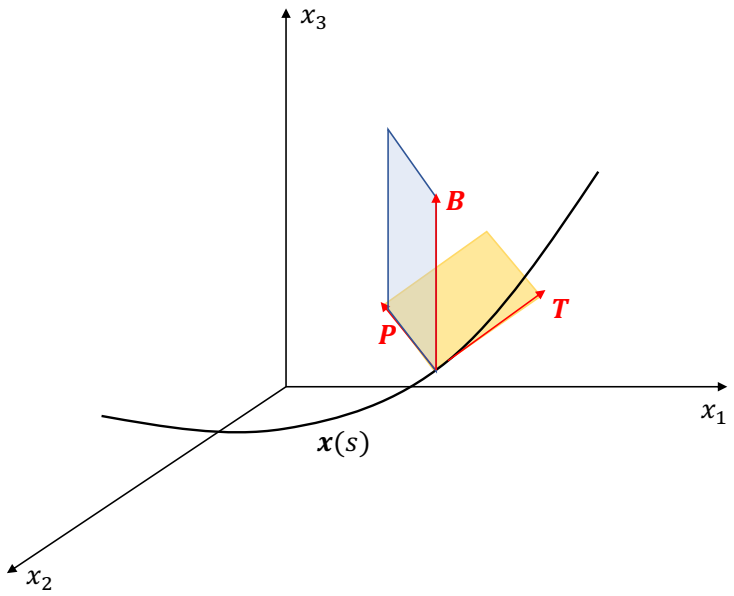

Figure 10.2. A curve C with the moving trihedron defined by the vector $\boldsymbol{T}, \boldsymbol{P}, \boldsymbol{B}$. The yellow and blue rectangles are the osculating and the normal plane respectively.

where $\tau(s) = -(\boldsymbol{P}(s)|\dot{\boldsymbol{B}}(s))$ is called the **torsion** of the curve C at the point $\boldsymbol{x}(s)$ (L.I. de la Vallé (1825)[263]), or at times also *second curvature*. The following Theorem holds (we omit the proof):

Theorem 10.1.1. *A curve, with non-vanishing curvature κ, is plane if and only if its torsion vanishes identically.*

From a geometrical perspective, the torsion τ thus measures how much the curve "leaves" the osculating plane, while the curvature κ is related to the degree of curvature on the osculating plane. In light of this, it should be clear that $\boldsymbol{T}, \boldsymbol{P}, \boldsymbol{B}$ and their first derivatives contain much of the information about the local geometry of a curve in E_3 In particular, because of their linear independence, one can write any vector defined at a point of a curve C in terms of $\boldsymbol{T}, \boldsymbol{P}, \boldsymbol{B}$. This applies also to the derivative vectors $\dot{\boldsymbol{T}}, \dot{\boldsymbol{P}}, \dot{\boldsymbol{B}}$. The corresponding formula are due to *Frenet*[264] and they are one of the most important results of the theory of curves. With some simple algebra, one finds, in matrix notation,

$$\begin{pmatrix} \dot{\boldsymbol{T}} \\ \dot{\boldsymbol{P}} \\ \dot{\boldsymbol{B}} \end{pmatrix} = \begin{pmatrix} 0 & \kappa & 0 \\ -\kappa & 0 & \tau \\ 0 & -\tau & 0 \end{pmatrix} \begin{pmatrix} \boldsymbol{T} \\ \boldsymbol{P} \\ \boldsymbol{B} \end{pmatrix} \tag{10.8}$$

10.1.2 Surfaces

Let consider the following real single-valued vector function

$$\boldsymbol{x}(u^1, u^2) = (x_1(u^1, u^2), x_2(u^1, u^2), x_3(u^1, u^2)) \tag{10.9}$$

in the two real variables u^1 u^2, which is defined on a bounded and simply connected set B on the plane (u^1, u^2). Any point $(u^1, u^2) \in B$ is associated then to a point $P \in E_3$ with position vector $\boldsymbol{x}(u^1, u^2)$. We denote by $\mathcal{M}$ the set of points we get when (u^1, u^2) vary in B. Equation (10.9) is said to be a *parametric representation* of the set $\mathcal{M}$ and, from a

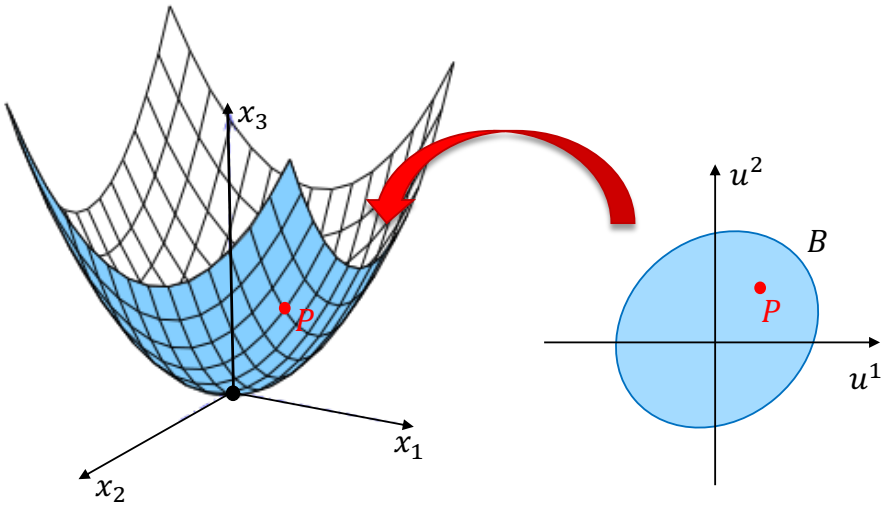

Figure 10.3. A surface $\mathcal{M}$ represented in terms of the vector-valued function $\boldsymbol{x} = \boldsymbol{x}(u^1, u^2)$. x_1, x_2, x_3 define the coordinate system in the Euclidean space E_3, while u^1, u^2 are the coordinates on the domain B. Each point P of the set $\mathcal{M}$ corresponds to just one ordered pair (u^1, u^2) in B.

geometrical point of view, it represents a *surface* (2-dimensional space[4]) embedded in E_3[5].

Remark 2. *The reason for using superscripts and subscripts will be explained in Subsection 10.2.1, when dealing with transformation laws.*

In order to apply differential calculus to a geometric "object" like that defined from Equation (10.9), we must require the existence of a certain number of partial derivatives of $\boldsymbol{x}(u^1, u^2)$ w.r.t. u^α (henceforth, we use a Latin index to refer to the Cartesian coordinate in E_3 and a Greek index to refer to the parameters u^1, u^2 of B). In addition, we must exclude the possibility that $\boldsymbol{x}(u^1, u^2)$ represents merely a curve in E_3. This amount to make the following assumptions:

(i) The function $\boldsymbol{x}(u^1, u^2)$ is of class C^r with $r \geq 1$. Each point of $\mathcal{M}$ corresponds to just one pair (u^1, u^2) in B.

(ii) The Jacobian matrix of elements $J_i^\alpha = \partial x_i / \partial u^\alpha$ is of rank 2 in B.

A parametric representation that satisfies Assumptions (i) and (ii) is said to be an *allowable representation*. Assumption (ii) excludes the possibility that $\mathcal{M}$ represents a curve[6], for which $\text{rank}(J) = 1$. Moreover, is a necessary and sufficient condition for the linear independence of the following vectors

$$\boldsymbol{x}_1 := \frac{\partial \boldsymbol{x}}{\partial u^1} \quad \text{and} \quad \boldsymbol{x}_2 := \frac{\partial \boldsymbol{x}}{\partial u^2}$$

that will play a central role in the later development of the theory.

There is no unique parametric representation of the set $\mathcal{M}$. Indeed, one may impose

[4]Here, we will always use the term "space", although it is understood that these are more generally (and rigorously) differentiable manifolds (see footnote 1 on pag. 141.

[5]This is not the unique allowable representation of a surface. Indeed, in some context it is more convenient to define the surface as the graph of a two-variables function (when possible), $z = f(x, y)$.

[6]There may be points where $\text{rank}(J) < 2$. These are called *singular point for the representation*. If they are singular w.r.t. any allowable representation of $\mathcal{M}$, they are referred to *singular points of* $\mathcal{M}$. An example are poles of a sphere.

the following transformation law

$$u^\alpha = u^\alpha(\bar{u}^\beta) \quad (\alpha, \beta = 1, 2) \tag{10.10}$$

to obtain a new parametric representation $\boldsymbol{x}(\bar{u}^1, \bar{u}^2)$. Of course, for such a new representation to be an allowable representation, it has to satisfy again Assumptions (i) and (ii). We therefore require that

(i) The functions (10.10) are defined in a domain $\bar{B}$ such that the corresponding range of values includes B.

(ii) The functions (10.10) are a one-to-one transformations of class C^r with $r \geq 1$ everywhere in $\bar{B}$.

(iii) The Jacobian D of the matrix of elements $D^{\alpha\beta} = \partial u^\alpha / \partial \bar{u}^\beta$ is different from zero everywhere in $\bar{B}$.

A coordinate transformation satisfying these conditions is said to be an *allowable coordinate transformation*. By means of (10.10), we may classify allowable representations into *equivalence classes*. Namely, we say that two allowable representation are equivalent if they belong to the same equivalence class, *i.e.* there is a transformation law of the form (10.10) mapping one into the other. We are now in position to give the following

Definition 10.1.1. *A surface is a point set in space E_3 which can be represented by an allowable representations of an equivalence class.*

Because of the Assumption (i) on the parametric representation, the correspondence between the points of a surface and the ordered pair (u^1, u^2) is one-to-one. Therefore, u^1 and u^2 can be considered as *coordinates* on $\mathcal{M}$. The corresponding curves $u^1 = \text{const}$ and $u^2 = \text{const}$ are called *coordinate curves*.

Let turn now our attention to curves on a surface. A curve C on a surface $\mathcal{M}$ can be determined by a parametric representation of the form $u^\alpha = u^\alpha(t)$, of class C^r with $r \geq 1$ where t is a real parameter[7] in a given interval $I : a \leq t \leq b$. When we substitute such representation into the parametric representation of $\mathcal{M}$, we get a set of points of coordinates $x^i(u^\alpha(t))$ defining the curve C on the surface. As for generic curves in E_3, we could introduce the local Frenet reference of frame specified by the vectors $\boldsymbol{T}, \boldsymbol{P}, \boldsymbol{B}$ at each point of the curve. However, as we shall see in the following, for the present case we may exploit the geometrical structure of the surface on which the curve is defined to introduce a new reference of frame.

Following the arguments of Subsection 10.1.1, it is still convenient to introduce the *tangent vector* $\boldsymbol{T}(t)$ again by taking the first derivative of $\boldsymbol{x}(u^\alpha(t))$ w.r.t. t. Hence, we get

$$\boldsymbol{T}(t) = \frac{d\boldsymbol{x}}{dt} = \frac{\partial \boldsymbol{x}}{\partial u^1}\frac{du^1}{dt} + \frac{\partial \boldsymbol{x}}{\partial u^2}\frac{du^2}{dt} = \boldsymbol{x}_\alpha u'^\alpha \tag{10.11}$$

Remark 3. *In the last step of Equation 10.11 we have used the Einstein summation convention. If in a product, an index figures twice, once as superscript and once as subscript, summation must be carried out from 1 to 2 w.r.t. that letter. The summation sign is omitted. We adopt this convention henceforth.*

Therefore, the unit tangent vector of the curve C at a point P on the surface $\mathcal{M}$ is a linear combination of the above introduced vectors, $\boldsymbol{x}_1, \boldsymbol{x}_2$, The latter are vectors tangential to surface coordinate curves passing through the point P. If P is not a singular point for

[7]For the present discussion, it is irrelevant whether the curve is defined through a natural representation $\boldsymbol{x}(s)$ or not.

the allowable parametric representation at hand, then $\boldsymbol{x}_1, \boldsymbol{x}_2$ are linear independent and we have the following definition

Definition 10.1.2. *The vectors $\boldsymbol{x}_1$ and $\boldsymbol{x}_2$ span a plane called **tangent plane** ($T_P(\mathcal{M})$) that is tangent to the surface $\mathcal{M}$ at the point P. Such plane contains tangent vectors of any curve on $\mathcal{M}$ passing through P.*

With the above definitions, we are now able to introduce the first concepts of Riemannian geometry.

10.2 Basic concepts of Riemannian geometry: the first fundamental form

As we pointed out in the introduction to Section 10.1, most of the key results on differential geometry of curved surfaces arises from the study of curves. The first task we consider is thus the determination of the element of arc ds^2 of a curve C defined on a surface. We will see that this problem leads to one of the most important concept in the theory of surfaces.

Let consider a curve C, represented as $u^\alpha(t)$, on surface $\mathcal{M} : \boldsymbol{x}(u^1, u^2)$. From Equation 10.11, we may represent a displacement vector from a point $P \in C$ on the surface as $d\boldsymbol{x} = \boldsymbol{x}_\alpha du^\alpha$. Hence, from the definition of line element of C given in Equation 10.1, we find

$$ds^2 = (d\boldsymbol{x}|d\boldsymbol{x}) = (\boldsymbol{x}_1|\boldsymbol{x}_1)(du^1)^2 + 2(\boldsymbol{x}_1|\boldsymbol{x}_2)du^1du^2 + (\boldsymbol{x}_2|\boldsymbol{x}_2)(du^2)^2 \tag{10.12}$$

We introduce the notation $(\boldsymbol{x}_\alpha|\boldsymbol{x}_\beta) = g_{\alpha\beta}$, so that we can write

$$\boxed{ds^2 = g_{\alpha\beta}du^\alpha du^\beta} \tag{10.13}$$

Such quadratic form is called the **first fundamental form**. Its discriminant g is given by

$$g = \det(g_{\alpha\beta}) = g_{11}g_{22} - g_{12}^2$$

We shall see later in this Section that the first fundamental form enables us to measure arc lengths, angles and areas on a surface. Therefore, it is said to define a *metric* on a surface. The coefficients $g_{\alpha\beta}$ are the components of a *tensor* called the **metric tensor**. The concept of a tensor will be explained shortly in Subsection 10.2.1 in connection with coordinate transformation laws.

Definition 10.2.1. *A Riemannian space is a space in which a Riemannian metric, i.e. a metric defined by a positive definite*[8]*, quadratic differential form, is introduced.*

In consequence of such definition, surfaces are two-dimensional Riemannian spaces, and their corresponding geometry is a Riemannian geometry.

Before looking at the relevant applications of the first fundamental form, it is worthy to introduce some basic concepts about tensor calculus. As we mentioned in the introduction, tensor calculus enables to approach the theory of differential geometry from a more general perspective. Being a special case of the general theory, we will see that also many aspects of the theory of surfaces are simplified when treated with the aid of some basic rules governing tensor calculus. Moreover, the latter allows an immediate generalization to Riemannian spaces of higher dimensions.

[8] In the mathematical literature, the term "pseudo-Riemannian" is at times used to denote an indefinite Riemannian metric.

10.2.1 Transformation laws: contravariant and covariant tensors

Let consider an allowable coordinate transformation

$$u^\alpha = u^\alpha(\bar{u}^\beta) \tag{10.14}$$

Henceforth, we drop the restriction of the dimension ($n = 2$), that is both α and β now range from 1 to n, where $n > 2$ is the dimension of a generic Riemannian space. The transformation law given in Equation 10.14 and its inverse[9] can be written in the form

$$u^\alpha = f^\alpha(\bar{u}^1, \bar{u}^2, ..., \bar{u}^n) \tag{10.15}$$

$$\bar{u}^\alpha = h^\alpha(u^1, u^2, ..., u^n) \tag{10.16}$$

Therefore, we may also write $u^\alpha = f^\alpha(h^1, h^2, ..., h^n)$. Differentiating w.r.t. u^β and exploiting the laws of partial differentiation, we find

$$\frac{\partial u^\alpha}{\partial u^\beta} = \frac{\partial f^\alpha}{\partial h^\gamma}\frac{\partial h^\gamma}{\partial u^\beta}$$

Since u^α and u^β are independent if $\alpha \neq \beta$, we obtain

$$\frac{\partial u^\alpha}{\partial \bar{u}^\gamma}\frac{\partial \bar{u}^\gamma}{\partial u^\beta} = \delta^\alpha_\beta$$

By the same token,

$$\frac{\partial \bar{u}^\alpha}{\partial u^\gamma}\frac{\partial u^\gamma}{\partial \bar{u}^\beta} = \delta^\alpha_\beta$$

where δ^α_β is the delta Kronecker symbol ($\delta^\alpha_\beta = 0$ (1) whether $\alpha \neq \beta$ ($\alpha = \beta$)). From the rules of partial differentiation, we have the following relations between the differentials in the coordinate systems $(du^\alpha, d\bar{u}^\beta)$

$$d\bar{u}^\beta = \frac{\partial \bar{u}^\beta}{\partial u^\alpha} du^\alpha \tag{10.17}$$

Conversely, we find

$$du^\gamma = \frac{\partial u^\gamma}{\partial \bar{u}^\beta} d\bar{u}^\beta \tag{10.18}$$

We say that Equation 10.14 *induces* a homogenous linear transformation on the differentials. Notice that the coefficients of such transformation are functions of the coordinates. A transformation of the kind (10.17) is referred to as a *contravariant transformation law.* More precisely, we say that

Definition 10.2.2. *A set of real numbers $T^1, T^2, ..., T^n$ associated to a point P of n-dimensional (Riemannian) space constitute the components of a contravariant tensor of first order or type (0,1)-tensor if, under an allowable coordinate transformation of the kind* (10.14)*, they transform according to*

$$\bar{T}^\beta = \frac{\partial \bar{u}^\beta}{\partial u^\alpha} T^\alpha \tag{10.19}$$

Notice that the above definition holds also for a generic space, without the need of a metric. type $(0, 1)$-tensor are usually referred to as *contravariant vector.* The corresponding components v^α of a contravariant vector $\boldsymbol{v}$, are indicated by a superscript. Definition 10.2.2 can be easily extended to more general type $(0, s)$-tensor, *i.e.* a set of n^s real numbers

[9] We are assuming that $u^\alpha = u^\alpha(\bar{u}^\beta)$ is of class C^r with $r \geq 1$. Then, its inverse exists and is of the same class.

$T^{\alpha_1,\alpha_2,...,\alpha_s}$ with $\alpha_1,\alpha_2,...,\alpha_s = 1,...n$ specified by s superscripts, transforming according to

$$\bar{T}^{\beta_1,\beta_2,...,\beta_s} = \frac{\partial \bar{u}^{\beta_1}}{\partial u^{\alpha_1}} \frac{\partial \bar{u}^{\beta_2}}{\partial u^{\alpha_2}} \cdots \frac{\partial \bar{u}^{\beta_s}}{\partial u^{\alpha_s}} T^{\alpha_1,\alpha_2,...,\alpha_s} \tag{10.20}$$

Remark 4. *In general, the quantities $T^{\alpha_1,\alpha_2,...,\alpha_s}$ will be given not only to a point P but on a certain region D of the space. In other words, they will be functions of coordinates defined in D. Then, we say that in D a type $(0,s)$-**contravariant tensor field** is given. Type $(0,1)$-contravariant tensor fields are generally known as vector fields.*

Let consider again the first fundamental form $ds^2 = g_{\alpha\beta} du^\alpha du^\beta$. Being the line element of a curve C, ds^2 must be an *invariant* w.r.t. any allowable coordinate transformation. Therefore, we have to ask how the quantities $g_{\alpha\beta}$ must behave under an allowable coordinate transformation in order that ds^2 be an invariant. In doing so, we must consider that the quantities du^α, du^β behave as contravariant vectors. We may consider this problem from a more general perspective, looking at the quantity

$$I = v_\alpha v^\alpha$$

We assume I to be an invariant w.r.t. any allowable coordinate transformation and v^α the components of a contravariant vector. We have

$$\bar{v}_\beta \bar{v}^\beta = v_\alpha v^\alpha$$

By substitution of the inverse of the contravariant transformation law (10.23), we find

$$\bar{v}_\beta \bar{v}^\beta = v_\alpha \bar{v}^\beta \frac{\partial u^\alpha}{\partial \bar{u}^\beta} \tag{10.21}$$

Such relation must hold for any arbitrary vector v^α. Hence, by comparing the coefficients of corresponding components $\bar{v}^\beta$ on both side of Equation (10.21), we find

$$\bar{v}_\beta = \frac{\partial u^\alpha}{\partial \bar{u}^\beta} v_\alpha \tag{10.22}$$

Equation (10.22) defines a transformation law that differs from the contravariant transformation law expressed in Definition 10.2.2. Therefore, this leads us to the following

Definition 10.2.3. *A set of real numbers $T_1, T_1, ..., T_n$ associated to a point P of n-dimensional (Riemannian) space constitute the components of a covariant tensor of first order or type $(1,0)$-tensor if, under an allowable coordinate transformation of the kind* (10.14)*, they transform according to*

$$\bar{T}_\beta = \frac{\partial u^\alpha}{\partial \bar{u}^\beta} T_\alpha \tag{10.23}$$

The extension to a general $(r,0)$-tensor field is trivial

$$\bar{T}_{\beta_1,\beta_2,...,\beta_r} = \frac{\partial u^{\beta_1}}{\partial \bar{u}^{\alpha_1}} \frac{\partial u^{\beta_2}}{\partial \bar{u}^{\alpha_2}} \cdots \frac{\partial u^{\beta_r}}{\partial \bar{u}^{\alpha_r}} T_{\alpha_1,\alpha_2,...,\alpha_r} \tag{10.24}$$

In light of Equation (10.20) and (10.24), we are now in position to give the general definition of a (mixed) (r,s)-tensor field. Namely,

Definition 10.2.4. *A set of n^{r+s} real numbers $T^{\beta_1,\beta_2,...,\beta_s}_{\alpha_1,\alpha_2,...,\alpha_r}$ associated to a point P of n-dimensional (Riemannian) space constitute the components of a mixed type (r,s)-tensor if, under an allowable coordinate transformation of the kind* (10.14)*, they transform according*

to

$$\bar{T}^{\kappa_1,\kappa_2,\ldots,\kappa_s}_{\gamma_1,\gamma_2,\ldots,\gamma_r} = \frac{\partial u^{\alpha_1}}{\partial \bar{u}^{\gamma_1}} \cdots \frac{\partial u^{\alpha_r}}{\partial \bar{u}^{\gamma_r}} \frac{\partial \bar{u}^{\kappa_1}}{\partial u^{\beta_1}} \cdots \frac{\partial \bar{u}^{\kappa_s}}{\partial u^{\beta_s}} T^{\beta_1,\beta_2,\ldots,\beta_s}_{\alpha_1,\alpha_2,\ldots,\alpha_r} \tag{10.25}$$

In consequence of the above discussion, one can easily prove the two following theorems:

Theorem 10.2.1. *Under an allowable coordinate transformation of kind* (10.14)*, the coefficients $g_{\alpha\beta}$ of the first fundamental form transform according to*

$$\bar{g}_{\mu\nu} = \frac{\partial u^{\alpha}}{\partial \bar{u}^{\gamma}} \frac{\partial u^{\beta}}{\partial \bar{u}^{\nu}} g_{\alpha\beta}$$

i.e. they are the components of a type (0,2)-covariant tensor field.

Theorem 10.2.2. *Under an allowable coordinate transformation of kind* (10.14)*, the discriminant g of the first fundamental form transforms according to*

$$\bar{g} = D^2 \bar{g} \qquad g = \bar{D}^2 \bar{g}$$

where D ($\bar{D}$) are the Jacobians of the (inverse) coordinate transformation.

Before moving on, it is worthy to list some basic rules of tensor calculus. By addition of corresponding components of two tensors of the same type, $T^{\beta_1,\ldots,\beta_s}_{\alpha_1,\ldots,\alpha_r}$ and $S^{\beta_1,\ldots,\beta_s}_{\alpha_1,\ldots,\alpha_r}$, we obtain a tensor with components

$$V^{\beta_1,\ldots,\beta_s}_{\alpha_1,\ldots,\alpha_r} = T^{\beta_1,\ldots,\beta_s}_{\alpha_1,\ldots,\alpha_r} + S^{\beta_1,\ldots,\beta_s}_{\alpha_1,\ldots,\alpha_r}$$

which is called the *sum* of those tensors. If we multiply every component of a tensor by a scalar we obtain a tensor of the same type. It follows that *the totality of tensor of the same type defined at a point P of a n-dimensional Riemannian space form a vector space* ($\mathcal{T}^s_r$).

Any tensor of second order can be represented as a sum of a symmetric and a skew-symmetric one

$$T_{\alpha\beta} = \frac{1}{2}\left(T_{\alpha\beta} + T_{\beta\alpha}\right) + \frac{1}{2}\left(T_{\alpha\beta} - T_{\beta\alpha}\right)$$

Remark 5. *The metric tensor $g_{\alpha\beta}$ is symmetric, that is its skew-symmetric part vanishes identically.*

If we equate two indices of a mixed (r, s)-tensor, a contravariant and a covariant index, and sum w.r.t. this pair of indices, we obtain a $(r-1, s-1)$-tensor. Such operation is called *contraction* of the given tensor. Notice that by a contraction of a $(1, 1)$-tensor we obtain a scalar

$$v^{\alpha}_{\alpha} = v^1_1 + v^2_2 + \ldots + v^n_n$$

10.2.2 Vectors on a surface

We will now apply the knowledge gained on tensor calculus to the theory of surfaces. Therefore, in the following we will restrict our attention to two-dimensional Riemannian space embedded again in E_3 and to first order tensors, *i.e.* vectors. In the preceding Subsection, we have introduced covariant and contravariant vectors as entirely different and independent entities. This is the case when the space under investigation is not endowed with a metric tensor. However, as we shall see in this Subsection, in Riemannian space we may correlate these two types of vectors and, in addition, interpret them geometrically in a very simple manner.

First, we have the following

Definition 10.2.5. *A vector $\boldsymbol{v}$ bound at a regular point P of a surface $\mathcal{M}$ which lies in the tangent plane $T_P(\mathcal{M})$ at P is called a vector in the surface $\mathcal{M}$ at P.*

Therefore, the vectors on $\mathcal{M}$ are just a subset of the set of *all* vectors bound at P, which of course includes also vectors that do not belong to the tangent plane. In light of this Definition, it is natural to express $\boldsymbol{v}$ in terms of $\{\boldsymbol{x}_\alpha\}$, *i.e.* the (local) basis spanning the tangent plane. Hence

$$\boldsymbol{v} = v^\alpha \boldsymbol{x}_\alpha = v^1 \boldsymbol{x}_1 + v^2 \boldsymbol{x}_2 \tag{10.26}$$

We should remind that $\boldsymbol{x}_\alpha$ are tangent to the coordinated curves though P on $\mathcal{M}$ but they are not unit vectors. In particular, their lengths are related to the metric tensor through

$$\sqrt{(\boldsymbol{x}_\alpha|\boldsymbol{x}_\alpha)} = \sqrt{g_{\alpha\alpha}}$$

The ordered pair v^1, v^2 are the lengths (taken with a suitable sign) of the respective parallel projections of $\boldsymbol{v}$ upon the axis of the coordinate system defined by $\boldsymbol{x}_\alpha$ in $T_P(\mathcal{M})$, measured in units of $\sqrt{g_{11}}$ and $\sqrt{g_{22}}$ respectively. The vector $\boldsymbol{v}$, as geometrical object, is an invariant, and, therefore, under an allowable coordinate transformation $\bar{u}^\beta = \bar{u}^\beta(u^\alpha)$, we have

$$\boldsymbol{v} = \bar{v}^\beta \boldsymbol{x}_{\bar{\beta}} \tag{10.27}$$

where

$$\boldsymbol{x}_{\bar{\beta}} \equiv \frac{\partial \boldsymbol{x}}{\partial \bar{u}^\beta}$$

Since

$$\boldsymbol{x}_\alpha = \boldsymbol{x}_{\bar{\beta}} \frac{\partial \bar{u}^\beta}{\partial u^\alpha}$$

we find

$$\boldsymbol{v} = v^\alpha \boldsymbol{x}_\alpha = v^\alpha \boldsymbol{x}_\beta \frac{\partial \bar{u}^\beta}{\partial u^\alpha} \tag{10.28}$$

By comparing (10.27) and (10.28), we obtain

$$\bar{v}^\beta = \frac{\partial \bar{u}^\beta}{\partial u^\alpha} v^\alpha \tag{10.29}$$

In other words, we have proved the following

Theorem 10.2.3. *The contravariant components v^α of a vector $\boldsymbol{v}$ in a surface $\mathcal{M}$ at a regular point P are the lengths (taken with a suitable sign) of the parallel projections of $\boldsymbol{v}$ on the axes of the (parallel) coordinate system in $T_P(\mathcal{M})$ defined by vectors $\boldsymbol{x}_\alpha$; those lengths are measured in units of $\sqrt{g_{11}}$ and $\sqrt{g_{22}}$ respectively.*

Instead of taking the parallel projections of $\boldsymbol{v}$, we may as well consider its orthogonal projections on the axes of the above defined coordinate system. Let then γ_α be the angle between $\boldsymbol{v}$ and $\boldsymbol{x}_\alpha$. The length of the orthogonal projection L_α will be

$$\begin{aligned} L_\alpha &= |\boldsymbol{v}| \cos(\gamma_\alpha) = \frac{|\boldsymbol{x}_\alpha|}{|\boldsymbol{x}_\alpha|} |\boldsymbol{v}| \cos(\gamma_\alpha) \\ &= \frac{(\boldsymbol{x}_\alpha|\boldsymbol{v})}{\sqrt{(\boldsymbol{x}_\alpha|\boldsymbol{x}_\alpha)}} = \frac{1}{\sqrt{g_{\alpha\alpha}}} (\boldsymbol{x}_\alpha|\boldsymbol{v}) \end{aligned} \tag{10.30}$$

Hence, the number $(\boldsymbol{x}_\alpha|\boldsymbol{v})$ is the length (taken with a suitable sign) of the orthogonal projection of $\boldsymbol{v}$ on the $\boldsymbol{x}_\alpha$-coordinate axis, measured in units of $1\sqrt{g_{\alpha\alpha}}$. Of course, these numbers will depend on the choice of the coordinates on $\mathcal{M}$. Therefore, under an allowable

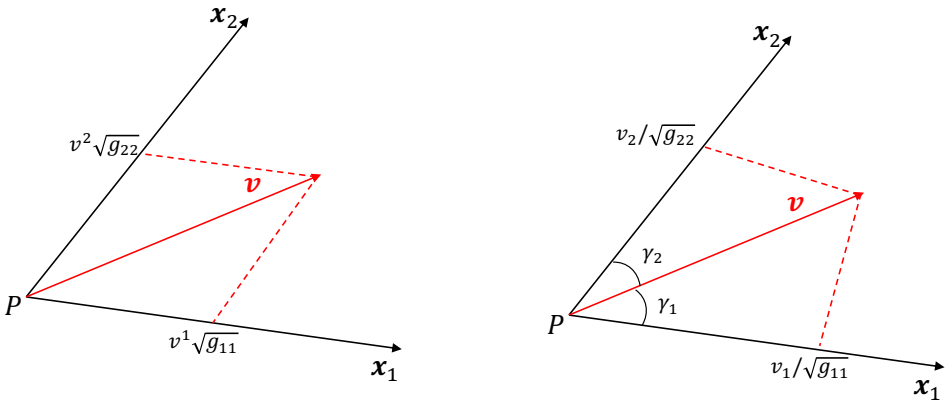

Figure 10.4. Controvariant (v^α) and covariant (v_α) components of a vector $\boldsymbol{v}$ interpreted as the parallel (Left) and orthogonal (Right) projections on the vectors spanning the tangent plane $(\boldsymbol{x}_1, \boldsymbol{x}_2)$.

coordinate transformation, we find

$$\bar{v}_\beta = (\boldsymbol{x}_{\bar{\beta}}|\boldsymbol{v}) = \frac{\partial u^\alpha}{\partial \bar{u}^\beta}(\boldsymbol{x}_\alpha|\boldsymbol{v}) = v_\alpha \frac{\partial u^\alpha}{\partial \bar{u}^\beta} \tag{10.31}$$

We have thus obtained the following result

Theorem 10.2.4. *The covariant components v_α of a vector $\boldsymbol{v}$ in a surface $\mathcal{M}$ at a regular point P are the lengths (taken with a suitable sign) of the orthogonal projections of $\boldsymbol{v}$ on the axes of the coordinate system in $T_P(\mathcal{M})$ defined by vectors $\boldsymbol{x}_\alpha$; those lengths are measured in units of $1/\sqrt{g_{11}}$ and $1/\sqrt{g_{22}}$ respectively.*

We have thus provided a geometrical interpretation of contravariant and covariant components of a vector. Now, by replacing $\boldsymbol{v}$ in $(\boldsymbol{x}_\alpha|\boldsymbol{v})$ with its expansion in the tangent plane, we find

$$v_\alpha = (\boldsymbol{x}_\alpha|v^\beta \boldsymbol{x}_\beta) = g_{\alpha\beta} v^\beta \tag{10.32}$$

in other words, the metric tensor establishes a correspondence between the covariant and contravariant components of a vector. More generally, one says that v^α are the components of a contravariant vector, that is said to be an element of the tangent plane (or space for $n > 2$) $T_P(\mathcal{M})$ at the point P; v_α are instead the components of a covariant vector, that is an element of the *dual* tangent space $T_P^\star(\mathcal{M})$. Therefore, the *metric tensor establishes a one-to-one mapping between the tangent space and its dual.*[10]. Furthermore, if $\boldsymbol{v}_1$ and $\boldsymbol{v}_2$ are two contravariant vectors belonging to the same tangent space , the bilinear form

$$(\boldsymbol{v}_1|\boldsymbol{v}_2) = g_{\alpha\beta} v^\alpha v^\beta \tag{10.33}$$

is obviously an invariant and can be regarded as an inner (or scalar) product of the vectors $\boldsymbol{v}_1$ and $\boldsymbol{v}_2$ at P[11].

The one-to-one mapping between the tangent space and its dual possess an inverse and it is the *contravariant* metric tensor $g^{\alpha\beta}$ to establish the connection between contravariant and covariant components. The covariant and the controvariant metric tensor are *conjugate* that is

$$g_{\alpha\gamma} g^{\gamma\beta} = \delta_\alpha^\beta \tag{10.34}$$

[10] Notice that for an arbitrary space devoid of a metric no such relationship exists.

[11] Again, in arbitrary space devoid of a metric, the scalar product between two vectors of the same kind is an ill-defined quantity. One can only define the inner product of vectors which are respectively co- and controvariant, *i.e.* the operation of "index contraction" we have introduced above, $v^\alpha v_\alpha$

In closing this Subsection, we should mention the special case in which $g_{\alpha\beta} = \delta_{\alpha\beta}$[12] at a given point P of $\mathcal{M}$. In such situation, we have

$$v_\alpha = g_{\alpha\beta} v^\beta = \delta_{\alpha\beta} v^\beta = v^\alpha \tag{10.36}$$

that is, the covariant and contravariant components are identical. This is the rather special case in which the tangent vectors $\boldsymbol{x}_\alpha$ are orthogonal, that is the tangent space $T_P(\mathcal{M})$ is Euclidean and, as consequence, the parallel and orthogonal projections of the vector $\boldsymbol{v}$ coincide[13].

A more general case is the one in which the metric tensor is everywhere constant (see footnote 13 of pag. 153). In this case, we say that

Definition 10.2.6. *A space endowed with a Riemannian metric is* flat *whenever it admits a coordinate systems for which the components of the metric tensor are constants everywhere.*

10.2.3 Normal to a surface

We have seen that at each point P of a surface $\mathcal{M}$ we can associate the two basis vectors $\boldsymbol{x}_1$ and $\boldsymbol{x}_2$ that are tangential to the coordinated curves defined on the surface and span the tangent plane $T_P(\mathcal{M})$ at that point. Since we are assuming that the two-dimensional surface is embedded in E_3, we can define a unit vector $\boldsymbol{N}$ orthogonal to both $\boldsymbol{x}_\alpha$ and such that $\boldsymbol{x}_1, \boldsymbol{x}_2, \boldsymbol{N}$ define a local right-handed coordinated system at P. Such vector is called **unit normal vector** and is given by

$$\boldsymbol{N} = \frac{\boldsymbol{x}_1 \times \boldsymbol{x}_2}{|\boldsymbol{x}_1 \times \boldsymbol{x}_2|} \tag{10.37}$$

where $\times$ denote the standard cross-product in E_3. Since

$$\begin{aligned} |\boldsymbol{x}_1 \times \boldsymbol{x}_2| &= |\boldsymbol{x}_1|^2 |\boldsymbol{x}_2|^2 \sin^2\alpha = g_{11} g_{22} (1 - cos^2\alpha) \\ &= g_{11} g_{22} - (\boldsymbol{x}_1 | \boldsymbol{x}_2)^2 \equiv g \end{aligned}$$

We have

$$\boldsymbol{N} = \frac{1}{\sqrt{g}} (\boldsymbol{x}_1 \times \boldsymbol{x}_2) \tag{10.38}$$

[12]The reader may find misleading the distinction between $\delta_{\alpha\beta}$ or δ^α_β, since these two mathematical "objects" have basically the same effect. These two Kronecker deltas are just two particular cases of the so-called *generalized Kronecker delta*, $\delta^{\beta_1,\ldots,\beta_r}_{\alpha_1,\ldots,\alpha_r}$ a *numerical* (r,r)*-tensor* defined as

$$\delta^{\beta_1,\ldots,\beta_r}_{\alpha_1,\ldots,\alpha_r} = \det \begin{pmatrix} \delta^{\beta_1}_{\alpha_1} & \delta^{\beta_1}_{\alpha_2} & \ldots & \delta^{\beta_1}_{\alpha_r} \\ \delta^{\beta_2}_{\alpha_1} & \delta^{\beta_2}_{\alpha_2} & \ldots & \delta^{\beta_2}_{\alpha_r} \\ \ldots & \ldots & \ldots & \ldots \\ \delta^{\beta_r}_{\alpha_1} & \ldots & \ldots & \delta^{\beta_r}_{\alpha_r} \end{pmatrix} \tag{10.35}$$

The generalized Kronecker delta is then the sum of $r!$ terms, each of which is a product of r "standard" Kronecker deltas.

[13]In this regard, we should mention that it is always possible to find a linear transformation on the tangent space $T_P(\mathcal{M}$ which reduces the scalar product $(\boldsymbol{v}|\boldsymbol{v}) = |\boldsymbol{v}|^2$ to a sum of squares, *i.e.*

$$|\boldsymbol{v}|^2 = (\bar{v}^1)^2 + (\bar{v}^2)^2 + \ldots + (\bar{v}^n)^2$$

where $\bar{v}^\alpha$ denotes the components in the new coordinate system in $T_P(\mathcal{M})$. This is clearly the linear transformation which reduces the coefficients $g_{\alpha\beta}$ of the metric tensor defined at P to Kronecker deltas $\delta_{\alpha\beta}$. In general, such liner transformation will not have the same effect also on a neighboring tangent space at Q, $T_Q(\mathcal{M})$. Nevertheless, this result tells us that the tangent space at a point P of a Riemannian space is essentially Euclidean. In other words, *Riemannian spaces with positive definite metric are locally Euclidean.* If it is possible to find a linear transformation which is such that the transformed metric tensor are independent of the positional coordinates and thus constants everywhere, it follows that the Riemannian space is simply an Euclidean space.

Notice that the sense of the unit normal vector depends on the choice of the coordinates on S.

Definition 10.2.7. *A surface is said to be orientable, if there does not exist a closed curve C through a point P which is such that, when displacing continuously a positive unit normal vector from P along C and back to P, one obtains a positive normal direction at P opposite to the original one.*

An example of a non-orientable surface is the *Möebius strip*. In the following, we will restrict our attention to orientable surfaces.

10.3 Measurement of lengths, angles and areas in a surface

With the knowledge gained on the basis of Riemannian geometry and tensor calculus, we are now able to look at the applications of the first fundamental form. In particular, we will see that the latter enables us to measure lengths, angles and elements of area in a surface.

Let consider a contravariant vector $\boldsymbol{v}$ at point P of the surface $\mathcal{M}$. From the above discussion, its length is given by

$$|\boldsymbol{v}| = \sqrt{(\boldsymbol{v}|\boldsymbol{v})} = \sqrt{g_{\alpha\beta}v^\alpha v^\beta} = \sqrt{v_\alpha v^\alpha} \tag{10.39}$$

where, in the last step, we have used the property of the (contravariant) covariant metric tensor to (raise) lower an index of a contravariant (covariant) vector (or tensor). Such property clearly follows from the mapping between the tangent space and its dual. The angle γ between two controvariant vectors $\boldsymbol{v}$ and $\boldsymbol{w}$ is given by

$$\cos(\gamma) = \frac{(\boldsymbol{v}|\boldsymbol{w})}{|\boldsymbol{v}||\boldsymbol{w}|} = \frac{g_{\alpha\beta}v^\alpha w^\beta}{\sqrt{g_{\mu\nu}v^\mu w^\nu}\sqrt{g_{\sigma\gamma}v^\sigma w^\gamma}} = \frac{v_\alpha w^\alpha}{\sqrt{v_\beta v^\beta}\sqrt{w_\gamma w^\gamma}} \tag{10.40}$$

Let consider now two curves $C_1 : u^\alpha = f_1^\alpha(t)$ and $C_2 : u^\alpha = f_2^\alpha(t)$ on a surface $\mathcal{M} : \boldsymbol{x}(u^1, u^2)$ which intersect at P. By definition, the angle θ of intersection is the angle between the vectors tangent to C_1 and C_2 at P, *i.e.*

$$\boldsymbol{v_1} = \frac{d}{dt}(\boldsymbol{x}(f_1^\alpha(t))) = \boldsymbol{x}_\alpha (f_1^\alpha)'$$
$$\boldsymbol{v_2} = \frac{d}{dt}(\boldsymbol{x}(f_2^\alpha(t))) = \boldsymbol{x}_\alpha (f_2^\alpha)'$$

where $'$ denotes the derivative w.r.t. t. According to Equation (10.40) we then obtain

$$\cos(\theta) = \frac{g_{\alpha\beta}(f_1^\alpha)'(f_2^\beta)'}{\sqrt{g_{\mu\nu}(f_1^\mu)'(f_1^\nu)'}\sqrt{g_{\sigma\tau}(f_2^\sigma)'(f_2^\tau)'}} \tag{10.41}$$

If C_1 and C_2 intersect orthogonally at P, then $\cos(\gamma) = 0$, *i.e.*

$$g_{\alpha\beta}(f_1^\alpha)'(f_2^\beta)' = 0$$

We may apply the above arguments to the tangent vectors to the coordinates curves on

$\mathcal{M}$, namely $\boldsymbol{x}_1$ and $\boldsymbol{x}_2$. We find then that the angle between the coordinates curves is

$$\cos(\theta) = \frac{g_{12}}{\sqrt{g_{11}g_{22}}} \tag{10.42}$$

We have then the following

Theorem 10.3.1. *A coordinate system on $\mathcal{M}$ is orthogonal, that is the coordinate curves intersect orthogonally at any point, if and only if $g_{12} = 0$ everywhere on the surface.*

The metric tensor allows also to compute the area of a portion H of a surface $\mathcal{M}$. Here, we just provide the final result[14], namely

Definition 10.3.1. *The area $A(H)$ of a portion H of a surface $\mathcal{M} : \boldsymbol{x}(u^1, u^2)$ is defined by the double integral*

$$A(H) = \iint_U \sqrt{g} du^1 du^2 \tag{10.43}$$

where U denotes the domain in the u^1u^2-plane corresponding to H. The expression

$$dA = \sqrt{g} du^1 du^2 \tag{10.44}$$

is called the element of area of H.

We can convince ourselves about the validity of the above definition looking at the expression (10.44). Indeed the area element can be interpreted geometrically as the area of an "infinitesimal parallelogram" whose sides are the vectors $\boldsymbol{x}_1 du^1$ and $\boldsymbol{x}_2 du^2$. From the definition of cross product, we have indeed

$$|\boldsymbol{x}_1 du^1 \times \boldsymbol{x}_2 du^2| = |\boldsymbol{x}_1 \times \boldsymbol{x}_2| du^1 du^2$$

and $|\boldsymbol{x}_1 \times \boldsymbol{x}_2| = \sqrt{g}$. Therefore, the area $A(H)$ is the "sum" of these infinitesimal parallelograms which locally approximate the surface $\mathcal{M}$.

10.4 The second fundamental form

In this and the subsequent Sections, we will investigate the geometrical shape of surface in a neighborhood of any of its points. As we pointed out in Section 10.1, it will be natural to start from the study of the curvature of curves on the surface under examination. We first notice the following simple fact: at any point of a curve C on a *flat* surface, the unit principal normal $\boldsymbol{P}$ and the unit surface normal $\boldsymbol{N}$ are always orthogonal to each other. On the other hand, for a curve on a generic surface, the unit principal normal lies in the same (normal) plane containing the unit surface normal vector, but their angle will depend on the geometrical shape of the surface around the point under consideration. As consequence, on generic surface, the curvature vector $\boldsymbol{k}$ of a curve will have both a normal component - lying in the normal plane - and a tangential component - lying in the tangent plane. This simple observation will lead us to the definition of the so-called **normal** and **geodesic curvature**, that are of fundamental importance in the differential geometry of surfaces.

First, let γ be the angle between the unit principal normal $\boldsymbol{P}$ and the unit surface normal $\boldsymbol{N}$. Then,

$$\cos(\gamma) = (\boldsymbol{P}|\boldsymbol{N}) \tag{10.45}$$

[14] A proof of this result can be found at pag. 111 of the book "Differential Geometry" by Kreyszig(1991).

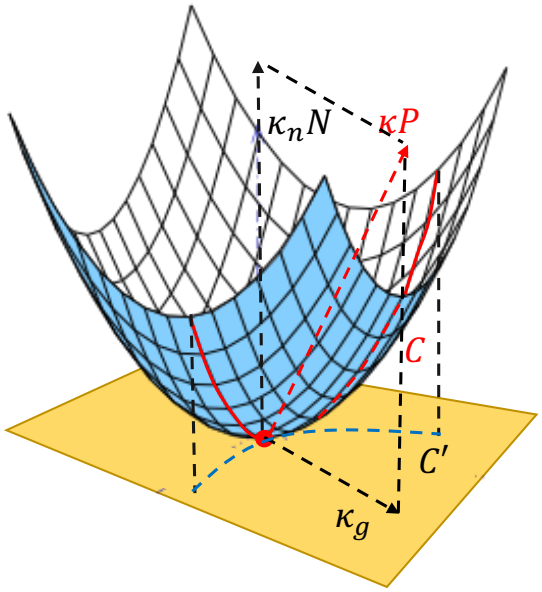

Figure 10.5. A representation of a curve C on a surface. The curvature κ of the curve C has two components: one along the surface normal $\boldsymbol{N}$, the so-called normal curvature κ_n; one lying in the tangent plane (yellow) and directed along the vector $\boldsymbol{N} \times \boldsymbol{T}$, the so-called geodesic curvature κ_g. The latter coincide with the curvature of the curve C' obtained by projecting orthogonally the curve C on the tangent plane

Notice that the value of such scalar product will change along the curve C. From Subsection 10.1.1, we have $\dot{\boldsymbol{T}} = \kappa \boldsymbol{P}$, hence $\boldsymbol{P} = \ddot{\boldsymbol{x}}/\kappa$, where $\boldsymbol{x}(u^1, u^2)$ is the surface parametrization. Therefore

$$\kappa \cos(\gamma) = (\ddot{\boldsymbol{x}}|\boldsymbol{N}) \tag{10.46}$$

Let now look for an explicit expression of $\ddot{\boldsymbol{x}}$. We have

$$\ddot{\boldsymbol{x}} = \frac{d}{dt}(\boldsymbol{x}_\alpha \dot{u}^\alpha) = \boldsymbol{x}_{\alpha\beta}\dot{u}^\alpha \dot{u}^\beta + \boldsymbol{x}_\alpha \ddot{u}^\alpha \tag{10.47}$$

Substituting Equation (10.47) into the scalar product $(\ddot{\boldsymbol{x}}|\boldsymbol{N})$ and reminding that $(\boldsymbol{x}_\alpha|\boldsymbol{N}) = 0$, we find

$$(\ddot{\boldsymbol{x}}|\boldsymbol{N}) = (\boldsymbol{x}_{\alpha\beta}|\boldsymbol{N})\dot{u}^\alpha \dot{u}^\beta \tag{10.48}$$

We introduce the notation $\Omega_{\alpha\beta} = (\boldsymbol{x}_{\alpha\beta}|\boldsymbol{N})$. Notice that the value of $\Omega_{\alpha\beta}$ will depend on both the curve and the surface under examination. Moroever, since $\boldsymbol{x}_{\alpha\beta}$ is symmetric under the permutation of its indices, so it is $\Omega_{\alpha\beta}$. The corresponding quadratic form

$$\Omega_{\alpha\beta} du^\alpha du^\beta = \Omega_{11}(du^1)^2 + 2\Omega_{12}(du^1 du^2) + \Omega_{22}(du^2)^2 \tag{10.49}$$

is called the **second fundamental form**. Differentiating the orthogonality relation $(\boldsymbol{x}_\alpha|\boldsymbol{N}) = 0$ we find

$$(\boldsymbol{x}_{\alpha\beta}|\boldsymbol{N}) + (\boldsymbol{x}_\alpha|\boldsymbol{N}_\beta) = 0$$

Therefore, from the definition of $\Omega_{\alpha\beta}$ we also get the following important relations

$$\Omega_{\alpha\beta} = -(\boldsymbol{x}_\alpha|\boldsymbol{N}_\beta) \tag{10.50}$$

For the first fundamental form, we could write $ds^2 = g_{\alpha\beta} du^\alpha du^\beta \equiv (d\boldsymbol{x}|d\boldsymbol{x})$. Similarly, for

the second fundamental form, we have

$$\Omega_{\alpha\beta}du^{\alpha}du^{\beta} = -(d\boldsymbol{x}|d\boldsymbol{N}) \tag{10.51}$$

Equation (10.51) thus shows that the second fundamental form is invariant w.r.t. any allowable coordinate representation which preserves the sense of $\boldsymbol{N}$. Furthermore, the coefficients $\Omega_{\alpha\beta}$ have to behave as the components of a type $(0,2)$-tensor.

Remark 6. *While the first fundamental form is positive definite, the second fundamental form may vanish. In particular, as we shall see in Subsection 10.4.2, the sign of the discriminant $\Omega = \Omega_{11}\Omega_{22} - \Omega_{12}^2$ of the second fundamental form at a given point of the surface is strictly related to the shape of the surface around that point.*

10.4.1 Normal and geodesic curvature

Now let t be *any* allowable parameter of the curve C. Then, we may write

$$\dot{u}^{\alpha} = \frac{du^{\alpha}}{dt}\frac{dt}{ds} \equiv \frac{(u^{\alpha})'}{s'} \tag{10.52}$$

Hence, in consequence of Equations (10.48), (10.49) and (10.52), we may write the second term of (10.46) as

$$\kappa\cos(\gamma) = \frac{\Omega_{\alpha\beta}(u^{\alpha})'(u^{\beta})'}{(s')^2} = \frac{\Omega_{\alpha\beta}(u^{\alpha})'(u^{\beta})'}{g_{\alpha\beta}(u^{\alpha})'(u^{\beta})'}$$

or

$$\kappa\cos(\gamma) = \frac{\Omega_{\alpha\beta}du^{\alpha}du^{\beta}}{g_{\alpha\beta}du^{\alpha}du^{\beta}} \tag{10.53}$$

Relation (10.53) is one of the most important result of the theory of surfaces. To understand its geometrical implications, let consider a curve $C : u^{\alpha} = u^{\alpha}(s)$ with curvature $\kappa = \kappa(s)$ and let $\gamma = \gamma(s)$ be the angle between the unit principal normal vector $\boldsymbol{P}(s)$ to C and the corresponding unit surface normal $\boldsymbol{N}(u^1(s), u^2(s))$ to $\mathcal{M}$. Obviously, the direction of the unit tangent vector $\boldsymbol{T} = \boldsymbol{x}_{\alpha}\dot{u}^{\alpha}$ to C is determined by the ratio $\dot{u}^1/\dot{u}^2$. On the other hand, the values of the first and second fundamental form are fixed at any point P of the surface under scrutiny, *i.e.* they are independent of the special choice of the curve C on $\mathcal{M}$ passing through P. This means that the curvature $\kappa(s)$ of C at P depends solely on the direction of the unit tangent vector and of the unit principal normal vector to C at P. Since these vectors span the osculating plane, we have the following

Theorem 10.4.1. *All curves of class C^r with $r \geq 2$ on a surface $\mathcal{M}$ which pass through any fixed point P and have at P the same osculating plane, which does not coincide with the tangent plane $T_P(\mathcal{M})$ of the surface at P, also have the same curvature at P.*

Let then restrict our attention to the class of curves with common tangent at P. The direct consequence of Theorem 10.4.1 is that the right-hand side of Relation (10.53) is constant, that is, the curvature of these curves depends only on the angle γ between $\boldsymbol{P}$ and $\boldsymbol{N}$ at P.This result is generally known as the *Meusnier theorem*[265] , which thus specifies the distribution of the curvatures of the set of all curves which pass through P in a given direction. For those curves, we may write

$$\kappa\cos(\gamma) = \kappa_n \tag{10.54}$$

where κ_n is a constant when a fixed tangent direction has been chosen. The geometrical

significance of κ_n can be understood in a simple manner as follows. If $\gamma = 0$, then $\kappa \equiv \kappa_n$; if $\gamma = \pi$ then $\kappa = -\kappa_n$. In other words, $|\kappa_n|$ is the *curvature of the curve of intersection of the surface $\mathcal{M}$ and a plane passing through both the tangent to the curve at P and the normal to $\mathcal{M}$ at P*. These curves form a very special class of curves that usually referred to as **normal sections** of $\mathcal{M}$. κ_n is then called the **normal curvature** and one thus introduce the *normal curvature vector* as

$$\boldsymbol{k}_n = \kappa_n \boldsymbol{N} \tag{10.55}$$

We shall see in the following that the study of normal sections lies at the heart of the curvature theory of surfaces. Nevertheless, to understand such state of affairs, we need to briefly consider also a more general situation.

Let consider a curve $C : u^\alpha = u^\alpha(s)$ and denote with C' the orthogonal projection of C on the tangent plane $T_P(\mathcal{M})$ at P. We define the **geodesic curvature** κ_g (Liouville(1850)) of C at P as the curvature of the projected curve C' at P, taken with a suitable sign. The sign of κ_g is defined as follows: let suppose that the curvature of C' at P is not zero; then κ_g is positive if the centre of curvature of C' at P lies in the direction of the unit vector

$$\boldsymbol{E} = \boldsymbol{N} \times \boldsymbol{T} \tag{10.56}$$

where $\boldsymbol{N}$ is the usual surface normal at P and $\boldsymbol{T}$ the tangent vector to C at P. κ_g has a negative sign if the centre of curvature lies in the opposite direction. Looking at Figure **??**, it is clear that for the geodesic curvature we may write

$$|\kappa_g| = \kappa \sin(\gamma) \tag{10.57}$$

Therefore, in light of the previous discussion on the normal curvature, we may write the curvature vector $\boldsymbol{k}(s) = \kappa(s)\boldsymbol{P}(s)$ of the curve C as the sum of the normal curvature vector $\boldsymbol{k}_n(s)$ and of the *geodesic curvature vector* $\boldsymbol{k}_g = \kappa_g \boldsymbol{E}$

$$\boxed{\boldsymbol{k} = \boldsymbol{k}_n + \boldsymbol{k}_g = \kappa_n \boldsymbol{N} + \kappa_g \boldsymbol{E}} \tag{10.58}$$

In general the geodesic curvature will depend not only on the curve C considered but also on the surface on which the curve is defined. The only exception to this occurs when $\dot{\boldsymbol{T}} = 0$ and therefore $\kappa_g = 0$. Curves for which the geodesic curvature vanishes identically are called *geodesics*[15].

There is fundamental difference between the normal curvature κ_n and the geodesic curvature κ_g: the former depends on both fundamental forms, while[16]

Theorem 10.4.2. *The geodesic curvature κ_g of a curve C on a surface $\mathcal{M}$ depends on the first fundamental form only (and also, of course, on C).*

Let now move back to normal sections. From the definition of the geodesic curvature, it follows that, if we project a normal section on the tangent plane, we obtain a *straight line*, which by definition has a vanishing curvature, *i.e.* $\kappa_g \equiv 0$. Normal sections are therefore special curves for which the curvature vector is entirely determined by the normal curvature.

We may summarize the above results as follows: for a generic curve C on a surface $\mathcal{M}$, the curvature vector has both a tangential and a normal component w.r.t. the tangent plane

[15] An example may be the equator of a sphere, since in this case $\boldsymbol{T}, \dot{\boldsymbol{T}}$ and $\boldsymbol{N}$ lie in a plane.

[16] We omit the proof of this fundamental theorem, which requires to find a representation of κ_g depending on functions of $g_{\alpha\beta}$. The reason is that the proof requires the knowledge of the *Christoffel symbols*, which we will introduce in Section

$T_P(\mathcal{M})$, that correspond to the concept of geodesic κ_g and normal curvature κ_n. Normal sections are a rather special class of curves for which $\kappa_g = 0$ and they are determined by the intersection of the surface $\mathcal{M}$ and a plane passing through both the tangent to the curve at P and the normal to $\mathcal{M}$ at P. In a sense, we may say that normal sections are *intrinsic* curves of a surface since, at fixed tangent direction, their curvature is determined entirely by surface properties, namely the fundamental forms. Since we are interested in gaining information about the curvature properties of a surface, in the following we will restrict our attention to normal sections only.

10.4.2 Elliptic, parabolic and hyperbolic points

In the preceding Subsection, we saw that, in consequence of the Meusnier theorem, we can restrict our attention to normal sections of a surface $\mathcal{M}$. The curvature of such curves is entirely determined by the normal curvature κ_n that reads as

$$\kappa_n = \frac{\Omega_{\alpha\beta} du^\alpha du^\beta}{g_{\alpha\beta} du^\alpha du^\beta} \tag{10.59}$$

Equation 10.59 enables us to distinguish from three possible forms of $\mathcal{M}$ in a neighborhood of a point at which $\Omega_{\alpha\beta}$ are not vanishing. We know that the first fundamental form is always positive definite, therefore the sign of κ_n depends solely on the second fundamental form. If $\boldsymbol{v} = (v^1, v^2)$ is the vector specifying a given direction bound at P, the problem translates to the study of the sign of the equation $\Omega_{11}(v^1)^2 + \Omega_{22}(v^2)^2 + 2\Omega_{12}(v^1 v^2) = 0$. Setting $x = v^1/v^2$, we need to solve

$$\Omega_{11}x^2 + 2\Omega_{12}x + \Omega_{22} > 0$$

The solutions will depend on the sign of the discriminant Δ at the point P, which is given by

$$\Delta = 4(\Omega_{12}^2 - \Omega_{11}\Omega_{22}) \equiv -4\Omega \tag{10.60}$$

where Ω is the discriminant of the second fundamental form.

(i) If $\Delta < 0$ ($\Omega > 0$), the associated equation admits two complex solutions. Therefore, κ_n "maintains" the sign, or, in other words, has the same sign for all possible directions of the normal sections at P. A point of this kind is called an **elliptic point** of the surface. An example is provided by the ellipsoid or the sphere, for which any point is an elliptic point.

(ii) If $\Delta = 0$ ($\Omega = 0$), we have a single solution to the associated equation, *i.e.* we can identify a direction from P specified by $\boldsymbol{v}$ for which $\kappa_n = 0$, also known as *asymptotic direction*[17]. P is then called a **parabolic point** of the surface. Any point of a cylinder or of a cone (with the exception of the apex) is parabolic.

(iii) If $\Delta > 0$ ($\Omega < 0$), there will exist two possible directions for which $\kappa_n = 0$. Therefore κ_n does not maintain the sign for all directions. The two asymptotic directions separate the directions for which κ_n is positive from those for which is negative. P is then called a **hyperbolic** or **saddle point** of a surface.

Notice that, due to the invariance property of the second fundamental form under a coordinate transformation, the distinction established above is independent of the choice of the coordinate system on the surface. Hence, it is a "true" characterization of the shape of a surface around any of its points.

[17] More generally, any curve for which $\kappa_n = 0$ is called an *asymptotic curve.*

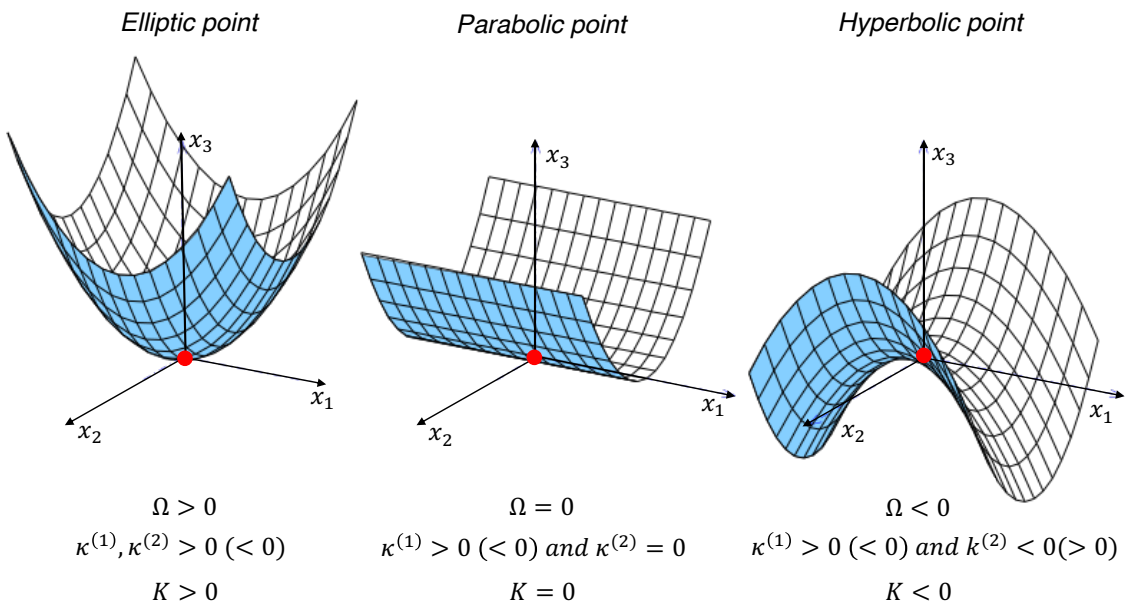

Figure 10.6. A representation of an elliptic, parabolic and hyperbolic point (denoted with a red dot), and the corresponding values of the discriminant of the second fundamental form (Ω), the principal curvatures $\kappa^(i)$ and the Gaussian curvature K.

10.5 Principal curvatures

In light of the preceding discussion about the normal curvature, it is natural to ask for directions for which κ_n attains its maximum and minimum values. Obviously, this question does not make sense at points of a surface for which κ_n is constants, *i.e.* is independent of the direction of the normal sections. Such property holds if and only if the coefficients of the second fundamental form $\Omega_{\alpha\beta}$ are proportional to $g_{\alpha\beta}$. We have then the following

Definition 10.5.1. *A point P is said to be an* **umbilic point** *if at that point the following relation holds*

$$\Omega_{\alpha\beta} = \lambda(u^1, u^2) g_{\alpha\beta} \tag{10.61}$$

In this case $\Omega = \lambda^2 g$. Therefore, since $g > 0$, if $\lambda \neq 0$, we have $\Omega > 0$ and the point is referred to as an *elliptic umbilic*. If $\lambda = 0$, also $\Omega = 0$, and the point is called a *parabolic umbilic* (or *flat* or *planar umbilic*).

Henceforth, we assume then that the point P is not an umbilic point. We first determine those directions for which the normal curvature has an extreme value. To this aim, let re-write Relation (10.59) as

$$(\Omega_{\alpha\beta} - \kappa_n g_{\alpha\beta}) l^\alpha l^\beta \tag{10.62}$$

where we have set $l^\gamma = du^\gamma$. In addition, we set

$$\Pi_{\alpha\beta} = \Omega_{\alpha\beta} - \kappa_n g_{\alpha\beta} \tag{10.63}$$

If we differentiate Equation (10.63) w.r.t. l^γ treating κ_n as a constant[18], we get

$$\begin{aligned} \frac{\partial}{\partial l^\gamma}(\Pi_{\alpha\beta} l^\alpha l^\beta) &= \Pi_{\alpha\beta}\left(\frac{\partial l^\alpha}{\partial l^\gamma} l^\beta + l^\alpha \frac{\partial l^\beta}{\partial l^\gamma}\right) \\ &= \Pi_{\alpha\beta}(\delta^\alpha_\gamma l^\beta + \delta^\beta_\gamma l^\alpha) \\ &= (\Pi_{\gamma\alpha} + \Pi_{\alpha\gamma})\, l^\alpha \end{aligned}$$

[18]Remind that $d\kappa_n = 0$ is a necessary condition for κ_n to be an extreme value.

Since both $g_{\alpha\beta}$ and $\Pi_{\alpha\beta}$ are symmetric, we have $\Pi_{\alpha\gamma} \equiv \Pi_{\gamma\alpha}$, hence we obtain

$$\Pi_{\gamma\alpha} l^{\alpha} = 0 \Longrightarrow (\Omega_{\alpha\beta} - \kappa_n g_{\alpha\beta})\, l^{\alpha} = 0 \tag{10.64}$$

A (contravariant) vector whose components are l^{α} - which is not a null vector - can satisfy Equation (10.64) if and only if the determinant of $(\Omega_{\alpha\beta} - \kappa_n g_{\alpha\beta})$ vanishes identically. Hence

$$(\Omega_{11}\kappa_n g_{11})(\Omega_{22} - \kappa_n g_{11}) - (\Omega_{12} - \kappa_n g_{12})^2 = 0$$

With some straightforward algebra, we arrive at

$$\kappa_n^2 g - \kappa_n(\Omega_{11} g_{22} + \Omega_{22} g_{11} - 2\Omega_{12} g_{12}) + \Omega = 0 \tag{10.65}$$

The roots of Equation (10.65) determines those directions for which the normal curvature κ_n attains its extreme values. These directions are called the **principal directions of normal curvature** at the point P under consideration. The corresponding values of κ_n are called **principal curvatures** of the surface $\mathcal{M}$ at P and they are denoted as $\kappa^{(1)}$ and $\kappa^{(2)}$.

The principal directions and principal curvatures are of basic importance in the curvature theory of surface. Therefore, in the following, we will consider them in more detail. First of all, we state the following

Theorem 10.5.1. *The roots of Equation* (10.65) *are real. At any point which is not an umbilic point, the principal directions are orthogonal.*

The proof of this Theorem is rather simple. The reality of the principal directions follows directly from their geometrical interpretation. For the orthogonality, let $l^{\alpha(1)}$ and $l^{\alpha(2)}$ be those directions. Hence, they satisfy

$$(\Omega_{\alpha\gamma} - k^{(i)} g_{\alpha\gamma}) l^{\alpha(i)} = 0 \tag{10.66}$$

with $i = 1, 2$. If we multiply the corresponding Equations (10.66) by $l^{\gamma(2)}$ and $l^{\gamma(1)}$, sum w.r.t. γ and subtract the equations thus obtained, we get

$$(\kappa^{(2)} - \kappa^{(1)}) g_{\alpha\gamma} l^{\alpha(1)} l^{\gamma(2)} = 0$$

Since $\kappa^{(1)} \neq \kappa^{(2)}$, it follows that the principal directions are orthogonal.

Definition 10.5.2. *A curve on a surface $\mathcal{M}$ whose direction at every point is a principal direction is known as a* **line of curvature** *of $\mathcal{M}$.*

Notice that, since Equation (10.65) is quadratic, through any (not umbilic) point of a surface of class C^r with $r \geq 3$, there pass exactly two curves, which, according to Theorem 10.5.1, are orthogonal. Hence, we also have

Theorem 10.5.2. *The lines of curvature on any real surface $\mathcal{M}$ of class C^r with $r \geq 3$ are real curves. If $\mathcal{M}$ has no umbilics the lines of curvature form an orthogonal net everywhere on $\mathcal{M}$.*

Consequently, one may always choose coordinates u^1, u^2 on $\mathcal{M}$ so that the coordinates curves are the lines of curvature of the surface under examination. If we introduce this kind of coordinates, then Equation (10.64) must be satisfied for $du^{\alpha} = 0$. This leads to the following system of linear equations

$$\begin{aligned} g_{12}\Omega_{22} - g_{22}\Omega_{12} &= 0 \\ g_{11}\Omega_{12} - g_{12}\Omega_{22} &= 0 \end{aligned}$$

Excluding umbilics, the determinant $\Omega_{22}g_{11} - \Omega_{11}g_{22}$ is different from zero, therefore the above system admits only the trivial solutions $g_{12} = \Omega_{12} = 0$. We have thus proved the following

Theorem 10.5.3. *The coordinates curves of any allowable coordinate system on a surface $\mathcal{M}$ coincide with the lines of curvature if and only if for this system*

$$g_{12} = \Omega_{12} = 0 \tag{10.67}$$

at any point where those coordinates are allowable.

10.5.1 Gaussian and Mean curvature

Let return on Equation (10.65) and divide it by g

$$\kappa_n^2 - \left[\frac{1}{g}\left(\Omega_{11}g_{22} + \Omega_{22}g_{11} - 2\Omega_{12}g_{12}\right)\right]\kappa_n + \frac{\Omega}{g} = 0 \tag{10.68}$$

From the theory of second order equations, we are now able to introduce the two following concepts

Definition 10.5.3. *The product*

$$K = \kappa^{(1)}\kappa^{(2)} = \frac{\Omega}{g} \tag{10.69}$$

is called the **Gaussian curvature** *of the surface $\mathcal{M}$ at the point P.*

Definition 10.5.4. *The arithmetic mean of the principal curvatures*

$$H = \frac{1}{2}(\kappa^{(1)} + \kappa^{(2)}) = \frac{1}{2}\Omega_{\alpha\beta}g^{\alpha\beta} = \frac{1}{2}\Omega_{\alpha}^{\alpha} \tag{10.70}$$

is called the **mean curvature** *of the surface $\mathcal{M}$ at the point P.*

According to their definition, it immediately follows that K and $|H|$ are invariant w.r.t. any allowable coordinate transformation. The sign of H depends instead on the orientation of the surface, because of the explicit dependence on $\Omega_{\alpha\beta}$. Because of its invariance property, the Gaussian curvature K can be considered as the main "intrinsic" measure of the curvature of a surface at a given point P. Since $g > 0$ always holds, we thus have

Theorem 10.5.4. *At elliptic points, the Gaussian curvature is positive ($K > 0$), at parabolic ones it vanishes ($K = 0$), and at hyperbolic ones it is negative ($K < 0$).*

When the coordinate curves on a surface are the lines of curvature, one can easily find that principal curvatures, the Gaussian and the mean curvatures are given by the following simple expressions

$$\kappa^{(1)} = \frac{\Omega_{11}}{g_{11}} \qquad \kappa^{(2)} = \frac{\Omega_{22}}{g_{22}} \tag{10.71}$$

$$K = \frac{\Omega_{11}\Omega_{22}}{g_{11}g_{22}} \tag{10.72}$$

$$H = \frac{1}{2}\left(\frac{\Omega_{11}}{g_{11}} + \frac{\Omega_{22}}{g_{22}}\right) \tag{10.73}$$

In closing this Section, we state and prove one of the most important Theorem on the normal and principal curvatures, which will turn out to be very useful for our later discussion in Chapter 11.

Theorem 10.5.5 (L.Euler[266]). *Let α be the angle between a direction at a point P and the principal direction at P corresponding to $\kappa^{(1)}$. Then*

$$\kappa_n = \kappa^{(1)} \cos^2(\alpha) + \kappa^{(2)} \sin^2(\alpha \tag{10.74}$$

where κ_n is the normal curvature corresponding to the considered direction at P.

The Euler's theorem allows thus to express the normal curvature at a point of *any* curve on the surface as a function of the principal curvatures $\kappa^{(i)}$. To prove this Theorem, let assume P to be not umbilic. We choose coordinates on $\mathcal{M}$ so that the coordinate curves are the lines of curvature. Then, since $\Omega_{12} = 0$, we may write

$$\kappa_n = \frac{\Omega_{11}(du^1)^2 + \Omega_{22}(du^2)^2}{ds^2} \tag{10.75}$$

Thanks to Equation (10.71), Equation (10.75) reduces to

$$\kappa_n = \kappa^{(1)} g_{11}(\dot{u}^1)^2 + \kappa^{(2)} g_{22}(\dot{u}^2)^2 \tag{10.76}$$

Now the direction under consideration is determined by the vector $\dot{\boldsymbol{x}} = \boldsymbol{x}_\alpha \dot{u}^\alpha$, and the direction corresponding to $\kappa^{(1)}$ is given by the vector $\boldsymbol{x}_1$. Since the lines of curvature are orthogonal, and $|\dot{\boldsymbol{x}}| = 1$, the angle α between $\boldsymbol{x}_1$ and $\dot{\boldsymbol{x}}$ and the angle $\beta = \pi/2 - \alpha$ between $\boldsymbol{x}_2$ and $\dot{\boldsymbol{x}}$ are given by

$$\cos(\alpha) = \frac{(\boldsymbol{x}_1|\dot{\boldsymbol{x}})}{|\boldsymbol{x}_1||\dot{\boldsymbol{x}}|} = \sqrt{g_{11}}\dot{u}^1$$
$$\sin(\alpha) = \cos(\beta) = \frac{(\boldsymbol{x}_2|\dot{\boldsymbol{x}})}{|\boldsymbol{x}_2||\dot{\boldsymbol{x}}|} = \sqrt{g_{22}}\dot{u}^2$$

Therefore, comparing the above expression with Equation (10.76) we obtain the Euler's theorem. This completes the proof.

The concepts introduced in these pages represent the minimal background on differential geometry for the understanding of the discussion exposed in Chapter 11. An application of such concepts is exposed in the box 10.1, where the simple case of a spherical surface is considered. For the sake of completeness, the author has decided to add a further Section for the interested reader, where the theory of curvature is put on firmer grounds thanks to the introduction of the so-called *curvature tensor*, though still restricting the attention to spaces endowed with a metric.

Box 10.1: The sphere S_2

We consider a sphere S_2 of radius R embedded in E_3 with parametrization $\boldsymbol{x} = \boldsymbol{x}(R\cos(\phi)\cos(\theta), R\cos(\phi)\sin(\theta), R\sin(\phi))$, with $0 \leq \theta \leq 2\pi$ and $-\pi/2 \leq \phi \leq \pi/2$ (see the Figure below).

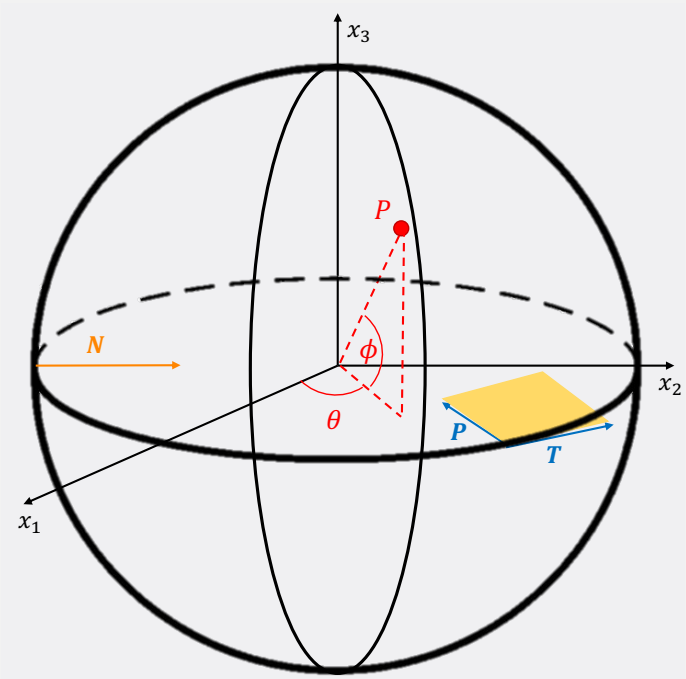

First, let determine the analytical expression of the vectors $\boldsymbol{x}_\theta$ and $\boldsymbol{x}_\phi$ spanning the tangent plane $T_P(S_2)$ at a given point of the sphere:

$$\boldsymbol{x}_\theta = \frac{\partial \boldsymbol{x}}{\partial \theta} = (-R\cos(\phi)\sin(\theta), R\cos(\phi), 0)$$
$$\boldsymbol{x}_\phi = \frac{\partial \boldsymbol{x}}{\partial \phi} = (-R\sin(\phi)\cos(\theta), -R\sin(\phi)\sin(\theta), R\cos(\phi)$$

Hence, we can determine the components $g_{\alpha\beta}$ of the metric tensor in this representation

$$g_{\theta\theta} = (\boldsymbol{x}_\theta|\boldsymbol{x}_\theta) = R^2(\cos^2(\phi)\sin^2(\theta) + \cos^2(\phi)\cos^2(\theta)) = R^2\cos^2(\phi)$$
$$g_{\phi\phi} = (\boldsymbol{x}_\phi|\boldsymbol{x}_\phi) = R^2(\sin^2(\phi)\cos^2(\theta) + \sin^2(\phi)\sin^2(\theta) + \cos^2(\phi)) = R^2$$
$$g_{\theta\phi} = g_{\phi\theta} = (\boldsymbol{x}_\theta|\boldsymbol{x}_\phi) = R^2(\sin(\phi)\cos(\theta)\sin(\theta)\cos(\phi) - \sin(\phi)\sin(\theta)\cos(\phi)\cos(\theta)) = 0$$

For the (unnormalized) surface normal $\boldsymbol{N}'$, we have

$$\boldsymbol{N}' = \boldsymbol{x}_\theta \times \boldsymbol{x}_\phi = \det\begin{pmatrix} \boldsymbol{i} & \boldsymbol{j} & \boldsymbol{k} \\ -R\cos(\phi)\sin(\theta) & R\cos(\phi)\cos(\theta) & 0 \\ -R\sin(\phi)\cos(\theta) & -R\sin(\phi)\sin(\theta) & R\cos(\phi) \end{pmatrix}$$
$$= (R^2\cos^2(\phi)\cos(\theta), R^2\cos^2(\phi)\sin(\theta), R^2\sin(\phi)\cos(\phi))$$

Since $||\boldsymbol{N}|| = \sqrt{(\boldsymbol{N}'|\boldsymbol{N}')} = R^2\cos(\phi)$, the corresponding unit surface normal is

$$\boldsymbol{N} = (\cos(\phi)\cos(\theta), \cos(\phi)\sin(\theta), \sin(\phi))$$

To compute the coefficients $\Omega_{\alpha\beta}$ of the second fundamental form, we need first to

obtain the second derivative $\boldsymbol{x}_{\alpha\beta}$, namely

$$\begin{aligned}\boldsymbol{x}_{\theta\theta} &= \frac{\partial \boldsymbol{x}_\theta}{\partial\theta} = (-R\cos(\phi)\cos(\theta), -R\cos(\phi)\sin(\theta), 0)\\ \boldsymbol{x}_{\phi\phi} &= (-R\cos(\phi)\cos(\theta), -R\cos(\phi)\sin(\theta), -R\sin(\phi))\\ \boldsymbol{x}_{\theta\phi} &= \boldsymbol{x}_{\phi\theta} = (R\sin(\phi)\sin(\theta), -R\sin(\phi)\cos(\theta), 0)\end{aligned}$$

Therefore,

$$\begin{aligned}\Omega_{\theta\theta} &= (\boldsymbol{x}_{\theta\theta}|\boldsymbol{N}) = -R\cos^2(\phi)\\ \Omega_{\phi\phi} &= (\boldsymbol{x}_{\phi\phi}|\boldsymbol{N}) = -R\\ \Omega_{\theta\phi} &= \Omega_{\phi\theta} = (\boldsymbol{x}_{\theta\phi}|\boldsymbol{N}) = 0\end{aligned}$$

To sum up, we have

$$g_{\theta,\phi} = \begin{pmatrix} R^2\cos^2\phi & 0\\ 0 & R^2\end{pmatrix} \qquad \Omega_{\theta,\phi} = \begin{pmatrix} -R^2\cos^2\phi & 0\\ 0 & -R\end{pmatrix}$$

As a special curve on S_2, let consider the equator $\phi = 0$. The corresponding normal curvature κ_n will be given by

$$\kappa_n = \frac{-R(d\theta)^2 - R(d\phi)^2}{R^2(d\theta)^2 + R^2(d\phi)^2} \equiv -\frac{1}{R}$$

that is, $|\kappa_n| = 1/R$, *i.e.* the curvature of circle. Indeed, the equator is the normal section of the sphere (also called a *great circle*), obtained by the intersection of S_2 with a plane passing through its centre. Notice that in this case, the angle γ between the unit surface normal and the unit principal normal of the equator is precisely $\gamma = 0$, that is $\kappa \equiv \kappa_n$.
Since $g_{\theta\phi} = \Omega_{\theta\phi} = 0$, it follows that the coordinate curves $\theta = k$ and $\phi = k$ with k a constant, are the lines of curvature of the sphere (see Theorem 10.5.3). Therefore, the principal curvatures are simply given by

$$\kappa^{(1)} = \frac{-R\cos^2(\phi)}{R^2\cos^2(\phi)} = -\frac{1}{R} \qquad \kappa^{(2)} = \frac{-R}{R^2} = -\frac{1}{R}$$

Indeed, we can always draw a great circle passing through any point P of a sphere. In other words, *any* direction from a point P of a sphere has the curvature of a great circle, $-1/R$, *i.e.* any point of a sphere is umbilic. For the Gaussian and mean curvature we find

$$K = \kappa^{(1)}\kappa^{(2)} = -\frac{1}{R^2} \qquad H = \frac{1}{2}(\kappa^{(1)} + \kappa^{(2)}) = -\frac{1}{R}$$

Obviously, the mean curvature H coincides with the principal curvatures since for the sphere the curvature is constant everywhere.

10.6 The curvature tensor

We first derive an explicit expression for the vectors $\boldsymbol{N}_\alpha = \partial\boldsymbol{N}/\partial u^\alpha$. For this purpose, let consider the unit surface normal $\boldsymbol{N}$ at a point P of a surface $\mathcal{M}$ and differentiate the relation $(\boldsymbol{N}|\boldsymbol{N}) = 1$

$$(\boldsymbol{N}_\alpha|\boldsymbol{N}) = 0$$

Hence, the vectors $\boldsymbol{N}_\alpha$ must lie in $T_P(\mathcal{M})$, *i.e.*

$$\boldsymbol{N}_\alpha = c_\alpha^\gamma \boldsymbol{x}_\gamma$$

To determine the coefficients c_α^γ, let take the scalar product with $\boldsymbol{x}_\sigma$

$$(\boldsymbol{N}_\alpha|\boldsymbol{x}_\sigma) = c_\alpha^\gamma g_{\gamma\sigma}$$

Since $(\boldsymbol{N}_\alpha|\boldsymbol{x}_\sigma) = -\Omega_{\alpha\sigma}$ and $g_{\gamma\sigma}g^{\sigma\tau} = \delta_\gamma^\tau$, we find

$$(\boldsymbol{N}_\alpha|\boldsymbol{x}_\sigma)g^{\sigma\tau} = -\Omega_{\alpha\tau}g^{\sigma\tau} = c_\alpha^\gamma g_{\gamma\sigma}g^{\sigma\tau} = c_\alpha^\tau$$

but $\Omega_{\alpha\sigma}g^{\sigma\tau} \equiv \Omega_\alpha^\tau$. Then

$$\boxed{\boldsymbol{N}_\alpha = -\Omega_\alpha^\beta \boldsymbol{x}_\beta} \tag{10.77}$$

which are known as the *formulae of Weingarten.*

Let now consider the following partial derivatives

$$\boldsymbol{x}_{\alpha\beta} = \frac{\partial^2 \boldsymbol{x}}{\partial u^\alpha \partial u^\beta}$$

These vectors may be written as linear combinations of all three vectors $\boldsymbol{x}_1, \boldsymbol{x}_2, \boldsymbol{N}$, *i.e.*

$$\boldsymbol{x}_{\alpha\beta} = \Gamma_{\alpha\beta}^\gamma \boldsymbol{x}_\gamma + a_{\alpha\beta}\boldsymbol{N} \tag{10.78}$$

We shall then determine the coefficients $\Gamma_{\alpha\beta}^\gamma$ and $a_{\alpha\beta}$. To this aim, let multiply both side of Equation (10.78) by $\boldsymbol{N}$; since $(\boldsymbol{x}_\gamma|\boldsymbol{N}) = 0$ and $(\boldsymbol{x}_{\alpha\beta}|\boldsymbol{N}) = \Omega_{\alpha\beta}$, we find

$$a_{\alpha\beta} \equiv \Omega_{\alpha\beta}$$

In other words, *the coefficients of the second fundamental form can be interpreted also as the normal components of the vectors* $\boldsymbol{x}_{\alpha\beta}$. In order to determine the coefficients $\Gamma_{\alpha\beta}^\gamma$, we take the scalar product with $\boldsymbol{x}_\lambda$

$$(\boldsymbol{x}_{\alpha\beta}|\boldsymbol{x}_\lambda) = \Gamma_{\alpha\beta}^\gamma (\boldsymbol{x}_\gamma|\boldsymbol{x}_\lambda) = \Gamma_{\alpha\beta}^\gamma g_{\gamma\lambda}$$

Since $(\boldsymbol{x}_\gamma|\boldsymbol{x}^\tau) = \delta_\gamma^\tau$, with $\boldsymbol{x}^\tau = g^{\rho\tau}\boldsymbol{x}_\rho$, we thus find

$$\Gamma_{\alpha\beta}^\tau = (\boldsymbol{x}_{\alpha\beta}|\boldsymbol{x}^\tau) = (\boldsymbol{x}_{\alpha\beta}|\boldsymbol{x}_\lambda)g^{\lambda\tau} \tag{10.79}$$

In this way, we have then completely determined the coefficients appearing in the linear combination (10.78). Nevertheless, we can show that $\Gamma_{\alpha\beta}^\gamma$ can be expressed in terms of the components of the metric tensor and their derivatives only. Moreover, we shall see that these coefficients are of fundamental importance not only for the theory of surfaces but also in the context of the general theory of spaces devoid of a metric. We first introduce the following notation

$$\Gamma_{\alpha\beta\gamma} := (\boldsymbol{x}_{\alpha\beta}|\boldsymbol{x}_\gamma) \tag{10.80}$$

These quantities are called **Christoffel symbols of the first kind**. From the properties of the metric tensor, we have

$$\Gamma_{\alpha\beta\gamma} = g_{\lambda\gamma}\Gamma_{\alpha\beta}^\lambda \tag{10.81}$$

or

$$\Gamma_{\alpha\beta}^\tau = g^{\gamma\tau}\Gamma_{\alpha\beta\gamma} \tag{10.82}$$

The quantities $\Gamma^{\tau}_{\alpha\beta}$ are called **Christoffel symbols of the second kind** (E.B. Christoffel(1869)).Since $\boldsymbol{x}_{\alpha\beta} = \boldsymbol{x}_{\beta\alpha}$, Christoffel symbols of both kinds are symmetric w.r.t. the permutation of the first two (covariant) indices,

$$\Gamma_{\alpha\beta\gamma} = \Gamma_{\beta\alpha\gamma} \qquad \Gamma^{\tau}_{\alpha\beta} = \Gamma^{\tau}_{\beta\alpha}$$

To find a representation of the Christoffel symbols in terms of the metric tensor and its derivative only, let differentiate the expression $g_{\alpha\gamma} = (\boldsymbol{x}_{\alpha}|\boldsymbol{x}_{\gamma})$ w.r.t. u^{β}

$$\frac{g_{\alpha\gamma}}{\partial u^{\beta}} = (\boldsymbol{x}_{\alpha\beta}|\boldsymbol{x}_{\gamma}) + (\boldsymbol{x}_{\alpha}|\boldsymbol{x}_{\gamma\beta}) \equiv \Gamma_{\alpha\beta\gamma} + \Gamma_{\gamma\beta\alpha} \tag{10.83}$$

From the symmetry properties of $g_{\alpha\beta}$ and the Christoffel symbols of the first kind, we may also write

$$\frac{g_{\gamma\beta}}{\partial u^{\alpha}} = \Gamma_{\gamma\alpha\beta} + \Gamma_{\beta\alpha\gamma} \tag{10.84}$$

$$\frac{g_{\beta\alpha}}{\partial u^{\gamma}} = \Gamma_{\beta\gamma\alpha} + \Gamma_{\alpha\gamma\beta} \tag{10.85}$$

Adding (10.83) and (10.84) and subtracting (10.85), taking into account the symmetry in the first two indices, we arrive at the following important formula

$$\Gamma_{\alpha\beta\gamma} = \frac{1}{2}\left(\frac{\partial g_{\beta\gamma}}{\partial u^{\alpha}} + \frac{\partial g_{\gamma\alpha}}{\partial u^{\beta}} - \frac{\partial g_{\alpha\beta}}{\partial u^{\gamma}}\right) \tag{10.86}$$

Since $\Gamma^{\tau}_{\alpha\beta} = g^{\gamma\tau}\Gamma_{\alpha\beta\gamma}$, we have automatically proved that also the Christoffel symbols of the second kind can be written entirely in terms of the metric tensor and its derivatives. Therefore, to sum up, the second partial derivatives $\boldsymbol{x}_{\alpha\beta}$ of the vector function $\boldsymbol{x}(u^1, u^2)$ representing a surface $\mathcal{M}$ are given by the following linear combination

$$\boxed{\boldsymbol{x}_{\alpha\beta} \equiv \Gamma^{\gamma}_{\alpha\beta}\boldsymbol{x}_{\gamma} + \Omega_{\alpha\beta}\boldsymbol{N}} \tag{10.87}$$

where $\Gamma^{\gamma}_{\alpha\beta}$ are functions of the components of the metric tensor and $\Omega_{\alpha\beta}$ are the coefficients of the second fundamental form. These relations are known as the *formulae of Gauss*.

Remark 7. *One can prove that the Christoffel symbols of the first and second kind are not components of any tensor. Indeed, under an allowable coordinate transformation* $u^{\alpha} =$

$u^\alpha(\bar{u}^\beta)$*, they transform according to*[19] (e.g. *for the second kind)*

$$\bar{\Gamma}^\tau_{\sigma\lambda} = \frac{\partial \bar{u}^\tau}{\partial u^\gamma}\frac{\partial u^\alpha}{\partial \bar{u}^\sigma}\frac{\partial u^\beta}{\partial \bar{u}^\lambda}\Gamma^\gamma_{\alpha\beta} - \frac{\partial^2 \bar{u}^\tau}{\partial u^\alpha \partial u^\beta}\frac{\partial u^\alpha}{\partial \bar{u}^\sigma}\frac{\partial u^\beta}{\partial \bar{u}^\lambda} \tag{10.88}$$

The formulae of Weingarten and Gauss are in a sense similar to the formulae of Frenet. For a curve of class C^r with $r \geq 2$, we saw that at any point P we can associate the vectors $\boldsymbol{T}, \boldsymbol{P}, \boldsymbol{B}$ and that any vector bound at P can be represented as a linear combination of the corresponding derivatives $\dot{\boldsymbol{T}}, \dot{\boldsymbol{P}}, \dot{\boldsymbol{B}}$, provided that they exist. For a surface, the situation is somewhat similar but now the relevant vectors are $\boldsymbol{x}_1, \boldsymbol{x}_2$ - spanning the tangent space $T_P(\mathcal{M})$ - and the surface normal $\boldsymbol{N}$, with their derivatives expressed by the above derived formulae. The question that naturally arises is the following: if functions $g_{\alpha\beta}(u^1, u^2)$ and $\Omega_{\alpha\beta}(u^1, u^2)$ are given, there always exists a surface such that the given functions are the coefficients of the corresponding fundamental forms? In other words, we are asking whether the partial differential equations defined by the formulae of Weingarten and Gauss do always admit solutions. The answer is of course negative unless certain integrability conditions are satisfied. We shall see in the following that, in the search of such integrability conditions, we will arrive at one of the most important result in differential geometry, the so-called *Theorema Egregium*.

Let $\mathcal{M} : \boldsymbol{x}(u^1, u^2)$ be a surface of class C^r with $r \geq 3$. Then, we must have

$$\frac{\partial \boldsymbol{x}_{\alpha\beta}}{\partial u^\lambda} = \frac{\partial \boldsymbol{x}_{\alpha\lambda}}{\partial u^\beta}$$

which, by keeping the same notation used so far, we re-write as

$$\boldsymbol{x}_{\alpha\beta\lambda} = \boldsymbol{x}_{\alpha\lambda\beta} \tag{10.89}$$

From $\boldsymbol{x}_{\alpha\beta} = \Gamma^\gamma_{\alpha\beta}\boldsymbol{x}_\gamma + \Omega_{\alpha\beta}\boldsymbol{N}$, we thus find

$$\boldsymbol{x}_{\alpha\beta\lambda} = \frac{\partial \Gamma^\gamma_{\alpha\beta}}{\partial u^\lambda}\boldsymbol{x}_\gamma + \Gamma^\gamma_{\alpha\beta}\boldsymbol{x}_{\gamma\lambda} + \frac{\partial \Omega_{\alpha\beta}}{\partial u^\lambda}\boldsymbol{N} + \Omega_{\alpha\beta}\boldsymbol{N}_\lambda$$

[19] In general theory of differential geometry of arbitrary spaces (devoid of a metric and not embedded in a "bigger" Euclidean space), a set of coefficients Γ^j_{hk} satisfying the transformation law (10.88) is called *affine connection*, and a space endowed with such set an *affinely connected space*. The concept of affine connection arises from the following simple observation: if X^j are the components of a contravariant vector field, the corresponding differential dX^j does not behave as a contravariant vector field; this suggest the introduction of a new type of differential DX^j

$$DX^j = dX^j + P^j(u^p, X^h, du^k)$$

where u^p denotes again the coordinate system on the space. One can prove that, in order for DX^j to transform according to a contravariant vector field, we must have $P^j = \Gamma^j_{hk}X^h du^k$, where Γ^j_{hk} have to satisfy precisely the transformation law (10.88). The operator D is also called *absolute differential*. For a scalar field $\phi(u^k)$ of class C^1, it is natural to write $d\phi = (\partial\phi/\partial u^k)du^k$. Therefore, one may wonder about the existence of a counterpart of this relation for absolute differentials. For this purpose, one needs to construct a tensorial analogue of partial derivatives. The latter is the so-called *covariant derivative*

$$\nabla_k X^p = \frac{\partial X^p}{\partial u^k} + \Gamma^p_{hk}X^h \qquad DX^p = \nabla_k X^p du^k$$

which can be proved to constitute the components of a type $(1,1)$ tensor (thus ensuing again that DX^j is $(1,0)$ tensor). This is how the concept of covariant derivative is introduced from the more general perspective of tensor calculus. The *connection* with the Riemannian geometry is immediate once it is recognized that an affine connection can always be constructed from a symmetric, non-singular $(0,2)$-tensor field $a_{ij}(u^p)$ of class C^1. When the latter is identified with the metric tensor, one thus obtains the Christoffel symbols defined in the main text.

In consequence of the formulae of Weingarten and Gauss, we can also write

$$\boldsymbol{x}_{\alpha\beta\lambda} = \frac{\partial \Gamma^{\gamma}_{\alpha\beta}}{\partial u^{\lambda}} \boldsymbol{x}_{\gamma} + \Gamma^{\gamma}_{\alpha\beta}(\Gamma^{\sigma}_{\gamma\lambda}\boldsymbol{x}_{\sigma} + \Omega_{\gamma\lambda}\boldsymbol{N}) - \Omega_{\alpha\beta}\Omega^{\tau}_{\lambda}\boldsymbol{x}_{\tau} + \frac{\partial \Omega_{\alpha\beta}}{\partial u^{\lambda}}\boldsymbol{N}$$

With a straightforward manipulation of the indices, we obtain

$$\boldsymbol{x}_{\alpha\beta\lambda} = \left(\frac{\partial \Gamma^{\sigma}_{\alpha\beta}}{\partial u^{\lambda}} + \Gamma^{\gamma}_{\alpha\beta}\Gamma^{\sigma}_{\gamma\lambda} - \Omega_{\alpha\beta}\Omega^{\sigma}_{\lambda} \right) \boldsymbol{x}_{\sigma} + \left(\Gamma^{\rho}_{\alpha\beta}\Omega_{\rho\lambda} + \frac{\partial \Omega_{\alpha\beta}}{\partial u^{\lambda}} \right) \boldsymbol{N} \tag{10.90}$$

and by interchanging β and γ,

$$\boldsymbol{x}_{\alpha\lambda\beta} = \left(\frac{\partial \Gamma^{\sigma}_{\alpha\lambda}}{\partial u^{\beta}} + \Gamma^{\gamma}_{\alpha\lambda}\Gamma^{\sigma}_{\gamma\beta} - \Omega_{\alpha\lambda}\Omega^{\sigma}_{\beta} \right) \boldsymbol{x}_{\sigma} + \left(\Gamma^{\rho}_{\alpha\lambda}\Omega_{\rho\beta} + \frac{\partial \Omega_{\alpha\lambda}}{\partial u^{\beta}} \right) \boldsymbol{N} \tag{10.91}$$

In order for (10.90) to be equal to (10.91), in the difference $\boldsymbol{x}_{\alpha\beta\lambda} - \boldsymbol{x}_{\alpha\lambda\beta} = 0$, the coefficients of each vector must vanish. Hence, in the case of $\boldsymbol{N}$ we find that the following formula must hold

$$\Gamma^{\rho}_{\alpha\beta}\Omega_{\rho\lambda} - \Gamma^{\rho}_{\alpha\lambda}\Omega_{\rho\beta} + \frac{\partial \Omega_{\alpha\beta}}{\partial u^{\lambda}} - \frac{\Omega_{\alpha\lambda}}{\partial u^{\beta}} = 0 \tag{10.92}$$

These relations are called the *formulae of Mainardi-Codazzi*[267, 268]. For the coefficient of $\boldsymbol{x}_{\sigma}$, we find instead

$$R^{\sigma}_{\alpha\lambda\beta} = \Omega_{\alpha\beta}\Omega^{\sigma}_{\lambda} - \Omega_{\alpha\lambda}\Omega^{\sigma}_{\beta} \tag{10.93}$$

where we have set

$$R^{\sigma}_{\alpha\lambda\beta} = \frac{\partial \Gamma^{\sigma}_{\alpha\beta}}{\partial u^{\lambda}} - \frac{\partial \Gamma^{\sigma}_{\alpha\lambda}}{\partial u^{\beta}} - \Gamma^{\gamma}_{\alpha\beta}\Gamma^{\sigma}_{\gamma\lambda} - \Gamma^{\gamma}_{\alpha\lambda}\Gamma^{\sigma}_{\gamma\beta} \tag{10.94}$$

the quantities $R^{\sigma}_{\alpha\lambda\beta}$ are the components of a type $(1,3)$ tensor that is called the **Riemann curvature tensor**[20]. Formulae (10.92) and (10.93) are precisely the integrability conditions we were looking for. At this point, we shall investigate a little more the Riemann curvature tensor and find a geometrical interpretation that justify its name[21]. To this purpose, let first define the *covariant Riemann curvature tensor*

$$R_{\tau\alpha\lambda\beta} = g_{\sigma\tau}R^{\sigma}_{\alpha\lambda\beta} \tag{10.95}$$

which is a type $(0,4)$ tensor. From its definition and with some index manipulation, one can

[20] In arbitrary spaces endowed with just an affine connection Γ^{j}_{hk} the curvature tensor is introduced in a similar manner, as a natural extension to the concept of "curvature" given in the theory of calculus, namely it is related to a ("second") repeated covariant derivative. In particular, for a type $(1,0)$ tensor field X^{j}, we have

$$\nabla_k \nabla_h X^j - \nabla_h \nabla_k X^j = R^{j}_{lhk} X^l + S^{l}_{hk} \nabla_l X^j$$

where $S^{j}_{hk} = \Gamma^{j}_{hk} - \Gamma^{j}_{kh}$ are the components of a type $(1,2)$-tensor called *torsion tensor*. In Riemannian spaces, due to the symmetry property of Christoffel symbols in its covariant indices, it clearly follows that $S^{j}_{hk} \equiv 0$. For this reason, Riemannian spaces are said to be *torsion-free spaces*.

[21] The geometrical interpretation of the curvature tensor in affinely connected spaces (see footnote 20 on 169) is more tricky to understand, because of the absence of the geometrical structure brought by the metric tensor. In a nutshell, the geometrical meaning of R^{j}_{lhk} emerges when one looks for the necessary conditions for a vector field $X^{j}(t)$ defined on curve C on the space $\mathcal{M}$ to be *parallel*. A vector field $X^{j}(t)$ is said to be parallel along a curve C if and only if the partial differential equations $DX^{j} = 0$ are satisfied along C, where D denotes again the absolute differential (see footnote 19 on 168). From such definition, one can prove that a necessary condition for X^{j} to be parallel is

$$R^{j}_{lhk} X^l = 0$$

show that also the components of the covariant Riemann tensor can be entirely expressed in terms of the coefficients of the second fundamental form, namely

$$R_{\tau\alpha\lambda\beta} = \Omega_{\alpha\beta}\Omega_{\lambda\tau} - \Omega_{\alpha\lambda}\Omega_{\beta\tau}$$

From the symmetry property of the Christoffel symbols, it is immediate to prove that the curvature tensor $R^{\sigma}_{\alpha\lambda\beta}$ is skew-symmetric under the permutation of the index λ and β. In addition, it holds

$$R^{\sigma}_{\alpha\lambda\beta} + R^{\sigma}_{\lambda\beta\alpha} + R^{\sigma}_{\beta\alpha\lambda} = 0 \tag{10.96}$$

Then, in consequence of (10.96) and (10.95), we also have

$$R_{\tau\alpha\lambda\beta} = -R_{\tau\alpha\beta\lambda} \tag{10.97}$$

i.e. the covariant Riemann curvature tensor is skew-symmetric under the permutation of its last two indices. Similarly, one can prove that it is skew-symmetric also under the permutation of the first two indices,

$$R_{\tau\alpha\lambda\beta} = -R_{\alpha\tau\lambda\beta} \tag{10.98}$$

From (10.97) ,we can write the following formula

$$R_{\tau\alpha\lambda\beta} + R_{\lambda\beta\alpha\tau} + R_{\beta\alpha\tau\lambda} = 0 \tag{10.99}$$

The latter, combined with (10.98) and (10.97), leads to the following additional symmetry property

$$R_{\tau\alpha\lambda\beta} = R_{\lambda\beta\tau\alpha} \tag{10.100}$$

From (10.97), (10.98) and (10.100) together, it follows that, for a two-dimensional Riemannian space where the curvature tensor has $n^4 = 2^4 = 16$ components, only four components are different from zero, namely

$$R_{1212} = R_{2121} = \Omega_{22}\Omega_{11} - (\Omega_{12})^2 = \Omega$$
$$R_{2112} = R_{1221} = (\Omega_{12})^2 - \Omega_{22}\Omega_{11} = -\Omega$$

These relations have an important consequence: *since the Christoffel symbols depend only on the coefficients $g_{\alpha\beta}$ of the first fundamental form, the same holds for the components of the Riemann curvature tensor and, therefore, also for the discriminant Ω of the second fundamental form.*. Recalling then the definition of the Gaussian curvature, we can now state the following

Theorem 10.6.1 (Theorema egregium (Gauss1827)[269])**.** *The Gaussian curvature K of a surface is independent of the second fundamental form but depends only on the coefficients*

The above condition is not always satisfied in general, since the components R^{j}_{lhk} depend on the particular connection assigned to the space under consideration. However, it is possible to construct a special connection for which the components of the curvature tensor vanishes everywhere. This is the case of the so-called *flat spaces*, for which Euclidean space are an example. Hence, for flat spaces, $R^{j}_{lhk}X^{j} = 0$ becomes a necessary and sufficient condition. If we apply the condition $DX^{j} = 0$ to the case of the tangent vector (field) $u^{j}(t)$ to a curve C, we can prove that the curve $u^{j} = u^{j}(t)$ has to to satisfy the following differential equations

$$\frac{d^2u^{j}}{dt^2} + \Gamma^{j}_{hk}\frac{dx^{h}}{dt}\frac{dx^{k}}{dt} = 0$$

The curves satisfying the above equations are referred to as *autoparallel curves*. If one identify the affine connection with the Christoffel symbols of a Riemannian space, it can be proved that solutions of the above equations are precisely the *geodesics* of the Riemannian space ($\kappa_g = 0$). In other words, geodesics are curves for which the tangent vector at a point P can be obtained from the *parallel transport* of the tangent vector to a neighboring point Q.

$g_{\alpha\beta}$ of the first fundamental form, and their first and second derivatives

$$K = \frac{R_{1212}}{g} \tag{10.101}$$

The importance of such conclusion lies in the fact that it makes the Gaussian curvature K a true *intrinsic invariant*. Indeed, according to Definition 10.5.3, K depends on the coefficients $\Omega_{\alpha\beta}$ of the second fundamental form, which are well defined if and only if the space is embedded in E_3[22], being the normal components of the vectors $\boldsymbol{x}_{\alpha\beta}$. On the other hand, from the Theorema Egregium, it follows that the existence of $g_{\alpha\beta}$ with their derivatives is sufficient for the development of self-consistent theory of curvature. In other words, once $g_{\alpha\beta}$ are given, no appeal whatsoever need to be made to the fact that the Riemannian space is embedded, and "true" *intrinsic theory* of Riemannian spaces can be developed.

In closing this Section, we state also an other important result of differential geometry, which allows to put on firmer grounds what we have discussed in Chapter 6 concerning Euler's formula applied to fullerenes (see Section 6.2 and footnote 13 at page 72).

Theorem 10.6.2 (Gauss-Bonnet)**.** *Let $\mathcal{M}$ be a surface of class C^r with $r \geq 3$ and $\partial\mathcal{M}$ a closed curve of class C^p with $p \geq 2$, representing the boundary of the surface, if any. Then*

$$\int_{\partial\mathcal{M}} \kappa_g(s)ds + \int_{\mathcal{M}} KdA = 2\pi\chi(\mathcal{M}) \tag{10.102}$$

where $\kappa_g(s)$ is the geodesic curvature along the curve $\partial\mathcal{M}$, parametrized in terms of its arc length s, K is the Gaussian curvature of $\mathcal{M}$ and dA the element of area of $\mathcal{M}$.

This theorem was first published by O. Bonnet in 1848, but it was probably already known to Gauss, and it is therefore referred to as the *Gauss-Bonnet theorem*[23]. Equation (10.102) can be regarded as an integral identity that the Gaussian curvature (K) of a surface and the curvature of its boundary (κ_g) have to satisfy. The quantity $\chi(\mathcal{M})$, called the **Euler's characteristic**, can be then regarded as a *topological invariant*, a number that describes the shape of the surface *regardless of the way it is bent*[24]. When the Gauss-Bonnet theorem is applied to surfaces of *polyhedra*, it leads to the expression of the Euler's characteristic given in Chapter 6, namely

$$\chi = V - E + F \tag{10.103}$$

where V , E and F are, respectively, the numbers of vertices, edges and faces in the given polyhedron. χ is then 1 and 2 for any convex polyhedron in two and three dimensions,

[22] Of course, the same conclusions can be extended to higher dimensions, considering a V_{n-1} Riemannian manifold embedded in E_n.

[23] A proof in the context of n-dimensional Riemannian manifold can be found at pag. 281 of the book by D. Lovelock and H. Rund(1989)

[24] As a simple application, let consider for instance a flat surface. The Gaussian curvature is everywhere vanishing ($K = 0$) and the integrated geodesic curvature along the edges is zero as well. Therefore, for a flat surface, like a sheet of paper, $\chi = 0$. If we bend the sheet of paper to form a cylindrical surface, we still get $\chi = 0$ for the corresponding cylinder, since the Gaussian curvature is again identically vanishing. On the other hand, we cannot find a continuous deformation that bends the sheet of paper into a sphere of radius R, since for the sphere

$$\int_{\mathcal{M}} KdA = \frac{1}{R^2}(4\pi R^2) = 2\pi\chi$$

that is, the Euler's characteristic is $\chi = 2$.

respectively, but it can take different values in more complicated objects, *e.g.*, the octahemioctahedron ($\chi = 0$) or the cubohemioctahedron ($\chi = -2$). It is extended to smooth surfaces by triangulation, *i.e.*, for planar objects by subdivision into triangles, and in higher dimensions by subdivision into simplices[25].

[25] A simplex is a generalization of the notion of a triangle to arbitrary dimensions. Those that can be fully represented in three-dimensional space are the 0-simplex (a point), the 1-simplex (a line segment), the 2-simplex (a triangle) and a 3-simplex (a tetrahedron). In general, a n-simplex can be constructed with n linearly independent vectors drawn from a common origin by considering the basis vectors and their differences.

Chapter 11

Hybridization and Local Curvature

So far, the description of curved systems has been restricted to simple geometrical models, that limit to assess the distortion around C atoms through pyramidalization (*POAV*) or rehybridization. If one wants to go beyond such a description, the very first task to address is defining the "curvature" at a C atom, and eventually, relating this curvature with its atomic-scale effects, namely the above-mentioned hybridization and pyramidalization. This non-trivial problem has not been tackled in the literature so far, according to the author's knowledge.

In this Chapter, we will discuss a new model that draws the theory of *Riemannian geometry* to properly define the curvature at carbon atoms. Hence, we will show how this curvature enters the definition of the geometry around carbons (*i.e.* bond angle and hybridization). To validate our model, we will then present some applications to simple but interesting systems.

11.1 The model

Let $T_0\mathcal{M}$ be the tangent space to the 2-surface $\mathcal{M} \subset \mathbb{R}^3$ at the point $\boldsymbol{x}_0$ where a C atom is found. Let $\boldsymbol{e}_1$ and $\boldsymbol{e}_2$ two unit vectors along the line of principal curvatures[1], $\kappa^{(1)}$ $\kappa^{(2)}$ respectively, in such a way that $(\boldsymbol{e}_1, \boldsymbol{e}_2, \boldsymbol{N})$, with $\boldsymbol{N}$ the surface normal, forms a right-handed reference system. For instance, for the surface of a carbon nanotube with the normal oriented outward, $\boldsymbol{e}_1$ is the unit vector orthogonal to the tube axis (associated to the curvature $\kappa = -1/R$, with R the tube diamater) and $\boldsymbol{e}_2$ is the one directed along the tube axis (associated to $\kappa = 0$, a direction of vanishing normal curvatures) (see Subsection).

Let consider then a neighboring atom at a point $\boldsymbol{x} \in \mathcal{M}$, its position $\Delta\boldsymbol{x} = \boldsymbol{x} - \boldsymbol{x}_0$ relative to $\boldsymbol{x}_0$ and the projection $\boldsymbol{X}$ of the latter onto $T_0\mathcal{M}$. The vector $\boldsymbol{X} \in T_0\mathcal{M}$ can be used to define a curve $\gamma(t) \in \mathbb{R}^3$ joining $\boldsymbol{x}_0$ to $\boldsymbol{x}$ with normal curvature κ_n at $\boldsymbol{x}_0$. The curve is not unique unless we fix the "shape" of the surface around $\boldsymbol{x}_0$, a rather delicate issue that boils down to the meaning of "surface interpolating the carbon atom sheet" and of "curvature" at a carbon atom. Henceforth, we make the simplest choice of a *locally quadratic* shape because of its advantages w.r.t. possible alternatives, *e.g.* a spherical surface of radius κ^{-1} tangent to $T_0\mathcal{M}$. Compared to the latter, for instance, our choice gives rise to simpler analytical expressions, it is free of constraints[2] and it does describe a locally spherical surface when the bond length ρ is such that $\rho \ll \kappa^{-1}$ (see Subsection 11.2.1).

Let then $\hat{\boldsymbol{X}} = \boldsymbol{X}/||\boldsymbol{X}||$ be the unit vector along the direction $\boldsymbol{X}$, s the curve parameter

[1]These vectors clearly coincide with the tangent vectors $\boldsymbol{x}_\alpha \equiv \partial\boldsymbol{x}/\partial u^\alpha$ to the coordinate curves once the latter are chosen to be the lines of curvature.

[2]It may be worth noticing that if a neighboring C atom has to lie on the spherical surface tangent to $T_0\mathcal{M}$ the length $\rho_\parallel$ of the projected bond on $T_0\mathcal{M}$ is restricted by the condition $\rho_\parallel \leq \kappa^{-1}$, with $\kappa = 1/R$.

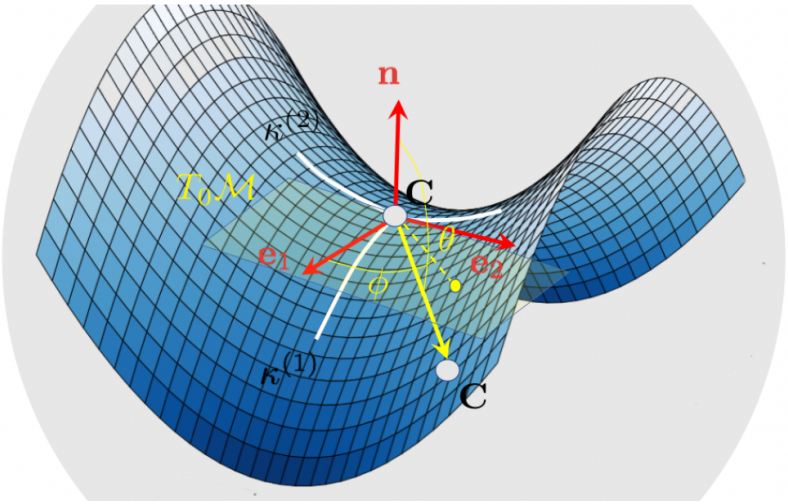

Figure 11.1. Schematics showing a surface $\mathcal{M}$, the tangent plane $T_0\mathcal{M}$ at a C atom, the reference system $(\boldsymbol{e}_1, \boldsymbol{e}_2, \boldsymbol{n})$ identified by the lines of principal curvatures and a bond to a neighboring C atom (yellow arrow).

and κ_n the normal curvature at $\boldsymbol{x}_0$. Under our assumptions we have $\dot{\gamma}(0) = d\gamma/ds(0) = \hat{\boldsymbol{X}}$, $\ddot{\gamma}(0) = \kappa_n \boldsymbol{n} = \ddot{\gamma}(s)$[3]. These guarantee that κ_n is indeed the curvature of the curve at $s = 0$, where $\boldsymbol{T} = \hat{\boldsymbol{X}}$ is the unit tangent vector and $\dot{\boldsymbol{T}}$ satisfies $(\dot{\boldsymbol{T}}|\boldsymbol{T}) = 0$ and $||\dot{\boldsymbol{T}}|| = |\kappa_n|$. In other words, the curve joining two neighboring carbons is a lines of curvature (*i.e.* with vanishing geodesic curvature, κ_g) of the locally quadratic surface, hence hereafter we set $\kappa_n \equiv \kappa$. Then

$$\dot{\gamma}(s) = \hat{\boldsymbol{X}} + \int_0^s \ddot{\gamma} ds = \hat{\boldsymbol{X}} + \kappa s \boldsymbol{N}$$
$$\gamma(s) = \boldsymbol{x}_0 + \int_0^s \dot{\gamma} ds = \boldsymbol{x}_0 + \hat{\boldsymbol{X}} s + \frac{1}{2}\kappa s^2 \boldsymbol{N}$$

Upon requiring that $\gamma(s) = \boldsymbol{x}$ for some $s = \bar{s}$, we find $\bar{s} = ||\boldsymbol{X}|| \equiv \rho_{\parallel}$ (the *projected* bond length onto the tangent space) since the condition

$$\gamma(\bar{s}) - \boldsymbol{x}_0 = \boldsymbol{X} + \frac{1}{2}\kappa ||\boldsymbol{X}||^2 \boldsymbol{N} \tag{11.1}$$

sets the projection of $\Delta\boldsymbol{x}$ onto $T_0\mathcal{M}$ to be $\boldsymbol{X}$. As a result the normal component of the relative position is determined by $\rho_{\parallel}$ and the (normal) curvature as $\frac{1}{2}\kappa||\boldsymbol{X}||^2\boldsymbol{N}$.

There remains to establish the relation between κ and the principal curvatures. To this end, let (r, θ, ϕ) be the spherical coordinate system associated to $(\boldsymbol{e}_1, \boldsymbol{e}_2, \boldsymbol{N})$ and

$$x = \rho \sin\theta \cos\phi$$
$$y = \rho \sin\theta \sin\phi$$
$$z = \rho \cos\theta$$

the coordinate of the relative position vector on the frame $(\boldsymbol{e}_1, \boldsymbol{e}_2, \boldsymbol{N})$ ($\rho \equiv$ bond length). Clearly, $\boldsymbol{X} = \rho\sin(\theta)\cos(\phi)\boldsymbol{e}_1 + \rho\sin(\theta)\sin(\phi)\boldsymbol{e}_2$, $\rho_{\parallel} = \rho\sin(\theta)$ and the (normal) curvature κ is related to the principal curvatures according to the Euler's theorem (see Theorem

[3] In other words, the curve joining two neighboring carbons is a parabolic curve with constant acceleration vector, given by the surface normal in $\boldsymbol{x}_0$, the position of the central carbon considered.

(10.5.5) on pag. 163)

$$\kappa_n = \kappa^{(1)} \cos^2(\phi) + \kappa^2 \sin^2(\phi)$$

Hence,

$$(\boldsymbol{n}|\Delta\boldsymbol{x}) = \frac{1}{2}\kappa_n \rho_{\|}^2 = \frac{1}{2}\left(\kappa^{(1)} x^2 + \kappa^2 y^2\right)$$

or equivalently

$$\Delta\boldsymbol{x} = x\boldsymbol{e}_1 + y\boldsymbol{e}_2 + \frac{1}{2}\left(\kappa^{(1)} x^2 + \kappa^2 y^2\right)\boldsymbol{N} \tag{11.2}$$

Equation (11.2) show that $\boldsymbol{X}$ uniquely defines $\Delta\boldsymbol{x}$, that is, the latter is entirely specified by the length $\rho_{\|}$ of $\boldsymbol{X}$ and its orientation ϕ ($\kappa_n \equiv \kappa_n(\phi)$), $\Delta\boldsymbol{x} = \Delta\boldsymbol{x}(\rho_{\|}, \phi)$.

Let consider now two displacement vectors, $\Delta\boldsymbol{x}_1$ and $\Delta\boldsymbol{x}_2$, corresponding to two bonds that the C at $\boldsymbol{x}_0$ makes with its nns. Let $||\Delta\boldsymbol{x}_i|| = \rho_i$ be the corresponding bond length and κ_i the (normal)curvature ($i = 1, 2$). The *bond angle* Θ_{12} is thus given by

$$\cos(\Theta_{12}) = \frac{(\Delta\boldsymbol{x}_1|\Delta\boldsymbol{x}_2)}{||\Delta\boldsymbol{x}_1|| \cdot ||\Delta\boldsymbol{x}_2} = \frac{1}{\rho_1\rho_2}\left((\boldsymbol{X}_1|\boldsymbol{X}_2) + \frac{1}{4}\kappa_1\kappa_2\rho_{1,\|}^2\rho_{2,\|}^2\right) \tag{11.3}$$

Let $\Delta\phi = \phi_1 - \phi_2$ be the bond angle projected onto $T_0\mathcal{M}$, hence $(\boldsymbol{X}_1|\boldsymbol{X}_2) = \cos(\Delta\phi)$. Equation (11.3) thus becomes

$$\cos(\Theta_{12}) = \sin(\theta_1)\sin(\theta_2)\left[\cos(\Delta\phi) + \frac{1}{4}\kappa_1\kappa_2\rho_1\rho_2\sin(\theta_1)\sin(\theta_2)\right] \tag{11.4}$$

which is a general relation that requires just the knowledge of the angles that each $\Delta\boldsymbol{x}_i$ makes with the surface normal, the projected bond angle $\Delta\phi$ and the normal curvatures κ_i (that are given once specified the orientation of the bond w.r.t. the lines of principal curvature)[4].

Now, κ_i and ρ_i set the value of $\sin(\theta_i)$, indeed

$$\sin^2(\theta_i) = \frac{\rho_{i,\|}^2}{\rho_i^2} \tag{11.5}$$

but $\rho_{i,\|}$ itself is determined by ρ_i and κ_i, upon noticing that

$$||\Delta\boldsymbol{x}_i||^2 \equiv \rho_i^2 = \rho_{i,\|}^2 + \frac{\kappa_i^2}{4}\rho_{i,\|}^4$$

which is a second order equation for $y = \rho_{i,\|}^2$ that admits the (positive) solution

$$\rho_{i,\|}^2 = \frac{2}{\kappa_i^2}\left(\sqrt{1 + \kappa_i^2\rho_i^2} - 1\right) \tag{11.6}$$

Note that, in the limit of vanishing curvature $\kappa_i \to 0$, $\rho_{i,\|}^2 \to \rho_i^2$. The substitution of the

[4]It may be worth noticing that the "curvature" properties enter here in the form of the product $\kappa_1\kappa_2$, which is the prototype of a Gaussian curvature defined through two generic normal curvatures.

above expression into Equation (11.5) gives[5]

$$\sin^2(\theta_i) = \frac{2}{\sqrt{1+\kappa_i^2\rho_i^2}+1} \tag{11.7}$$

With Equation (11.7), we can write down the following explicit formula

$$\begin{aligned}\cos(\Theta_{12}) = &\frac{2}{\sqrt{\left(\sqrt{1+\rho_1^2\kappa_1^2}+1\right)\left(\sqrt{1+\rho_2^2\kappa_2^2}+1\right)}}\cos(\phi_1-\phi_2)+ \\ &+\operatorname{sgn}(\kappa_1\kappa_2)\left(\frac{\sqrt{1+\rho_1^2\kappa_1^2}-1}{\sqrt{1+\rho_1^2\kappa_1^2}+1}\frac{\sqrt{1+\rho_2^2\kappa_2^2}-1}{\sqrt{1+\rho_2^2\kappa_2^2}+1}\right)^{1/2}\end{aligned} \tag{11.8}$$

We stress that this is a rather general expression and applies to *any* situation. It only requires the the lines of principal curvature, the associated curvatures and the orientation of the bonds with respect to such lines, in particular the angle $\Delta\phi = \phi_1 - \phi_2$ that the "projected bonds" make with each other. In the following, we apply it to some simple but interesting cases.

11.2 Applications

11.2.1 Spherical surface

The simplest case is that of a spherical surface, where each point is *umbilic*, *i.e.* $\kappa_1 = \kappa_2 = \kappa$ for any direction on the surface. Then, for the bond angle $\cos(\Theta_{12})$ we get

$$\cos(\Theta_{12}) = \sin(\theta_1)\sin(\theta_2)\left(\cos(\Delta\phi) + \frac{1}{4}K\rho_1\rho_2\sin(\theta_1)\sin(\theta_2)\right)$$

where K is the Gaussian curvature of the sphere. In the equilibrium situation where there are three σ bonds ($\rho_i \equiv \rho$) making a projected bond angle of $\Delta\phi = 2\pi/3$ and $\theta_i \equiv \theta$ ($\Theta_{12} \equiv \Theta$), the above expression reduces to

$$\cos(\Theta) = \sin^2(\theta)\left(-\frac{1}{2} + \frac{1}{4}K\rho^2\sin^2(\theta)\right)$$

since $\sin^2 = 2/(\sqrt{1+\rho^2\kappa^2}+1)$ (Equation (11.7)) and $K = +1/R^2$, with $R = \kappa^{-1}$ (see Subsection), we have

$$\boxed{\cos(\Theta) = 1 - \frac{3}{\sqrt{1+a^2}+1}} \tag{11.9}$$

where $a = \rho/R \equiv \kappa\rho$. In Section 6.1 we saw that, in the hypothesis of non-bent bonds, the Coulson's directionality theorem allows computing the hybridization indexes from the

[5] One can also write down θ_i as function of ρ_i and κ, using

$$\cot(\theta_i) = \sqrt{\frac{1}{2}(\sqrt{1+\rho_i\kappa_i}-1)}$$

to write

$$\cos(\theta_i) = \operatorname{sgn}(\kappa_i)\sqrt{\frac{\cot^2(\theta_i)}{\cot^2(\theta_i)+1}} = \operatorname{sgn}(\kappa_i)\sqrt{\frac{\sqrt{1+\rho_i^2\kappa_i^2}-1}{\sqrt{1+\rho_i^2\kappa_i^2}+1}}$$

since the plus (minus) sign holds for $\kappa_i > 0$ ($\kappa_i < 0$).

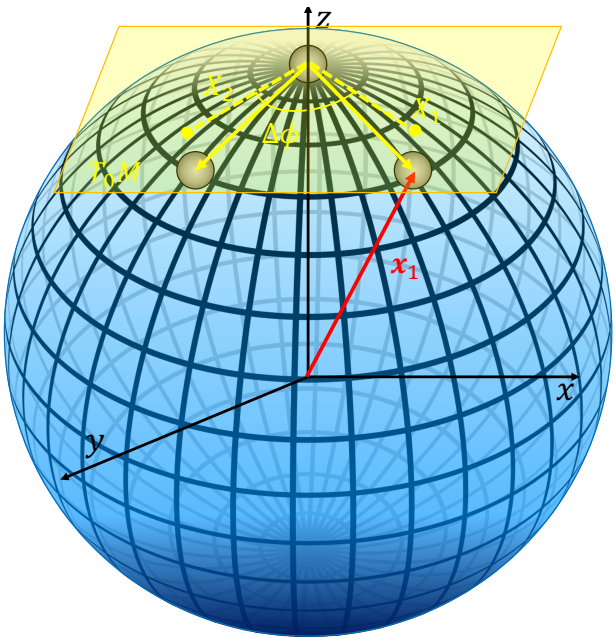

Figure 11.2. Schematics showing a spherical surface $\mathcal{M}$, the tangent plane $T_0\mathcal{M}$ at a C atom, the cartesian reference system (x, y, z), a position vector $\boldsymbol{x}_1$ (red arrow) and the projected bonds $\boldsymbol{X}_1, \boldsymbol{X}_2$ (dotted yellow arrows).

geometry around the C atom. Here, we assume that the C atom employs sp^τ hybrids to form the three σ bonds and a sp^λ hybrid to form the π-like bond. Therefore,

$$\cos(\Theta) = -\frac{1}{\tau} \qquad \lambda = \frac{1}{1 - 3(1+\tau)^{-1}} - 1$$

When using Equation (11.9) to compute the σ and π hybridization indexes we obtain

$$\boxed{\tau = \frac{1+\sqrt{1+a^2}}{2-\sqrt{1+a^2}} \qquad \lambda = \frac{1}{\sqrt{1+a^2}-1} - 1} \tag{11.10}$$

which give explicitly the hybridization indexes as functions of the sphere radius R. In the limit $R \gg \rho$,

$$\tau \approx \frac{2 + a^2/2}{1 + a^2/2} \approx 2 + \frac{3}{2}a^2 \qquad \lambda = 2\frac{1}{a^2}$$

which correctly reduce to $\tau = 2$ and $\lambda \to \infty$ for $R \to \infty$.

The spherical geometry is the simplest case where exact analytical expressions can be derived and, therefore, it allows putting on firmer ground the validity of the locally quadratic approximation that we assumed at the outset. To this aim, let $z = \sqrt{R^2 - x^2 - y^2}$ be a semisphere of radius R, defined as the graph of a two-dimensional function $f(x, y) = z$. In this representation, each point on the semisphere is

$$\boldsymbol{x}_i = \left(x_i, y_i, \sqrt{R^2 - x_i - y_i}\right)$$

Without loss of generality, we can assume a C atom to be located at the *North Pole* of the semisphere, *i.e.* $\boldsymbol{x}_0 = (0, 0, R)$. Let again $\boldsymbol{X}_1, \boldsymbol{X}_2 \in T_0\mathcal{M}$ be the projected bond vectors with its two nns and consider the equilibrium situation in which $\Delta\phi = 2\pi/3$. Under such

assumption, the nn coordinates are entirely determined by R and $\rho_{\parallel} = ||\boldsymbol{X}||$. Indeed

$$x_1 = ||\boldsymbol{X}_1|| = \rho_{\parallel}$$
$$y_1 = 0$$

while the second nn is rotated on the xy-plane by $2\pi/3$

$$x_2 = -\frac{1}{2}||\boldsymbol{X}_2|| = -\frac{1}{2}\rho_{\parallel}$$
$$y_2 = \frac{\sqrt{3}}{2}||\boldsymbol{X}_2|| = \frac{\sqrt{3}}{2}\rho_{\parallel}$$

The relative position vectors $\Delta\boldsymbol{x}_i = \boldsymbol{x}_i - \boldsymbol{x}_0$ $(i = 1, 2)$ then read as

$$\Delta\boldsymbol{x}_1 = \left(\rho_{\parallel}, 0, \sqrt{R^2 - \rho_{\parallel}^2} - R\right) \tag{11.11}$$

$$\Delta\boldsymbol{x}_2 = \left(-\frac{1}{2}\rho_{\parallel}, \frac{\sqrt{3}}{2}\rho_{\parallel}, \sqrt{R^2 - \rho_{\parallel}^2} - R\right) \tag{11.12}$$

From Equation (11.11) and (11.12), $\cos(\Theta)$ is readily obtained

$$\cos(\Theta) = \frac{1}{\rho^2}\left(2R^2 - \frac{3}{2}\rho_{\parallel}^2 - 2R\sqrt{R^2 - \rho_{\parallel}^2}\right) \tag{11.13}$$

In order to compare Equation (11.13) with Equation (11.9), we need to express $\rho_{\parallel}$ in terms of the fundamental variable ρ. First, we note that

$$||\Delta\boldsymbol{x}_1||^2 \equiv \rho^2 = 2R^2 - 2R\sqrt{R^2 - \rho_{\parallel}^2}$$

that can be inverted to give

$$\rho_{\parallel}^2 = R^2 - \frac{1}{R^2}\left(2R^2 - \rho^2\right)^2 \tag{11.14}$$

Equation (11.13) can be re-written as $\cos(\Theta) = 1 - (3/2)\rho_{\parallel}^2/\rho^2$, then substituting in this formula Equation (11.14), we arrive at

$$\boxed{\cos(\Theta) = 1 - \frac{3}{2}\left(1 - \frac{a^2}{4}\right)} \tag{11.15}$$

where $0 \leq a = \rho/R \leq \sqrt{2}$. In Figure 11.3, $\cos(\Theta)$ is plotted as function of a according to both Equations (11.9) and (11.15). When employing a locally quadratic approximation, we are "flattening" the geometry around the C atom w.r.t. the original spherical shape. Therefore, $\Delta\rho = \rho - \rho_{\parallel}$ is greater on the sphere than on the locally quadratic approximated surface. Accordingly, the approximation (overestimates) underestimates (Θ) $\cos(\Theta)$. Nevertheless, Figure 11.3 clearly shows that for a broad range of a - up to the rather unphysical case where $a \approx \frac{1}{2}$, *i.e.* $R = 2\rho$ - the quadratic and spherical models provide essentially the same result[6]. From Equation (11.15), σ and π hybridization index can be readily obtained

$$\boxed{\tau = \frac{8}{4 - 3a^2} \qquad \lambda = \frac{12 - 9a^2}{6a^2}}$$

[6]Clearly, $\cos(\Theta)$ is of the same order in a in both models, hence a significant difference appears only at the 4th order ($o(a^4)$) in the expansion of $\cos(\Theta)$ around $a = 0$.

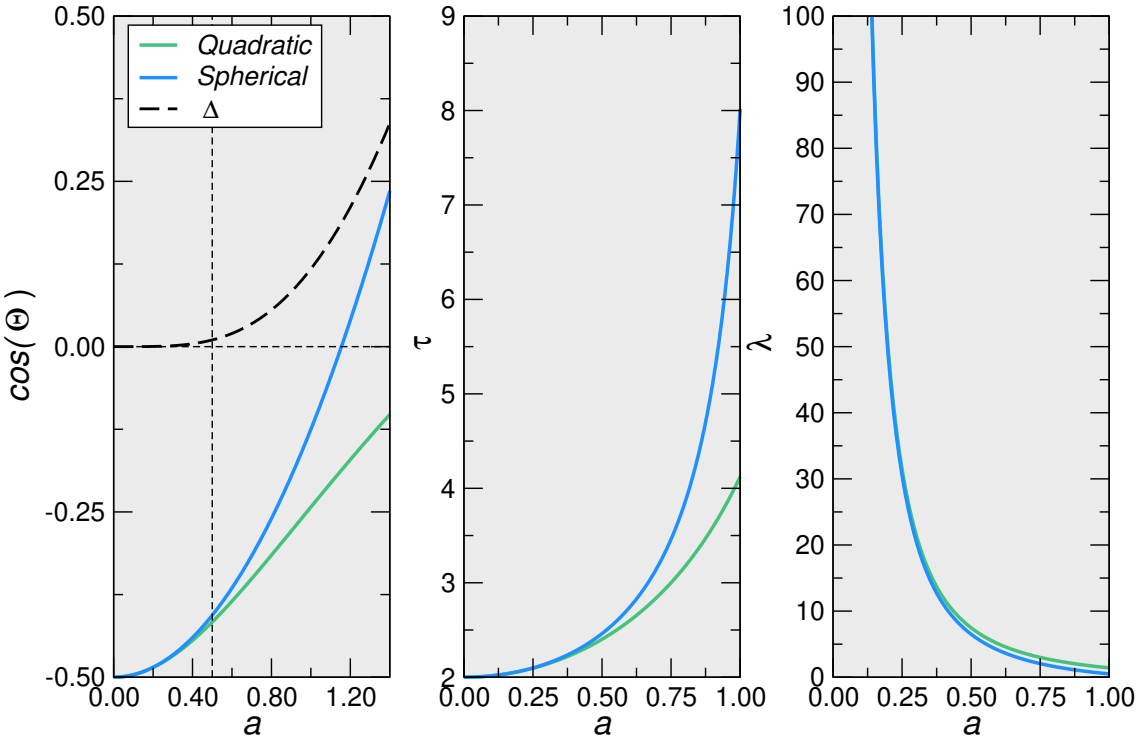

Figure 11.3. cos(Θ), τ and λ hybridization indexes plotted w.r.t. $a = \rho/R$, in the quadratic (green) and spherical (blue) model. For the bond angle cos(Θ) also shown their difference (Δ) with a black dotted line.

which correctly reduce to $\tau = 2$ and $\lambda \to \infty$ for $a \to 0$ ($R \to \infty$).

11.2.2 Nanotubes

As a second example, let consider a zig-zag nanotube, where there exist two equal bonds of length ρ forming an angle Θ with each other and an angle Θ' with the remaining one (the one directed along the tube axis). Let $\Delta\phi$, $\Delta\phi'$ be the corresponding projected bond angles, that satisfy $\Delta\phi + 2\Delta\phi' = 2\pi$.

If we cut the tube normally to its axis, along a zig-zag line, the C atoms form a regular polygon with N sides, of length l equal to the "widths" of the hexagons (the height can be arbitrary, as long as this geometry is of concern). Hence, according to the law of cosines[7] we have

$$l^2 = 2R^2\left(1 - \cos\left(\frac{2\pi}{N}\right)\right) \Longrightarrow l \equiv 2R\left|\sin\left(\frac{\pi}{N}\right)\right| \tag{11.16}$$

where R is the tube radius. For cos(Θ), we apply Equation (11.8), with $\kappa_1 = \kappa_2 \equiv \kappa$, $\rho_1 = \rho_2 \equiv \rho$, to get

$$\cos(\Theta) = \frac{2}{\sqrt{1+\rho^2\kappa^2}+1}\cos(\Delta\phi) + \frac{\sqrt{1+\rho^2\kappa^2}-1}{\sqrt{1+\rho^2\kappa^2}+1} \tag{11.17}$$

From Equation (11.16), (11.6) and $l = \rho_{\parallel}\sqrt{2\left(1-\cos(\Delta\phi)\right)}$ we can write cos(Θ) in terms

[7] This trigonometrical theorem relates the lengths of the sides of a triangle to the cosine of one of its angles. namely $c^2 = a^2 + b^2 + 2ab\cos(\gamma)$, where γ denotes the angle contained between sides of lengths a and b and opposite the side of length c.

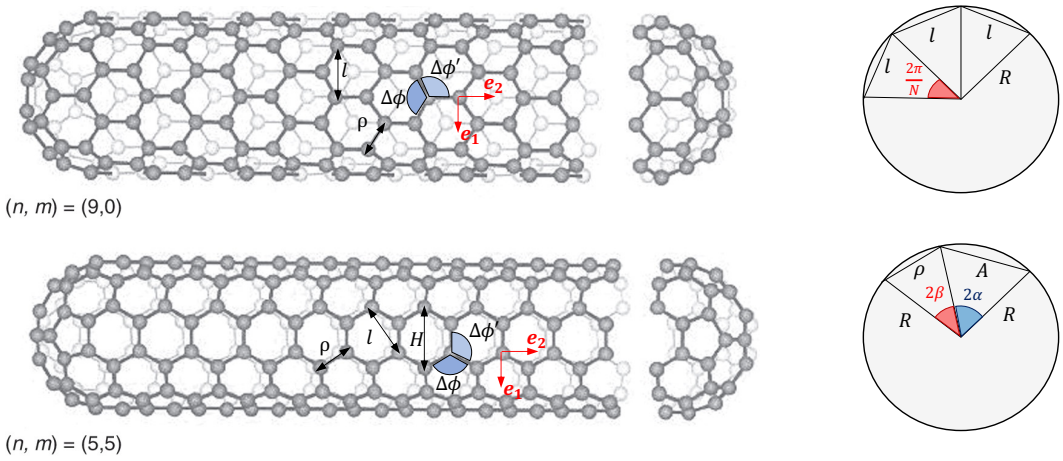

Figure 11.4. Schematics illustrating the main geometrical parameters of zig-zag and armchair nanotubes.

of ρ and R only. After some straightforward algebra, we have

$$\begin{aligned}\cos(\Theta) &= \frac{-4R^2\sin^2\left(\frac{\pi}{N}\right)+2\rho_\parallel^2}{\rho_\parallel^2(\sqrt{1+\rho^2\kappa^2}+1)}+\frac{\sqrt{1+\rho^2\kappa^2}-1}{\sqrt{1+\rho^2\kappa^2}+1}\\ &= -\frac{2R^2}{\rho^2}\sin^2\left(\frac{\pi}{N}\right)+\frac{\rho_\parallel^2}{\rho^2}+\frac{\sqrt{1+\rho^2\kappa^2}-1}{\sqrt{1+\rho^2\kappa^2}+1}\\ &= -\frac{2R^2}{\rho^2}\sin^2\left(\frac{\pi}{N}\right)+\frac{2}{\sqrt{1+\rho^2\kappa^2}+1}+\frac{\sqrt{1+\rho^2\kappa^2}-1}{\sqrt{1+\rho^2\kappa^2}+1}\end{aligned}$$

Hence

$$\boxed{\cos(\Theta) = 1-\frac{2R^2}{\rho^2}\sin^2\left(\frac{\pi}{N}\right)} \tag{11.18}$$

which correctly reduces to $\Theta \to \pi/3$ for vanishing curvature[8]. The average curvature κ readily follows from Euler's theorem, reminding that for the cylindrical geometry the principal curvatures are $\kappa^{(1)} = -1/R$ and $\kappa^{(2)} = 0$, hence

$$\kappa = \frac{1}{R}\sin^2\left(\frac{\Delta\phi}{2}\right) = \frac{R}{\rho_\parallel^2}\sin^2\left(\frac{\pi}{N}\right) = \frac{R}{\frac{2}{\kappa^2}(\sqrt{1+\rho^2\kappa^2}+1)}\sin^2\left(\frac{\pi}{N}\right)$$

The above equation can be solved in κ to give

$$\kappa = \frac{4R^2\sin^2\left(\frac{\pi}{N}\right)}{4\rho^2 - R^2\sin^4\left(\frac{\pi}{N}\right)}$$

and thus the projection of the bond onto $T_0\mathcal{M}$ is entirely determined by ρ and R through

$$\rho_\parallel = \sqrt{\frac{R}{\kappa}\sin^2\left(\frac{\pi}{N}\right)} = \sqrt{\frac{4\rho^2 - R^2\sin^4\left(\frac{\pi}{N}\right)}{4}}$$

[8]For vanishing curvature, $\pi/N \to 0$, hence $\sin^2(\pi/N) \to \pi^2/N^2$. In addition, for a $(n,0)$ zigzag nanotube, the tube radius R is related to the chiral index $n \equiv N$ through $2R = (\sqrt{3}/\pi)\rho N$ (see Box on page). Therefore

$$\cos(\Theta) \approx 1-\frac{2R^2}{\rho^2}\frac{\pi^2}{N^2} = 1-\frac{2R^2}{\rho^2}\pi^2\frac{3}{4\pi^2}\frac{\rho^2}{R^2} = -\frac{1}{2}$$

which correctly reduces to $\rho_{\|} \equiv \rho$ for $R \to \infty$ ($\pi/N \to 0$).

As done for the spherical surface, we may use Equation (**??**) to compute the σ hybridization index ($\tau_1 \equiv \tau_2$ for the two bonds with equal average curvature κ). Again, by Coulson's directionality theorem , $\cos(\Theta) = -1/\tau_1$, then by a straightforward calculation we get

$$\boxed{\tau_1 = \frac{\rho^2}{2R^2 \sin^2\left(\frac{\pi}{N}\right) - \rho^2}} \tag{11.19}$$

$$\boxed{w_1 = \frac{2R^2 \sin^2\left(\frac{\pi}{N}\right) - \rho^2}{2R^2 \sin^2\left(\frac{\pi}{N}\right)}} \tag{11.20}$$

where w_1 is the corresponding s-weight. As for the τ_3 hybridization index, corresponding to to the hybrids directed along the line of vanishing curvature, it can be determined from τ_1 and $\cos(\Theta')$. The latter follows again from Equation (11.8) with $k_2 \equiv k^{(2)} = 0$, *i.e.*

$$\cos(\Theta') = \frac{2}{\sqrt{2}\sqrt{\sqrt{1+\rho^2\kappa^2}+1}} \cos(\Delta\phi') = \sin(\theta)\cos(\Delta\phi')$$

Since $\Delta\phi' = \pi - (\Delta\phi/2)$ and $\cos(\Delta\phi') = -\cos(\Delta\phi/2)$, then

$$\boxed{\cos(\Theta') = -\sin(\theta)\cos\left(\frac{\Delta\phi}{2}\right)} \tag{11.21}$$

To remove the explicit dependence from the projected bond angle $\Delta\phi$, we can square the above expression and use $\sin(\Delta\phi/2) = (R/\rho\sin(\theta))\sin(\pi/N)$[9] to get

$$\cos^2(\Theta') = \frac{1}{\rho^2}\left(\rho_{\|}^2 - R^2\sin^2\left(\frac{\pi}{N}\right)\right) \tag{11.22}$$

With Equaton (11.22) at hand, the τ_3 hybridization index (and the w_3 s-weight) easily follows from $\tau_3 = 1/(\tau_1\cos^2(\Theta'))$, *i.e.*

$$\boxed{\tau_3 = \frac{2R^2\sin^2\left(\frac{\pi}{N}\right) - \rho^2}{\rho_{\|}^2 - R^2\sin^2\left(\frac{\pi}{N}\right)}} \tag{11.23}$$

$$\boxed{w_3 = \frac{\rho_{\|}^2 - R^2\sin^2\left(\frac{\pi}{N}\right)}{(\rho_{\|}^2 - \rho^2) + R^2\sin^2\left(\frac{\pi}{N}\right)}} \tag{11.24}$$

The calculation of the π hybridization index ($\tau_4 = \lambda$) is easily performed in the s-weight representation, from the conservation law $2w_1 + w_3 + w_4 = 1$. After som boring but straightforward algebra, we arrive at

$$w_4 = \frac{(\rho_{\|}^2 - \rho^2)(\rho^2 - 2R^2\sin^2\left(\frac{\pi}{N}\right))}{(\rho_{\|}^2 - \rho^2)R^2\sin^2\left(\frac{\pi}{N}\right) + R^4\sin^4\left(\frac{\pi}{N}\right)}$$

Upon noticing that

$$\rho_{\|}^2 - \rho^2 = -\frac{\kappa^2}{4}\rho_{\|}^4 = -\frac{R^2}{4}\sin^4\left(\frac{\pi}{N}\right)$$

[9] This follows from $l = 2\rho_{\|}\cos\left(\frac{\pi-\Delta\phi}{2}\right) = 2\rho_{\|}|\sin\left(\frac{\Delta\phi}{2}\right)|$ and $l = 2R|\sin(\pi/N)|$.

we find

$$\boxed{w_4 = \frac{2R^2 \sin^2\left(\frac{\pi}{N}\right) - \rho^2}{4R^2 - R^2 \sin^2\left(\frac{\pi}{N}\right)}} \tag{11.25}$$

$$\boxed{\lambda = \frac{4R^2 - 3R^2 \sin^2\left(\frac{\pi}{N}\right) + \rho^2}{2R^2 \sin^2\left(\frac{\pi}{N}\right) - \rho^2}} \tag{11.26}$$

which correctly reduce to $w_4 \to 0$ ($\lambda \to \infty$) when $R \to \infty$.

Equations (11.19), (11.23) and (11.25) express the σ and π hybridization indexes (or corresponding s-weights) in terms of the fundamental variables of the zig-zag nanotube, namely the tube radius R, the chiral index N and the bond length ρ. These expressions are rather cumbersome and may be difficult to handle. We may then seek for an approximation in the limit of small curvature $\kappa \approx 0$ (*i.e.* for a large diameter nanotubes). To this aim, let expand $sin^2(\pi/N)$ to second order around $\pi/N = 0$. For λ, we find

$$\begin{aligned}
\lambda &= 2\left(\frac{1 - \frac{3}{4}\sin^2\left(\frac{\pi}{N}\right) + \frac{1}{4}\frac{\rho^2}{R^2}}{\sin^2\left(\frac{\pi}{N}\right) - \frac{1}{2}\frac{\rho^2}{R^2}}\right) \\
&\approx 2\left(\frac{1 - \frac{9}{16}\frac{\rho^2}{R^2} + \frac{1}{4}\frac{\rho^2}{R^2}}{\frac{1}{4}\frac{\rho^2}{R^2}}\right) \\
&= 2\left(\frac{1 - \frac{5}{16}a^2}{\frac{1}{4}a^2}\right)
\end{aligned} \tag{11.27}$$

where $a = \rho/R$.

Beside the hybridization indexes, the effect of curvature on carbon hybridization can be assessed by the *pyramid angle*, introduced in Section 6.1. In case of zig-zag nanotubes, a convenient measure of the distortion is the angle that the π-like orbital makes with the σ-bond directed along the line of vanishing curvature, since by symmetry arguments it follows that the former has to be orthogonal to the plane formed by the other two σ-bonds with $\kappa \neq 0$. Such angle (γ) can be computed from $\cos(\gamma) = -1/\sqrt{\tau_3\tau_4}$ (see Section). A direct calculation gives

$$\boxed{\cos(\gamma) = -\frac{1}{2}\sqrt{\frac{4\rho^2 - R^2\sin^4\left(\frac{\pi}{N}\right) - 4R^2\sin^2\left(\frac{\pi}{N}\right)}{4R^2 - 3R^2\sin^2\left(\frac{\pi}{N}\right) + \rho^2}}} \tag{11.28}$$

At small curvature radii,

$$\begin{aligned}
\cos(\gamma) &\approx -\frac{1}{2}\sqrt{\frac{4\rho^2 - \frac{9}{16}\frac{\rho^2}{R^2} - 3\rho^2}{4R^2 - \frac{9}{4}\rho^2 + \rho^2}} \\
&= -\frac{1}{2}\sqrt{\frac{\rho^2}{4R^2}\left(\frac{1 - \frac{9}{16}a^2}{1 - \frac{5}{16}a^2}\right)} \\
&= -\frac{a}{4}\left(\frac{1 - \frac{9}{16}a^2}{1 - \frac{5}{16}a^2}\right)^{1/2}
\end{aligned} \tag{11.29}$$

In Figure 11.5, the hybridization indexes and the pyramid angles as computed from Equations (11.19), (11.23), (11.25), (11.28), (11.27) and (11.29) are plotted w.r.t. N and compared to the corresponding values obtained from the optimized geometries of $(N, 0)$ nanotubes (*i.e.* by a direct application of the Coulson's theorem). Overall, the derived

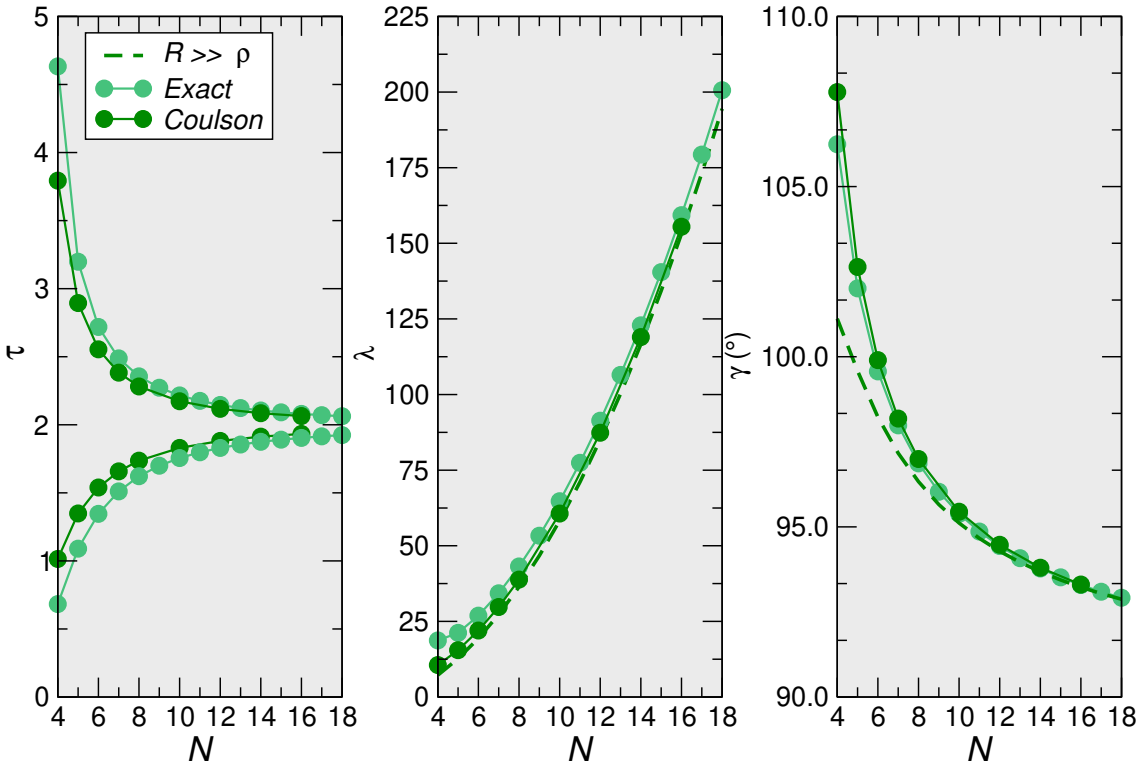

Figure 11.5. σ (τ), π (λ) hybridization indexes and pyramid angle (γ) obtained from Equations (11.19), (11.23), (11.25), (11.28) (dark green circles), their small-curvature approximations (dotted dark green line) and those obtained by application of Coulson's theorem to optimized structure of $(N, 0)$ nanotubes (light green circles).

Equations provide hybridization indexes that are in good agreement with those obtained from optimized structures. Noteworthy, our Equations precisely reproduce the behavior at large curvatures, which, for zig-zag nanotubes, appears to set in already at $N \simeq 10$.

Let consider now an armchair nanotube. The latter is a less lucky situation in which analytical expressions in terms of the only variable $a = \rho/R$ cannot be established. The reason is that all the three σ bonds are "affected" by curvature: two bonds are directed along two lines of equal average curvature κ and the third points towards the direction normal to the tube axis, *i.e.* with $\kappa = -1/R$. A formula, however approximated, that relates the bond angle Θ to the variables R, ρ and N can be written down by applying the following geometrical arguments. If we cut the again the nanotube along the direction normal to the tube axis, an irregular polygons of "short" and "long" sides, respectively equal to ρ and H, where H is the "height" of the hexagon, is formed. The number of ρ and H sides is equal and matches the nanotube chiral index N, hence for the corresponding central angles we can write $2\alpha N + 2\beta N = 2\pi$. In addition, $\sin(2\alpha) = H/(2R)$ and $\sin(2\beta) = \rho/(2R)$, therefore $\sin(\alpha) = \sin(\pi/N - \beta)$ and

$$\begin{aligned}\sin\left(\frac{\pi}{N} - \beta\right) &= \sin\left(\frac{\pi}{N}\right)\cos(\beta) - \cos\left(\frac{\pi}{N}\right)\sin(\beta) \\ &= \sqrt{1 - \frac{\rho^2}{4R^2}}\sin\left(\frac{\pi}{N}\right) - \frac{\rho}{2R}\cos\left(\frac{\pi}{N}\right)\end{aligned}$$

and

$$H = 2R\sqrt{1 - \frac{\rho^2}{4R^2}}\sin\left(\frac{\pi}{N}\right) - \rho\cos\left(\frac{\pi}{N}\right)$$

For the bond angle, $\cos(\Theta) = 1 - l^2/(2\rho^2)$, with l the "width" of the hexagon. Here, we

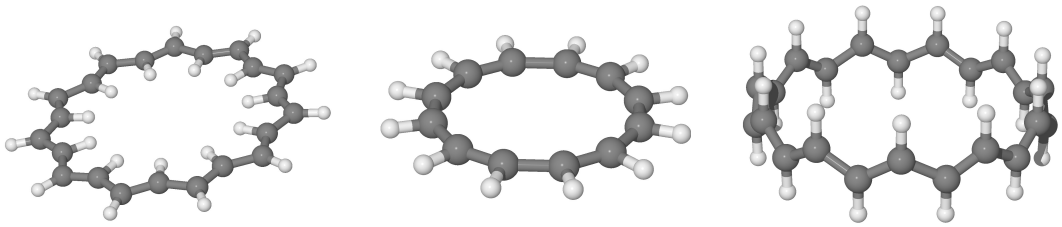

Figure 11.6. The anti-, cis- and trans-annulene structures

.

may set[10] $l^2 \approx H^2 - \rho^2$, thus getting

$$\cos(\Theta) \approx \frac{3}{2} - \frac{2R^2}{\rho^2}\sin^2\left(\frac{\pi}{N}\right) + \\ - \frac{1}{2}\cos\left(\frac{2\pi}{N}\right) + \frac{2R}{\rho}\sin\left(\frac{\pi}{N}\right)\cos\left(\frac{\pi}{N}\right)\sqrt{1-\frac{\rho^2}{4R^2}} \tag{11.30}$$

which correctly reduces to $\cos(\Theta) = -1/2$ in the limit of vanishing curvature.

11.2.3 1-dimensional systems: [n]-annulenes

Published papers: M. Cappelletti, M. Leccese, M. Cococcioni, D. M. Proserpio and R. Martinazzo, *The Different Story of π-bonds*, Molecules, 26, 3805, 2021.

As a last example, we consider [n]-annulenes, ring-closed carbon chains (with n atoms) that are the prototypical example of molecules to which Hückel theory applies. Because of their reduced dimensionality, [n]-annulenes represent a particularly attractive system and lend theirselves to both computational and analytical investigations even at large n. Therefore, before getting into the issue of curvature, it is worth introducing the main structural properties of such molecules and discussing some DFT calculations we performed.

[n]-annulenes can appear in three different structural variants (depicted in Figure 11.6), that generally referred to as *cis*, *anti* and *trans*. These three variants present different delocalized bonds between carbon p electrons and allow one to probe the role of the σ skeleton separately from that of the delocalized bond. This is a fundamental issue that lies at the heart of the theory of aromaticity and the nature of π-bonds. For a long time, chemists have deemed that aromaticity, which is generally related to uniform bond lengths (the infamous D_{6h} symmetry in benzene), was uniquely ascribed to an extended delocalization of π electrons. The latter represents, however, only part of the story, since π-bonds actually turn out to be *distortive* and favor non-uniform geometries. By reassessing the role of the σ skeleton, several works in the field have later shown that the onset of uniform bond lengths is due a rather delicate interplay between the σ and π bonds[270]. In this respect, one-dimensional systems such as [n]-annulenes are particularly attractive. Indeed, the planar structures, cis and anti, feature an exact σ-π separation and p-p interactions that are not affected by the ring size. It is their different σ skeleton to determine their relative stability, with cis structures preferred for small n and anti for large n. On the other hand, trans-annulenes feature an ideal "environment" for σ-bonding, only marginally affected by

[10] The equality sign strictly holds for an hexagon on a plane, where ρ, H and l forms a right triangle. In general, one should set $H^2 = l^2 + \rho^2 - 2l\rho\cos(\varphi)$ where φ is the angle between l and ρ. The employed formula can be then considered as an approximation to large radii. Larger deviation from the attended bond angles and hybridization indexes will occur at small N (for $N = 10$, $\varphi \approx 89.2$).

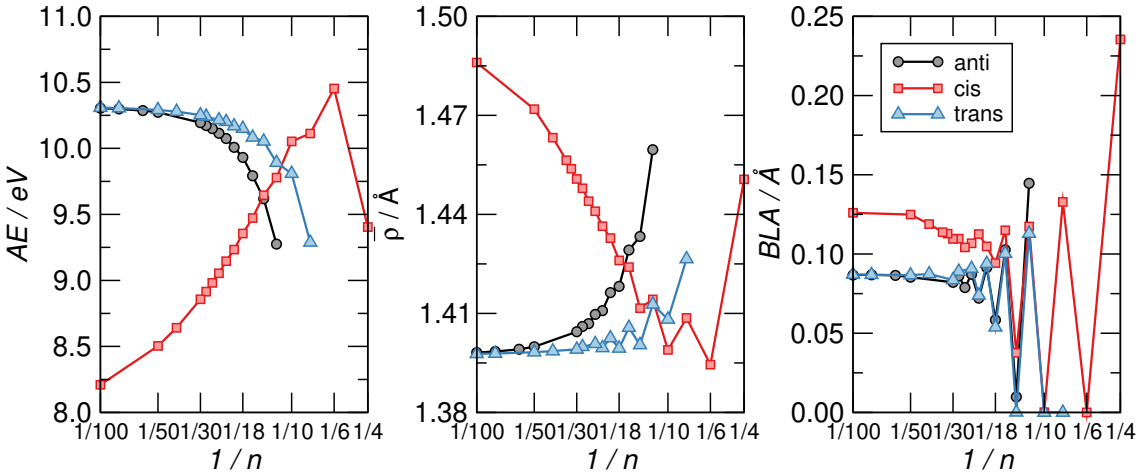

Figure 11.7. From left to right: The atomization energy per C atom (AE), the average CC bond length ($\bar{\rho}$) and the bond length alternation (BLA) for the C_nH_n structures exemplified in Figure 5, as functions of $1/n$, on a linear-log scale

the ring size, and a (cis-bent) interaction between p orbitals for π bonding that becomes increasingly important when increasing n[153].

We should note that the three structures have two different limits for $n \to \infty$: the first is the rather unphysical geometry attains by the cis-sequence, the second is the stable configuration of *trans-polyacetilene*, here reached from two different "directions". This infinite-size limit allows one accessing properties of the extended system, trans-polyacetilene, from a molecular perspective - free of finite-size effects thanks to the ring topology - and applying levels of theory that are much higher than those typically available in the condensed phase.

Figure 11.7 shows the results of DFT calculations we performed with the M06-2X functional, which, as seen in Chapter 3, is particularly suitable for this kind of systems. The left panel displays the atomization energy per C atom, *i.e.* the energy of the reaction $\frac{1}{n}C_nH_n \to C + H$, as a function of $1/n$ in a linear-log scale. The graph makes clear the stability order before-mentioned and the infinite-size limiting behavior alluded to, where the anti and trans sequence tend to the same common value AE ≈ 10.3 eV which is our computed AE for trans-polyacetilene. The latter is about 2 eV higher than the hypothetical chain with CH bonds made with pure C p orbitals, and CC σ bonds built with sp hydrids. In a sense, it is a carbyne-like system where for any structural unit C_2 a π bond is replaced with two (odd) CH bonds[153].

The middle panel of Figure 11.7 highlights the structural differences between the isomers in terms of the average CC bond length. Again, it shows that the stable structures share a common average CC bond lengths ($\bar{\rho}$), disregarding the evident alternation due to aromaticity-antiaromaticity for small n. The latter is more evident in the right panel of the same figure, where the *BLA* is seen to undergo wild oscillatory behavior which extends up to $n \approx 30$. The behavior of BLA highlights how the distortivity is highly modulated by aromatic-antiaromatic character of the π-cloud, with anti-aromatic molecules being highly distortive[11]. The BLA vanishes, or is vanishingly small, up to $n = 10$ for the cis-sequence and up to $n = 14$ for the other two sequences. The latter is clear-cut manifestation of the delicate interplay between the π distortivity and the σ resistivity[12].

Let return now on the study of curvature, and consider at first the simplest case of a cis structure. Here, all C atoms lie on a curve $\gamma(t)$, that is a one-dimensional circle S_1, whose

[11] An exception is for $n = 8$ where the poor overlap between p orbital gives to the π cloud a little weight on the overall energetics.

[12] The case $n = 4$ is a bit off the general trend, featuring much larger BLA and $\bar{R}$. This is probably a consequence of the ring strain, which is considered to be the major effect causing distortion in this system.

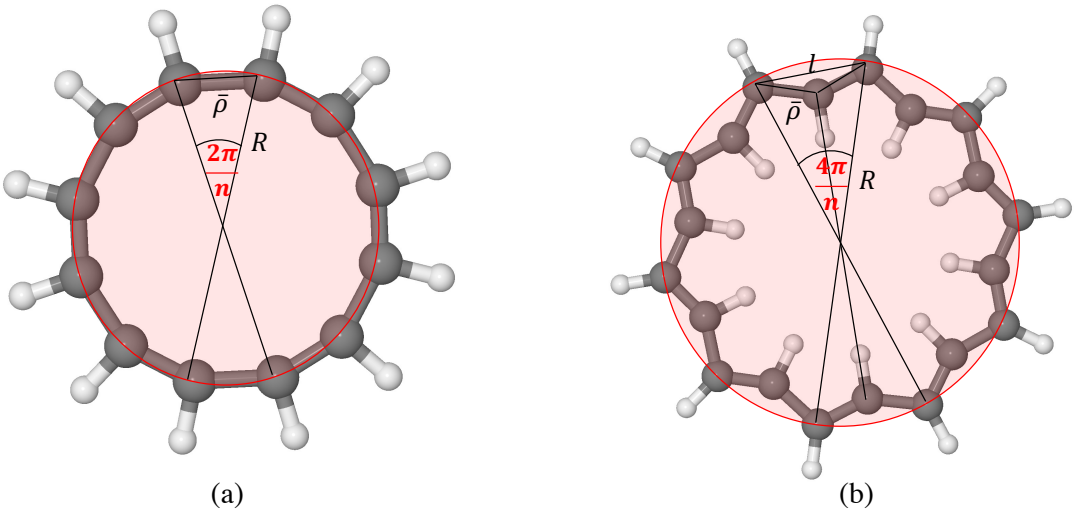

Figure 11.8. Schematics illustrating the main geometrical parameters of cis (a) and anti (b) $[n]$-annulenes.

curvature in each point is given by $\kappa = -1/R$. Therefore, the relationship between local curvature and hybridization we established above for two-dimensional systems translates in one dimension without noteworthy modifications, if one identify $\boldsymbol{e}_1$ with the curve tangent vector $\boldsymbol{T}(t) = \dot{\gamma}(t)$ and $\boldsymbol{N}$ as the *principal normal* $\dot{\boldsymbol{T}}(t)/||\dot{\boldsymbol{T}}(t)$. From simple geometrical arguments (see Figure 11.8 (a)), we have

$$R = \frac{\rho}{2\sin\left(\frac{\pi}{n}\right)}$$

and then the curvature is given by $\kappa = -2\sin(\pi/n)/\rho$. For the projected bond angle, $\cos(\Delta\phi) = \pi$, then, assuming equal bond lengths, from Equation 11.8, we get

$$\cos(\Theta) = \frac{-2}{\sqrt{1+\rho^2\kappa^2}+1} + \frac{\sqrt{1+\rho^2\kappa^2}-1}{\sqrt{1+\rho^2\kappa^2}+1} = \frac{\sqrt{1+\rho^2\kappa^2}-3}{\sqrt{1+\rho^2\kappa^2}+1}$$

or

$$\boxed{\cos(\Theta) = \frac{\sqrt{1+4\sin^2\left(\frac{\pi}{n}\right)}-3}{\sqrt{1+4\sin^2\left(\frac{\pi}{n}\right)}+1}} \tag{11.31}$$

From Equation 11.31, the τ_{CC} hybridization index $(-1/\cos(\Theta))$ and the corresponding s-weight can be readily obtained

$$\boxed{\tau_{\mathrm{CC}} = \frac{1+\sqrt{1+4\sin^2\left(\frac{\pi}{n}\right)}}{3-\sqrt{1+4\sin^2\left(\frac{\pi}{n}\right)}}} \tag{11.32}$$

$$\boxed{w_{\mathrm{CC}} = \frac{1}{4}\left(3-\sqrt{1+4\sin^2\left(\frac{\pi}{n}\right)}\right)} \tag{11.33}$$

which correctly reduce to $\tau_{\mathrm{CC}} \to 1$ ($w_{\mathrm{CC}} \to 1/2$, for $n \to \infty$, *i.e.* the hybrid involved in the CC σ-bond tends to a pure sp hybrid orbital. Factoring out the fourth hybrid which is a pure p, the knowledge of w_{CC} is sufficient to get w_{CH} from the s-weight conservation,

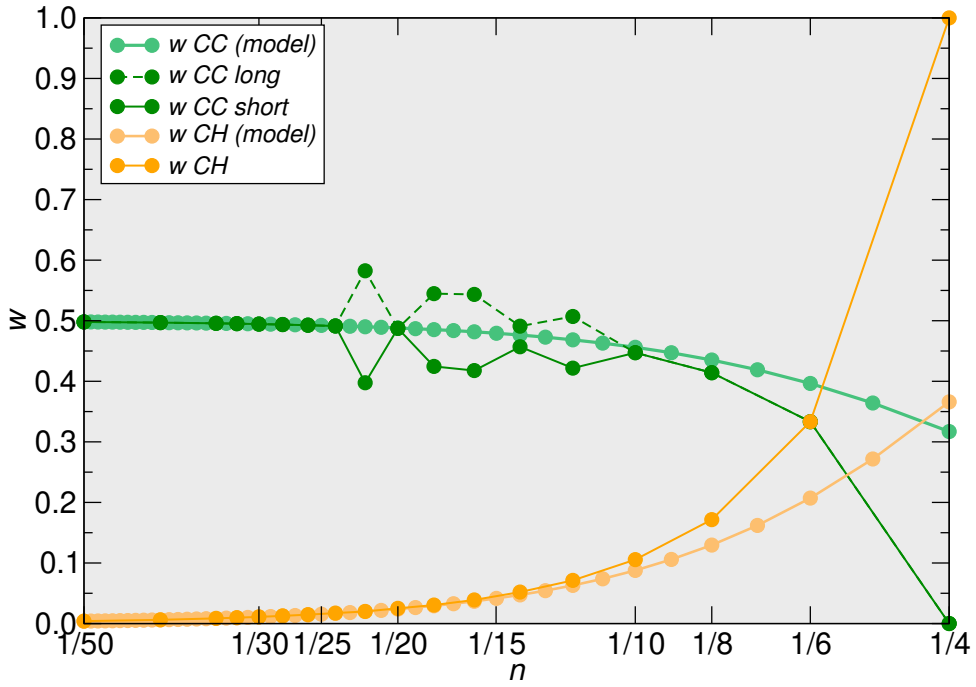

Figure 11.9. s weights (w) for the hybrid orbital employed by each C in the CC and CH σ bonds. Light and Dark colors refer to values obtained by our model and as extrapolated by geometrical structural optimization, respectively.

i.e. $w_{\mathrm{CH}} = 1 - 2w_{\mathrm{CC}}$. Then

$$\tau_{\mathrm{CH}} = \frac{3 - \sqrt{1 + 4\sin^2\left(\frac{\pi}{n}\right)}}{-1 + \sqrt{1 + 4\sin^2\left(\frac{\pi}{n}\right)}} \tag{11.34}$$

$$w_{\mathrm{CH}} = \frac{1}{2}\left(\sqrt{1 + 4\sin^2\left(\frac{\pi}{n}\right)} - 1\right) \tag{11.35}$$

For $n \to \infty$, $\tau_{\mathrm{CH}} \to \infty$ ($w_{\mathrm{CH}} \to 0$), *i.e.* the C atom employs a pure p orbital to bind the H atom. Figure 11.9 compares the s-weight computed according to Equations 11.33 and 11.35 to the hybridiziation obtained by the application of the Coulson's theorem to the cis geometries optimized with DFT. We note that for some n (*e.g.* $n = 12, 16, 18$), the C atom employs two different hybrids for the σ-bonds with its C nns. This feature is not due to the BLA, which characterizes every cis structure for $n \leq 12$, rather it is due to the CH bond and in particular whether the $\hat{\mathrm{HCC}}_1$ and $\hat{\mathrm{HCC}}_2$ angles are equal or not. Our analysis cannot take into account such situations since we have set CC σ-bonds to be equal at the outset. Nevertheless, the infinite-size limit is well reproduced, since in this limit the before-mentioned angles approach the same value of $\pi/2$.

BLA can be introduced in this model "by hand", upon considering that

$$\frac{n}{2}(2\alpha) + \frac{n}{2}(2\beta) = 2\pi$$

where 2α and 2β are the central angles in S_1 subtented respectively by the chords ρ_+ and ρ_- (the long and short bonds). Since $\alpha = (2\pi/n) - \beta$, we have

$$\sin(\alpha) = \sin\left(\frac{2\pi}{n}\right)\cos(\beta) - \sin(\beta)\cos\left(\frac{2\pi}{n}\right) \tag{11.36}$$

and

$$\rho_+ = \sin\left(\frac{2\pi}{n}\right)\sqrt{1+\frac{\rho_-^2}{4R^2}} - \rho_- \cos\left(\frac{2\pi}{n}\right) \tag{11.37}$$

Equations 11.36 and 11.37 allow relating ρ_+ and ρ_- with the curvature radius R, hence the curvature κ. With some algebra, one arrives at

$$\boxed{R = \frac{1}{2}\sqrt{\left(\frac{\rho_+ + \rho_- \cos\left(\frac{2\pi}{n}\right)}{\sin\left(\frac{2\pi}{n}\right)}\right)^2 + \rho_-^2}} \tag{11.38}$$

Reminding that $\kappa = -1/R$, $\cos(\Theta)$ can then be computed according to

$$\begin{aligned}\cos(\Theta) =& \frac{-2}{\sqrt{\left(\sqrt{1+\rho_+^2\kappa^2}+1\right)\left(\sqrt{1+\rho_-^2\kappa^2}+1\right)}} + \\ &+ \left(\frac{\sqrt{1+\rho_+^2\kappa^2}-1}{\sqrt{1+\rho_+^2\kappa^2}+1}\frac{\sqrt{1+\rho_-^2\kappa^2}-1}{\sqrt{1+\rho_-^2\kappa^2}+1}\right)^{1/2}\end{aligned}$$

Let consider now the case of trans-annulenes. In the following, we assume to have a closed bent-like chain of n carbon atoms with average bond lengths $\bar{\rho}$, thus disregarding any BLA. The curvature properties of trans structures are equivalent to that of a zig-zag nanotube (indeed they are to all effect the zig-zag lines of zig-zag nanotube) and allow then applying the equations derived in Subsection 11.2.2 with just a minor modification of the central angle. Indeed, here n represents the number of atoms along the chain (*i.e.* $n = 2N$) and then the relation between the central angle and the radius R reads as $\sin(2\pi/n) = l/2R$, with l the distance between a C atom and its nnn (the previous "width" of the hexagon in the nanotube geometry). Therefore, for the s weights we have

$$\boxed{w_{\mathrm{CC}} = \frac{2R^2\sin^2\left(\frac{\pi}{n}\right) - \bar{\rho}^2}{2R^2\sin^2\left(\frac{\pi}{n}\right)}} \tag{11.39}$$

$$\boxed{w_{\mathrm{CH}} = \frac{\bar{\rho}_\parallel^2 - R^2\sin^2\left(\frac{\pi}{n}\right)}{(\bar{\rho}_\parallel^2 - \bar{\rho}^2) + R^2\sin^2\left(\frac{\pi}{n}\right)}} \tag{11.40}$$

$$\boxed{w_\pi = \frac{2R^2\sin^2\left(\frac{\pi}{n}\right) - \bar{\rho}^2}{4R^2 - R^2\sin^2\left(\frac{\pi}{n}\right)}} \tag{11.41}$$

where $\bar{\rho}_\parallel^2$ can be determined from

$$\bar{\rho}_\parallel = \sqrt{\frac{4\bar{\rho} - R^2\sin^4\left(\frac{2\pi}{n}\right)}{4}}$$

Note that, as for zig-zag nanotubes, the curvature radius is related to n through $2\pi R \approx l(n/2) \approx \sqrt{3}\bar{\rho}(n/2)$ as $n \to \infty$.

The anti-structures displays a less trivial geometry where carbons lie on two distinct (but concentric) circumferences (see Figure 11.8 (b)) and have thus different hybridization. Since we are more interested in the $n \to \infty$ limit, where the anti sequence tends to trans-polyacetilene, we can directly look for an approximated expression of $\cos(\Theta)$ at small curvatures. To this aim, let consider that each C makes equal bond angles with its nn and

that $\bar{\rho}$ is the average bond length. Then, from simple geometrical arguments it follows

$$\cos(\Theta) = 1 - \frac{l^2}{2\bar{\rho}^2}$$

where l is the distance between nnn on the largest circumference of radius R, and it is related to n through

$$l^2 = \frac{2}{\kappa^2}\left(1 - \cos\left(\frac{4\pi}{n}\right)\right)$$

Hence, for $\cos(\Theta)$ we have

$$\cos(\Theta) = 1 - \frac{1}{\kappa^2\bar{\rho}^2}\left(1 - \cos\left(\frac{4\pi}{n}\right)\right) \tag{11.42}$$

As $n \to \infty$, the length of the largest circumference can be approximated by $n/2$ times the distance between nnn in trans-polyacetilene, l_{tP}, *i.e.* $2\pi\kappa^{-1} \approx (n/2)l_{\mathrm{tP}}$ and $\bar{\rho} \to \rho_{\mathrm{tP}}$. Let then expand the cosine around $1/n = 0$

$$\begin{aligned}\cos\left(\frac{4\pi}{n}\right) &= 1 - \frac{1}{2}\left(\frac{4\pi}{n}\right)^2 + \frac{1}{4!}\left(\frac{4\pi}{n}\right)^4 + o((1/n)^5) \\ &= 1 - \frac{8\pi^2}{n^2} + \frac{32\pi^4}{3n^2} + o((1/n)^5)\end{aligned} \tag{11.43}$$

Substituting Equation 11.43 into Equation 11.42 and replacing $n \approx 4\pi/(\kappa l_{\mathrm{tP}})$, we get

$$\begin{aligned}\cos(\Theta) &\approx 1 - \frac{1}{\kappa^2\rho_{\mathrm{tP}}^2}\left(1 - 1 + \frac{1}{2}l_{\mathrm{tP}}^2\kappa^2 - \frac{1}{24}l_{\mathrm{tP}}^4 + o(\kappa^5)\right) \\ &= 1 - \frac{l_{\mathrm{tP}}^2}{2\rho_{\mathrm{tP}}^2} + \frac{1}{24}\frac{l_{\mathrm{tP}}^4\kappa^2}{\rho_{\mathrm{tP}}^2} + o(\kappa^3) \\ &= \cos(\theta_{\mathrm{tP}}) + \frac{1}{24}\frac{l_{\mathrm{tP}}^4\kappa^2}{\rho_{\mathrm{tP}}^2} + o(\kappa^3)\end{aligned} \tag{11.44}$$

where θ_{tP} is the bond angle in trans-polyacetilene ($\approx 124.0°$). For the μ hybridization index we get

$$\boxed{\mu = -\frac{1}{\cos(\theta_{\mathrm{tP}}) + \frac{1}{24}\frac{l_{\mathrm{tP}}^4\kappa^2}{\rho_{\mathrm{tP}}^2}} = \mu_{\mathrm{tP}}\left(\frac{24\rho_{\mathrm{tP}}^2\cos(\theta_{\mathrm{tP}})}{24\rho_{\mathrm{tP}}^2\cos(\theta_{\mathrm{tP}}) + l_{\mathrm{tP}}^4\kappa^2}\right)} \tag{11.45}$$

which correctly reduces to $\mu \equiv \mu_{\mathrm{tP}}$, for $\kappa \to 0$.

11.3 σ-π Hubbard model and curvature

In this last Section, we see how the above derived equations relating the local curvature with the hybridization of C atoms can be exploited in a (2-state or 2-site) σ-π *Hubbard* bond model. The latter has been described in detail elsewhere[129], so here we limit to briefly outline its main features.

The starting point is the general Hubbard Hamiltonian H that in (second-quantization formalism) reads as

$$H = \sum_{i,\sigma}\varepsilon_i a_{i,\sigma}^{\dagger}a_{i,\sigma} - t\sum_{\sigma}a_{b,\sigma}^{\dagger}a_{a,\sigma} - t\sum_{\sigma}a_{a,\sigma}^{\dagger}a_{b,\sigma} + \sum_i U_i n_{i,\uparrow}n_{i,\downarrow}$$

where σ runs over the spins ($\sigma = (\uparrow, \downarrow)$), i runs over the two lattice sites ($i = (a, b)$), $a_{i,\sigma}(a^\dagger_{i,\sigma})$ destroys (creates) an electron in state (orbital) i with spin σ, ε_i are on-site energies, t is the hopping energy while U_i the on-site Coulomb repulsion. The problem can be readily re-formulated in first quantization formalism, where the Hamiltonian for two electrons reads as

$$H = h_1 + h_2 + V$$

with h_i the monoelectronic operator for the electron i and V the Coulomb repulsion. For orthogonal states, the equivalence between the two Hamiltonians is obtained upon setting

$$\begin{gathered}\langle a|h|a\rangle \approx \varepsilon_a \qquad \langle b|h|b\rangle \approx \varepsilon_b \\ \langle a|h|b\rangle = \langle b|h|a\rangle = -t \\ \langle aa|V|aa\rangle = U_a \qquad \langle bb|V|bb\rangle = U_b\end{gathered}$$

and neglecting the remaining e-e matrix elements. The ground-state energy and wavefunction can be obtained[13] as

$$\varepsilon = -2t\xi\Phi = \Phi_0 + \xi\Phi_g$$

where we have set $\varepsilon_a = \varepsilon_b = 0$ and $U_a = U_b = U$ and defined the *transmission factor*

$$\xi = \sqrt{1 + \frac{U^2}{16t^2}} - \frac{U}{4t}$$

When $U \ll t$, $\xi \to 1$ and $\varepsilon \approx -2t$, $\Phi \approx (1/\sqrt{2})(\phi_a(\boldsymbol{r}_1) + \phi_b(\boldsymbol{r}_1))(\phi_a(\boldsymbol{r}_2) + \phi_b(\boldsymbol{r}_2))$. This is the molecular orbital limit where the two electrons are paired in a molecular orbital and the bond energy attains its maximum value $2t$ (the factor of two is the number of electrons). On the other hand, when $U \gg t$, $\xi \to 0$ and the wavefunction takes a purely covalent form $\Phi \approx \Phi_0$ with a vanishing small binding energy $\sim 4t^2/U$.This is the Heitler-London (a.k.a. Heisenberg) limit, where the electrons reside on their nuclei in an entangled state.

The case of non-orthogonal states can be handled similarly, by setting $S = \langle a|b\rangle = \langle b|a\rangle$. One finds that the ground-state energy in this case reads as

$$\begin{aligned}\varepsilon =& \frac{4\bar{t}(1-S^2)S + U(1+S^2)}{2(1-S^2)^2} + \\ &- \sqrt{\left(\frac{4\bar{t}(1-S^2)S + U(1+S^2)}{2(1-S^2)^2}\right)^2 + \frac{4\bar{t}^2 + 2\bar{t}S(U - 2\bar{t}S)}{(1-S^2)^2}}\end{aligned}$$

where[14] $\bar{t} = t + \varepsilon_a S$.

One can apply the above model separately to σ and π-like bonds. For the sake of simplicity, we assume that C atoms make a non-bent σ-bond using sp^μ hybrids and π-like bond with sp^λ hybrids, leaving two further hybrids sp^τ for the remaining σ bonds with

[13]The calculation is easily performed in the $\langle\Phi_0|, \langle\Phi_g|$ basis, where $\langle\Phi_0|$ is the 2-electron wavefunction in the covalent configuration while $\langle\Phi_g|$ is the combination of ionic configurations

$$\begin{gathered}\Phi_0 = \frac{1}{\sqrt{2}}(\phi_a(\boldsymbol{r}_1)\phi_b(\boldsymbol{r}_2) + \phi_b(\boldsymbol{r}_2)\phi_a(\boldsymbol{r}_1)) \\ \Phi_g = \frac{1}{\sqrt{2}}(\Phi_a + \Phi_b)\end{gathered}$$

where $\Phi_a = \phi_a(\boldsymbol{r}_1)\phi_b(\boldsymbol{r}_2)$ and $\Phi_b = \phi_b(\boldsymbol{r}_1)\phi_b(\boldsymbol{r}_2)$.

[14]Note that, in the non-orthogonal case, the hopping energies depend on the reference energy of the one-electron Hamiltonian h, that is usually set to be the asymptotic limit of the one-electron potential. Therefore, one set $\bar{h} = h - \varepsilon_0$ and replace $\varepsilon_a \to \bar{\varepsilon}_a = \varepsilon_a - \varepsilon_0$ (same for b) and $t \to \bar{t} = -\langle a|h - \varepsilon_0|b\rangle = t + \varepsilon_0 S$.

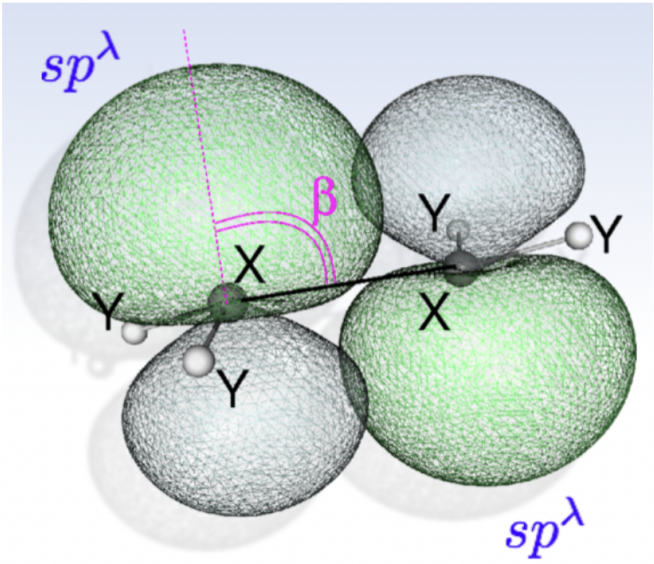

Figure 11.10. Schematics of the C_{2h} configuration taken from Ref. [129] considered for describing binding in a $Y_2X{=}XY_2$ molecule, illustrating the sp^λ used for the π bond, together with the angle β that they make with the XX axis. The central atoms X use further sp^τ and sp^μ hybrids for the XY and XX σ bonds.

two of the three nn (here, considered to be equal, like in a C_{2h} configuration, see Figure 11.10).

In the following we address the case of $U = 0$ and focus on the double bond. The sp^μ and sp^λ hybrids determine the effective overlap matrix elements and the hopping parameters, namely $S_\sigma^{\rm eff}, t_\sigma^{\rm eff}$ for the σ-bond and $S_\pi^{\rm eff}, t_\pi^{\rm eff}$ for the π-bond[15]. The two sp^μ (normalized) orbitals involved in the bond reads as

$$|\phi_a\rangle = \frac{1}{\sqrt{1+\mu}}(|s\rangle + \sqrt{\mu}|p\rangle) \tag{11.46}$$

$$|\phi_{a'}\rangle = \frac{1}{\sqrt{1+\mu}}(|s'\rangle + \sqrt{\mu}|p'\rangle) \tag{11.47}$$

Then by expanding the matrix elements $S_\sigma = \langle\phi_a|\phi_{a'}\rangle$ and $t_\sigma = -\langle\phi_a|h|\phi_b\rangle$ in terms of the atomic orbital contributions we get

$$\boxed{S_\sigma^{\rm eff} = \frac{1}{1+\mu}\{S_\sigma(ss) - 2\sqrt{\mu}S_\sigma(sp) - \mu S_\sigma(pp)\}} \tag{11.48}$$

$$\boxed{t_\sigma^{\rm eff} = \frac{1}{1+\mu}\{t_\sigma(ss) - 2\sqrt{\mu}t_\sigma(sp) - \mu t_\sigma(pp)\}} \tag{11.49}$$

with the following common definitions for AO matrix elements

$$\begin{aligned} S_\sigma(ss) &= \langle s|s'\rangle & t_\sigma(ss) &= -\langle s|h|s'\rangle \\ S_\sigma(sp) &= \langle s|p_x'\rangle & t_\sigma(sp) &= -\langle|s|h|p_x'\rangle \\ S_\sigma(pp) &= \langle p_x|p_x'\rangle & t_\sigma(pp) &= -\langle p_x|h|p_x'\rangle \end{aligned}$$

where x denotes the axis along the double-bond. According to the AO orientation, we have

[15] They also determine the on-site energies but these are irrelevant in the present model since in a total energy comparison they just give constant energy term that is geometry independent.

$t_\sigma(ss), S_\sigma(ss) \geq 0$, while $t_\sigma(sp)$, $S_\sigma(sp)$, $t_\sigma(pp)$, $S_\sigma(pp) \leq 0$.

For the π-bonds, the sp^λ hybrids use $|p\rangle$ and $|p'\rangle$ orbitals that make an angle of β with the x-axis (see Figure). Then, if z is the axis orthogonal to the bond axis, we have

$$\begin{aligned} |p\rangle &= \cos(\beta)|p_x\rangle + \sin(\beta)|p_z\rangle \\ |p'\rangle &= -\cos(\beta)|p'_x\rangle - \sin(\beta)|p'_z\rangle \end{aligned}$$

and thus

$$\boxed{\begin{aligned} S_\pi^{\text{eff}} &= \frac{1}{1+\lambda}\Bigg\{ S_\sigma(ss) - 2\sqrt{\lambda}\cos(\beta)S_\sigma(sp) + \\ &\qquad - \lambda\left(\cos^2(\beta)S_\sigma(pp) + \sin^2(\beta)S_\pi(pp)\right)\Bigg\} \end{aligned}} \tag{11.50}$$

$$\boxed{\begin{aligned} t_\pi^{\text{eff}} &= \frac{1}{1+\lambda}\Bigg\{ t_\sigma(ss) - 2\sqrt{\lambda}\cos(\beta)t_\sigma(sp) + \\ &\qquad - \lambda\left(\cos^2(\beta)t_\sigma(pp) + \sin^2(\beta)t_\pi(pp)\right)\Bigg\} \end{aligned}} \tag{11.51}$$

where, according to the AO orientations, $S_\sigma(ss)$, $S_\pi(pp)$, $t_\sigma(ss)$, $t_\sigma(pp) \geq 0$, and $S_\sigma(sp)$, $S_\sigma(pp)$, $t_\sigma(sp)$, $t_\sigma(pp) \leq 0$. Notice that, as $\beta \to \pi/2$ (limit of planar configuration), we have $\lambda \to \infty$, $S_\pi \to -S_\pi(pp)$ and $t_\pi \to -t_\pi(pp)$, consistently with the direction of p orbitals.

We turn now the attention to the relationship between the curvature and the above-defined parameters. Let focus on the σ-bond and consider the hybridization index μ as curvature-dependent, *i.e.* $\mu \equiv \mu(\kappa)$ where κ is the average curvature as introduced in Section 11.1. Since we are interested in the limit of small curvature, we can Taylor-expand the S_σ and t_σ around $\kappa = 0$, *i.e.* for t_σ

$$t_\sigma(\kappa) \approx t_\sigma(0) + \left.\frac{\partial t_\sigma}{\partial \kappa}\right|_{\kappa=0}\kappa + \frac{1}{2!}\left.\frac{\partial^2 t_\sigma^{\text{eff}}}{\partial \kappa^2}\right|_{\kappa=0}\kappa^2 + o(\kappa^3) \tag{11.52}$$

Let compute the first and second derivative of the effective hopping parameter w.r.t. κ from Equation (11.49). We have

$$\begin{aligned} \frac{\partial t_\sigma^{\text{eff}}}{\partial \kappa} &= -\frac{1}{(1+\mu)^2}\frac{\partial \mu}{\partial \kappa}\{t_\sigma(ss) - 2\sqrt{\mu}t_\sigma(sp) - \mu t_\sigma(pp)\} + \\ &\quad + \frac{1}{1+\mu}\left\{ -\frac{1}{\sqrt{\mu}}\frac{\partial \mu}{\partial \kappa}t_\sigma(sp) - \frac{\partial \mu}{\partial \kappa}t_\sigma(pp)\right\} \\ &= \frac{1}{1+\mu}\frac{\partial \mu}{\partial \kappa}\left\{ -t_\sigma^{\text{eff}} - \frac{1}{\sqrt{\mu}}t_\sigma(sp) - t_\sigma(pp)\right\} \end{aligned} \tag{11.53}$$

Let define the term in brackets in Equation (11.53) as $T(\mu) := -t_\sigma^{\text{eff}} - (1/\sqrt{\mu})t_\sigma(sp) - t_\sigma(pp)$. In terms of $t_\sigma(ss)$, $t_\sigma(sp)$, $t_\sigma(pp)$, the latter reads as

$$T(\mu) = \frac{1}{1+\mu}\left\{ -t_\sigma(ss) + \frac{\mu-1}{\sqrt{\mu}}t_\sigma(sp) - t_\sigma(pp)\right\}$$

For the second derivative, a straightforward calculation gives

$$\frac{\partial^2 t^{\text{eff}}}{\partial \kappa^2} = \frac{1}{1+\mu} T(\mu) \left\{ \frac{\partial^2 \mu}{\partial \kappa^2} - \frac{2}{(1+\mu)^2} \frac{\partial \mu}{\partial \kappa} \right\} + \frac{\sqrt{\mu}}{2(1+\mu)\mu^2} \frac{\partial \mu}{\partial \kappa} t_\sigma(sp) \tag{11.54}$$

Notice that, in our model, the hybridization index depends quadratically on κ, therefore the first derivative of μ w.r.t. κ vanishes at $\kappa = 0$. Hence, from Equation (11.52), (11.53) and (11.54) we find

$$t_\sigma^{\text{eff}} \approx t_\sigma^{\text{eff}}(0) + \frac{1}{2} \left\{ \frac{1}{2} T(\mu) \frac{\partial^2 \mu}{\partial \kappa^2} \right\} \kappa^2 + o(\kappa^3) \tag{11.55}$$

As a simple application, let consider the case of *syn*-[n]-annulenes, for which in Subsection 11.2.3 we derived explicit expression for the hybridization indexes as functions of κ. Here, we assume that each C atom makes σ-bonds with its nn involving sp^μ hybrids. Therefore

$$\mu = \frac{1 + \sqrt{1 + 4\sin^2(\pi/n)}}{3 - \sqrt{1 + 4\sin^2(\pi/n)}}$$
$$w_\mu = \frac{1}{4} \left(3 - \sqrt{1 + 4\sin^2(\pi/n)} \right)$$

For $n \to \infty$, we remind that $2\pi\kappa^{-1} \approx n\bar{\rho}$, where $\bar{\rho}$ is the average CC bond length, hence we can write

$$\frac{\partial}{\partial \kappa} = \frac{\bar{\rho}}{2\pi} \frac{\partial}{\partial x}$$
$$\frac{\partial^2}{\partial \kappa^2} = \frac{\bar{\rho}^2}{4\pi^2} \frac{\partial^2}{\partial x^2}$$

with $x \equiv 1/n$. Moreover, we can take advantage of the much more simple expression for the s-weight w_μ and use

$$\frac{\partial \mu}{\partial x} \equiv \frac{\partial}{\partial x} \left(\frac{1}{w} - 1 \right) = -\frac{1}{w^2} \frac{\partial w}{\partial x}$$

Hence

$$\begin{aligned} \frac{\partial w}{\partial x} &= \frac{\partial}{\partial x} \left(\frac{1}{4} \left(3 - \sqrt{1 + 4\sin^2(\pi x)} \right) \right) \\ &= -\pi \frac{1}{\sqrt{1 + 4\sin^2(\pi x)}} \sin(\pi x) \cos(\pi x) \end{aligned}$$

Note that, for $x = 0$, $\partial w / \partial x = 0$, as we mentioned above. For the second derivative, a straightforward calculation gives

$$\begin{aligned} \frac{\partial^2 w}{\partial x^2} = -\pi \frac{\partial}{\partial x} \left(\frac{1}{\sqrt{1 + 4\sin^2(\pi x)}} \right) \sin(\pi x) \cos(\pi x) + \\ - \frac{\pi}{\sqrt{1 + 4\sin^2(\pi x)}} (\cos^2(\pi x) - \sin^2(\pi x)) \end{aligned}$$

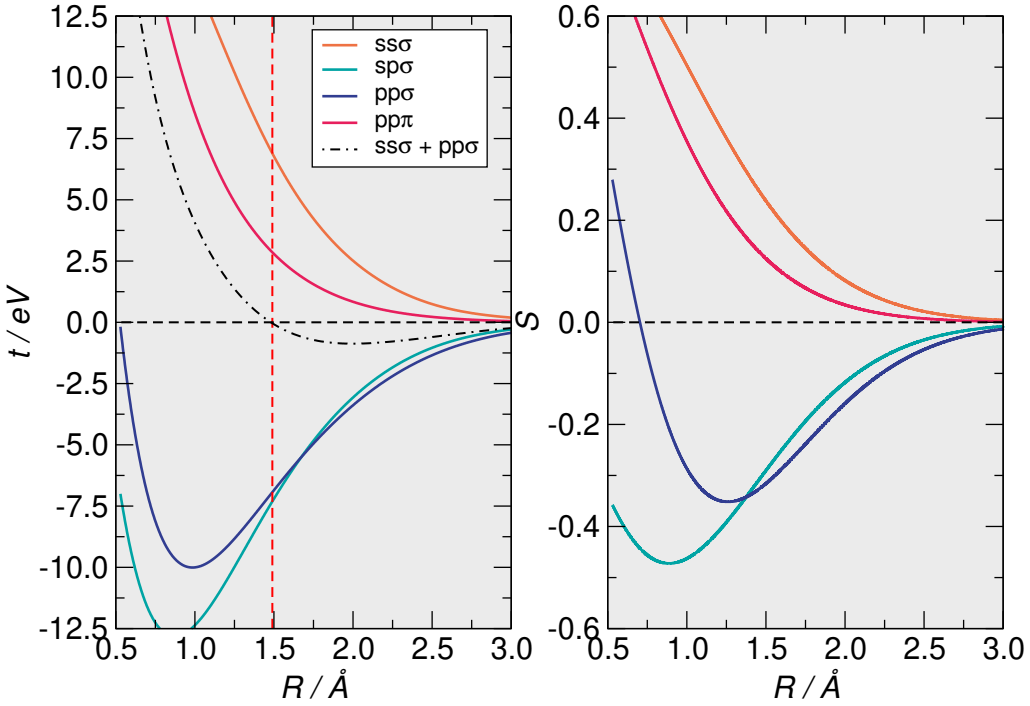

Figure 11.11. Hopping (left) and overlap (right) parameters in homonuclear atom pairs, as functions of the interatomic distances. Results from first principles calculations of Ref.s 2,3. The red dashed line denotes the average CC bond length of a cis-structure in the infinite size limit.

Substituting these derivates into the Taylor expansion (11.52), we arrive at

$$\boxed{t_\sigma^{\text{eff}} \approx t_\sigma^{\text{eff}}(0) + \frac{\bar{\rho}^2}{4\pi} T(\mu(0))\kappa^2} \tag{11.56}$$

where $T(\mu(0)) = -\frac{1}{2}\{t_\sigma(ss) + t_\sigma(pp)\}$ (C employs pure sp hybrids for the σ-bond in this limit). According to our calculations, the average bond length in cis-annulenes is expected to converge around $\sim 1.49\,\text{Å}$. Using realistic values of the parameters - analytically expressed in terms of Chebyschev polynomials, see Figure 11.11 - we find that $T(\mu) > 0$ and therefore increasing the curvature κ has the effect to strengthen the σ-bond. Accordingly, cis structures are preferred at large curvature radii, *i.e.* at small n, as we showed above.

The above analysis can be extended with minor modifications to π-bond and a similar Taylor-expansion can be written for the λ hybridization index.

11.3.1 A simple application: the bending-stiffness

In closing this Chapter, we show a rather simple analytical application of the above model to the calculation of a mechanical property of $[n]$-annulenes, namely the *bending stiffness*, K. The latter can be defined for a rod of length L as the second derivative of the energy density w.r.t. the curvature κ, or equivalently, for our C_nH_n molecules, as

$$K = \frac{1}{\bar{\rho}} \frac{\partial^2 \varepsilon}{\partial \kappa}$$

where $\varepsilon = E/n \equiv -AE$ is the formation energy per structural unit (provided that E is referenced to the atomization limit), $\bar{\rho}$ is the average bond length projected onto the molecular axis and κ^{-1} is the ring radius. Since in the limit we are interested, we have

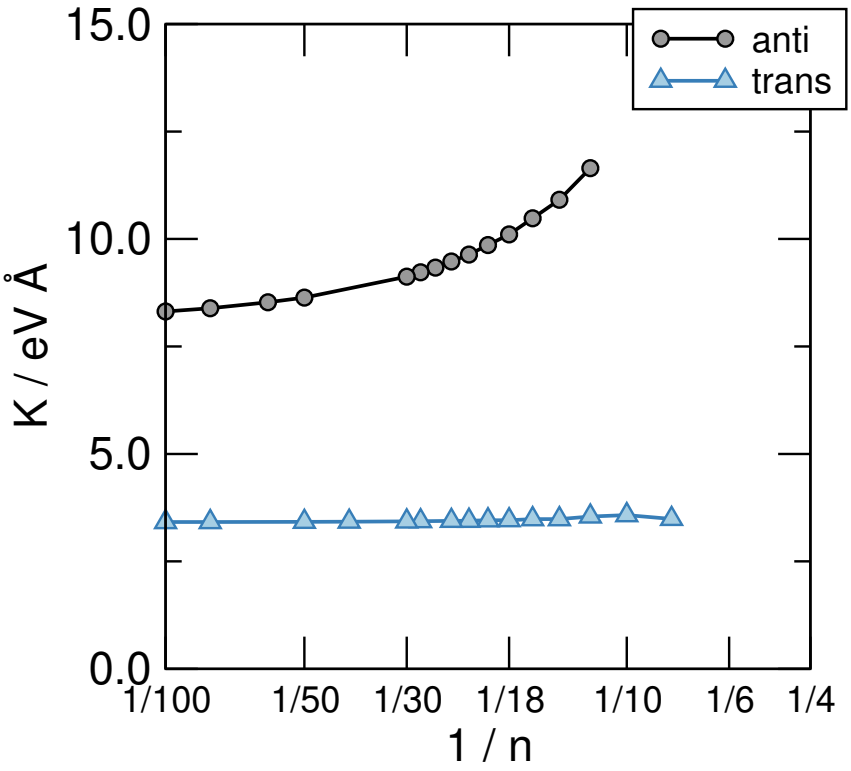

Figure 11.12. Bending stiffness of the structural sequences defined in Figure 11.6, on a linear-log scale.

again $2\pi\kappa^{-1} \approx n\bar{\rho}$, the bending stiffness takes the form

$$K = \lim_{n\to\infty} \frac{\bar{\rho}}{4\pi^2} \frac{\partial^2 \varepsilon}{\partial (1/n)^2} \tag{11.57}$$

Equation (11.57) can be used to obtain K by fitting the AE *vs.* $1/n$ curves shown in the left panel of Figure 11.7 to a smooth curve and taking its second derivative w.r.t. $1/n$. The results of such a calculation are shown in Figure 11.12, where the structures investigated are seen to attain clearly different limits as $n \to \infty$. Disregarding the unphysical limit of the cis-sequence, the anti and trans ones present rather different values of K, namely $K \approx 8.3$ eV Å for the first and $K \approx 3.3$ eV Å for the second. The latter two give the stiffness of trans-polyacetilene for bending in two different ways: While the limiting anti structure describes an in-plane deformation of the "ribbon", the trans- sequence mimics an out-of-plane deformation. In turn, the first one involves the σ backbone only - the bending of the σ-bonds between C atoms - while the second calls into question the π bonds only. The latter is thus a manifestation of the π-resistivity to cis-bending. This shows how atomic properties show up in the extended system and determine the properties of the material[153].

In Subsection 11.2.3 we have established a simple relationship between the σ hybridization index μ and the curvature κ for the anti structures. Therefore, since the bending-stiffness of anti-structures is determined by the σ bonds only and reminding that for $U = 0$, $\varepsilon_\sigma = -2t_\sigma^{\text{eff}}$, we can apply our curvature-dependent model to derive an analytical expression of K in terms of AO contributions. First, we use Equation (11.45) to compute the second-derivative $\partial^2\mu/\partial\kappa^2$ at $\kappa = 0$

$$\left.\frac{\partial^2 \mu}{\partial \kappa^2}\right|_{\kappa=0} = -\frac{1}{12} \frac{\mu_{\text{tP}} l_{\text{tP}}^4}{\rho_{\text{tP}}^2 \cos(\theta_{\text{tP}})} = -\frac{1}{3} \mu_{\text{tP}} \rho_{\text{tP}}^2 \frac{(1 - \cos(\theta_{\text{tP}}))}{\cos(\theta_{\text{tP}})}$$

Then, for the bending stiffness we get

$$\begin{aligned} K &= \lim_{\kappa\to 0}\frac{1}{\rho}\frac{\partial^2\varepsilon_\sigma}{\partial\kappa^2} = -\frac{2}{\rho_{\mathrm{tP}}}\frac{\partial^2 t_\sigma^{\mathrm{eff}}}{\partial\kappa^2}\bigg|_{k=0} \\ &= -\frac{2}{\rho_{\mathrm{tP}}}\frac{1}{1+\mu_{\mathrm{tP}}}T(\mu_{tP})\left(-\frac{1}{3}\mu_{\mathrm{tP}}\rho_{\mathrm{tP}}^2\frac{(1-\cos(\theta_{\mathrm{tP}}))}{\cos(\theta_{\mathrm{tP}})}\right) \\ &= \frac{2}{3}\frac{\mu_{\mathrm{tP}}\rho_{\mathrm{tP}}}{(1+\mu_{\mathrm{tP}})^2}\frac{(1-\cos(\theta_{\mathrm{tP}}))^2}{\cos(\theta_{\mathrm{tP}})}\left[-t_\sigma(ss)+\frac{\mu_{\mathrm{tP}}-1}{\sqrt{\mu_{\mathrm{tP}}}}t_\sigma(sp)-t_\sigma(pp)\right] \end{aligned} \tag{11.58}$$

In the above formula we may set $\theta = 124^\circ$ and $\rho_{\mathrm{tP}} = 1.398$ (average bond length in *trans*-polyacetylene). For the μ hybridization index, in *trans*-polyacetylene, each C actually employs two different hybrids in the σ-bonds with its two neighboring C atoms, namely $\mu_1 \approx 1.67$ and $\mu_2 \approx 1.90$. Accordingly, such hybridization indexes lead to an esteem of the bending stiffness in the range of $4.44(\mu = 1.67) - 5.31(\mu = 1.90)$ eV Å, which is overall close to the extrapolation to infinite size limit as obtained by DFT calculations (≈ 8.3 eV Å), despite we have worked in a bare tight-binding approximation ($U = 0$).

Chapter 12

Conclusions

In this work we have presented a detailed theoretical investigation of some π-conjugated carbon-based systems such as graphene and polycyclic aromatic hydrocarbons (PAHs). Our main purpose has been to understand changes in chemical properties occurring when these systems deviate from their original planar geometry and bend to form *curved* structures. Furthermore, we have looked for a mathematically rigorous description of the curvature of such systems and its effect on the atomic-scale - *e.g.* the re-hybridization of carbons - in order to go beyond the bare geometrical models adopted so far. Therefore, this subject has been approached from two perspectives: with DFT-based *ab-initio* calculations on relevant systems, and, with a rigorous mathematical analysis. Concerning the computational approach, we have mainly focused on the investigation of the H sticking, because of the relevance of this simple reaction in disparate fields, from astrophysics to hydrogen storage and graphene technology.

We have started from the basis, thus considering the world of *flat* π-systems. After an introduction on the physics of planar graphene and PAHs, and their reactivity towards H, we have presented an investigation of the *stepwise hydrogenation reaction of the coronene molecule* ($C_{24}H_{12}$), a small PAHs. The interest in this system has been motivated by the role that PAH are supposed to play in the chemistry of the *interstellar medium*. In particular, they may allow to shed light on a still unsolved and puzzling question in astrochemistry, namely the relative abundance of the H_2 in those regions where this small molecule should be mainly dissociated by UV photons and heat. In photodissociation regions, PAHs have been detected, with a chemical state strongly depending on the environment. At intermediate temperature and in areas with a lower UV flux, they are expected to exist mainly in their neutral and superhydrogenated forms, and they are supposed to act as catalyst for the H_2 formation. In order to understand their role, it is hence crucial to identify these superhydrogenated structures.

This work, in particular, has started thanks to a collaboration with the experimental group of Prof. Liv Hornekær from Aarhus University. They exposed a model molecule such as coronene, deposited on an inert substrate, to a H flux and recorded mass spectra at different exposure times in a temperature-programmed desorption experiment. This analysis has revealed that coronene molecules with a specific number of extra hydrogens, namely $n = 10, 14, 18, 24$, accumulate in the mixture during the exposure, thus suggesting a remarkable stability for these hydrogenated structures. Therefore, in order to spot them, we have studied systematically the energetics of a stepwise H addition to coronene, by means of DFT as implemented in the Gaussian16 code. At each hydrogenation level, we have computed the H binding energies (D) and adsorption barrier E_b, also taking into account the possibility of branching in the hydrogenation sequence. Contrary to previous works on similar systems, we have adopted a high-level density functional, namely the *meta-*

hybrid GGA M06-2X exchange-correlation functional, that we have selected after a careful benchmark of several modern functionals, developed by the Thrular's group (MPW1B95, M06, M06L, M06HF, M062X, M11).

In agreement with the experimental data, we have found large binding energies and sizeable barriers to further sticking for $n = 0, 2, 10, 14, 18, 24$, thereby suggesting for these species a great stability towards both abstraction/desorption and further hydrogenation. In particular, the exceptional stability of $n = 10, 14$ and 18 can be traced back to additional electronic effects, namely three, two or one residual aromatic rings that are left in the π-substystem when, respectively, 10, 14 and 18 H are attached to the molecule. On the other hand, $n = 24$ owes its great stability to a full saturation of the π-system.

Interestingly, the hydrogenation sequence can be entirely rationalized in terms of very simples *rules of thumb* that should apply equally well to any other PAH. In particular, for closed-shell molecules, *i.e.* when n is even, the factors driving the next H addition are the *π-coordination* and *π-hyperconjugation*. The former determines the *localization of frontier orbitals at the edges of the π electronic system, increasing the H affinity of those sp^2 sites that have the smallest number of sp^2 neighbors*. The latter, on the other hand, *discriminates between sites with the same π-coordination but different number of next-to-nearest neighbors in the π-lattice. In particular, the highest is such number the highest is the H affinity*. Instead, for open-shell molecules, *i.e.* when n is odd, the next addition is driven by the *unpaired electron density, which resides in a midgap state that delocalizes through Pauli's resonance and enhances the reactivity of ortho and para positions*.The study of the stepwise H addition to coronene thus helped us to identify the main driving forces of the H sticking into specific lattice positions of a planar π-conjugated system.

Exploiting the great accuracy of the M06-2X for PAHs, we have extended our analysis to larger clusters, such as circumcoronenene ($C_{54}H_{18}$) and doublecircumcoronene ($C_{96}H_{24}$). We have focused in particular on the computation of the H adsorption barriers, with the aim of extrapolating an estimate for the infinite-size limit, *i.e.* graphene. The reason is that the exact value of the adsorption barrier on graphene is still unknown in the literature, although most of the theoretical investigations converge towards a value close to $\sim 0.2\,\text{eV}$. For the larger, doublecircumcoronene, by properly taking account the BSSE affecting our atomic-orbital calculations, we have found $E_b \approx 335\,\text{meV}$. It is rather unlikely that this value reduces to $0.2\,\text{eV}$ when extrapolated at infinite size (for circumcoronene $E_b \approx 319\,\text{meV}$), and therefore our calculations suggest a much larger barrier height for H sticking on graphene than previously estimated.

Next, we have engaged into the exploration of the world of *curved* π-systems. First, we have investigated the *coroannulene* molecule ($C_{20}H_{10}$). The latter can be considered as the curved analog of coronene, that is obtained by simply replacing the inner 6-membered ring with a 5-membered ring, which are known to be the source of positive *Gaussian curvature*. Besides the possibility of a direct comparison with the flat relative, the interest in curved PAHs such as coroannulene comes again from our *Universe*: it has been recently suggested that some spectral features of the *unidentified infrared emissions* may due to non-planar components in aromatic molecules; furthermore, superhydrogenated curved PAHs may as well catalyze the H_2 formation in some regions of the ISM.

As for coronene, our analysis relies on a collaboration with the Aarhus surface science group, that repeated the experiment on coroannulene. The latter has revealed that coroannulene molecules with $n = 6, 8, 10, 12, 14, 16, 17, 18$ extra H accumulate in the mixture during the exposure, thus suggesting that these numbers of H lead to structures with remarkable stability. Therefore, in order to spot them, we have studied systematically the energetics of a stepwise H addition to coroannulene, with the previous successful strategy applied to coronene.

The curvature in coroannulene has the first effect to induce a sizeable rehybridization

and pyramidalization of the inner-ring C atoms. This translates into higher reactivity w.r.t. coronene, namely $D = 1.23\,\text{eV}$ *vs.* $D = 0.30\,\text{eV}$ on the central carbon. In other words, the curvature makes the edge localization of frontier orbitals less effective, contrary to what occurs on planar π-conjugated systems. By continuing the hydrogenation sequence, we have found large binding energies for $n = 0, 4, 6, 8, 10, 12, 14, 16, 18$. Overall, these findings are in good agreement with the experimental results and are further corroborated by the heights of the sticking barriers, which are found to be particularly large for $n = 0, 4, 8, 12, 14, 16$ and 18. Among these, the structure with $n = 14$ shows a prominent and persistent peak in the mass spectra, in agreement with the largest binding energy and barrier found for this structure along the hydrogenation sequence. Its exceptional stability can be traced back again to a residual aromaticity left by the previous hydrogenations, namely when $n = 14$ the remaining carbon atoms of the lattice form an aromatic ring, *i.e.* a stable motif that requires extra energy for further hydrogenation. However, some differences with the experiment arises and makes coroannulene a much more "tricky" molecule than coronene. First, the mass traces displays a build-up of the species $n = 16, 17, 18$ which appears to prevent the formation of perhydrocoroannulene ($n = 20$). This may be partly explained by the large barriers to hydrogenate $n = 18$ and the large stability of $n = 16$ and $n = 18$ when compared to $n = 20$. Yet, the mass spectra shows also a remarkable accumulation of the structure with $n = 17$, which is rather odd since odd-numbered species should be unstable towards further hydrogenation. Despite $n = 17$ has one of the largest binding energy among odd-numbered species and a vanishing barrier was detected to hydrogenate $n = 16$, it is still unclear why it accumulates in the experimental setting.

A careful analysis of the adsorption sites reveals that *the H addition is driven by an interplay between pyramidalization and π-coordination.* In particular, *highly pyramidalized sites with low π-coordination number display the largest H affinity - this is typically the case of central carbons once the nearby edges have been hydrogenated.* For open-shell molecules, the *unpaired density delocalization is still a good guiding principle*, as seen for coronene. Besides, we notice that a helpful principle to understand the reactivity of coroannulene is the so-called Clar number, *i.e.* the number of circles that one can draw with 6 delocalized π electrons in an aromatic Clar's structure. In particular, *the first positions to be hydrogenated are the ones which preserve the maximal Clar's number of coroannulene.* This highlights how *the aromaticity still plays a crucial role in determining the reactivity even in curved systems.*

The second curved structure we have considered is the *C/Si interface.* This system has drawn an ever-increasing interest in the last few years because it allows producing quasi-free standing graphene samples of extremely high-quality in a relative simple way. The mentioned interface presents two carbon layers - a "buffer layer" and a "monolayer" graphene - which are both curved because the C-lattice forms a Moiré structure on the SiC(0001) surface ($(6\sqrt{3}\times 6\sqrt{3})R30$ reconstruction) that displays CSi interactions of different strengths at the various lattice positions of the large supercell. Hence, in this system the curvature is of a totally different nature with respect to coroannulene, namely it is induced by an interaction with a substrate.

We have studied the H sticking on both the buffer and the monolayer, again focusing the attention on the effect of curvature on the H binding energy. The hydrogenation of the buffer layer is rather attractive also from the applied perspective, since it is expected to completely decouple the on top graphene layer, thereby making the latter really free-standing. Contrary to previous theoretical investigations on this system, we have considered a minimal structure (1310 atoms) modeling the clean buffer surface in the experimental surface reconstruction. In this way, we are able to take into account the long-range features of the interface, namely its curvature, on the H adsorption energetics.

According to our findings, *binding energies vary considerably across the buffer layer,*

ranging from 2 eV *to* 3.2 eV*, and turn out to be much larger than the energy released when binding H on planar free-standing graphene* (around ≈ 0.8 eV with DFT-PBE calculations). This great variability can be assigned to the unique geometrical structure of the buffer layer. Indeed, 4 different types of C atoms can be identified across the layer: three-coordinated C with 0, 1 or 2 nearest-neighbors (nn) that bind a Si atom of the underneath SiC or four-coordinated C, *i.e.* directly bonded to a Si atom. Three-coordinated C atoms with 2 Si-bonded nns show the largest H affinity for a combination of a geometrical and an electronic effect: *the strong CSi bonds in the nearby induce sizeable pyramidalization and break the π-bond, leaving a spin-density around the binding C, thus increasing its reactivity.*

Next, we have added a second graphene layer on top of the buffer layer, thus realizing the full C/Si interface (for a total number of atoms amounting to 1648). First, we have computed the bilayer binding energies ($E^{\rm bil}$) with both PBE and a VdW-inclusive functionals (VV). Interestingly, *when employing semilocal functionals in conjuction with atom-centered basis sets, the inclusion of the overbinding basis-set superposition error (BSSE) between the two layers provides a better estimate of* $E^{\rm bil}$ (74 meV *vs.* 61 meV with VdW-VV and BSSE removed with the standard CP-correction). In a sense, the BSSE can play the role of the missing long-range interactions of a semilocal functional such as PBE.

Then, we have computed the binding energies on several lattice positions of the monolayer graphene. Here, D are still quite large, even though the monolayer displays just a wavy profile with a corrugation not exceeding $\Delta z \approx 0.3$ Å. In particular, $D = 1.4{-}1.7$ eV, where *larger values are found on the convex areas of the layer*, in agreement with available experimental results.

The energetics of the H adsorption determines both the propensity of a surface to trap H atoms wandering above it and that of already adsorbed H to undergo abstraction reaction. In this case, the most relevant mechanism is the *Eley-Rideal* (ER) recombination, which is operative in a large range of temperatures. In the ER recombination, a H coming from the gas phase is captured by a H already adsorbed on the surface, thus forming a H_2 molecule. The reaction is barrier-less and hence its rate is determined by its exothermicity, *i.e.* the H binding energy. Therefore, in a second stage of the work, we have combined our DFT data with a quantum dynamical investigation of the *Eley-Rideal* (ER) reaction, with the main aim of understanding the impact of the peculiar *geography* of the buffer layer - *i.e.* its large D - on the ER reaction cross-sections. By means of a time-dependent wavepacket method on model LEPS potential energy surface, we have thus computed the ER cross-sections (σ) in a broad range of collision energies (E_{iz}) of the incident atom at different binding energies of the targon. The latter have been selected in a broad interval (1.2−3.2 eV), as provided by our DFT calculations on the C/Si interface. Despite the ER reaction is a barrier-less process, binding energy of the targon has a significant impact on the scattering cross sections. In particular, as D increases, σ starts to steeply decrease at collision energies which are smaller and smaller. Noteworthy, σ still exceeds 1 Å^2 in large range of binding energies ($D \approx 1.2{-}2.5$ eV), contrary to what observed on metal surfaces despite a comparable binding strength. For the largest values considered (3−3.2 eV), *cross section becomes almost vanishing at* $E_{iz} \gtrapprox 1.6$ eV *suggesting that the ER reaction hardly occurs* on sites with such high D, *i.e. three-coordinated C with two Si-bondend nns of the buffer layer.*

In the meanwhile, we have exploited some *known* concepts of *differential geometry of surfaces* to set up a *model that relates the geometry around a C atom (and its hybridization) to the local curvature of the surface.* To this aim, we have made the simplest assumption of a *locally quadratic surface around the C atom*, because this choice is free of constraints and gives raise to simple analytical expressions. First, we have expressed the vector joining two neighboring C ($\Delta \boldsymbol{x}$) in terms of the local basis ($\boldsymbol{e}_1, \boldsymbol{e}_2, \boldsymbol{N}$), where ($\boldsymbol{e}_1, \boldsymbol{e}_2$) span the tangent space to the surface at point where the C is found and $\boldsymbol{N}$ is the surface normal.

Under such assumptions, the normal components of $\Delta\boldsymbol{x}$ is given by the normal curvature κ_n of the curve joining two neighboring C. Considering two bonds, $\Delta\boldsymbol{x}_1, \Delta\boldsymbol{x}_2$, we have thus obtained for the bond angle Θ_{12},

$$\cos(\Theta_{12}) = \frac{2}{\sqrt{\left(\sqrt{1+\rho_1^2\kappa_1^2}+1\right)\left(\sqrt{1+\rho_2^2\kappa_2^2}+1\right)}}\cos(\phi_1-\phi_2)+$$
$$+\,\mathrm{sgn}(\kappa_1\kappa_2)\left(\frac{\sqrt{1+\rho_1^2\kappa_1^2}-1}{\sqrt{1+\rho_1^2\kappa_1^2}+1}\frac{\sqrt{1+\rho_2^2\kappa_2^2}-1}{\sqrt{1+\rho_2^2\kappa_2^2}+1}\right)^{1/2}$$

The above expression only requires the knowledge of the lines of principal curvature, the associated curvatures $(\kappa^{(1)}, \kappa^{(2)}$ *- which allows to express the normal curvature of any curve on the surface (here* κ_1 *and* κ_2*) thanks to the so-called Euler's theorem - and the orientation of the bonds w.r.t. such lines, in particular the angle* $\Delta\phi = \phi_1 - \phi_2$ *that the projected bonds make with each other.* Since the bond angles are related to the hybridization through the Coulson's directionality theorem, the above expression allows to compute the σ and π hybridization indexes in terms of the local curvature. We have validated such a model by applying it to simple but interesting situations (spherical surfaces, carbon nanotubes and closed-ring C chains). This paves the way to analyze curvature in π-systems beyond the bare geometrical models adopted so far: *we are now in a position to include the effect of rehybridization, hence to deal with arbitrary curvatures.*

Appendix A

Thermodynamics of PAH hydrogenation

Let consider the stepwise hydrogenation reaction of coroannulene. With the complete energetics at hand (Chapter 7), a thermodynamic analysis can be performed and temperature and pressure effects can be included in our DFT calculations. Before showing our results, we introduce some relevant thermodynamical quantities. First, let consider the following chemical equilibria[1]

$$\begin{gathered} \mathrm{C_{20}H_{10+n}} + H \rightarrow \mathrm{C_{20}H_{10+n+1}} \\ \mathrm{2H} \rightarrow \mathrm{H_2} \end{gathered}$$

We define the *fractional hydrogenation level* as

$$f = \frac{N^0(H)}{N^0(H)/2 + N^0(Co)} \tag{A.1}$$

where $N^0(H)$ is the total number of (extra) hydrogen available in a given sample and $N^0(Co)$ the total number of coroannulene molecules (bare *plus* hydrogenated coroannulene). The free energy of n-fold hydrogenated structure is

$$G_n = E_n - k_b T \ln \mathcal{Z}_n^{int} + k_b T \ln \left(\frac{p_n}{\xi_n} \right)$$

where E_n is the DFT zero-point corrected energy, $\mathcal{Z}$ the internal partition function, p_n the partial pressure and ξ_n the thermal pressure, *i.e.* $\xi_n = k_b T / \lambda_n^3$with λ_n^3 the *De Broglie thermal wavelength*. The internal partition function accounting for rotational, vibrational and electronic contributions is given by

$$\mathcal{Z}_n^{int} \simeq \frac{1}{\sigma_n} \left(\frac{T}{\theta} \right)^{3/2} \prod_{j=1}^{F_n} \left[1 - \exp \left(-\frac{\hbar \omega_j^{(n)}}{k_b T} \right) \right] \mathcal{Z}_n^{el} \tag{A.2}$$

where $\theta_n = \hbar^2 / 2 I^{(n)} k_b T$ is the rotational temperature of the n-fold hydrogenated structure with $I^{(n)} = (\pi I_A^{(n)} I_B^{(n)} I_C^{(n)})^{1/3}$ being its moment of inertia, given in terms of the principal values of inertia tensor, $\omega_j^{(n)}$ the normal mode frequencies ($j = 1, 2, ...F_n$ where F_n is the number of vibrational degrees of freedom, $F_n = 3(36 + n) - 6$) and $\mathcal{Z}_n^{el}$ the electronic partition function, $\mathcal{Z}_n^{el} = 1 +$ mod $(n, 2)$. For molecular hydrogen, the classical limit of rotational partition function is inappropriate at temperature $T \lesssim 100$ and one should

[1]The following considerations apply equally to coronene or any other PAH.

consider the sum over *all* states. To properly handle this situation, Equation (A.2) was still employed in the slightly modified form

$$\mathcal{Z}_{H_2}^{int} \simeq \frac{1}{2}\frac{k_b T}{hcB}\left(1-\exp\left(-\frac{\hbar\omega}{k_b T}\right)\right) \tag{A.3}$$

where the rotational constant B was adjusted in order to make the entropy, $S = -k_b T \ln \mathcal{Z}$, continuous at 298.15 K (where S was computed from the *Shomate equation*[2].).

If one is interested in determining the most stable species at a given thermodynamic condition, one may consider the "formation reaction"

$$C_{20}H_{10} + \frac{n}{2}H_2 \rightarrow C_{20}H_{10+n}$$

and the corresponding Gibbs free energy

$$\begin{aligned}\Delta G_f(P,T,f^0) = G_n(P,T) - G_0(P-p_{hy},T) + \\ - \frac{n}{2}G_{H_2}(p_{hy},T)\end{aligned}$$

where $p_{hy} = f^0 P$ and look, for given conditions, P, T and f^0, for the smallest values. Following this strategy, we have computed the formation Gibbs free energy for each hydrogenated species in a broad range of temperature and total pressure ($1 \leq T \leq 600$ K and $10^{-13} \leq P \leq 10$ bar) for several fractional hydrogenation levels. Figure A.1 shows a phase diagram for $f^0 = 1/2$. Because of the exothermicity of the hydrogenation reaction, we note that high T and low P (low T and high P) hinder (favor) the formation of superhydrogenated species. At the thermodynamical conditions employed in the experiment ($T \approx 200$ K and $P \approx 10^{-13}$ (UHV)), perhydrocoroannulene is unstable w.r.t. less hydrogenated species. This suggests that fully superhydrogenation is hardly reached at these thermodynamical conditions. Instead a preferential formation of $n = 14$ is indicated, in agreement with the experimental findings[3].

A.1 Mixture free energy

As a complementary approach to the thermodynamical analysis of PAH hydrogenation, we have considered a mixture of PAHs and (atomic/molecular) hydrogen and the problem of minimizing the mixture free energy. The initial mixture composition can be defined in terms of the number of molecules per each hydrogenated specie, N_n^0, plus the number of H atoms, N_H^0, and H_2 molecules, $N_{H_2}^0$. The associated initial Gibbs free energy is G_{mix}^0. The mixture composition can then be optimized *stochastically*, by introducing random variations on each mixture components. After any variation, the mixture free energy, G_{mix}^1 is re-computed and compared with that of the previous composition: if lower, $G_{mix}^1 < G_{mix}^0$, the newly random-generated composition is "saved" and used for the next step; otherwise that composition is "discarded" and another random-generated composition is checked until $G_{mix}^1 < G_{mix}^0$ is found. We have applied this stochastic procedure to a mixture with

[2]Shomate Equation for standard entropy S° (J/mol K) reads as

$$S^\circ = A\ln(t) + Bt + C\frac{t^2}{2} + D\frac{t^3}{3} - \frac{E}{2t^2} + G$$

where $t = T/1000$ is the reduced temperature (K) and A, B, C, D, E, G are temperature-dependent parameters (their values can be found in the NIST Chemistry WebBook[271].

[3]We have seen in Chapter 7 that mass traces also displays a build-up of $n = 16-18$ species. The phase diagram shown here provides a complementary picture of the coroannulene superhydrogenation but is, of course, far from being able to capture the complexity of the experiment.

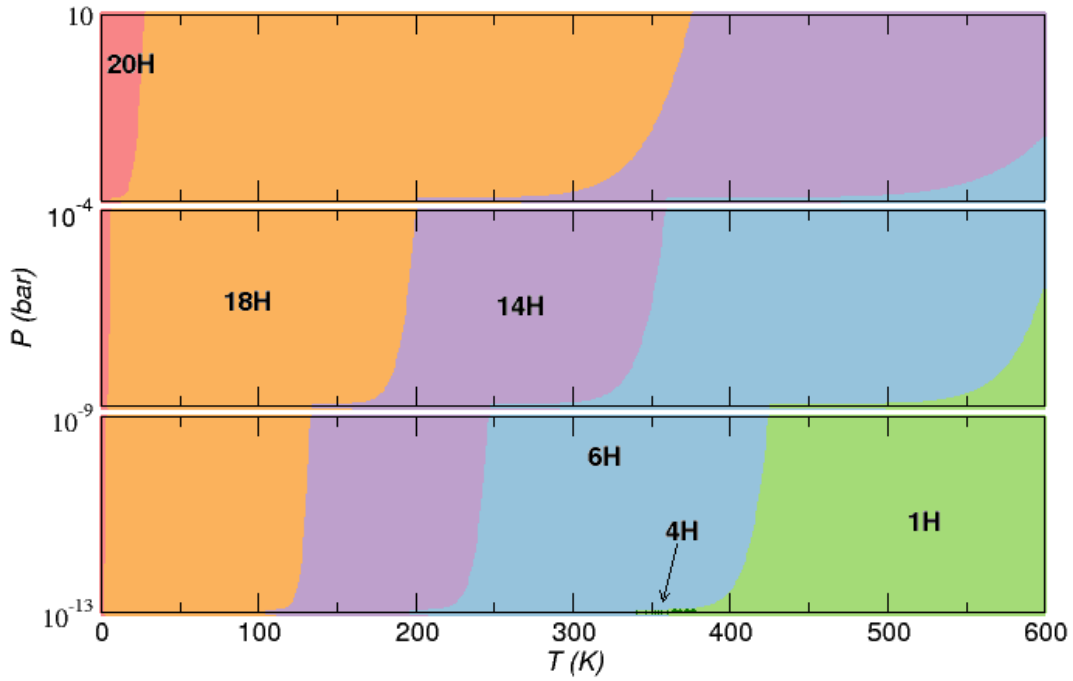

Figure A.1. Phase-diagram at $f^0 = 1/2$ showing the most stable hydrogenated molecules (nH) at given thermodynamical conditions. Colored areas delimit the region of thermodynamical stability; different colors are used for different nH.

initial composition consisting of only bare coroannulene and an excess of H_2, *i.e.* setting $N_i^0 \simeq 0$ with $i = 1, .., 20$ and $N_H^0 \simeq 0$. In principle, one may introduce random variations on each N_i from the very first optimization step. However, a more reasonable choice consists in allowing the $(i+1)$ structure to "form" in the mixture only once the mixture with the hydrogenated molecules up to $n = i$ has reached the equilibrium[4]. In the following, we describe in detail the computational strategy employed[5].

A.1.1 Computational strategy

The composition of a mixture at a give step i is specified by a set $C = [N_{\rm H}^{(i)}, N_{\rm H_2}^{(i)}, N_0^{(i)}, .., N_M^{(i)}]$, where $N_{\rm H}^{(i)}$ is the number of H atoms, $N_{\rm H_2}^{(i)}$ is the number of H_2 molecules and $N_n^{(i)}$ that of n-hydrogenated coroannulene molecules, where $n = 0, 1, ..M$ with M the total number of hydrogenation steps (*i.e.* $M = 20$ for coroannulene)[6]. Variations on the abundances are introduced by adding to these, $\delta N_H^{(i)}$, $\delta N_{\rm H_2}^{(i)}$, $\delta N_n^{(i)}$, that are given by (*e.g.* for $N_n^{(i)}$)

$$dN_n^{(i)} = \frac{1}{W} 2 \left(\xi - \frac{1}{2} \right) N_n^{(i)} \tag{A.4}$$

where $\xi \in [0, 1]$ is a (pseudo)-random number and W is a scaling factor that allows tuning the extent of random variations (for $W = 1$, $dN_n^{(i)} \in [-N_n^{(i)}, N_n^{(i)}]$). Henceforth, we omit

[4] In other words, we are assuming that each hydrogenation step is "independent" of the others. Then, the equilibrium composition is reached through multiple "local" equilbria, $C_{20}H_{10+n} + H \rightarrow C_{20}H_{10+n+1}$.

[5] Such approach was implemented in a FORTRAN90 code.

[6] Remind that this is the mixture with the optimized composition generated by the $i-1$ step.

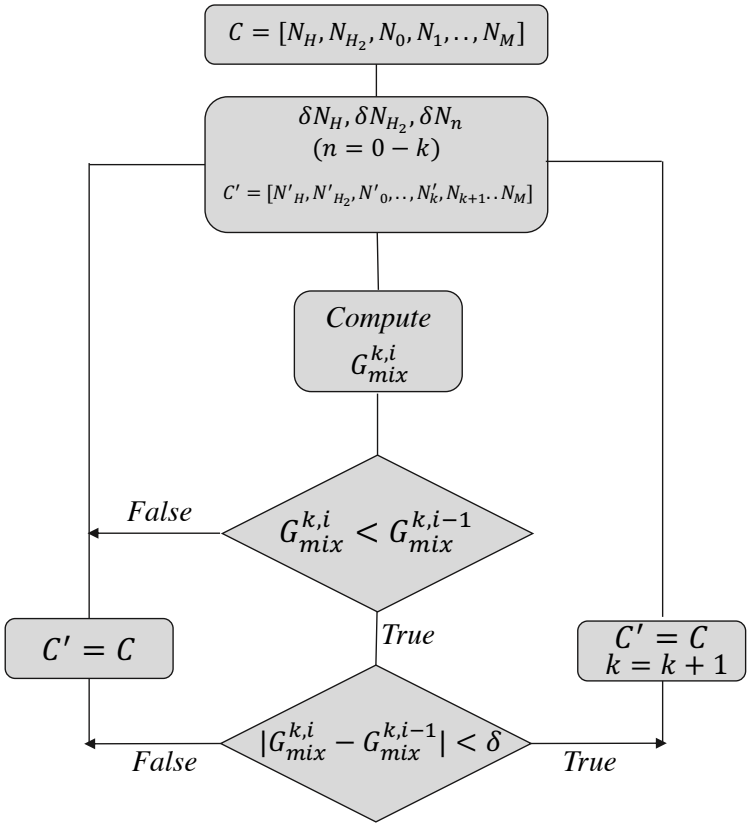

Figure A.2. Flowchart describing the optimization procedure.

the superscript i. To ensure the mass balance of coroannulene molecules, we first set

$$\tilde{N}_n = N_n + dN_n$$
$$\tilde{N}_t = \sum_n^M \tilde{N}_n$$

and then we properly re-define the random-variated populations at step i as

$$N'_n = \tilde{N}_n \frac{N_t^0}{\tilde{N}_t} \tag{A.5}$$

where N_t^0 is the total number of coroannulene molecules that has been fixed at the outset. Once the abundance of H atoms in the mixture is modified (according to Equation (A.4)), the new population of H_2 molecules is given by the mass conservation law

$$dN_{\mathrm{H}_2} = \frac{1}{2}\left(-dN_{\mathrm{H}} - \sum_n^M n dN'_n\right) \tag{A.6}$$

Notice that $dN'_n \neq dN_n$ are the final "true" random-variation, *i.e.* $dN'_n = N'_n - N_n$. With the newly random-generated mixture composition, the mixture Gibbs free energy is computed according to

$$G^{(i)}_{mix} = \sum_{n=0}^M N'_n G_n + N'_H G_H + N'_{H_2} G_{H_2}$$

As we mentioned before, we make the assumption of a stepwise optimization, where $[N_n, N_{n+1}, ..., N_M]$ populations are set to zero until $[N_{\rm H}, N_{\rm H_2}, N_0, ..., N_{n-1}]$ is optimized. In this sense, the full mixture composition optimization is divided into M sub-optimizations, that we call $K = 1, 2, ..., M$. The suboptimization $K = 1$ involves the species $n = 0, 1$, $K = 2$ the species $n = 0, 1, 2$, etc. Since the interval of the random variation depends on the input composition at that step (see Equation (A.4)), at the very first step when the abundance of N_n is "unconstrained", its value is set to a fraction (typically 1/100 but this can be tuned in the input file) of the most abundant specie in the mixture at that moment. This choice guarantees that the equilibrium is hardly changed. Flowchart in Figure A.2 summarize the optimization procedure.

At the end of any sub-optimization, the reached equilibrium composition defined in terms of number of molecules (N'_n) is saved and fitted according to

$$s(x) = \sum_{n=0}^{M} N'_n L_n(x)$$

where $L_n(x)$ is a *Lorentzian function*

$$L_n(x) = \frac{1}{\pi} \frac{\frac{\gamma}{2}}{(x-n)^2 + (\frac{\gamma}{2})^2}$$

with γ is a scale parameter (the *full width at half-maximum*) that allows tuning the shape of the lorentzian.

A.1.2 Simulation results

In the following, we show the results of several simulations at different temperatures and pressures. The top panel of the following Figures displays *all* the peaks appearing in the mixture composition during the optimization. The other panels display the mixture composition at end of a given sub-optimization (K).

Let first discuss the case of a stoichiometric excess of H_2 w.r.t the initial population of coroannulene molecules. We see that at low temperature ($T = 1$K) and pressure ($P = 10^{-13}$ bar), the stable structures - $n = 4, 6, 8, 10, 12, 14, 18, 20$ - we have identified in Chapter 7 accumulate in the mixture, as it is made evident by the appearance of intense peaks. Notice that, by following the mixture composition at different sub-optimization K, when a stable structure is allowed to form, *all* coroannulene molecules are hydrogenated at that hydrogenation level.

At low temperatures, increasing the pressure appears to have little effect on the mixture composition. On the other hand, the effect of temperature in hindering the hydrogenation is clear. At $T = 50$ K (and $P = 10^{-13}$ bar), peak at $n = 10$ is absent in the mixture composition. By the same token, $n = 20$ does not accumulate, thereby suggesting that perhydcoroannulene does not form at such thermodynamical conditions, in agreement with the phase-diagram of Figure A.1. Increasing further the temperature at $T = 200$ K, only peaks at $n = 6, 14$ show up (beside $n = 0$). Notice that, increasing the pressure to $P = 1$ bar, pushes the equilibrium towards superhydrogenated species, and peaks at $n = 4, 6, 8, 12$, etc. show up again in the mixture composition.

Our code allows simulating also non-stoichiometric situations. An example is shown below, where $N^0_{\rm H_2} \approx (1/2)N^s_{\rm H_2}$ where $N^s_{\rm H_2}$ is the stoichiometric quantity of H_2. We see that the stepwise hydrogenation arrives at most at $n = 10$, with a small fraction of hydrogenated molecules with $n = 12$.

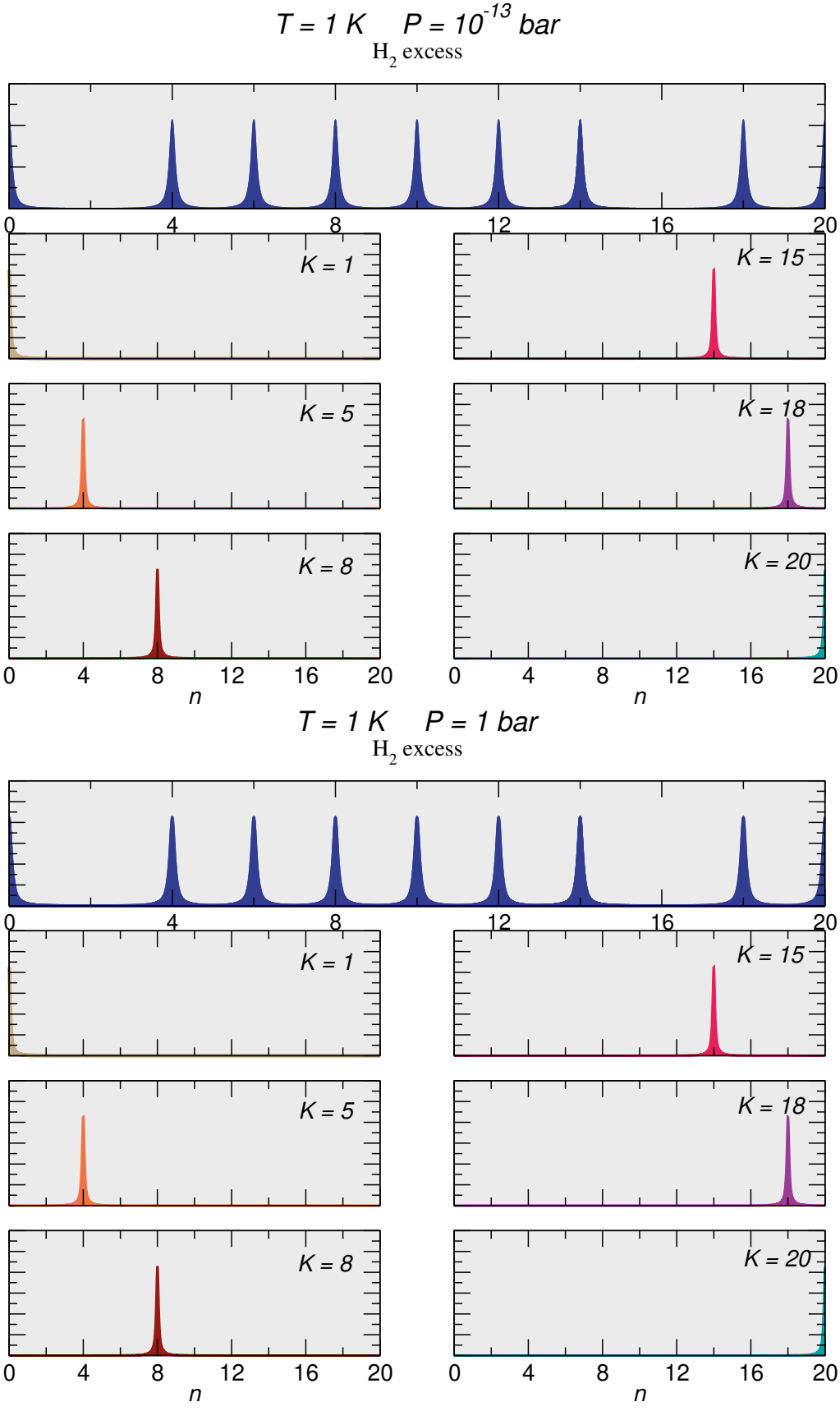
T = 1 K P = 10^-13 bar
H2 excess
0 4 8 12 16 20
K = 1
K = 15
K = 5
K = 18
K = 8
K = 20
0 4 8 12 16 20
n
0 4 8 12 16 20
n
T = 1 K P = 1 bar
H2 excess
0 4 8 12 16 20
K = 1
K = 15
K = 5
K = 18
K = 8
K = 20
0 4 8 12 16 20
n
0 4 8 12 16 20
n

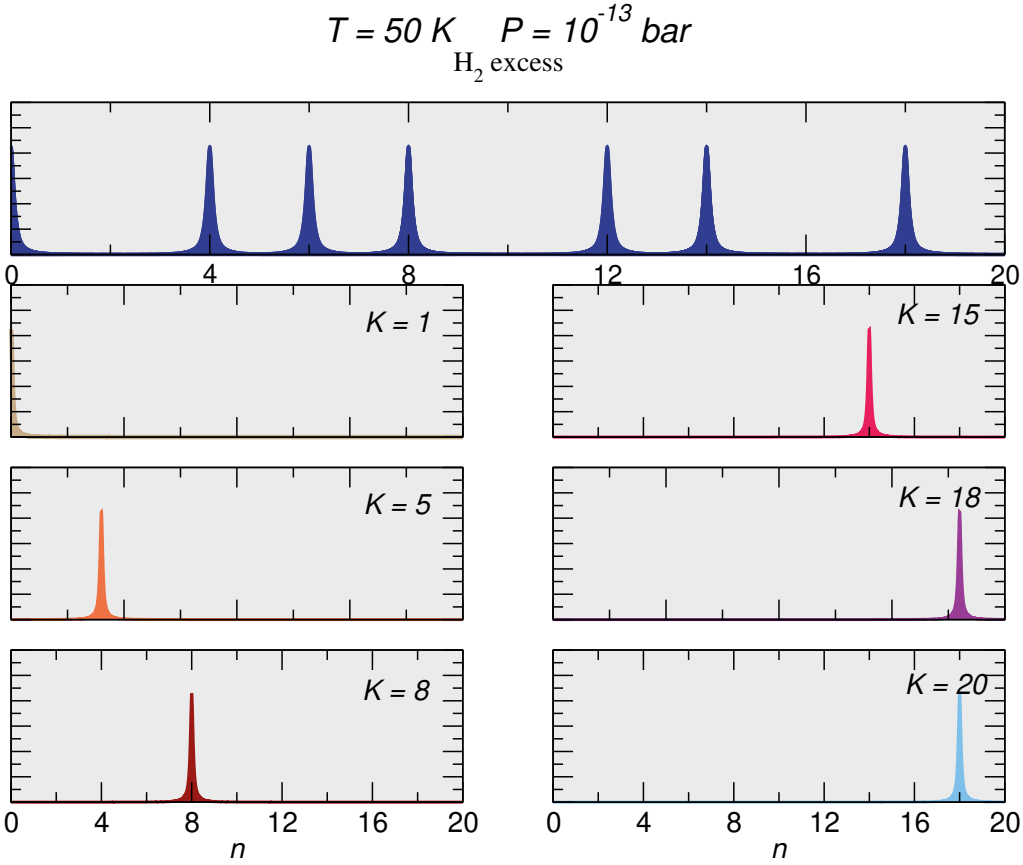
T = 50 K P = 10^-13 bar
H2 excess
0
4
8
12
16
20
K = 1
K = 15
K = 5
K = 18
K = 8
K = 20
n

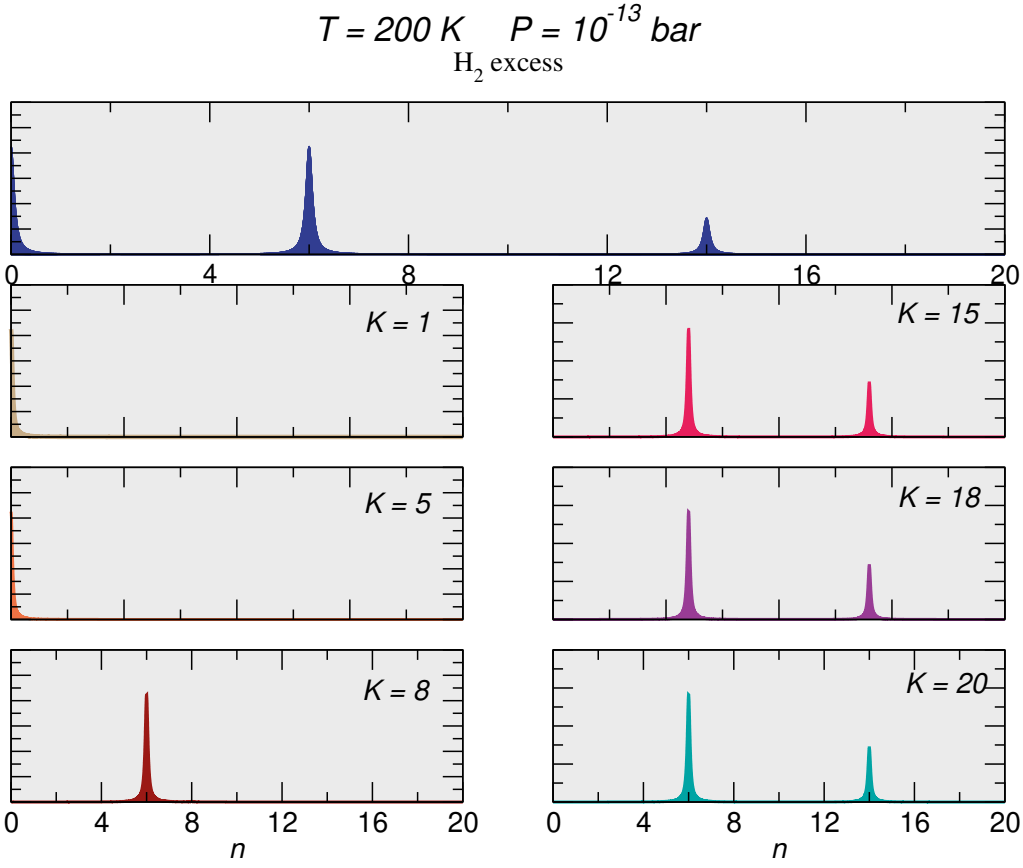
T = 200 K P = 10^-13 bar
H2 excess
0
4
8
12
16
20
K = 1
K = 15
K = 5
K = 18
K = 8
K = 20
n

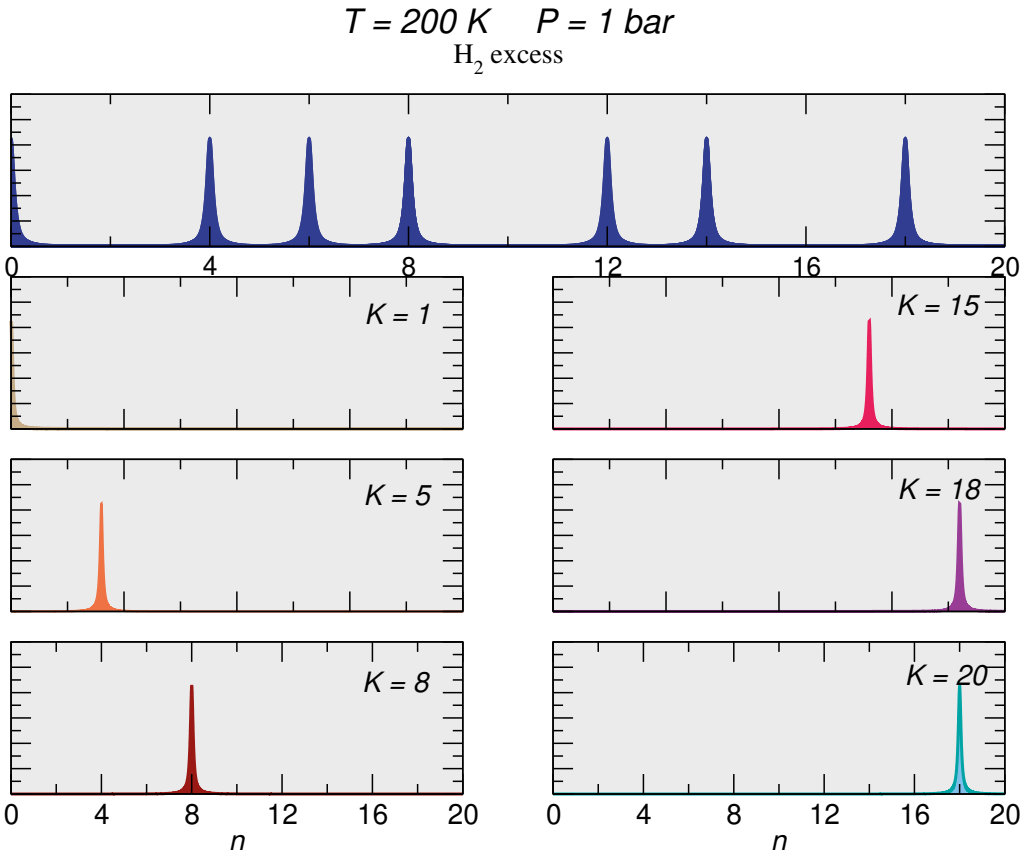
T = 200 K P = 1 bar
H2 excess
0
4
8
12
16
20
K = 1
K = 15
K = 5
K = 18
K = 8
K = 20
n

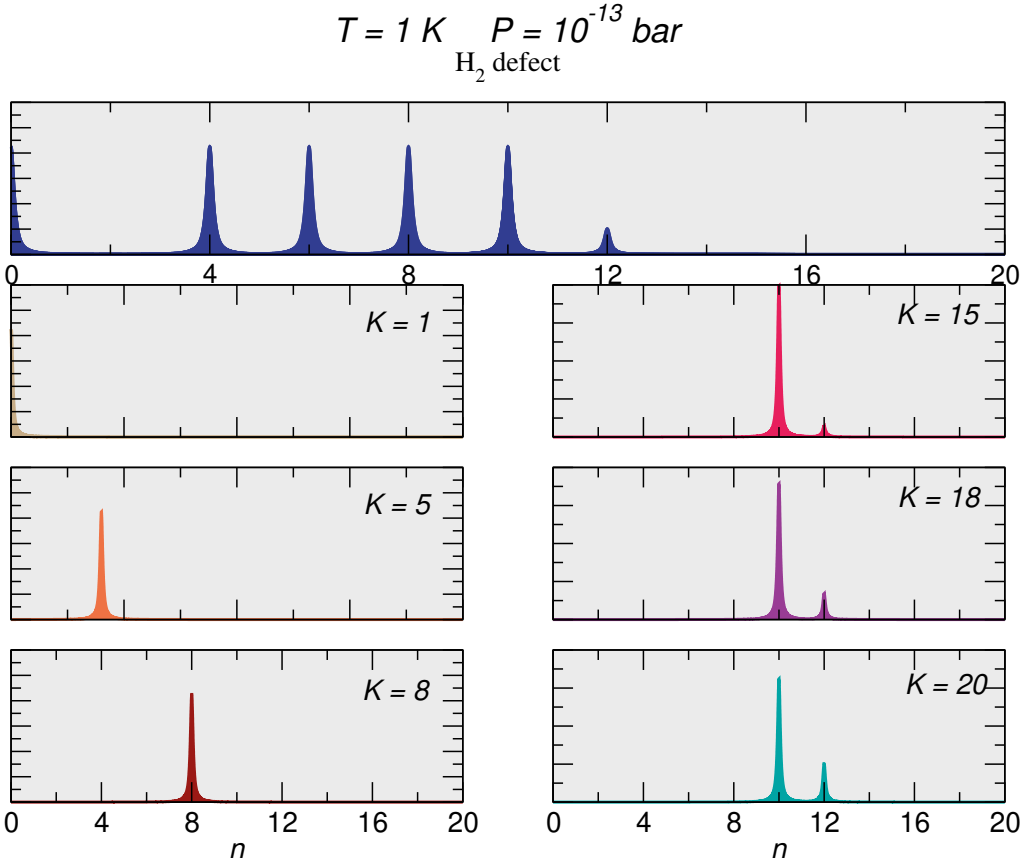
T = 1 K P = 10-13 bar
H2 defect
0
4
8
12
16
20
K = 1
K = 15
K = 5
K = 18
K = 8
K = 20
n

Appendix B

Scattering theory: an overview

In this Appendix[1], we give an overview of the *classical* and *quantum scattering theory*. In the following, we introduce the simplest case in which the collision partners do not have an internal structure (*single-channel* scattering theory). Although the scattering between two H atoms described in the main text does not match this situation[2], such simplification allows introducing some basic concepts, such as that of *scattering operator* or *cross-section*, which are at the heart of the scattering theory. In closing this section, we will give some hints about how the theory is extended to the case of a *multi-channel* problem. For a more comprehensive and detailed discussion on the matter, the interested reader is referred to the book of J.R. Taylor (1972)[272].

Let start with a classical approach to the scattering problem, which best fits the "picture" of scattering that we can have in mind. The *projectile* and the *target* are the "actors" of a scattering event[3]. The latter can be divided into three main "scenes":

(i) long before the collision, the projectile and the target are far away from each other, thus they do not experience any interaction. They move according to their initial conditions;

(ii) As the projectile enters the "interaction region", that is in the nearby of the target, both atoms undergo a very complicated motion that depends on the interaction potential;

(iii) long after the collision, the projectile and the target move again freely, with a motion determined by the earlier collision.

In classical mechanics, one may follow the motion of the system throughout the entire scattering process, thus defining a trajectory $\boldsymbol{x}(t)$, or "orbit". However, since the interaction region is of few atomic diameters, the actual orbit during the tiny "collision times"[4] is not observable in a scattering experiment. On the contrary, in a typical scattering experiment one "prepares" an initial state and then, roughly speaking, records the final state long after the collision. Therefore, we are just interested in the asymptotic limits, where the actual

[1] The writing of this Appendix served as a moment to re-organize the knowledge on scattering theory and quantum dynamics acquired during the period spent at the *LCAR* laboratory of the *University of Toulouse* in the group of Prof. Didier Lemoine.

[2] Actually, *all* the chemically interesting collisions are *multi-channel* scattering problems, that occur with some change in the internal structure of the colliding parterns

[3] Here, we deal with a gas-phase scattering process. However, most of the results shown in this Appendix can be extended with minor modifications to a gas-surface reaction.

[4] Even for a "slow" collision like that of a thermal neutron scattering off a big molecule, the collision time is around 10^{-10} s. Chemical reactions can be even faster, especially when involving light atoms such as H, with collision times in the order of femtoseconds.

orbit $\boldsymbol{x}(t)$ is no more than a free motion

$$\boldsymbol{x}(t) \xrightarrow{t\to-\infty} \boldsymbol{x}_{in}(t) = \boldsymbol{a}_{in} + \boldsymbol{v}_{in}t \tag{B.1}$$

$$\boldsymbol{x}(t) \xrightarrow{t\to+\infty} \boldsymbol{x}_{out}(t) = \boldsymbol{a}_{out} + \boldsymbol{v}_{out}t \tag{B.2}$$

where $\boldsymbol{v}_{in}$ is the initial velocity and $\boldsymbol{a}_{in}$ defines the position the system would have in absence of interaction at $t = 0$. Similarly, $\boldsymbol{v}_{out}$ is the final velocity and $\boldsymbol{a}_{out}$ is the position that the system would have had at time $t = 0$ if it had moved freely all the time. If we are able to compute $(\boldsymbol{a}_{out}, \boldsymbol{v}_{out})$ from the initial conditions $(\boldsymbol{a}_{in}, \boldsymbol{v}_{in})$, the scattering problem is entirely solved. There is a one-to-one correspondence between the "in" asymptote and the "out asymptote, which is defined by the actual orbit $\boldsymbol{x}(t)$. Hence, every orbit with an in asymptote has an out asymptote and for every pair of such asymptotic states there exists an actual orbit $\boldsymbol{x}(t)$. However, the opposite is not true, because a general potential $V(x)$ supports also states that are bound all the time, in contrast to the earlier defined "scattering orbits". The set of bound and scattering orbits make up all the possible orbits of the system.

Moving to quantum mechanics, we can no longer "assign" simultaneously a definite position and momentum to our system (the celebrated *Heisenberg's uncertainty principle*). The latter is defined by an abstract state vector $|\psi_t\rangle$ in a given Hilbert space $\mathcal{H}$, obeying the time-dependent Schrödinger's equation

$$i\frac{d}{dt}|\psi_t\rangle = H|\psi_t\rangle \tag{B.3}$$

with H a time-independent Hamiltonian. Given the initial condition $|\psi_t\rangle = |\psi_0\rangle$ at $t = 0$, the general solution to Equation is

$$|\psi_t\rangle = e^{-iHt}|\psi_0\rangle = U(t)|\psi_0\rangle$$

where $U(t)$ is the *time-evolution operator*: a unitary[5] operator that maps the state at $t = 0$ to the state at time t. Keeping the same terminology used for the classical case, we can call $U(t)|\psi\rangle$ an "orbit", even if it is not a classical trajectory in $\mathbb{R}^3$. As we have stated in the introduction, we start by considering a very simple situation: a spinless particle that scatters off a fixed potential. For this problem, $\mathcal{H} = \mathcal{L}^2(\mathbb{R}^3)$ and the Hamiltonian reads as

$$H = H^0 + V(\boldsymbol{x})$$

where H^0 is the free-particle Hamiltonian and $V(\boldsymbol{x})$ a fixed potential[6]. We now assume that $U(t)|\psi\rangle$ describes the evolution of a scattering experiment. Again, we can talk about asymptotic limits, *i.e.* long before the collision

$$U(t)|\psi\rangle \xrightarrow{t\to-\infty} U^0(t)|\psi_{in}\rangle$$

where $U^0(t) = e^{-iH^0t}$ is the *free* time-evolution operator. Long after the collision,

$$U(t)|\psi\rangle \xrightarrow{t\to+\infty} U^0(t)|\psi_{out}\rangle$$

The scattering theory, like many other theories, is grounded on a set of fundamentals

[5] An operator is unitary if it is *isometric* ($U^\dagger U = 1$, that is $U(t)$ must conserve the norm of the state vector) and *surjective* ($UU^\dagger = 1$, that is every state must have a "past".).

[6] Both classical and quantum scattering theory does not apply to *all* types of potential, instead they require the latter to be "well-behaved" (see Chapter 2 of Taylor (1972)[272] for the conditions that the potential has to satisfy). Fortunately, this class of potential include almost all potentials of interest (square well, Yukawa, etc., but not the Coulomb potential!).

theorem. An exhaustive discussion of these theorems and their proofs is far beyond the scope of this section. Here, we just state them and elucidate their physical meaning and, more importantly, their consequences. The first is the so-called

Theorem B.0.1 (**Asymptotic conditions**). *For a "reasonable" potential V, $\forall|\psi_{in}\rangle \in \mathcal{H}$, there is a $|\psi\rangle$ such that*

$$U(t)|\psi\rangle - U^0(t)|\psi_{in}\rangle \to 0 \tag{B.4}$$

as $t \to -\infty$, and, likewise for $|\psi_{out}\rangle$ as $t \to +\infty$.

This theorem states that *every* state of the system can be an asymptotic state, that is to say, that, in a scattering experiment, one can choose arbitrarily the initial state. From this theorem, it follows that

$$|\psi\rangle = \lim_{t\to-\infty} U^\dagger(t)U^0(t)|\psi_{in}\rangle$$

and similarly for $|\psi_{out}\rangle$. We can then introduce two operators defined according to

$$\Omega_\pm = \lim_{t\to\mp\infty} U^\dagger(t)U^0(t)$$

that are called *Möller wave operators*. Their meaning is the following: *acting on any vector in $\mathcal{H}$, the wave operators give the actual state at $t = 0$ that would evolve from (Ω_+) (or to (Ω_-)) the asymptote represented by that vector.* In a sense, the Möller operators are *half*-collision operator, because they divide the duration of the scattering process in two (infinite) time intervals.

The second fundamental theorem expresses an *orthogonality* condition. We have mentioned that among all the states in $\mathcal{H}$, there are bound and scattering states. Let call $\mathcal{B}$ the subspace spanned by the bound states and $\mathcal{R}_+$ ($\mathcal{R}_-$) the subspace of states with an in (out) asymptote. Therefore, one can easily prove that

Theorem B.0.2 (**Orthogonality**). *Under the validity of the asymptotic condition,*

$$\mathcal{R}_+ \perp \mathcal{B} \quad \mathcal{R}_- \perp \mathcal{B} \tag{B.5}$$

Such theorem implies that the scattering states *must* lie in a space spanned by the *continuum* eigenvectors of the spectrum of $\mathcal{H}$. The last theorem that lays the foundations for the scattering theory is *completeness* condition

Theorem B.0.3 (**Asymptotic completeness**.). *The subspace $\mathcal{R}_+$ coincides with the subspace $\mathcal{R}_-$ and they are the orthogonal complements of $\mathcal{B}$. In other words, $\mathcal{H} = \mathcal{R} + \mathcal{B}$.*

The physical meaning of this theorem is that *every* orbit with an "in" asymptote has an "out" asymptote. Furthermore, the scattering and the bound orbits are *all* possible orbits of the system. From a formal point of view, such theorem states that the Möller operators have a common image and therefore one can introduce a well-defined operator that realizes a one-to-one correspondence between $|\psi_{in}\rangle$ and $|\psi_{out}\rangle$. Namely, we may write

$$|\psi_{out}\rangle = \Omega_-^\dagger|\psi\rangle = \Omega_-^\dagger\Omega_+|\psi_{in}\rangle$$

and introduce the so-called *scattering operator*, $S = \Omega_-^\dagger\Omega_+$. S is at the heart of the scattering theory and the reason can easily be understood. Let try to answer to the following question: what is the probability that a particle entering the collision with a state $|\phi\rangle$ emerges in the state $|\xi\rangle$? From the definition of the Möller operators we have that $|\phi_+\rangle = \Omega_+|\phi\rangle$ is the actual state at $t = 0$ that evolve from the in asymptote (and

similarly $|\xi_-\rangle$ is the state that would evolve into the out asymptote). Therefore, we may write

$$\begin{aligned} w(\xi \leftarrow \phi) &= |\langle \xi_- | \phi_+ \rangle|^2 \\ &= |\langle \xi | \Omega_-^\dagger \, \Omega_+ | \phi \rangle|^2 \\ &= |\langle \xi | S | \phi \rangle|^2 \end{aligned} \tag{B.6}$$

Albeit $w(\xi \leftarrow \phi)$ is not directly measurable in a scattering experiment[7], the expression (B.6) suggests that the S-matrix elements play a fundamental role in the scattering theory. We shall therefore proceed in finding an expression of the S-matrix elements on a "convenient" basis.

Since S is a mapping between free asymptotic states, it commutes with H^0, and therefore they share a common set of eigenvectors. We can choose, for instance, the momentum basis $|\boldsymbol{p}\rangle$, whose spatial wave function is the plane wave

$$\langle \boldsymbol{x} | \boldsymbol{p} \rangle = \frac{1}{\sqrt{(2\pi)^3}} e^{i \boldsymbol{p} \boldsymbol{x}}$$

with the normalization[8]

$$\langle \boldsymbol{p}' | \boldsymbol{p} \rangle = \delta_3(\boldsymbol{p}' - \boldsymbol{p})$$

and look for the matrix elements $\langle \boldsymbol{p}' | S | \boldsymbol{p} \rangle$. The result[9] is

$$\boxed{\langle \boldsymbol{p}' | S | \boldsymbol{p} \rangle = \delta_3(\boldsymbol{p}' - \boldsymbol{p}) - 2\pi i \delta(E_{p'} - E_p) t(\boldsymbol{p}' \leftarrow \boldsymbol{p})} \tag{B.7}$$

The first delta Dirac function selects equal values of the initial and final momentum, *i.e.* it is a non-scattering term that leaves the momentum unchanged. The second term describes instead a scattering process: the energy is conserved but not the individual components of the momentum. The key information is found in the term $t(\boldsymbol{p}' \leftarrow \boldsymbol{p})$, which is a smooth function that is strictly related to an observable of the scattering experiment, namely the differential cross-section, that we shall discuss shortly. It is worthy to note that this function is defined only *on-shell*, *i.e.* when $E_{p'} = E_p$[10]. Most often, one re-write the decomposition (B.7) of S as

$$\boxed{\langle \boldsymbol{p}' | S | \boldsymbol{p} \rangle = \delta_3(\boldsymbol{p}' - \boldsymbol{p}) + \frac{i}{2\pi m} \delta(E_{p'} - E_p) f(\boldsymbol{p}' \leftarrow \boldsymbol{p})} \tag{B.8}$$

[7] Because of some intrinsic limits of the experiments and the laws of quantum mechanics: one cannot produce or uniquely identify the state $\phi\rangle$ and $\xi\rangle$. One we can instead measure is the *differential cross-section* (see below).

[8] Remind that H^0 has *improper* eigenvectors, *i.e.* vectors that are not normalizable in the usual sense and therefore do not belong to the Hilbert space. However, these vectors are such that their integral on a bound interval $[\alpha, \alpha + \Delta\alpha]$, normalized as

$$x(\alpha, \Delta\alpha) = \frac{1}{\Delta\alpha} \int_\alpha^{\alpha + \Delta\alpha} x_{\alpha'} d\alpha'$$

belongs to the Hilbert space even in the limit $\Delta\alpha \to 0$.

[9] In the derivation, one decompose S in $1 + R$, where R is the difference between the scattering operator and its value in the absence of interactions (namely the identity operator)and recognize that both S and R commutes with H^0.

[10] One can extend this definition *off-shell* and define an operator T, *aka* T-matrix, whose matrix elements are $t(\boldsymbol{p}' \leftarrow \boldsymbol{p})$ when $\boldsymbol{p}'^2 = \boldsymbol{p}^2$.

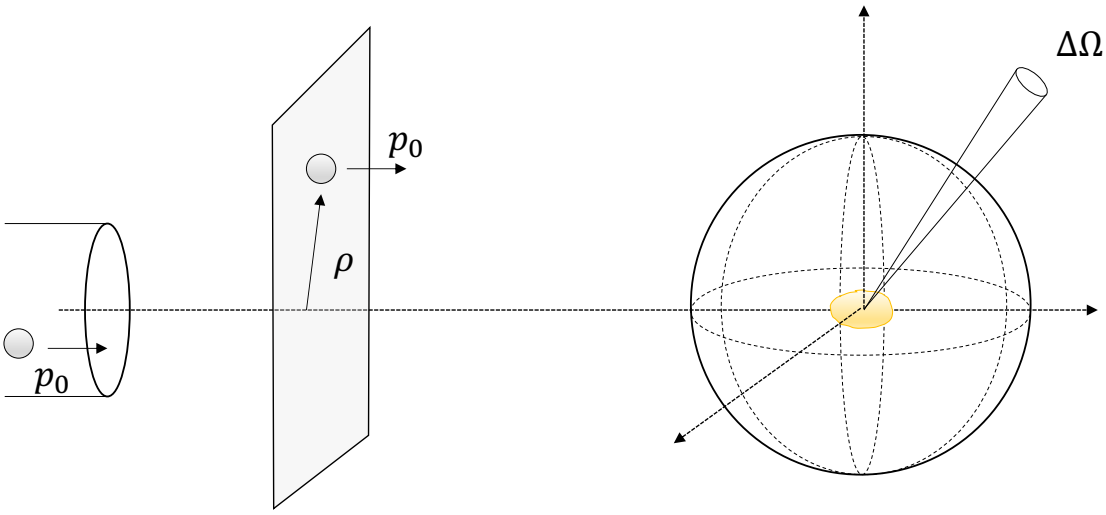

Figure B.1. A pictorial representation of an idealized scattering experiment. On the left it is represented an "ideal" beam machine; on the right a target.

where $f(\boldsymbol{p}' \leftarrow \boldsymbol{p})$ is known as *scattering amplitude* and it is related $t(\boldsymbol{p}' \leftarrow \boldsymbol{p})$ through

$$f(\boldsymbol{p}' \leftarrow \boldsymbol{p}) = -(2\pi)^2 m t(\boldsymbol{p}' \leftarrow \boldsymbol{p}) \tag{B.9}$$

B.1 Cross-sections

Let return on the analysis on a typical scattering experiment and reflect a bit more on what we can extract from such experiment.

From quantum mechanics, we know that $\langle \boldsymbol{p}|\psi_{out}\rangle$ determines the probability that long after the collision the particle is found with momentum $\boldsymbol{p}$. In the experiment, however, one cannot measure such probability, rather one measures the probability that the particles emerges in a solid angle $d\Omega$ about the direction $\hat{\boldsymbol{p}}$, where the counter is placed. That is one look at

$$w(d\Omega \leftarrow \psi_{in}) = d\Omega \int_0^\infty p^2 dp |\psi_{out}|^2$$

where we integrate over the magnitude of $\boldsymbol{p}$, because we are interested just in the direction of the emerging particle (the magnitude is fixed by the energy conservation!). As for the initial state $|\psi_{in}\rangle$, we just know that, in momentum representation, $\psi_{in}(\boldsymbol{p})$, is peaked around a value $\boldsymbol{p}_0$. By all means, an accelerator will not produce the same wave packet over and over again. Rather, we can imagine that it will produces states $|\phi_\rho\rangle$ that differ by some displacement $\boldsymbol{\rho}$, that we call *impact parameter*

$$\phi_{\boldsymbol{\rho}}(\boldsymbol{p}) = e^{-i\boldsymbol{\rho}\boldsymbol{p}}\phi(\boldsymbol{p})$$

We can assume such $\boldsymbol{\rho}$ to be randomly distributed in the plane perpendicular to $\boldsymbol{p}_0$. Therefore, if we repeat the experiment several times with random $\boldsymbol{\rho_i}$, then we can write

$$N_{sc}(d\Omega) = \int d^2\boldsymbol{\rho}\; n_{inc} w(d\Omega \leftarrow \phi_{\boldsymbol{\rho}})$$

where n_{inc} is the number of projectiles incident per unit area perpendicular to $\boldsymbol{p}_0$. Note that both n_{inc} and N_{sc} can be measured in a scattering experiment. Because $\boldsymbol{\rho}_i$ are randomly

distributed, n_{inc} is uniform, hence

$$N_{sc}(d\Omega) = n_{inc} \int d^2\boldsymbol{\rho}\; w(d\Omega \leftarrow \phi_{\boldsymbol{\rho}})$$

The integral over $\boldsymbol{\rho}$ can be interpreted in the following way: it is an *area integral* over the plane perpendicular to $\boldsymbol{p}_0$, in which each element of of area $d^2\boldsymbol{\rho}$ is weighted by the probability factor $w(d\Omega \leftarrow \phi_{\boldsymbol{\rho}})$. In view of this, such term is called *effective cross-sectional area* of the target potential for scattering of the wave packet ϕ_ρ into $d\Omega$, and it is indicated with $\sigma(d\Omega \leftarrow \phi)$. In the classical limit, the probability $w(d\Omega \leftarrow \phi_{\boldsymbol{\rho}})$ can assume the values 0 or 1, therefore the integral picks out just the actual area which scatters into $d\Omega$. If the wavefunction is sufficiently peaked about $\boldsymbol{p}_0$, the cross-section σ will be independent of any detail of $\phi(\boldsymbol{p})$, except for $\boldsymbol{p}_0$ itself. Therefore, such condition allows removing the unrealistic assumption that the accelerator produces states that differ just by a lateral displacement. We shall then write $\sigma(d\Omega \leftarrow \phi) = \sigma(d\Omega \leftarrow \boldsymbol{p}_0)$[11]. Through our discussion we have always made use of an infinitesimal angle $d\Omega$. In such limit, σ is proportional to $d\Omega$ itself and therefore we may write

$$\sigma(d\Omega \leftarrow \boldsymbol{p}_0) = \frac{d\sigma}{d\Omega}(\boldsymbol{p} \leftarrow \boldsymbol{p}_0) d\Omega$$

where $d\sigma/d\Omega$ is the so-called *differential cross-section* and represents the most detailed information obtainable from the scattering experiment.

At last, we shall find the relationship between the observable cross-section and the scattering amplitude introduced above. The derivation is, however, somewhat long[12]. Here, we limit to give the final expression, namely

$$\boxed{\frac{d\sigma}{d\Omega}(\boldsymbol{p} \leftarrow \boldsymbol{p}_0) = |f(\boldsymbol{p} \leftarrow \boldsymbol{p}_0)|^2} \tag{B.10}$$

This is a central result: it expresses *the observable differential cross-section in terms of the matrix elements of the S scattering operator*[13]. The remaining task would be to compute such matrix elements from the actual potential $V(\boldsymbol{x})$ that defines our system. We will not cover this further step here but we mention that $f(\boldsymbol{p} \leftarrow \boldsymbol{p}_0)$ can be closely related to the Fourier transform of the $V(x)$. In closing this Section, we shall discuss briefly the case of a two spinless particle scattering and the multi-channel scattering theory, which allows introducing some useful concepts for the next Section.

B.2 Scattering of two-spinless particles

The two-particle scattering problem can be reduced to that of one-particle scattering from a fixed potential if one works in the so-called *CM* representation. Let consider the two-

[11] Realistically, the accelerator will produce wave packets of different shapes and impact parameters, then we must average over both variables. However, if wave packets are well peaked around a given momentum, the average over different impact parameters will produce a result that is independent of the shape.

[12] see Section 3-e (p.49) of Taylor book (1972)[272]

[13] A crucial assumption in the derivation of such result is that the region where $\phi(\boldsymbol{p})$ is appreciable different from zero must be small, so that $f(\boldsymbol{p} \leftarrow \boldsymbol{p}_0)$ can be reasonably assumed to be constant. In other words, the momentum wave function must be sharply peaked compared to f. In principle, this requirement can always be met.

particle[14] Hamitlonian

$$H = \frac{\boldsymbol{p}_1^2}{2m_1} + \frac{\boldsymbol{p}_2^2}{2m_2} + V(\boldsymbol{x}) = H^0 + V(\boldsymbol{x}) \tag{B.11}$$

with $V(\boldsymbol{x}) = V(\boldsymbol{x}_1 - \boldsymbol{x}_2)$ a local and translational invariant potential. We can re-express Equation (B.11) in terms of the *total* and *relative* momenta, defined according to

$$\begin{aligned} \bar{\boldsymbol{P}} &= \boldsymbol{p}_1 + \boldsymbol{p}_2 \\ \boldsymbol{P} &= \frac{m_2\boldsymbol{p}_1 - m_1\boldsymbol{p}_2}{m_1 + m_2} \end{aligned}$$

The Hamiltonian in the CM frame then reads as

$$H = \frac{\bar{\boldsymbol{P}}^2}{2M} + \left[\frac{\boldsymbol{P}^2}{2m} + V(\boldsymbol{x})\right] = H_{\text{CM}} + H_{\text{rel}} \tag{B.12}$$

where $M = m_1 + m_2$ and $m = (m_1 m_2)/(m_1 + m_2)$. Since H_{CM} and H_{rel} depends on independent variables, $\bar{\boldsymbol{P}}$ and $\boldsymbol{P}$ respectively, they commute. Therefore, for the time-evolution operator of the system we have

$$\begin{aligned} U(t) &= e^{-iHt} = e^{-i(H_{\text{CM}} + H_{\text{rel}})t} \\ &= e^{-iH_{\text{CM}}t} \otimes e^{-iH_{\text{rel}}t} \end{aligned} \tag{B.13}$$

where $\otimes$ denotes the *tensor product*[15]. From Equation (B.13) establishes that the center-of-mass and relative motions are independent. Furthermore, the CM evolves like a free-particle while the relative motion evolves like a single-particle in a fixed potential[16]. Inheriting the theory established for the single-particle problem, we can then expect the *two-particle Möller operators* taking the form[17]

$$\boldsymbol{\Omega}_\pm = 1_{\text{CM}} \otimes \Omega_\pm$$

where 1_{CM} is an identify operator acting on $\mathcal{H}_{\text{CM}}$ that accounts for the fact that the CM follows a free motion, while $\Omega_\pm$ are standard Möller operator acting on $\mathcal{H}_{\text{rel}}$. By the same token, the scattering operator reads as

$$\boxed{\boldsymbol{S} = \boldsymbol{\Omega}_-^\dagger \boldsymbol{\Omega}_+ = 1_{\text{CM}} \otimes S} \tag{B.14}$$

Note that $[\boldsymbol{S}, \bar{\boldsymbol{P}}] = 0$, hence the *total* momentum is conserved.

The remaining task would be computing the differential cross-section. For the problem at hand, the differential cross-section can be defined in various *frames of reference*. In most

[14] We consider here the case of two *distict* particles.

[15] Remind that we are now dealing with a two-particle Hilbert space. If $\mathcal{H}_1$ and $\mathcal{H}_2$ are the Hilbert spaces of particle 1 and 2 respectively, than the full Hilbert space is $\mathcal{H} = \mathcal{H}_1 \otimes \mathcal{H}_2$. It is possible to show that, if $|\phi\rangle_1$ ($|\eta\rangle_2$) is an orthonormal basis of $\mathcal{H}_1$ ($\mathcal{H}_2$), then $|\phi\rangle_1 \otimes |\eta\rangle_2$ is an orthonormal basis of $\mathcal{H}$. Hence, any $|\psi\rangle \in \mathcal{H}$ can be written as a linear combination of product states $|\phi\rangle \otimes |\eta\rangle$ or, in other words, product states span the entire two-particle Hilbert space. Linear operators can be extended on tensor product spaces upon defining their action on product states, namely $(A \otimes B)(|\phi\rangle \otimes |\eta\rangle = A|\phi\rangle \otimes B|\eta\rangle$.

[16] Note that in the original factorization of $\mathcal{H} = \mathcal{H}_1 \otimes \mathcal{H}_2$, one can write

$$U^0(t) = \exp\left(-i\frac{\boldsymbol{p}_1^2}{2m_1}\right) \otimes \exp\left(-i\frac{\boldsymbol{p}_2^2}{2m_2}\right)$$

for the *free* time-evolution operator but not for the $U(t)$.

[17] This is not a rigorous way of introducing the two-particle Möller operators. We should prove again the asymptotic condition and completeness, but this is not relevant for the present discussion.

experiments one works in the so-called *laboratory frame* defined by the condition that the target is at rest, as it is usually the case. In theoretical calculations, however, it most convenient to adopt the so-called *CM frame*, defined by the condition that the CM is at rest, *i.e.* $\langle \bar{\boldsymbol{P}} \rangle \equiv 0$. In such frame of reference[18], it is possible to show that the differential cross-section reads as

$$\boxed{\frac{d\sigma}{d\Omega}(\boldsymbol{p} \leftarrow \boldsymbol{p}_0) = |f(\boldsymbol{p} \leftarrow \boldsymbol{p}_0)|^2} \tag{B.15}$$

which matches Equation (B.1) of the one-particle scattering problem with the novelty that now $\boldsymbol{p}_0$ and $\boldsymbol{p}$ are the initial and final momenta of the projectile *measured in the CM frame*.

B.3 Extension to multi-channel scattering

To conclude this overview on the scattering theory, we briefly discuss the case of a *multi-channel* collision process. The term is used to refer to (more realistic) situations in which the colliding partners do have an *internal structure*, which can change as a consequence of the collision. *Any* molecular collision describing a chemical reaction is of this kind and therefore there is an obvious need of extending the theory described in the previous Sections to such processes. Beside the increase of the dimensionality of the problem, the first striking difference w.r.t. the single-channel case is that we can no longer identify a *unique* scattering coordinate that brings the system in the asymptotic situation when $t \to \pm\infty$. Indeed, we do not have a single asymptotic situation any more, because now molecules can rearrange themselves. For instance, let consider the scattering between an atom T adsorbed on a surface S and a projectile P, like the one we are interested in. Several outcomes of the collision are possible

$$P + TS \longrightarrow \begin{array}{l} PT + S \\ PS + T \\ P + T + S \\ PS + TS \end{array}$$

Each of these asymptotic situations defines a so-called *arrangement*, which corresponds to a particular asymptotic Hamiltonian H^a

$$H^a = K^a + h^a$$

where K^a is the kinetic energy of the scattering motion in the given arrangement and h^a is the *internal* Hamiltonian of the arrangement. The latter is given by the sum of the molecular Hamiltonians of each fragment.

The internal Hamiltonian h^a has one or more bound states. Each of these bound states defines the so-called *channel* in the given arrangement. For instance, the $PT + S$ arrangement of the aforementioned reaction, the rovibrational quantum numbers (ν, j) of the product molecule PT define the channel of the arrangement. In a given (ν, j) channel, the molecule PT moves freely. In the total Hilbert space $\mathcal{H}$, one can then identify *channel subspaces* $\mathcal{H}^{(\alpha,a)} \subset \mathcal{H}$ that are spanned by vectors of the form

$$|\psi^{(\alpha,a)}\rangle = |\xi\rangle|\phi_\alpha\rangle$$

where $|\xi\rangle$ is a vector describing the translational motion in the given arrangement a, while $|\phi^\alpha\rangle$ is the α-th bound state vector of the internal Hamiltonian h^a. At a given total en-

[18] An typical "in" state of a collision process in the CM frame is of the type $\phi_1(\boldsymbol{p}_1)\phi_2(\boldsymbol{p}_2)$, where ϕ_1 describes the state of a projectile emerging from an accelerator or a collimator, while ϕ_2 is a target state. Both need to be well-peaked in momentum space, namely ϕ_1 about $\boldsymbol{p}_0$ and ϕ_2 about $-\boldsymbol{p}_0$ ($\bar{\boldsymbol{P}} = \boldsymbol{p}_1 + \boldsymbol{p}_2 = 0$).

ergy, only some channel spaces will be available as asymptotic spaces, while other will be forbidden. The former are therefore termed as *open channels*, while the latter as *closed channels*[19]. Once this basic structure of the multi-channel theory is established, one can prove that theorems such as the asymptotic condition and asymptotic completeness still hold, bearing in mind that now we have *channel evolution operators* ($U^{\alpha}(t)$, *channel components* of the "in" and "out" scattering asymptotes and *channel Möller operators*

$$\Omega_{\pm}^{\alpha} = \lim_{t \to \mp\infty} U_t^{\dagger} U_t^{\alpha}$$

The latter allow to introduce *a set of scattering operators*

$$S_{\beta\alpha} = (\Omega_{-}^{\beta})^{\dagger} \Omega_{+}^{\alpha}$$

which establish the connection between "in" and "out" asymptotic channel components

$$|\psi_{out}^{\beta}\rangle = S_{\beta\alpha} |\psi_{in}^{\alpha}\rangle$$

We do not go further inside into the details of the multi-channel theory. The interested reader is again referred to the excellent book[20] of Taylor (1972)[272] if (s)he wishes to deepen (her) his knowledge on this fascinating and rigorous approach to collision processes involved in chemical reactions.

[19] Different channels spaces in the same arrangement are orthogonal with each other.

[20] see in particular Chapters 16-18.

Bibliography

[1] P. R. Wallace. The Band Theory of Graphite. *Phys. Rev.*, 71:622–634, 1947.

[2] N. D. Mermin. Crystalline Order in Two Dimensions. *Phys. Rev.*, 176:250, 1968.

[3] K. S. Novoselov and K. Geim and S. V. Morozov and J. Zhang and S. V. Dubunos and I. V. Grigorieva and A. A. Firsov. Electric Field Effect in Atomically Thin Carbon Films. *Science*, 306:666–669, 2004.

[4] T. Mueller and F. Xia and P. Avouris. Graphene photodetectors for high-speed optical communications. *Nature Photonics*, 4:297–301, 2010.

[5] I. A. Kinloch and J. Suhr and J. Lou and R. J. Young and P. M. Ajayan. Composites with carbon nanotubes and graphene: An outlook. *Science*, 362:547–553, 2018.

[6] K. S. Kim and Y. Zhao and H. Jang and S. Y. Lee and J. M. Kim and K. S. Kim and J.-H. Ahn and P. Kim and J.-Y. Choi and B. H. Hong. Large-scale pattern growth of graphene films for stretchable transparent electrodes. *Nature*, 457:706–710, 2009.

[7] T. Kuila and S. Bose and A. K. Mishra and P. Khanra N. H.Kim and J. H. Lee. Chemical functionalization of graphene and its applications. *Progress in Materials Science*, 57:1061–1105, 2012.

[8] R. Martinazzo and S. Casolo and G.F. Tantardini. The effect of atomic,Äìscale defects and dopants on graphene electronic structure. *Physics and applications of Graphene*, 00, 2011.

[9] S. Casolo and R. Martinazzo and G.F. Tantardini. Band Engineering in Graphene with Superlattices of Substitutional Defects. *J. Phys. Chem. C*, 115:3250, 2011.

[10] R. Martinazzo and S. Casolo and G. F. Tantardini. Symmetry,Äìinduced band,Äìgap opening in graphene superlattices. *Phys. Rev. B*, 81:245420, 2010.

[11] S. Casolo and G. F. Tantardini and R. Martinazzo. Insights into H_2 formation in space from ab initio molecular dynamics. *PNAS*, 110:6674–6677, 2013.

[12] G. Vidali. H_2 Formation on Interstellar Grains. *Chem. Rev.*, 113:8762–8782, 2013.

[13] V. Tozzini and V. Pellegrini. Prospects for hydrogen storage in graphene. *Phys. Chem. Chem. Phys.*, 15:80–89, 2013.

[14] A. Davydova and E. Despiau-Pujo and G. Cunge and D. B. Graves. H^+ ion-induced damage and etching of multilayer graphene in H_2 plasmas. *J. Appl. Phys.*, 121:133301, 2017.

[15] R. E. Peierls. . *Helv. Phys. Acta*, 7:819, 1934.

[16] L. D. Landau. On the theory of phase transitions. *Phys. Z. Sowjet*, 11:26, 1937.

[17] M. Sunjić and Z. Lenac. Finite-Size Effects in Wigner Crystallization of Electrons on Liquid-Helium Layers. *EPL*, 11:431, 1990.

[18] A. H. Castro Neto and F. Guinea and N. M. R. Peres and K. S. Novoselov and A. K. Geim. The electronic properties of graphene. *Rev. Mod. Phys.*, 81:109, 2009.

[19] M. J. Allen and V. C. Tung and R. B. Kaner. Honeycomb Carbon: A Review of Graphene. *Chem. Rev.*, 110:132–145, 2009.

[20] R. R. Nair P. Blake and A. N. Grigorenko and K. S. Novoselov and J. Booth and Staubern and M. R. Peres and A. K. Geim. Fine Structure Constant Defines Visual Transparency of Graphene. *Science*, 320:1308, 2008.

[21] C. Lee and X. Wei and J. W. Kysar and J. Hone. Measurement of the Elastic Properties and Intrinsic Strength of Monolayer Graphene. *Science*, 321:385–388, 2008.

[22] D. C. Elias and R. R. Nair and T. M. G. Mohiuddin and S. V. Morozoz and P. Blake and M. P. Halsall and A. C. Ferrari and D. W. Boukhvalov and M. I. Katsnelson and A. K. Geim and K. S. Novoselov. Control of graphene's properties by reversible hydrogenation: evidence for graphane. *Science*, 323:589–590, 2009.

[23] S. Stankovich and D. A. Dikin and G. H. B. Dommett and K. M. Kohlhaas and E. J. Zimney and E. A. Stach and R. D. Piner and S. T. Nguyen and R. S. Ruoff. Graphene-based composite materials. *Nature*, 442:282–286, 2006.

[24] A. Reina and X. Jia and J. Ho and D. Nezich and H. Son and V. Bulovic and M. S. Dresselhaus and J. Kong. Large Area, Few-Layer Graphene Films on Arbitrary Substrates by Chemical Vapor Deposition. *Nano Lett.*, 9:30–35, 2009.

[25] C. Riedl, C. Coletti, and U.Starke. Structural and electronic properties of epitaxial graphene on SiC(0001): A review of growth, characterization, transfer doping and hydrogen intercalation. *J. Phys. D*, 37:374009, 2010.

[26] X. Yang and X. Dou and A. Rouhanipour and L. Zhi and H. J. Räder and K. Müllen. Two-Dimensional Graphene Nanoribbons. *J. Am. Chem. Soc.*, 130:4216–4217, 2008.

[27] M. Katsnelson. *Graphene: Carbon in Two Dimensions.* Cambridge University Press, 2012.

[28] J. M. Soler, E. Artacho, J. D. Gale, A. Garcia, J. Junquera, P.Ordejon, and D. Sanchez-Portal. The siesta method for ab initio order-n materials simulation. *J. Phys. Condens. Matt.*, 14:2745–2779, 2002.

[29] J. P. Hobson and W. A. Nierenberg. The Statistics of a Two-Dimensional, Hexagonal Net. *Phys. Rev.*, 89:662, 1953.

[30] M. Bonfanti and S. Achilli and R. Martinazzo. Sticking of atomic hydrogen on graphene. *J. Phys.: Condens. Matt.*, 30:283002, 2018.

[31] L. Jeloaica and V. Sidis. DFT investigation of the adsorption of atomic hydrogen on a cluster-model graphite surface. *Chem. Phys. Lett.*, 300:157–162, 1999.

[32] D. Neumann and G. Meister and U. Kürpick and A. Goldmann and J. Roth and V. Dose. Interaction of atomic hydrogen with the graphite single-crystal surface. *Appl. Phys. A*, 55:489–492, 1992.

[33] S. Casolo, G. F. Tantardini and R. Martinazzo. Hydrogen Recombination and Dimer Formation on Graphite from Ab Initio Molecular Dynamics Simulations. *J. Phys. Chem. A*, 120:5032, 2016.

[34] M. Bonfanti and B. Jackson and K.H. Hughes and I. Burghardt and R. Martinazzo. Quantum dynamics of hydrogen atoms on graphene: II Sticking. *J. Chem. Phys.*, 143:124704, 2015.

[35] E. Ghio and L. Mattera and C. Salvo and F. Tommasini and U. Valbusa. Vibrational spectrum of H and D on the (0001) graphite surface from scattering experiments. *J. Chem. Phys.*, 73:556, 1980.

[36] M. Bonfanti and R. Martinazzo and G. F. Tantardini, and A. Ponti. Physisorption and Diffusion of Hydrogen Atoms on Graphite from Correlated Calculations on the H,àíCoronene Model System. *J. Phys. Chem. C*, 111:5825–5829, 2007.

[37] I. Meyer. The ‚Äúchemical Hamiltonian approach‚Äù and the scf method. *J. Mol. Struct.:THEOCHEM*, 165:255–272, 1988.

[38] P. Salvador and B. Paizs and M. Duran and S. Suhai. On the effect of the BSSE on intermolecular potential energy surfaces. Comparison of a priori and a posteriori BSSE correction schemes. *J. Comp. Chem.* , 22:765–786, 2001.

[39] L. Hornekaer and E. Rauls and W. Xu and Z. Sljivancanin and R. Otero and I. Stensgaard and E. Laegsgaard and B. Hammer and F. Besenbacher. Clustering of Chemisorbed H(D) Atoms on the Graphite (0001) Surface due to Preferential Sticking. *Phys. Rev. Lett.*, 97:186102, 2006.

[40] S. Casolo and O. M. Løvvik and R. Martinazzo and G. F. Tantardini. Understanding adsorption of hydrogen atoms on graphene. *J. Chem. Phys.*, 130:054704, 2009.

[41] X. Sha and B. Jackson. Quantum studies of H atom trapping on a graphite surface. *J. Chem. Phys.*, 122:014709, 2005.

[42] J. Kerwin and B. Jackson. The sticking of H and D atoms on a graphite (0001) surface: The effects of coverage and energy dissipation. *J. Chem. Phys.*, 128:084702, 2008.

[43] A. O. Caldeira and A. J. Leggett. Influence of Dissipation on Quantum Tunneling in Macroscopic Systems. *Phys. Rev. Lett.*, 46:211, 1981.

[44] H. D. Meyer and F. Gatti and G. A. Worth. *Multidimensional Quantum Dynamics: MCTDH Theory and Applications.* (Weinheim: Wiley), 2009.

[45] H. Wang and M. Toss. Multilayer formulation of the multiconfiguration time-dependent Hartree theory. *J. Chem. Phys.*, 119:1289, 2003.

[46] M. Bonfanti and B. Jackson and K.H. Hughes and I. Burghardt and R. Martinazzo. Quantum dynamics of hydrogen atoms on graphene: I System-bath modeling. *J. Phys. Chem.*, 143:124703, 2015.

[47] E. H. Lieb. Two theorems on the Hubbard model. *Phys. Rev. Lett.*, 62:1201, 1989.

[48] S. Morisset and F. Aguillon and M. Sizun and V. Sidis. Quantum dynamics of H_2 formation on a graphite surface through the Langmuir Hinshelwood mechanism. *J. Phys. Chem.* , 121:6493–6501, 2004.

[49] S. Morisset and F. Aguillona and M. Sizun and V. Sidis. Wave-packet study of H_2 formation on a graphite surface through the Langmuir,ÄìHinshelwood mechanism. *J. Chem. Phys.*, 122:194702, 2005.

[50] E. Aréou and G. Cartry and J.-M. Layet and T. Angot. Hydrogen-graphite interaction: Experimental evidences of an adsorption barrier. *J. Chem. Phys.*, 134:014701, 2011.

[51] L. Hornekaer and Z. Sljivancanin and W. Xu and R. Otero and E. Rauls and I. Stensgaard and E. Laegsgaard and B. Hammer and F. Besenbacher. Metastable Structures and Recombination Pathways for Atomic Hydrogen on the Graphite (0001) Surface. *Phys. Rev. Lett.*, 96:156104, 2006.

[52] M. Bonfanti and S. Casolo and A. Ponti and G. Tantardini and R. Martinazzo R. A few simple rules governing hydrogenation of graphene dots. *J. Chem. Phys.*, 135:164701, 2011.

[53] A. G. G. M. Tielens. The molecular universe. *Rev. Mod. Phys.*, 85:1021, 2013.

[54] E. L. O. Bakes and A. G. G. M. Tielens. The Photoelectric Heating Mechanism for Very Small Graphitic Grains and Polycyclic Aromatic Hydrocarbons. *ApJ*, 427:822, 1994.

[55] E. L. O. Bakes and A. G. G. M. Tielens. The Effects of Polycyclic Aromatic Hydrocarbons on the Chemistry of Photodissociation Regions. *ApJ*, 499:258, 1998.

[56] S. Yamamoto. *Introduction to Astrochemistry: Chemical Evolution from Interstellar Clouds to Star and Planet Formation.* Wiley, 2014.

[57] W. Duley and D.A. Williams. *Interstellar Chemistry.* London: Academic Press, 1984.

[58] G. Hinshaw and D. Larson and E. Komatsu and D. N. Spergel and C. L. Bennett and J. Dunkley and M. R. Nolta and M. Halpern and R. S. Hill and N. Odegard and L. Page and K. M. Smith and J. L. Weiland and B. Gold and N. Jarosik and A. Kogut and M. Limon and S. S.Meyer and G. S. Tucker and E. Wollack. Nine-year Wilkinson Microwave Anisotropy Probe (WMAP) Observations: Cosmological Parameter Results. *AjP Suppl.*, 208:19, 2013.

[59] T. W. Hartquist and D.A. Williams. *The Chemically Controlled Cosmos* . Cambridge University Press., 1995.

[60] A. G. G. M. Tielens and D. Hollenbach. Photodissociation regions. I. Basic model. *ApJ*, 291:747, 1985.

[61] A. G. G. M. Tielens and D. Hollenbach. Photodissociation regions. II. A model for the Orion photodissociation region. *ApJ*, 291:722, 1985.

[62] S. S. Prasad and S. P. Tarafdar. UV radiation field inside dense clouds - Its possible existence and chemical implications. *ApJ*, 267:603, 1983.

[63] R. J. Gould and E. E. Salpeter. The Interstellar Abundance of the Hydrogen Molecule. I. Basic Processes. *ApJ*, 138:393, 1963.

[64] D. Hollenbach and E. E. Salpeter. Surface Recombination of Hydrogen Molecules. *ApJ*, 163:155, 1971.

[65] N. Katz and I. Furman and O. Biham and V. Pirronello and G. Vidali. Molecular Hydrogen Formation on Astrophysically Relevant Surfaces. *ApJ*, 522:305, 1999.

[66] L. Hornekaer and A. Baurichter and V. V. Petrunin and D. Field and A. C. Luntz. Importance of Surface Morphology in Interstellar H_2 Formation. *Science*, 302:1943–1946, 2003.

[67] S. Cazaux and A. G. G. M. Tielens. H_2 formation on grain surfaces. *ApJ*, 604:222, 2004.

[68] E. Rauls and L. Hornekaer. Catalyzed routes to molecular hydrogen formation and hydrogen addition reactions on neutral polycyclic aromatica hydrocarbons under interstellar conditions. *ApJ*, 679:531–536, 2008.

[69] A. Leger and J. L.Puget. Identification of the "unidentified" IR emission features of interstellar dust ? *A&A*, 500:279–282, 1984.

[70] E. Peeters and A. L. Mattioda and D. M. Hudgins and L. J. Allamandola. Polycyclic Aromatic Hydrocarbon Emission in the 15-21 Micron Region. *A&A*, 617:65, 2004.

[71] A. G. G. M. Tielens. Interstellar Polycyclic Aromatic Hydrocarbon Molecules. *ARA A&A*, 46:289–337, 2008.

[72] W. W. Duley. Polycyclic aromatic hydrocarbons, carbon nanoparticles and the diffuse interstellar bands. *Faraday Discuss.*, 133:415, 2006.

[73] L. J. Allamandola and A. G. G. M. Tielens and J. R. Barker. Interstellar Polycyclic Aromatic Hydrocarbons: The Infrared Emission Bands, the Excitation/Emission Mechanism, and the Astrophysical Implications. *ApJS*, 71:733, 1989.

[74] M. P. Bernstein and S. A. Sandford and L. J. Allamandola. The Mid-Infrared Absorption Spectra of Neutral Polycyclic Aromatic Hydrocarbons in Conditions Relevant to Dense Interstellar Clouds. *ApJS*, 161:53, 2005.

[75] M. P. Bernstein and S. A. Sandford and L. J. Allamandola and J. S. Gillette and S. J. Clemett and R. N. Zare. UV irradiation of polycyclic aromatic hydrocarbons in ices: production of alcohols, quinones, and ethers. *Science*, 283:1135–1138, 1999.

[76] J. E. Elsila and M. R. Hammond and M. P. Bernstein and S. A. Sandford and R. N. Zare. UV photolysis of quinoline in interstellar ice analogs. *Meteorit. Planet. Sci.*, 41:785, 2006.

[77] V. Wakelam and E. Herbst. Polycyclic Aromatic Hydrocarbons in Dense Cloud Chemistry. *ApJ*, 680:371, 2008.

[78] E. Habart and F. Boulanger and L. Verstraete and G. Pineau des Forets and E. Falgarone and A. Abergel. H_2 infrared line emission across the bright side of the ρ Ophiuchi main cloud. *A&A*, 397:623–634, 2003.

[79] V. Le Page and T. P. Snow and V. M. Bierbaum. Molecular Hydrogen Formation catalyzed by polycyclic aromatic hydrocarbons in the interstellar medium. *ApJ*, 704:274, 2009.

[80] B. Klaerke and Y. Toker and D. B. Rahbek and L. Hornekaer and L. H. Andersen. Formation and stability of hydrogenated PAHs in the gas phase. *A&A*, 549:84, 2013.

[81] S. Cazaux and L. Boschman and N. Rougeau and G. Reitsma and R. Hoekstra and D. Teillet-Billy and S. Morisset and M. Spaans and T. Schlathölter. The sequence to hydrogenate coronene cations: A journey guided by magic numbers. *Scientific Reports*, 6:19835, 2016.

[82] G. Reitsma and L. Boschman and M. J. Deuzeman and O. Gonzalez-Magana and S. Hoekstra and S. Cazaux and R. Hoekstra and T. Schlathölter. Deexcitation dynamics of superhydrogenated polycyclic aromatic hydrocarbon cations after soft-x-ray absorption. *Phys. Rev. Lett.*, 1:113, 2014.

[83] M. Gatchell and M. H. Stockett and N. de Ruette and T. Chen and L. Giacomozzi and R. F. Nascimento and M. Wolf and E. K. Anderson and R. Delaunay and V. Vizcaino and P. Rousseau and L. Adoui and B. A. Huber and H. T. Schmidt and H. Zettergren and H. Cederquist. Failure of hydrogenation in protecting polycyclic aromatic hydrocarbons from fragmentation. *Phys. Rev. A*, 92:050702, 2015.

[84] M. Wolf and H. V. Kiefer and J. Langeland and L. H. Andersen H. Zettergren H. T. Schmidt and H. Cederquist M. H. Stockett. Photostability of superhydrogenated PAHs determined by action spectroscopy experiments. *ApJ*, 832:24, 2016.

[85] J. D. Thrower and B. Jørgensen and E. E. Friis and S. Baouche and V. Mennella and A. C. Luntz and M. Andersen and B. Hammer and L. Hornekaer. Experimental evidence for the formation of highly superhydrogenated polycyclic aromatic hydrocarbons through H atom addition and their catalytic role in H_2 formation. *ApJ*, 752:3, 2012.

[86] J. D. Thrower and E. E. Friis and A. L. Skov and B. Jørgensena and L. Hornekaer. Hydrogenation of PAH molecules through interaction with hydrogenated carbonaceous grains. *Phys. Chem. Chem. Phys.*, 16:3381–3387, 2014.

[87] A. L. Skov and J. D. Thrower and L. Hornekaer. Polycyclic aromatic hydrocarbons ,Äì catalysts for molecular hydrogen formation. *Faraday Discuss.*, 168:223–234, 2014.

[88] M. P. Bernstein and S. A. Sandford and L. J. Allamandola. Hydrogenated Polycyclic Aromatic Hydrocarbons and the 2940 and 2850 Wavenumber (3.40 and 3.51 micron) Infrared Emission Features. *ApJ*, 472:L127, 1996.

[89] P. Pilleri and C. Joblin and F. Boulanger and T. Onaka. Mixed aliphatic and aromatic composition of evaporating very small grains in NGC 7023 revealed by the 3.4/3.3 μm ratio. *A&A*, 577:A16, 2015.

[90] G. C. Sloan and M. Jura and W. W. Duley and K. E. Kraemer and J. Bernard-Salas and W. J. Forrest and B. Sargent and A. Li and D. J. Barry and C. J. Bohac. The Unusual Hydrocarbon Emission from the Early Carbon Star HD 100764: The Connection between Aromatics and Aliphatics. *ApJ*, 664:1144, 2007.

[91] M. Goto and S. Kwok and H. Takami and M. Hayashi and W. Gaessler and Y. Hayano and M. Iye and Y. Kamata and T. Kanzawa and N. Kobayashi. Diffraction-Limited 3 μm Spectroscopy of IRAS 04296+3429 and IRAS 05341+0852: Spatial Extent of Hydrocarbon Dust Emission and Dust Evolutionary Sequence. *ApJ*, 662:389, 2007.

[92] P. A. Jensen and M. Leccese and F. D. S. Simonsen and A. W. Skov and M. Bonfanti and J. D. Thrower and R. Martinazzo and L. Hornekaer. Identification of Stable Configurations in the Superhydrogenation Sequence of Polycyclic Aromatic Hydrocarbon Molecules. *MNRAS*, 000:1–7, 2019.

[93] Y. Zhao and G. Truhlar. The M06 suite of density functionals for main group thermochemistry, thermochemical kinetics, noncovalent interactions, excited states, and transition elements: two new functionals and systematic testing of four M06-class functionals and 12 other functionals. *Theor. Chem. Acc.*, 120:215, 2008.

[94] Y. Wang, H. Qian, K. Morokuma, and S. Irle. Coupled Cluster and Density Functional Theory Calculations of Atomic Hydrogen Chemisorption on Pyrene and Coronene as Model Systems for Graphene Hydrogenation. *J. Phys. Chem. A*, 116:7154–7160, 2012.

[95] Y Zhao and D.G. Truhlar. Density Functional for Spectroscopy:,Äâ No Long-Range Self-Interaction Error, Good Performance for Rydberg and Charge-Transfer States, and Better Performance on Average than B3LYP for Ground States. *J. Phys. Chem. A*, 110:13126–13130, 2006.

[96] R. Peverati and D. G. Truhlar. Improving the accuracy of hybrid meta-gga density functionals by range separation. *Phys. Chem Lett.*, 2:2810–2817, 2011.

[97] Y. Zhao and D. G. Thrular. The m06 suite of density functionals for main group thermochemistry, thermochemical kinetics, noncovalent interactions, excited states, and transition elements: Two new functionals and systematic testing of four m06 functionals and twelve other functionals,. *Theor. Chem. Account*, 120:215–241, 2007.

[98] J. Tirado-Rives and W. L. Jorgensen. Performance of B3LYP Density Functional Methods for a Large Set of Organic Molecules. *J. Chem. Theory Comput.*, 4:297–306, 2008.

[99] Y. Zhao and D. G. Thrular. Hybrid Meta Density Functional Theory Methods for Thermochemistry, Thermochemical Kinetics, and Noncovalent Interactions:,Äâ The MPW1B95 and MPWB1K Models and Comparative Assessments for Hydrogen Bonding and van der Waals Interactions. *J. Phys. Chem. A* , 108:6908–6918, 2004.

[100] Y. Zhao and D. G. Truhlar. A density functional that accounts for medium-range correlation energies in organic chemistry. *Org. Lett.*, 8:5753–5755, 2006.

[101] A. Karton. How reliable is dft in predicting relative energies of polycyclic aromatic hydrocarbon isomers? comparison of functionals from different rungs of jacob,Äôs ladder. *J. Comp. Chem.*, 37:49, 2016.

[102] T. Takatani, E. G. Hohenstein, M. Malagoli, M. S. Marshall, and C. D. Sherril. Basis set consistent revision of the s22 test set of noncovalent interaction energies. *J. Chem. Phys.*, 8, 2010.

[103] M. J. Frisch, G. W. Trucks, H. B. Schlegel, G. E. Scuseria, M. A. Robb, J. R. Cheeseman, G. Scalmani, V. Barone, G. A. Petersson, H. Nakatsuji, X. Li, M. Caricato, A. V. Marenich, J. Bloino, B. G. Janesko, R. Gomperts, B. Mennucci, H. P. Hratchian, J. V. Ortiz, A. F. Izmaylov, J. L. Sonnenberg, D. Williams-Young, F. Ding, F. Lipparini, F. Egidi, J. Goings, B. Peng, A. Petrone, T. Henderson, D. Ranasinghe, V. G. Zakrzewski, J. Gao, N. Rega, G. Zheng, W. Liang, M. Hada, M. Ehara, K. Toyota, R. Fukuda, J. Hasegawa, M. Ishida, T. Nakajima, Y. Honda, O. Kitao, H. Nakai, T. Vreven, K. Throssell, J. A. Montgomery, Jr., J. E. Peralta, F. Ogliaro, M. J. Bearpark, J. J. Heyd, E. N. Brothers, K. N. Kudin, V. N. Staroverov, T. A. Keith, R. Kobayashi, J. Normand, K. Raghavachari, A. P. Rendell, J. C. Burant, S. S. Iyengar, J. Tomasi, M. Cossi, J. M. Millam, M. Klene, C. Adamo, R. Cammi, J. W. Ochterski, R. L. Martin, K. Morokuma, O. Farkas, J. B. Foresman, and D. J. Fox. Gaussian16 Revision C.01, 2016.

[104] M. Kayanuma, U. Nagashima, H. Nushihara, T. Kyotani, and H. Ogawa. Adsorption and diffusion of atomic hydrogen on a curved surface of microporous carbon: A theoretical study. *Chem. Phys. Lett.*, 495:251–255, 2010.

[105] M. Bonfanti and R. Martinazzo. Comment on "theoretical study of the dynamics of atomic hydrogen adsorbed ongraphene multilayers". *Phys. Rev. B*, 97:117401, 2018.

[106] M. Moaied and J. V. Alvarez and J. J. Palacios. Hydrogenation-induced ferromagnetism on graphite surfaces. *Phys. Rev. B*, 90:11, 2014.

[107] M. Moaied and J. A. Moreno and M. J. Caturla and F. Ynduráin and J. J. Palacios. Theoretical study of the dynamics of atomic hydrogen adsorbed on graphene multilayers. *Phys. Rev. B*, 91:155419, 2015.

[108] I. Brihuega and F. Yndurain. Selective Hydrogen Adsorption in Graphene Rotated Bilayers. *J. Phys. Chem. B*, 122:595,Äì600, 2018.

[109] Y. Ferro and F. Marinelli and A. Allouche. Density functional theory investigation of H adsorption on the basal plane of boron-doped graphite. *J. Chem. Phys.*, 118:5650, 2003.

[110] E. Hückel. Zur quantentheorie der doppelbindung. *Physik*, 7:423–456, 1930.

[111] S. Ijima. Helical microtubules of graphitic carbon. *Nature*, 354:56–58, 1991.

[112] S. Ijima and T. Ichihashi. Single-shell carbon nanotubes of 1-nm diameter. *Nature*, 363:603–605, 1993.

[113] E. Thostenson and Z. Ren and Tsu-WeiChou. Advances in the science and technology of carbon nanotubes and their composites: a review. *Composites Science and Technology*, 61:1899–1912, 2001.

[114] Y. Miyake and H. Shinokubo. Hetero[8]circulenes: synthetic progress and intrinsic properties. *Chem. Commun.*, 56:15605–15614, 2020.

[115] A. M. Butterfield and B. Gilomen, and J. S. Siegel. Kilogram-Scale Production of Corannulene. *Org. Process Res. Dev.*, 16:664–676, 2012.

[116] E. Nestoros and M. C. Stuparu. Corannulene: a molecular bowl of carbon with multifaceted properties and diverse applications. *Chem. Commun.*, 54:6503–6519, 2018.

[117] Y. Shen and C. Chen. Helicenes: Synthesis and Applications. *Chem. Rev.*, 112:1463–1535, 2012.

[118] H. W. Kroto and J. R. Heath and S. C. O'Brien and R. F. Curl and R. E. Smalley . C_{60}: Buckminsterfullerene. *Nature*, 318:162–163, 1985.

[119] H. W. Kroto and A. W. Allaf and S. P. Balm. C_{60}: Buckminsterfullerene. *Chem. Rev.*, 91:1213–1235, 1991.

[120] H. Kroto. Symmetry, space, stars and C_{60}. *Rev. Mod. Phys.*, 69:703, 1997.

[121] J.C. Meyer and A.K. Geim and M.I. Katsnelsond and K.S. Novoselov and D. Obergfelle and S. Rothe and C. Girita and A. Zettl. On the roughness of single- and bi-layer graphene membranes. *Solid State Commun.*, 143:101–109, 2007.

[122] A. Fasolino and J.H. Los and M. I. Katnelson. Intrinsic ripples in graphene. *Nature Materials*, 6:858–861, 2007.

[123] S. Park and D.Srivastava and K. Cho. Generalized Chemical Reactivity of Curved Surfaces: Carbon Nanotubes. *Nano Lett.*, 3:1273–1277, 2003.

[124] A. Rossi and S. Piccinin and V. Pellegrini and S. de Gironcoli and V. Tozzini. Nano-Scale Corrugations in Graphene: A Density Functional TheoryStudy of Structure, Electronic Properties and Hydrogenation. *J. Phys. Chem. C*, 119:7900–7910, 2015.

[125] J. Sabalot-Cuzzubbo and G. Salvato-Vallverdu and D. Begue and J. Cresson). Relating the molecular topology and local geometry: Haddon,Äôs pyramidalization angle and the Gaussian curvature. *J. Chem. Phys.*, 152:244310, 2020.

[126] R.C. Haddon. Pyramidalization: Geometrical Interpretation of the π-Orbital Axis Vector in Three Dimensions. *J. Phys. Chem.*, 91:3719, 1987.

[127] R.C. Haddon. Measure of nonplanarity in conjugated organic molecules: which structurally characterized molecule displays the highest degree of pyramidalization? *J. Am. Chem. Soc.*, 112:3385–3389, 1990.

[128] R. C. Haddon. Comment on the Relationship of the Pyramidalization Angle at a Conjugated Carbon Atom to the σ-Bond Angles. *J. Phys. Chem. A*, 105:4164–4165, 2001.

[129] M. Pizzocchero and M. Bonfanti and R. Martinazzo. To bend or not to bend, the dilemma of multiple bonds. *Phys. Chem. Chem. Phys.*, 21:26342–26350, 2019.

[130] P. Schwerdtfeger and L. N Wirz and J. Avery. The topology of fullerenes. *WIREs Comput. Mol. Sci*, 5:96–145, 2015.

[131] E. Osawa. Superaromaticity. *Kagaku*, 25:854–863, 1970.

[132] I. Stankevich and M. Nikerov and D. Bochvar. Structural chemistry of crystalline carbon: geometry, stability, electronic spectrum. *Russ Chem Rev*, 53:640,Äì665, 1984.

[133] D.Bochvar and E. G. Galpern. Electronic structure of the molecules C_{20} and C_{60}. *Proc. Acad. Sci*, 209:239–241, 1973.

[134] W. Krätschmer and L.D. Lamb and K. Fostiropoulos and D. Huffman. Solid C_{60}: a new form of carbon. *Nature*, 347:354–358, 1990.

[135] A. Omont and H. F. Bettinger. Intermediate-size fullerenes as degradation products of interstellar polycyclic aromatic hydrocarbons. *Astronomy & Astrophysics*, 650:13, 2021.

[136] J. Cami and J. Bernard-Salas and E. Peeters and S. E. Malek. Detection of C_{60} and C_{70} in a young planetary nebula. *Science*, 329:1180, 2010.

[137] J. Cami and E. Peeters and J. Bernard-Salas and G. Doppmann and J. De Buizer. The Formation of Fullerenes in Planetary Nebulae. *Galaxies*, 6:101, 2018.

[138] A. Candian and J. Zhen and A. G. G. M. Tielens. The aromatic universe. *Phys. Today*, 71:38–43, 2018.

[139] O. Berné and A. G. G. M. Tielens. Formation of buckminsterfullerene (C_{60}) in interstellar space. *PNAS*, 109:401–406, 2012.

[140] J.J. Bernal and P. Haenecour and J. Howe and T. J. Zega and S. Amari and L. M. Ziurys. Formation of Interstellar C_{60} from Silicon Carbide Circumstellar Grains. *Astro. J. Lett.*, 883:L43, 2019.

[141] R. Partha and J. L. Conyers. Biomedical applications of functionalized fullerene-based nanomaterials. *Int. J. Nanomedicine*, 4:261–275, 2009.

[142] J. Shi and L. Wang and J. Gao and Y. Liu and J. Zhang and R. Ma and R. Liu and Z. Zhang. A fullerene-based multi-functional nanoplatform for cancer theranostic applications. *Biomaterials*, 35:5571–5784, 2014.

[143] A. Hirsch and Z. Chen and H. Jiao. Spherical Aromaticity in I_h Symmetrical Fullerenes: The $2(N+1)2$ Rule. *Angew. Chem. Int. Ed. Engl.*, 39:3915–3917, 2000.

[144] M. Bühl and A. Hirsch. Spherical Aromaticity of Fullerenes. *Chem. Rev.*, 101:1153,Äì1184, 2001.

[145] P. B. Karadov. Do large polycyclic aromatic hydrocarbons and graphene bend?How popular theoretical methods complicate finding the answerto this question. *Chem. Phys. Lett.*, 646:190–196, 2016.

[146] A. H. Galué and D. G. Leines . Origin of Spectral Band Patterns in the Cosmic Unidentified Infrared Emission. *Phys. Rev. Lett.*, 119:171102, 2017.

[147] P. Sundararajan and M. Tsuge and M. Baba and Y.-P. Lee. Infrared Spectrum of Protonated Corannulene $H^+C_{20}H_{10}$ in Solid para-Hydrogen and its Potential Contribution to Interstellar Unidentified Infrared Bands. *ACS Earth Space Chem.*, 2:1001–1010, 2018.

[148] F. J. Lovas and R. J. McMahon and J.-U. Grabow and M. Schnell and J. Mack and L. T. Scott and R. L. Kuczkowski. Interstellar Chemistry: A Strategy for Detecting Polycyclic Aromatic Hydrocarbons in Space. *J. Am.Chem. Soc.*, 127:4345,àí4349, 2005.

[149] L.S. Bernstein and R. M. Shroll and G. A. Galazutdinov and Y. Beletsky. Spectral Deconvolution of the 6196 and 6614 ÅDiffuse Interstellar Bands Supports a Common-carrier Origin. *Astrophys. J.*, 859:174, 2018.

[150] R. Naaman and D. H. Waldeck. Chiral-Induced Spin Selectivity Effect. *J. Phys. Chem. Lett.*, 3:2178–2187, 2012.

[151] R. C. Haddon. Unified Theory of Resonance Energies, Ring Currents, and Aromatic Character in the $(4n+2)\pi$-Electron Annulenes. *J. Am. Chem. Soc.*, 101:1722, 1979.

[152] M. Liu and Vasilii and I. Artyukhov and H. Lee and F. Xu and B. I. Yakobson. Carbyne from First Principles: Chainof C Atoms, a Nanorod or a Nanorope. *ACS Nano*, 7:10075, 2013.

[153] M. Cappelletti and M. Leccese and M. Cococcioni and D. M. Proserpio and R. Martinazzo. The Different Story of π Bonds. *Molecules*, 26:3805, 2021.

[154] J. C. Meyer and A. K. Geim and M. I. Katsnelson and K. S. Novoselov and T. J. Booth and S. Roth . The structure of suspended graphene sheets. *Nature*, 446:60–63, 2007.

[155] A. L. Vazquez de Parga and F. Calleja and B. Borca and M. C. G. Passeggi and Jr.and J. J. Hinarejos and F. Guinea and R. Miranda. Periodically Rippled Graphene: Growth and Spatially Resolved Electronic Structure. *Phys. Rev. Lett.*, 100:056807, 2008.

[156] V. Geringer and M. Liebmann and T. Echtermeyer and S. Runte and M. Schmidt and R. Rückamp and M. C. Lemme and M. Morgenstern. Intrinsic and extrinsic corrugation of monolayer graphene deposited on SiO_2. *Phys. Rev. B*, 102:076102, 2009.

[157] D. W. Boukhvalov and M. I. Katsnelson. Enhancement of chemical activity in corrugated graphene. *J. Phys. Chem. C*, 113:14176,Äì14178, 2009.

[158] P. Z. Sun and Q. Yang and W. J. Kuang and Y. V. Stebunov and W. Q. Xiong and J. Yu and R. R. Nair and M. I. Katsnelson and S. J. Yuan and I. V. Grigorieva and M. Lozada-Hidalgo and F. C. Wang and A. K. Geim. Limits on gas impermeability of graphene. *Nature*, 579:229, 2020.

[159] V. Tozzini and V. Pellegrini. Reversible hydrogen storage by controlled buckling of graphene layers. *J. Phys. Chem. C*, 115:25523–25528, 2011.

[160] R. Balog and B. Jorgensen and J. Wells and E. Laegsgaard and P. Hofmann and F. Besenbacher and Liv Hornekaer. Atomic Hydrogen Adsorbate Structures on Graphene. *J. Am. Chem. Soc.*, 131:8744–8745, 2009.

[161] C. Riedl, U. Starke, J. Bernhardt, M. Franke, and K. Heinz. Structural properties of the graphene-SiC(0001) interface as a key for the preparation of homogeneous large-terrace graphene surfaces. *Phys. Rev. B*, 76:245406, 2007.

[162] F. Guinea and M. I. Katsnelson and M. A. H. Vozmediano. Midgap states and charge inhomogeneities in corrugated graphene. *Phys. Rev. B*, 77:075422, 2008.

[163] F. Xu and H. Yu and A. Sadrzadeh and B. I. Yakobson. Riemann Surfaces of Carbon as Graphene Nanosolenoids. *Nano Lett.*, 16:34–39, 2016.

[164] L. C. Felix and F. W. Cristiano and D.S.Galvao. Mechanical and energy-absorption properties of schwarzites. *Carbon*, 157:670–680, 2020.

[165] S. Ho Pun and Q. Miao. Toward Negatively Curved Carbons. *Acc. Chem. Res.*, 51:1630–1642, 2018.

[166] Z. Zhang and J. Chen and B. Li. Negative Gaussian curvature induces significantsuppression of thermal conduction in carbon crystals. *Nanoscale*, 9:14208–14214, 2003.

[167] A. Lherbier and H. Terrones and J.-C. Charlier. Three-dimensional massless Dirac fermions in carbon schwarzites. *Phys. Rev. B.*, 90:125434, 2014.

[168] N. Park and M. Yoon and S. Berber and J. Ihm and E. Osawa and D. Tomanek. Magnetism in All-Carbon Nanostructures with Negative Gaussian Curvature. *Phys. Rev. Lett.*, 91:237204, 2003.

[169] E. Braun and Y. Leeb and S. Mohamad Moosavib and S. Barthelb and R. Mercadod and I. A. Baburine and D. M. Proserpio and B. Smit. Generating carbon schwarzites via zeolite-templating. *PNAS*, 115:E8116, 2018.

[170] J. Hass, W. A. de Heer, and E. H. Conrad. The growth and morphology of epitaxial multilayer graphene. *J. Phys.: Condens. Matter*, 20:323202, 2008.

[171] N. Mishra, J. Boeckl, N. Motta, and F. Iacopi. Graphene growth on silicon carbide: a review. *Phys. Stat. Sol.*, 213:2277–2289, 2016.

[172] A.J. Van Bommel, J.E. Crombeen, and A.V. Tooren. LEED and Auger electron observations of the SiC(0001) surface. *Surface Science*, 48:463–472, 1975.

[173] S. Goler, C. Coletti, V. Piazza, P. Pingue, F. Colangelo, V. Pellegrini, K. V. Emtsev, S. Forti, U. Starke, F. Beltram, and S. Heun. Revealing the atomic structure of the buffer layer between SiC(0001) and epitaxial graphene. *Carbon*, 51:249–254, 2013.

[174] K.V. Emtsev, F. Speck, T. Seyller, L. Ley, and J.D. Riley. Interaction, growth, and ordering of epitaxial graphene on SiC(0001) surfaces: A comparative photoelectron spectroscopy study. *Phys. Rev. B*, 77:155303, 2008.

[175] A. Ismach, C. Druzgalski, S. Penwell, A. Schwartzberg, M. Zheng, A. Javey, J. Bokor, and Y. Zhang. Direct Chemical Vapor Deposition of Graphene on Dielectric Surfaces. *Nano. Lett.*, 10:1542–1548, 2010.

[176] Y.Gamo, A.Nagashima, M.Wakabayashi, M.Terai, and C.Oshima. Atomic structure of monolayer graphite formed on Ni(111). *Surface Science*, 374:61–64, 1997.

[177] P. W Sutter, J.-I. Flege, and E. A Sutter. Epitaxial graphene on ruthenium. *Nat. Mater.*, 7:406–411, 2008.

[178] S. Marchini, S. Günther, and J. Wintterlin. Scanning tunneling microscopy of graphene on Ru(0001). *Phys. Rev. B*, 76:075429, 2007.

[179] W. Zhao, S. M. Kozlov, O. Höfert, K. Gotterbarm, M. P.A. Lorenz, F. Vines, C. Papp, A. Görling, and H.P. Steinrück. Graphene on Ni(111): Coexistence of Different Surface Structures. *J. Phys. Chem. Lett.*, 2:759–764, 2011.

[180] S. Hertel, D. Waldmann, J. Jobst, A. Albert, M. Albrecht, S. Reshanov, A. Schöner, M. Krieger, and H.B. Weber. Tailoring the graphene/silicon carbide interface for monolithic wafer-scale electronics. *Nat. Comm.*, 3:957, 2012.

[181] S.Kim, J. Ihm, H. J. Choi, and Y.-W. Son. Origin of Anomalous Electronic Structures of Epitaxial Graphene on Silicon Carbide. *Phys. Rev. Lett.*, 100:176802, 2008.

[182] T.Ohta, A. Bostwick, J.L. McChesney, T. Seyller, K. Horn, and E. Rotenberg. Interlayer Interaction and Electronic Screening in Multilayer Graphene Investigated with Angle-Resolved Photoemission Spectroscopy. *Phys. Rev. Lett.*, 98:206802, 2007.

[183] F. C. Bocquet and R. Bisson and J.-M. Themlin and J.-M. Layet and T. Angot. Reversible hydrogenation of deuterium-intercalated quasi-free-standing graphene on SiC(0001). *Phys. Rev. B*, 85:201401(R), 2012.

[184] F. C. Bocquet and R. Bisson and J.-M. Themlin and J.-M. Layet and T. Angot. Deuterium adsorption on (and desorption from) SiC(0001)-(3×3), $(\sqrt{3} \times \sqrt{3})R30°$, $(6\sqrt{3} \times 6\sqrt{3})R30°$ and quasi-free standing graphene obtained by hydrogen intercalation. *J. Phys. D: Appl. Phys.*, 47:094014, 2014.

[185] J. Sforzini, L. Nemec, T. Denig, B. Stadtmüller, T.-L. Lee, C. Kumpf, S. Soubatch, U. Starke, P. Rinke, V. Blum, F. C Bocquet, and F. S. Tautz. Approaching Truly Freestanding Graphene: The Structure of Hydrogen-Intercalated Graphene on 6H-SiC(0001). *Phys. Rev. Lett.*, 114:106804, 2015.

[186] S. Watcharinyanon, C. Virojanadara, J.R. Osiecki, A.A. Zakharov, R. Yakimova, R.I.G. Uhrberg, and L.I. Johansson. Hydrogen intercalation of graphene grown on 6H-SiC(0001). *Surface Science*, 605:1662–1668, 2011.

[187] Maciej J. Szary, Semir El-Ahmar, and Tymoteusz Ciuk. The impact of partial h intercalation on the quasi-free-standing properties of graphene on SiC(0001). *Applied Surface Science*, 541:148668, 2021.

[188] C. Riedl, C. Coletti, T. Iwasaki, A. A. Zakharov, and U. Starke. Quasi-free-standing Epitaxial Graphene on SiC Obtained by Hydrogen Intercalation. *Phys. Rev. Lett.*, 103:246804, 2009.

[189] Y.-P. Lin, Y. Ksari, and J.-M. Themlin. Hydrogenation of the buffer-layer graphene on 6H-SiC (0001): A possible route for the engineering of graphene- based devices. *Nano Research*, 8:839–850, 2015.

[190] F. Varchon, P. Mallet, J.-Y. Veuillen, and L. Magaud. Ripples in epitaxial graphene on the Si-terminated SiC(0001) surface . *Phys. Rev. B*, 77:235412, 2008.

[191] The Editors of Encyclopaedia Britannica. Moiré pattern. https://www.britannica.com/science/moire-pattern.

[192] M. Xu, Y. R. Girish, K. P. Rakesh, P. Wua, H. M. Manukumar, S. M. Byrappa, Udayabhanu, and K. Byrappa. Recent advances and challenges in silicon carbide (SiC) ceramic nanoarchitectures and their applications. *Mat. Today Comm.*, 28:102533, 2021.

[193] T. Kimoto and J. A. Cooper. *Fundamentals of Silicon Carbide Technology.* Wiley, 2014.

[194] R. Wu, K. Zhou, C. Y. Yue, J. Wei, and Y. Pan. Recent progress in synthesis, properties and potential applications of SiC nanomaterials Renbing. *Progress in Material Science*, 72:1–60, 2015.

[195] H. Moissan. Étude du siliciure de carbone de la météorite de canon diablo. *Compt. Rend.*, 140:405, 1905.

[196] E. G. Acheson. Production of artificial crystalline carbonaceous materials, carborundum. English Patent 17911, 1892.

[197] S. Yoshida, E. Sakuma, H. Okumura, S. Misawa, and K. Endo. Heteroepitaxial growth of SiC polytypes. *J. App. Phys.*, 62:303, 1987.

[198] N. K. Kildahl. Bond Energy Data Summarized. *J. Chem. Educ.*, 72:423, 1995.

[199] C. A. Klein and F. G. Cardinale. Young's modulus and Poisson's ratio of CVD diamond. *Diamond and Related Materials* , 2:918–923, 1992.

[200] M. A. Hopcroft, W. D. Nix, and T. W. Kenny. What is the Young's Modulus of Silicon? *J. Micromechanical System*, 19:229–238, 2010.

[201] C.A. Zorman and R.J. Parro. Micro- and nanomechanical structures for silicon carbide MEMS and NEMS. *Phys. Status Solidi B*, 245:195203, 2008.

[202] K. Daviau and K. K. M. Lee. Decomposition of silicon carbide at high pressures and temperatures. *Phys. Rev. B*, 96:174102, 2017.

[203] K.Daviau and K. K. M. Lee. High-Pressure, High-Temperature Behavior of Silicon Carbide: A Review. *Crystal*, 8:217, 2018.

[204] A. V. Sinelnik and A. V. Semenov. Theoretical study of the band structure of 2H-SiC and 4H-SiC of silicon carbide polytypes. *Cond. Matt. Phys.*, 24:23706, 2021.

[205] P. J. Collings. Simple measurement of the band gap in silicon and germanium. *American J. Phys.*, 48:197, 1980.

[206] P. Kusch, S. Breuer, M. Ramsteiner, L. Geelhaar, H. Riechert, and S. Reich. Band gap of wurtzite GaAs: A resonant Raman study. *Phys. Rev. B*, 86:075317, 2012.

[207] C. Codreanu, M. Avram, E. Carbunescu, and E. Iliescu. Comparison of 3C-SiC, 6H-SiC and 4H-SiC MESFETs performances. *Mat. Science in Semiconductos Processing*, 3:137–142, 2000.

[208] H. M. Hobgood, M. Brady, W. Brixius, G. Fechko, R.C. Glass, D. Henshall, J. R. Jenny, R.T. Leonard, D.P. Malta, S. G. Müller, V. F. Tsvetkov, and C. H. Carter Jr. Status of Large Diameter SiC Crystal Growth for Electronic and Optical Applications. *Mater. Sci. Forum*, 3:338–342, 2000.

[209] C. J. Glassbrenner and Glen A. Slack. Thermal Conductivity of Silicon and Germanium from 3 K to the Melting Point. *Phys. Rev.*, 134:1058, 1964.

[210] Luxmi, N. Srivastava, G. He, R. M. Feenstra, and P. J. Fisher. Comparison of graphene formation on C-face and Si-face SiC0001 surfaces. *Phys. Rev. B*, 82:235406, 2010.

[211] K. V. Emtsev, A. Bostwick, K. Horn, J. Jobst, Ga. L. Kellogg, L. Ley, J. L. McChesney, T. Ohta, S. A. Reshanov, J. Röhrl, E. Rotenberg, A. K. Schmid, D. Waldmann, H. B. Weber, and T. Seyller. Towards wafer-size graphene layers by atmospheric pressure graphitization of silicon carbide. *Nature Materials*, 8:203–207, 2009.

[212] J. Schardt, J. Bernhardt, U. Starke, and K. Heinz. Crystallography of the (3x3) surface reconstruction of 3C-SiC(111),4H-SiC(0001) and 6H-Si(0001) surfaces retrieved by low-energy electron diffraction. *Phys. Rev. B*, 62:1035, 2000.

[213] L.Li and I.S.T.Tsong. Atomic structures of 6H-SiC(0001) and $(000\bar{1})$ surfaces. *Surface Science*, 351:141–148, 1996.

[214] M. H. Tsai, C. S. Chang, John D. Dow, and I. S. T. Tsong. Electronic contributions to scanning-tunneling-microscopy images of an annealed β-SiC(111) surface. *Phys. Rev. B*, 45:1327, 1992.

[215] U. Starke and C. Riedl. Epitaxial graphene on SiC(0001) and SiC$(000\bar{1})$ from surface reconstructions to carbon electronics. *J. Phys.: Condens. Matter*, 21:134016, 2009.

[216] U. Starke and J. Schardt amnd M. Franke. Morphology, bond saturation and reconstruction of hexagonal SiC surfaces. *App. Phys. A*, 65:587–596, 1997.

[217] A. Mattausch and O. Pankratov. Ab Initio Study of Graphene on SiC. *Phys. Rev. Lett.*, 99:076802, 2007.

[218] L. Nemec, V. Blum, P. Rinke, and M. Scheffler. Thermodynamic Equilibrium Conditions of Graphene Films on SiC. *Phys. Rev. Lett.*, 111:065502, 2013.

[219] K. Yagyu, T. Tajiri, A. Kohno, K. Takahashi, H. Tochihara, H. Tomokage, and T. Suzuki. Fabrication of a single layer graphene by copper intercalation on a SiC(0001) surface. *Appl. Phys. Lett.*, 104:053115, 2014.

[220] C. Coletti, K. V. Emtsev, A. A. Zakharov, T. Ouisse, D. Chaussende, and U. Starke. Large area quasi-free standing monolayer graphene on 3C-SiC(111). *Appl. Phys. Lett.*, 99:081904, 2011.

[221] W. Norimatsu and M. Kusunoki. Transitional structures of the interface between graphene and 6H-SiC(0001) . *Chem. Phys. Lett.*, 468:52–56, 2009.

[222] T. Ohta, A. Bostwick, T. Seyller, K. Horn, and E. Rotenberg. Controlling the electronic structure of bilayer graphene. *Science*, 313:951–954, 2006.

[223] A. Al-Temimy, C. Riedl, and U. Starke. Low temperature growth of epitaxial graphene on SiC induced by carbon evaporation. *Appl. Phys. Lett.*, 95:231907, 2009.

[224] C. Bouhafs, S. Pezzini, F. R. Geisenhof, N. Mishra, V. Misekis, Y. Niu, C. Struzzi, R. T. Weitz, A. A. Zakharov, S. Forti, and C. Coletti. Synthesis of large-area rhombohedral few-layer graphene by chemical vapor deposition on copper. *Carbon*, 177:282–290, 2021.

[225] R. R. Haering. Band structure of rhombohedral graphite. *Can. J. Phys.*, 36:352, 1958.

[226] K. V. Emtsev, T. Seyller, F. Speck, L. Ley, P. Stojanov, J.D. Riley, and R.C.G. Leckey. Initial Stages of the Graphite-SiC(0001) Interface Formation Studied by Photoelectron Spectroscopy. *Mater. Sci. Forum*, 556:525, 2007.

[227] S. Y. Zhou, G.-H. Gweon, A. V. Fedorov, P. N. First, W. A. De Heer, D.-H. Lee, F. Guinea, A. H. Castro Neto, and A. Lanzara. Substrate-induced bandgap opening in epitaxial graphene. *Nature Materials*, 6:770, 2007.

[228] C. Riedl, A. A. Zakharov, and U. Starke. Precise in situ thickness analysis of epitaxial graphene layers on SiC(0001) using low-energy electron diffraction and angle resolved ultraviolet photoelectron spectroscopy. *Appl. Phys. Lett.*, 93:033106, 2008.

[229] C. Coletti, C. Riedl, D. S. Lee, B. Krauss, L. Patthey, K. von Klitzing, J. H. Smet, and U. Starke. Charge neutrality and band-gap tuning of epitaxial graphene on SiC by molecular doping. *Phys. Rev. B*, 81:235401, 2010.

[230] H. Pinto, R. Jones J. P. Goss, and P. R. Briddon. p-type doping of graphene with F4-TCNQ. *J. Phys.: Condens. Matter*, 21:402001, 2009.

[231] N. P. Guisinger, G. M. Rutter, J. N. Crain, P. N. First, and J. A. Stroscio. Exposure of Epitaxial Graphene on SiC(0001) to Atomic Hydrogen. *Nano Lett.*, 9:1462–1466, 2009.

[232] A. Markevich, R. Jones, S. Öberg, M. J. Rayson, J. P. Goss, and P. R. Briddon. First-principles study of hydrogen and fluorine intercalation into graphene-SiC(0001) interface. *Phys. Rev. B*, 86:45453, 2012.

[233] J. Slawinska, H. Aramberri, M.C. Munoz, and J.I. Cerdá. Ab initio study of the relationship between spontaneous polarization and p-type doping in quasi-freestanding graphene on H-passivated SiC surfaces. *Carbon*, 93:88–104, 2015.

[234] C. Yu anmd Q. Liu, J. Li, W. Lu, Z. He, S. Cai, and Z. Feng. Preparation and electrical transport properties of quasi free standing bilayer graphene on SiC (0001) substrate by H intercalation. *Appl. Phys. Lett.*, 105:183105, 2014.

[235] G. Sclauzero and A. Pasquarello. Carbon rehybridization at the graphene/SiC(0001) interface: Effect on stability and atomic-scale corrugation. *Phys. Rev. B*, 85:161405, 2012.

[236] G. Sclauzero and A. Pasquarello. First-principles study of H adsorption on graphene/SiC(0001). *Phys. Status Solidi*, 250:2523–2528, 2013.

[237] S. Goler, C. Coletti, V. Tozzini, V. Piazza, T. Mashoff, F. Beltram, V. Pellegrini, and S. Heun. Influence of Graphene Curvature on Hydrogen Adsorption: Toward Hydrogen Storage Devices. *J. Phys. Chem. C*, 117:50, 2013.

[238] L. Hedberg and K. Hedberg and P.-c. Cheng and L. T. Scott. Gas-Phase Molecular Structure of Corannulene, $C_{20}H_{10}$. An Electron-Diffraction Study Augmented by ab Initio and Normal Coordinate Calculations. *J. Phys. Chem. A*, 104:7689–7694, 2000.

[239] L. T. Scott and M. M. Hashemi and M. S. Bratcher. Corannulene bowl-to-bowl inversion is rapid at room temperature. . *Am. Chem. Soc.*, 114:1920–1921, 1992.

[240] M. G. Evans and M. Polanyi. Inertia and driving force of chemical reactions. *Trans. Faraday Soc.*, 34:11, 1938.

[241] E. Clar. *The Aromatic Sextet*. Wiley, 1972.

[242] A. Garcia, N. Papior, A. Akhtar, E. Artacho, V. Blum, E. Bosoni, P. Brandimarte, M. Brandbyge, J. I. Cerda, F. Corsetti, R. Cuadrado, V. Dikan, J. Ferrer, J. Gale, P. Garcia-Fernandez, V. M. Garcia-Suarez, S. Garcia, G. Huhs, S. Illera, R. Korytar, P. Koval, I. Lebedeva, L. Lin, P.Lopez-Tarifa, S. G. Mayo, S. Mohr, P. Ordejon, A. Postniko, Y. Pouillon, M. Pruneda, R. Robles, D. Sanchez-Portal, J.M. Soler, R. Ullah, V. W.-Z. Yu, and J. Junquera. Siesta: Recent developments andapplications. *J. Chem. Phys.*, 152:204108, 2020.

[243] J. P. Perdew, K. Burke, and M. Ernzerhof. Generalized gradient approximation made simple. *Phys. Rev. Lett.*, 77:3865, 1996.

[244] O. A. Vydrov and T. Van Voorhis. Nonlocal van der waals density functional:the simpler the better. *J. Chem. Phys.*, 133:244103, 2010.

[245] M. Pizzochero, O. Leenaerts andB. Partoens, R. Martinazzo, and F. M Peeters. Hydrogen adsorption on nitrogen and boron doped graphene. *J. Phys.: Condens. Matter*, 27:425502, 2015.

[246] L. F. Huang, M. Y. Ni, G. R. Zhang, W. H. Zhou, Y. G. Li, X. H. Zheng, and Z. Zeng. Modulation of the thermodynamic, kinetic, and magnetic properties of the hydrogen monomer on graphene by charge doping. *J. Chem. Phys.*, 135:064705, 2011.

[247] M. Persson and B. Jackson. Flat surface study of the Eley-Rideal dynamics of recombinative desorption of hydrogen on metal surface. *J. Chem. Phys.*, 102:1078, 1994.

[248] R. I. Hal and I. Cadez and M. Landau and F. Pichou and C. Schermann. Vibrational Excitation of Hydrogen via Recombinative Desorption of Atomic Hydrogen Gas on a Metal Surface. *Phys. Rev. Lett.*, 60:337, 1988.

[249] P. J. Eenshuistra and J. H. M. Bonnie and J. Los and H. J. Hopman. Observation of Exceptionally High Vibrational Excitation of Hydrogen Molecules Formed by Wall Recombination. *Phys. Rev. Lett.*, 60:341, 1988.

[250] C. T. Rettner. Dynamics of the direct reaction of hydrogen atoms adsorbed on Cu(111) with hydrogen atoms incident from the gas phase. *Phys. Rev. Lett.*, 69:383, 1992.

[251] K. R. Lykke and B. D. Kay. *Laser Photoionization and Desorption Surface Analysis Technique.* edited by N. S. Nogar, 1990.

[252] S. Sato. . *Nippon Kagaku Zasshi*, 77:1202, 1956.

[253] B. Jackson and D. Lemoine. Eley-Rideal reactions between H atoms on metal and graphite surfaces: The variation of reactivity with substrate. *J. Chem. Phys.*, 114:474, 2001.

[254] X. Sha and B. Jackson, and D. Lemoine. Quantum studies of Eley-Rideal reactions between H atoms on a graphite surface. *J. Chem. Phys.*, 116:7158, 2002.

[255] R. Martinazzo and G. F. Tantardini. Quantum study of Eley-Rideal reaction and collision induced desorption of hydrogen atoms on a graphite surface. I. H chemisorbed case. *J. Chem. Phys.*, 124:124702, 2006.

[256] M. Pasquini and M. Bonfanti and R. Martinazzo. Full quantum dynamical investigation of the Eley-Rideal reaction forming H2 on a movable graphitic substrate at T = 0 K. *Phys. Chem. Chem. Phys.*, 20:9779, 2018.

[257] D. Lemoine. The discrete Bessel transform algorithm. *J. Chem. Phys.*, 101:3936, 1994.

[258] D. Lemoine and B. Jackson. Quantum wave packet approach to the Eley,ÄìRideal reactive scattering between a gas phase atom and an adsorbate. *Comput. Phys. Commun.*, 137:415,426, 2001.

[259] D. Lemoine. A note on orthogonal discrete Bessel representations. *J. Chem. Phys.*, 118:6697, 2003.

[260] E. Kreyszig. *Differential Geometry.* Dover, 1991.

[261] B. Riemann. *Über die Hypothesen, welche der Geometrie zu Grande liegen.* Göttingen, 1854.

[262] D. Lovelock and H. Rund. *Tensors, Differential Forms and Variational Principles.* Dover, 1989.

[263] L. I. de la Vallée. *Traité de géometrie descriptive.* Paris, 1825.

[264] F. Frenet. Sur les courbes á double courbure. *Thése, Toulouse*, 1847.

[265] J. B. M. Ch. Neusnier. Mémoire sur la courbure des surfaes. *Mém. des Savants étrangers*, 10:504, 1785.

[266] L. Euler. Recherches sur la courbure des surfaces. *Mem. de l'Acad. des Sciences, Berlin*, 16:119–143, 1760.

[267] G. Mainardi. *Giorn. Ist. Lomb.*, 9:360, 1856.

[268] D. Codazzi. *Annali di Mat.* , 2:273, 1868.

[269] C.F. Gauss. Disquisitiones generales circa superficies curvas. *Collected papers*, 4:217–258, 1827.

[270] S. Shaik and A. Shurki and D. Danovich and P. C. Hiberty. A Different Story of π-DelocalizationsThe Distortivity of π-Electrons and Its Chemical Manifestations. *Chem. Rev.*, 101:1501–1539, 2000.

[271] National Istitute of Standards and Technology (NIST) U.S. Department of Commerce. Hydrogen shomate equation. https://webbook.nist.gov/cgi/cbook.cgi?ID=C1333740&Mask=1&Type=JANAFG&Plot=on.

[272] J. R. Taylor. *Scattering Theory: The Quantum Theory on Nonrelativistic Collisions*. Wiley, 1972.